

Ph.D. Dissertation

Assessment of planetary boundary-layer schemes with advanced remote sensing instruments and air quality modelling

A thesis submitted to the Universitat Politècnica de Catalunya
in partial fulfillment for the degree of
Doctor of Philosophy

Robert F. Banks

Directors:

Dr. José María Baldasano Recio (Dept. of Earth Sciences, Barcelona Supercomputing Center-Centro Nacional de Supercomputación [BSC-CNS], Barcelona; and Environmental Modelling Lab., Universitat Politècnica de Catalunya [UPC], Barcelona)

Dr. Santiago Gassó i Domingo (Dept. of Eng. de Projectes i de la Construcció [DEPC], Universitat Politècnica de Catalunya [UPC], Barcelona)

Universitat Politècnica de Catalunya
Doctoral Program in Environmental Engineering

Barcelona, April 2016



UNIVERSITAT POLITÈCNICA
DE CATALUNYA
BARCELONATECH



Environmental Engineering



UNIVERSITAT POLITÈCNICA
DE CATALUNYA
BARCELONATECH



Environmental Engineering

For Cassie and Keegan



UNIVERSITAT POLITÈCNICA
DE CATALUNYA
BARCELONATECH



Environmental Engineering



“A new truth is a truth, an old error is an error.”

- Benjamin Franklin (1734)



UNIVERSITAT POLITÈCNICA
DE CATALUNYA
BARCELONATECH



Environmental Engineering



Acknowledgements

The research leading to these results has received funding from the European Union Seventh Framework Programme (FP7/2007-2013): People, ITN Marie Curie Actions Programme (2012-2016) in the frame of ITaRS under grant agreement n° 289923.

First of all, my sincere gratitude to my Ph.D. supervisors, Dr. José María Baldasano and Dr. Santiago Gassó Domingo, for their guidance and strong support during the project. The advice and comments from Dr. Baldasano helped make this project a success. In addition, thanks to the Barcelona Supercomputing Center – Centro Nacional de Supercomputación (BSC-CNS) for hosting me during the 3-year stay of the Ph.D. thesis. Support provided by the BSC-CNS and associated staff was very helpful and appreciated.

I would also like to thank those I had the pleasure and luck to work with in my secondment to the National Technical University of Athens (NTUA) in May-June 2014. Thanks to Prof. Alexandros Papayannis for giving me this opportunity and being my supervisor during this visit, and to Athina Argyrouli, Dr. Panos Kokkalis, Dr. Ioannis Binietoglou, and Dr. Lev Labzovsky for their help and technical support.

Special thanks to Dr. Francesc Rocadenbosch, Dr. Adolfo Comerón, and Dr. Michaël Sicard at the UPC Remote Sensing Laboratory for use of the extended Kalman filter technique, and for valuable discussions throughout the Ph.D. thesis. A special recognition to Dr. Jordi Tiana-Alsina for his contributions to the analysis of lidar observations. In addition, I wish to thank Victor Valverde for his assistance with the air quality simulations in the final stages of the project.

Finally, this Ph.D. was also possible thanks to the collaboration of many scientists, including Dr. Jasper Lewis and Dr. Ellsworth (Judd) Welton from NASA. I would like to acknowledge all the co-authors of the publications done in the framework of this thesis. In addition, thanks to Dr. Susanne Crewell (Project Coordinator) and Ms. Sarah Henkel (Program Assistant) for excellent execution of the ITaRS network.

WRF simulations were executed on the MareNostrum supercomputer at the BSC-CNS, under grants SEV-2011-00067 of Severo Ochoa program and CGL-2013-46736-R, awarded by the Spanish Government. Also, credit (UE FP7-INFRA-2010-1.1.16) to the ACTRIS (Aerosols, Clouds, and Trace gases Research InfraStructure) network. A grateful acknowledgement to the NOAA Air Resources Laboratory (ARL) for the provision of the HYSPLIT transport and dispersion model and/or READY website (<http://www.ready.noaa.gov>) used in this publication. A special thanks to Albert Soret and Kim Serradell for their assistance with the cluster analysis algorithm. Also, thanks to the Meteorological Service of Catalonia for providing the Barcelona radiosonde data.



Abstract

Urban air pollution is of major concern in Spain and also throughout Europe and globally with numerous effects on human health and ecosystems. Since air quality (AQ) is predominantly a problem for human health and the environment, the lowest levels of the atmosphere are the most important to investigate, mainly the planetary boundary-layer (PBL). Atmospheric variables (i.e. temperature, humidity, winds) in the PBL are critically important as inputs for accurate simulations in AQ models. From a modeling standpoint PBL height can be extremely difficult to compute accurately due to the fact that boundary layer processes occur at smaller geographical scales than mesoscale meteorological models can resolve. To that end, atmospheric models make use of parameterizations to represent the boundary layer structure in the lower atmosphere.

This Ph.D. thesis evaluates the sensitivity of high-resolution AQ simulations from the CALIOPE AQ forecast system (www.bsc.es/caliope) in the distribution of gaseous photochemical pollutants using different PBL schemes in the Weather Research and Forecasting (WRF) model. The project is separated into three main activities.

First, was an evaluation of available methods for estimating PBL height from lidar measurements based on data from the Barcelona multiwavelength Raman lidar, a member site of the European Aerosol Research Lidar Network (EARLINET). Lidar-estimated PBL heights were compared with those obtained from radiosoundings. It was found that a time-adaptive extended Kalman filter (EKF) technique provided lidar estimates closest ($R^2 = 0.96$) to values estimated with radiosoundings. The 13-yr average PBL height was 1.28 ± 0.4 km with the EKF method, which is similar to previous studies.

In the second activity, eight PBL schemes from the WRF model were evaluated as compared to observations over Barcelona and Athens. Instrumentation included two lidars, and numerous radiosondes and surface meteorological stations. Data from Athens was collected during the 39-day HygrA-CD field campaign, which took place in summer 2014. In both studies it was generally found that non-local PBL schemes perform



better. For example, the non-local asymmetric convective model version 2 (ACM2) scheme showed coefficient of determination values of 0.33 and 0.15, for the Barcelona and Athens studies, respectively. WRF model simulations with the ACM2 scheme only slightly under-estimated PBL heights in Athens during Etesians events, with a mean bias around 0.11 km.

In the final activity, four WRF PBL schemes were sensitivity-tested with model simulations from the CALIOPE AQ forecast system, as compared with surface observations from ground AQ stations and lidar data from the Barcelona micropulse lidar (MPL), a new station in the NASA Micropulse Lidar Network (MPLNET). It was found that WRF model-simulated PBL height and surface meteorology can largely impact the simulations of air pollution variables (O_3 , NO_2 , PM_{10}). CMAQ model simulations coupled to WRF with the ACM2 and Bougeault–Lacarrère (BouLac) PBL schemes performed the best for surface ozone concentrations (O_3) at rural background stations, with correlation values of 0.82 and 0.79 compared to surface AQ observations, respectively. In addition, spatial analysis of the CMAQ model simulations showed the lowest biases using the ACM2 and BouLac schemes.

The outcome from this project is a deeper understanding of the sensitivity of AQ simulations to model PBL schemes, which may result in more accurate operational AQ forecasts.

Publications derived from thesis

International Journals Included in the Science Citation Index (SCI):

Banks, R. F. and J. M. Baldasano (2016), Impact of WRF model PBL schemes on air quality simulations over Catalonia, Spain, *Atmos. Chem. Phys.*, Submitted.

Labzovskii, L., I. Biniotoglou, A. Papayannis, **Banks, R.F.**, and J. M. Baldasano (2016), Comparison of two methods for relative humidity retrieval using lidar and radiometer, *Atmos. Meas. Tech.*, In prep.

Papayannis, A., A. Argyrouli, A. Bougiatioti, E. Remoundaki, S. Vratolis, A. Nenes, J. Van de Hey, M. Komppula, S. Solomos, S. Kazadzis, **R. F. Banks**, L. Labzovskii, I. Kalogiros, C. G. Tzanis, I. Biniotoglou, and C. S. Zerefos (2016), From hygroscopic aerosols to cloud droplets: the HygrA-CD Campaign in the Athens basin – An overview, *Sci. Total Environ.*, Submitted.

Banks, R. F., S. Crewell, S. Henkel, and J. M. Baldasano (2016), European training network for young atmospheric researchers, *AGU Eos* **97**, doi:10.1029/2016EO045899 .

Banks, R. F., J. Tiana-Alsina, J. M. Baldasano, F. Rocadenbosch, A. Papayannis, S. Solomos, and C. G. Tzanis (2016), Sensitivity of boundary layer variables to PBL schemes in the WRF model based on surface meteorological observations, lidar, and radiosondes during the HygrA-CD campaign, *Atmos. Research*, In press.

Labzovskii, L., I. Biniotoglou, A. Papayannis, **Banks, R.F.**, and J. M. Baldasano (2015), Use of lidar water vapor retrieval for assessment of model capability to simulate water vapor profiles, in *Proc. SPIE 9645*, **96450G**, doi:10.1117/12.2195638.

Banks, R. F., J. Tiana-Alsina, J. M. Baldasano, and F. Rocadenbosch (2015), Performance evaluation of boundary-layer height from lidar and the Weather Research and Forecasting model at an urban coastal site in the north-east Iberian Peninsula, *Bound.-Lay. Meteorol.*, **157(2)**, 265-292, doi:10.1007/s10546-015-0056-2, Open access.

Banks, R. F., J. Tiana-Alsina, J. M. Baldasano, and F. Rocadenbosch (2014), Retrieval of boundary layer height from lidar using extended Kalman filter approach, classic methods, and backtrajectory cluster analysis, in *Proc. SPIE 9242*, **92420F**, doi:10.1117/12.2072049, *Best student paper award*.

Conference contributions:

Banks, R.F., J. M. Baldasano, and M. Pandolfi (2016), Meteorological applications of a continuously-operating micropulse lidar in Barcelona, Spain, *96th Annual Meeting of the Amer. Meteorol. Soc.*, 09.-14.01.2016, New Orleans, USA, [poster].

Lewis, J., **R. Banks**, T. Berkoff, E. Welton, E. Joseph, A. Thompson, P. Decola, and J. Hegarty (2015), Spatiotemporal variability in observations of urban mixed-layer heights from surface-based lidar systems during DISCOVER-AQ 2011, *AGU Fall Meeting 2015*, 14.-18.12.2016, San Francisco, USA. [poster]

Banks, R.F. and J. M. Baldasano (2015), Impact of WRF PBL schemes on boundary-layer simulations using lidar, modelling, and observations during Spring 2015: Towards improvement of an air quality forecast system, *Met. and Clim. – Met. Aspects of Air Qual. (MAC-MAQ) conference*, 16.-18.09.2015, Sacramento, USA. [talk]

Banks, R.F., J. Tiana Alsina, J. M. Baldasano, F. Rocadenbosch, and A. Papayannis (2015), Sensitivity of boundary layer variables to WRF model PBL schemes during the 2014 Athens HygrA-CD campaign, *EGU General Assembly 2015*, 12.-17.04.2015, Vienna, Austria, Geophys. Res. Abstracts (17), EGU2015-455. [poster]

Labzovskii, L., I. Biniotoglou, A. Papayannis, **Banks, R.F.**, and J. M. Baldasano (2015), Evaluation of model-simulated water profiles as a tool for aerosol hygroscopicity studies: based upon lidar and microwave radiometer measurements from the HygrA-CD campaign, *EGU General Assembly 2015*, 13.04.2015, Vienna, Austria, Geophys. Res. Abstracts (17), EGU2015-658. [talk]

- Banks, R. F.**, J. M. Baldasano, F. Rocadenbosch, M. Sicard, and A. Comerón (2014), PBL height retrieval over Barcelona from EARLINET and Micro-Pulse lidars, and WRF mesoscale meteorological model, *4th Joint ACTRIS WP2/WP20 Workshop*, 28.-31.10.2014, Lille, France. [talk]
- Banks, R. F.**, J. Tiana-Alsina, J. M. Baldasano, F. Rocadenbosch, (2014), Retrieval of boundary layer height from lidar using extended Kalman filter approach, classic methods, and backtrajectory cluster analysis, *2014 SPIE Remote Sensing Conference*, 21.-25.09.2014, Amsterdam, The Netherlands. [talk]
- Banks, R.F.**, J. Baldasano, A. Comerón, M. Sicard, and F. Rocadenbosch (2013), Inter-comparison of lidar methods for obtaining planetary boundary-layer height from a July 2012 monitoring campaign over the Iberian Peninsula in the framework of EARLINET, *Abstract A43A-0225 presented at 2013 Fall Meeting, AGU, San Francisco, Calif., 9-13 Dec.* [poster]

ITaRS-related presentations:

- Banks, R.F.**, J. Tiana-Alsina, J. Baldasano, F. Rocadenbosch, and A. Papayannis (2014), Investigation of planetary boundary-layer properties over Athens, Greece during the 2014 HygrA-CD campaign, *2nd ITaRS Summer School*, 08.09.2014, Jülich, Germany.
- Banks, R.F.**, J. Baldasano, and F. Rocadenbosch (2014), Determination of boundary-layer heights from lidar using Kalman filter, classic methods, and synoptic cluster analysis, *ITaRS-Mid-term Review Meeting*, 19.-21.02.2014, Potsdam, Germany.
- Banks, R.F.**, J. M. Baldasano, A. Comerón, M. Sicard (2013), Inter-comparison of lidar methods for obtaining planetary boundary-layer height from a July 2012 monitoring campaign over the Iberian Peninsula in the framework of EARLINET, *1st ITaRS Summer School*, 23.09.-04.10.2013, Bucharest, Romania.



UNIVERSITAT POLITÈCNICA
DE CATALUNYA
BARCELONATECH



Environmental Engineering



Table of Contents

1	Introduction.....	1
1.1	Air quality over Europe	1
1.1.1	Air quality forecast systems: why are they needed?.....	4
1.1.2	Importance of PBL schemes in numerical weather prediction.....	5
1.1.3	Previous works evaluating PBL schemes and AQ models	9
1.2	The Initial Training for Atmospheric Remote Sensing (ITaRS) network	10
1.2.1	General description of the ITaRS network.....	11
1.3	Ph.D. mobility context: Secondment to National Technical University of Athens	13
1.3.1	Overview of the HygrA-CD field campaign.....	13
1.3.2	Outcomes.....	14
1.4	Motivation of Ph.D.....	14
1.5	Main objectives.....	15
1.5.1	Obj. 1: Evaluation of available methods for estimating PBL height from lidar measurements	15
1.5.2	Obj. 2: Examine sensitivity of model-simulated boundary-layer variables to PBL parameterization schemes in the WRF model.....	15
1.5.3	Obj. 3: Analyze impact of WRF PBL schemes to photochemical and aerosol simulations from the CALIOPE air quality forecast system.....	16
1.6	Organization of the Ph.D. thesis	16
2	Inter-comparison of lidar methods for obtaining planetary boundary-layer height from a July 2012 monitoring campaign over the Iberian Peninsula in the framework of EARLINET	17
2.1	Introduction.....	17



2.2	Data and methodology.....	18
2.2.1	Characteristics of lidar instruments used.....	18
2.2.2	Methods for estimating PBL height from lidar	20
2.2.3	Calculation of PBL height from radiosonde launches	22
2.2.4	Synoptic situation	22
2.3	Results and discussion.....	24
2.4	Conclusions	27
3	Performance evaluation of boundary-layer height from lidar and the Weather Research and Forecasting model at an urban coastal site in the north-east Iberian Peninsula	29
3.1	Introduction	30
3.2	Model configuration, observations, and cluster analysis	33
3.2.1	WRF model set-up.....	33
3.2.2	Elastic backscatter lidar	37
3.2.3	Radiosoundings	39
3.2.4	Back-trajectory cluster analysis.....	40
3.3	Methods to estimate PBL height from lidar	41
3.3.1	Classic methods	41
3.3.2	UPC extended Kalman filter technique	42
3.4	Results and discussion.....	45
3.4.1	Objectively determined synoptic cluster types.....	45
3.4.2	PBL height comparisons between lidar methods and radiosounding	48
3.4.3	Performance evaluation of WRF model PBL schemes	51
3.4.4	Representative cases of most frequent synoptic clusters.....	54
3.4.5	Surface energy fluxes.....	60
3.6	Conclusions	60

4	Sensitivity of boundary-layer variables to PBL schemes in the WRF model based on surface meteorological observations, lidar, and radiosondes during the Hygr A-CD campaign.....	65
4.1	Introduction	66
4.2	Model configuration, synoptic conditions, and observations	68
4.2.1	WRF model configuration	68
4.2.2	Identification of primary synoptic situations	73
4.2.3	PBL height from backscatter lidar	75
4.2.4	Surface meteorological observations and radiosoundings	77
4.3	Results and discussion	79
4.3.1	Near-surface meteorological variables (T2, RH2, WS10)	79
4.3.2	PBL height intercomparison	87
4.3.3	Impact of PBL schemes on vertical profiles	93
4.3.4	Sensible heat flux comparison.....	95
4.4	Comparison to previous studies.....	97
4.5	Conclusions	99
5	Impact of WRF model PBL schemes on air quality simulations over Catalonia, Spain	101
5.1	Introduction	102
5.2	Models, case study, and observations.....	104
5.2.1	Description of case study.....	104
5.2.2	Modelling strategy.....	106
5.2.3	Evaluation data	110
5.3	Results and discussion.....	111
5.3.1	Evaluation of WRF meteorology.....	111
5.3.2	Air quality evaluation.....	119
5.4	Conclusions	124
6	Conclusions and future research	127



6.1	Synthesis of results.....	127
6.1.1	Methods to estimate PBL height from lidar	128
6.1.2	Evaluation of model PBL schemes over Barcelona and Athens	130
6.1.3	Impact of WRF PBL schemes on air quality simulations.....	131
6.2	Future research lines.....	133
	References	135



List of Tables

<i>Table 2.1 Characteristics of the four EARLINET lidar stations, as of the 2012 monitoring campaign.</i>	20
<i>Table 3.1 Summary of WRF model v3.4.1 experiment sets with PBL parametrization schemes and surface-layer schemes used in the study. Also shown are the operational methods of PBL height for each scheme, along with the threshold values used.</i>	35
<i>Table 3.2 Summary of instrument specifications for the two UPC lidar instruments used in this study: time periods (2007 – 2010) and (2010 – 2013). Also shown are the ranges determined for the initial state vector to the EKF method and the threshold ranges selected for the threshold method.</i>	38
<i>Table 3.3 Mean value (km) of lidar-EKF and mean relative bias ($(\text{WRF model} - \text{lidar EKF})/(\text{lidar EKF})$) of PBL heights diagnosed with WRF model simulations using eight PBL schemes. <i>Italic-faced type is used when the PBL height from the WRF model is within $\pm 20\%$ of the lidar estimates. Results shown for total (All) lidar days and when grouped by 7 synoptic clusters arriving at 1.5 km. Bold-faced type represent the closest PBL schemes for each synoptic cluster and the total.</i></i>	53
<i>Table 4.1 Summary of WRF v3.4.1 experiment sets with PBL parametrization schemes (PBL SCHEME) and surface-layer schemes (SFC LAYER) used in study.</i>	71
<i>Table 4.2 Statistics of 2-m air temperature (T2) and relative humidity (RH2), and 10-m wind speed (WS10) between WRF PBL schemes and observations (N=12096). Performance indicators; mean bias (MB) and standard deviation (STDEV), coefficient of determination (R^2), and root mean-squared error (RMSE) for the campaign average.</i>	82
<i>Table 4.3 Similar to Table 4.2, except calculated according to Continental synoptic flow (N = 5040), Etesians synoptic flow (N = 4368), and Saharan synoptic flow (N=2688) types.</i>	84
<i>Table 4.4 Statistics for PBL height showing performance between eight WRF PBL schemes and lidar-EKF estimates. Performance indicators include coefficient of determination (R^2), mean bias (MB), standard deviation (STDEV) and root mean-squared error (RMSE). MB and RMSE are calculated as WRF model – lidar. Statistical sets are grouped according to campaign average (ALL), and three primary synoptic flows. Number (N) of observations are shown in parentheses.</i>	90
<i>Table 5.1 Four WRF PBL schemes evaluated in this study, including long name, turbulent kinetic energy closure type, associated surface layer scheme, and operational method and threshold value for diagnosing PBL height.</i>	109
<i>Table 5.2 Statistics of surface meteorological variables; mean bias (MB) and linear correlation coefficient (r), between WRF model-simulations and METAR observations at Barcelona, Girona, and Reus. MB is calculated as WRF model – observed. Variables</i>	



included in the analysis are 2-m air (T_2) and dew point (TD_2) temperature (in $^{\circ}\text{C}$), and 10-m zonal (U_{10}) and meridional (V_{10}) wind components (in m s^{-1}). _____ 114

Table 5.3 Statistics of surface photochemical and aerosol variables; mean bias (MB) and linear correlation coefficient (r), between CALIOPE AQFS-simulations and network observations at urban, suburban, and rural background stations. Two stations are averaged for each station type (shown in Fig. 1d). MB is calculated as CALIOPE AQFS – observed. Variables included ($\mu\text{g m}^{-3}$) are surface ozone (O_3), nitrogen dioxide (NO_2), and particulate matter less than $10 \mu\text{m}$ (PM_{10}). _____ 123

List of Figures

<i>Figure 1.1</i> Map of stations over Europe which measure air quality (AQ) variables. Color code of the station represents the classification of the forecast most negative AQ variable for the day based on Directive 2008/50/EC and Royal Decree 102/2011 where blue = good, green = admissible, yellow = improvable, red = bad, and dark red = very bad. Source: http://www.bsc.es/caliope/en/niveles/Europa	3
<i>Figure 1.2</i> Schematic of a typical PBL diurnal cycle. Adapted from Stull (1988)	6
<i>Figure 1.3</i> Illustration of different processes occurring in the PBL. credit: Jimy Dudhia, NCAR	8
<i>Figure 1.4</i> Map representing the geographical distribution of ITaRS partners. Linkages are deepened through secondments; typically one to their co-supervisor at another academic partner (P1-P9) and one to an associated partner (i.e., a private company; P10-P19).	11
<i>Figure 2.1</i> Locations of the four EARLINET lidar instruments, including elevation above sea level (m) and vertical range resolution of the raw lidar measurements.	19
<i>Figure 2.2</i> (Left) Surface meteorological analysis from 12:00 UTC on 9 July 2012, including mean sea-level pressure (hPa, black lines), 500-hPa geopotential heights (orange dashed lines), and surface station data. (Right) Infrared satellite image from 12:00 UTC on 9 July 2012. credits: Meteocentre and Sat24.com	23
<i>Figure 2.3</i> Two-day backward trajectory analysis from the NOAA HYSPLIT model, with endpoints of the four lidar stations on 9 July 2012. The analysis is performed arriving at three heights; 500-m, 1500-m, and 3000-m.	24
<i>Figure 2.4</i> Lidar RSCS time-height series from 6:00 UTC on 9 July 2012 to 6:00 UTC on 12 July 2012 at Barcelona. Overlaid are 15-min time-averaged PBL height estimates using the GM, IPM, and WCT methods. Also shown are the estimates of PBL height from radiosonde launches (balloons) using the bulk Richardson number approach. Approximate sunrise and sunset times are indicated with symbols. An extended time period with low-level clouds is highlighted by a bold red box.	25
<i>Figure 2.5</i> Lidar RSCS time-height series from 6:00 UTC on 9 July 2012 to 6:00 UTC on 12 July 2012 at Granada. Overlaid are 15-min time-averaged PBL height estimates using the GM, IPM, and WCT methods. Also shown are the estimates of PBL height from radiosonde launches (balloons) using the bulk Richardson number approach. Approximate sunrise and sunset times are indicated with symbols. Areas of secondary aerosol layers (dust) are highlighted with bold red ovals.	26

Figure 2.6 Lidar RSCS time-height series from 6:00 UTC on 9 July 2012 to 6:00 UTC on 12 July 2012 at Evora. Overlaid are 15-min time-averaged PBL height estimates using the GM, IPM, and WCT methods. Approximate sunrise and sunset times are indicated with symbols. Areas of low SNR are highlighted with bold red rectangles. _____ 27

Figure 3.1 Model domain configuration (a) with the European-level parent domain (d01, 12 km × 12 km resolution), Iberian Peninsula domain (d02, 4 km × 4 km resolution), and the Barcelona geographical area domain (d03, 1 km × 1 km resolution). The Iberian Peninsula and Barcelona domains with associated topography are shown in (b). The topographic map is further zoomed in to the Barcelona domain (c), with a bold red star denoting the location of the lidar site. _____ 33

Figure 3.2 1-min lidar power × range-squared (PR2) profile (A.U.) at 532 nm wavelength (solid black line) from 17 June 2013 at 1209 UTC. Annotated are the EKF characteristic parameters (R_{bl} , a , A , and c). R_1 and R_2 are the start and end range limits defining the length of the observation vector passed to the filter. R'_1 and R'_2 are the start and end range limits of the erf-like PBL transition zone. _____ 44

Figure 3.3 Centroids (white diamonds) and frequency (% total) of the seven clusters arriving at 3 km (a), 1.5 km (b), and 0.5 km (c) altitudes. Clusters at 3 km: north (powder blue), east (cyan), south-west (orange), west (red), fast west (orange-red), north-west (blue), and slow south-west (yellow). Clusters at 1.5 km: north (powder blue), north-east (cyan), south-west (orange), west (red), fast west-north-west (blue), recirculations from the west (yellow), and recirculations from the east (light green). Clusters at 0.5 km: north (powder blue), north-east (cyan), south-west (orange), west (red), north-west (blue), recirculations from the west (yellow), and recirculations from the east (light green). Finally (d), monthly frequency (annual %) of occurrence of each cluster arriving at 1.5 km with same colour scheme. _____ 46

Figure 3.4 Histograms of the difference between lidar estimation method and radiosounding for a) extended Kalman filter, b) threshold, c) wavelet covariance transform, and d) variance methods. A Gaussian approximation (solid black line) and 1σ (dashed grey line) has been fit to each histogram. _____ 49

Figure 3.5 Scatter plots between PBL heights from lidar-based methods and radiosounding for extended Kalman filter (top left), threshold (top right), wavelet covariance transform (bottom left), and variance (bottom right) methods. 1σ outliers have been removed. Lidar observations have been colour-coded according to their cluster type arriving at 1.5 km altitude. The 1:1 line (solid red) has been added. _____ 51

Figure 3.6 Scatter plots between PBL height diagnosed by the WRF model using eight different PBL schemes and PBL height estimated with the lidar-EKF technique. Data points have been colour-coded according to their cluster type arriving at 1.5 km altitude. The 1:1 line (solid red) has been added. Coefficient of determination (R^2) values are computed based on the total data collection ($N = 45$). _____ 52

Figure 3.7 (a) Lidar power × range-squared (PR2) time-height series (A.U.) from 1202 – 1233 UTC, with 1-min PBL height (km asl) estimates from the EKF (magenta circles), threshold (black diamonds), variance (black triangles), and WCT (black squares) methods. Radiosonde-estimated PBL height at 1200 UTC is shown with a white dashed line. (b) WRF model-simulated PBL height (km asl) with 8 PBL schemes. Coincident lidar delineated with black vertical line. (c) WRF synoptic map of sea level pressure (hPa, shaded contours), and 850 hPa geopotential heights (blue lines) and winds (vectors) valid at 1200 UTC on 22 March using the YSU PBL scheme. _____ 55

<i>Figure 3.8</i> Same description as in Fig. 3.7, except for representative case on 3 July 2012.	56
<i>Figure 3.9</i> Same description as in Fig. 3.7, except for representative case on 3 August 2007.	58
<i>Figure 3.10</i> Same description as in Fig. 3.7, except for representative case on 22 April 2010.	59
<i>Figure 3.11</i> WRF model-simulated surface sensible heat flux ($W m^{-2}$) for a) 22 March 2009, b) 3 July 2012, c) 3 August 2007, and d) 22 April 2010. Model grid-point location closest to the Barcelona lidar site. Positive values indicate heat transfer from the land surface to the atmosphere.	61
<i>Figure 4.1</i> Model domain configuration for: (a) the European-level parent domain (d01, 12×12 km), (b) Greece domain (d02, 4×4 km), and (c) Greater Athens Area (GAA) domain (d03, 1×1 km). The Greece and GAA domains (red box) and associated topography are shown in 1b. The topographic map is further zoomed-in to the GAA domain (1c), with a bold red star denoting the location of the NTUA lidar site.	69
<i>Figure 4.2</i> Two-day FLEXPART-WRF backtrajectories (top) ending at Athens ($37.96N, 23.78E$) and synoptic maps simulated with the WRF model (bottom) representing (from left to right), Continental (25 May 2014), Etesians (13 June 2014), and Saharan (16 June 2014) flow types. Backward trajectories end at 1200 UTC with black dots showing 6-h position and colors denote trajectory height at receptor for 0.5 km (red), 1 km (blue dashed), 2 km (black), 3 km (red dashed), and 4 km (purple). Synoptic maps (valid 1200 UTC) show sea level pressure in hPa (coloured contours), geopotential height at 850-hPa in metres (blue lines), and 850-hPa winds (barbs).	74
<i>Figure 4.3</i> 100-s profile of molecular-normalised range-corrected power from the NTUA lidar at 0701 UTC on 25 May 2014. Initial state vector $[R_{bl} \ a \ c]$ with lower- and upper-range limits $[R_1 \ R_2]$ for the extended Kalman filter (EKF) PBL height technique are annotated in gray dashed lines.	77
<i>Figure 4.4</i> Location and elevation (meters above sea level) of the 14 surface meteorological stations (12 from the National Observatory of Athens, one from NTUA, and one from NCSR), and site of radiosonde launches (EMY). Spatial variations range from 500 m – 12 km apart and in elevation from 10 – 565 m asl.	78
<i>Figure 4.5</i> Campaign-averaged mean bias (MB, WRF – observation) for (a-b) 2-m air temperature ($T_2, ^\circ C$), (c-d) 2-m relative humidity (RH2, %), and (e-f) 10-m wind speed (WS10, $m s^{-1}$) at two stations (Anavyssos and Peristeri) from the NOA network, representative of coastal and inland influences, respectively.	80
<i>Figure 4.6</i> Same as in Fig. 4.5, but time-averaged for Continental synoptic flow days.	83
<i>Figure 4.7</i> Same as in Fig. 4.5, but time-averaged for Etesians synoptic flow days.	85
<i>Figure 4.8</i> Same as in Fig. 4.5, but time-averaged for Saharan synoptic flow days.	87
<i>Figure 4.9</i> Hourly-mean PBL height comparisons between the NTUA lidar (open black squares) and WRF PBL schemes (colored lines) for (a) campaign average, and (b) Continental flow, (c) Etesians flow, and (d) Saharan flow types. PBL height estimated by lidar with extended Kalman filter (EKF) technique.	89
<i>Figure 4.10</i> Lidar range-corrected power time-range color plots (a-c) at 1064 nm wavelength and simulated PBL height from the WRF model (d-f) for; top row) Continental, middle row) Etesians, and bottom row) Saharan synoptic flow types. Lidar time-range plots	

are overlaid with PBL height estimates (circles, 100-s resolution) using the extended Kalman filter technique, in addition to the 1-h mean PBL height (blue diamonds) calculated with nine 100-s estimates, along with 1σ standard deviation. _____ 92

Figure 4.11 Representative vertical profiles comparison of WRF model-simulated potential temperature (K), water vapor mixing ratio (g kg^{-1}), and wind speed (m s^{-1}) versus radiosonde launches at EMY (37.88N, 23.73E, 10 m asl). One set of profiles for (a-c) Continental (2 June 2014), (d-f) Etesians (22 May 2014), and (g-i) Saharan (16 June 2014) synoptic flow types. _____ 94

Figure 4.12 Model surface sensible heat flux (W m^{-2}) simulated with eight WRF PBL schemes at Anavyssos (column 1) and Peristeri (column 2) stations for representative synoptic flows (rows): (a) Continental (2 June 2014), (b) Etesians (22 May 2014), and (c) Saharan (16 June 2014) synoptic flow types. _____ 96

Figure 5.1 a) Two-day back-trajectory analysis ending at Barcelona on 7 May 2015 (12:00 UTC) at three arriving altitudes (0.5, 1.5, and 3 km). b) Surface analysis from 6:00 UTC on 7 May 2015, including mean sea-level pressure (hPa; solid black lines), 500-hPa geopotential heights (dashed red lines), and station observations. c) two one-way nested domains for the WRF and CALIOPE AQFS at the European level (12×12 km), and Iberian Peninsula (4×4 km). d) locations of METAR (blue boxes), lidar/radiosonde (orange diamond), and air quality measurement (red circles) stations. _____ 105

Figure 5.2 a) Time-range series of lidar normalized relative backscatter (NRB), overlaid with 1-min estimates of PBL height (magenta dots) and 15-min hourly-averaged PBL height centred on the synoptic hour (blue diamonds). b) mean bias (MB; WRF – lidar) and linear correlation coefficient (r) between PBL heights simulated from the WRF model and estimates from the lidar. c) time series on 7 May 2015 of daytime PBL height simulated by the WRF model and 15-min hourly averages (black squares) from the lidar, with $1-\sigma$ error bars. _____ 112

Figure 5.3 Time series on 7 May 2015 of WRF model-simulated 2-m air temperature (T_2 ; solid lines) and dew point temperature (TD_2 ; dashed lines) against METAR observations at; a) Barcelona, b) Girona, and c) Reus. _____ 115

Figure 5.4 Same as in Fig. 5.3, except for zonal (U_{10} ; solid lines) and meridional (V_{10} ; dashed lines) components of 10-m winds. _____ 116

Figure 5.5 Comparison of WRF model-simulated vertical profiles (colored lines and symbols) against a radiosounding (black solid line) on 7 May 2015 at 12:00 UTC for a) temperature, b) dew point temperature, c) zonal wind speed, and d) meridional wind speed. _____ 118

Figure 5.6 Spatial comparison of CALIOPE-simulated surface ozone concentration (O_3) from the control run (YSU; first column), and bias between tested WRF PBL schemes and the control run for the ACM2 (column 2), MYNN2 (column 3), and BouLac (column 4) schemes. Plots are shown for 6:00 UTC (first row), 12:00 UTC (second row), and 18:00 UTC (third row) on 7 May 2015. _____ 120

Figure 5.7 Same as in Fig. 5.6, except for surface concentration of nitrogen dioxide (NO_2). _____ 121

Figure 5.8 Same as in Fig. 5.6, except for surface concentration of particulate matter $< 10 \mu\text{m}$ (PM_{10}). _____ 122



List of symbols

$^{\circ}\text{C}$	degrees Celsius
a	wavelet dilation
b	wavelet translation
CO	carbon monoxide
hPa	hectopascal
K	Kelvin
N	number of samples
NO_2	nitrogen dioxide
O_3	ozone
PM	particulate matter
PM_{10}	particulate matter $< 10 \mu\text{g}$
$\text{PM}_{2.5}$	particulate matter $< 2.5 \mu\text{g}$
r	linear correlation coefficient
R^2	coefficient of determination
Ri_b	bulk Richardson number
Ri_{bc}	critical bulk Richardson number
SO_2	sulfur dioxide
T	air temperature
T_d	dew point temperature
W_f	convolution of Haar wavelet function
z	height
Θ_v	virtual potential temperature
σ	standard deviation



*other specific symbols are defined in the text.



List of Acronyms

ACCEPT	Analysis of the Composition of mixed-phase Clouds with Extended Polarization Techniques
ACM2	asymmetric convective model version 2
AIRS	Atmospheric Infrared Sounder
AMS	aerosol mass spectrometer
AQFS	air quality forecast system
ARW	Advanced Research WRF
BEP	Building Environment Parameterization
BOULAC	Bougeault–Lacarrère
BSC-CNS	Barcelona Supercomputing Center – Centro Nacional de Supercomputación
CESM	Community Earth System Model
CHARADME_{exp}	Characterization of Aerosol mixtures of Dust And Marine origin
CMAQ	Community Multi-scale Air Quality
EARLINET	European Aerosol Research Lidar Network
ECMWF	European Centre for Medium-range Weather Forecasts
EEA	European Environment Agency
EMEP	European Monitoring and Evaluation Programme
EMY	Hellenic National Meteorological Service
EPA	US Environmental Protection Agency
ESR	early-stage researcher
EU	European Union
EZ	entrainment zone
FA	free atmosphere
FLEXPART	Flexible Particle



FNL	Final Analysis
FT	free troposphere
GAA	Greater Athens Area
GFS	Global Forecast System
HERMES	High Elective Resolution Emission Modeling System
HygrA-CD	From Hygroscopic Aerosols to Cloud Droplets
HYSPLIT	Hybrid Single Particle Lagrangian Integrated Trajectory
INOE	National R&D Institute for Optoelectronics
IP	Iberian Peninsula
ITARS	Initial Training for Atmospheric Remote Sensing
JOYCE	Jülich Observatory for Cloud Evolution
LES	large eddy simulation
LiDAR	Light Detection and Ranging
MB	mean bias
METAR	Meteorological Terminal Aviation Routine Weather Report
ML	mixed layer
MM5	5 th generation mesoscale model
MODIS	Moderate Resolution Imaging Spectroradiometer
MPL	micropulse lidar
MPLNET	Micropulse Lidar Network
MRF	medium-range forecast
MYJ	Mellor-Yamada-Janjic
MYNN2	Mellor-Yamada-Nakanishi-Niino version 2
NASA	US National Aeronautics and Space Administration
NBL	nocturnal boundary layer
NCAR	National Center for Atmospheric Research (US)
NCEP	National Centers for Environmental Prediction (US)
NCSR	National Center for Scientific Research - Demokritos
NMMB	Nonhydrostatic Multiscale Model on the B-grid
NOA	National Observatory of Athens
NOAA	US National Oceanic and Atmospheric Administration
NRB	normalized relative backscatter



NTUA	National Technical University of Athens
OMI	Ozone Monitoring Instrument
PX	Pleim-Xiu
QNSE	Quasi-normal Scale Elimination
RL	residual layer
RMSE	root mean-squared error
RSCS	range-squared corrected signal
SNR	signal-to-noise ratio
TEMF	Total Energy Mass Flux
TKE	turbulent kinetic energy
UPC	Universitat Politècnica de Catalunya
UTC	universal coordinated time
UW	University of Washington
WHO	World Health Organization
WRF	Weather Research and Forecasting
YSU	Yonsei University

Acronyms defined by the author and frequently used in the manuscript*:

AQ	air quality
EKF	extended Kalman filter
GM	gradient method
IPM	inflection point method
PBL	planetary boundary layer
WCT	wavelet covariance transform

*other specific acronyms are defined in the text.



UNIVERSITAT POLITÈCNICA
DE CATALUNYA
BARCELONATECH



Environmental Engineering



Chapter 1

1 Introduction

This chapter provides an overview of air quality forecasting systems over Europe, including why they are necessary, the current state-of-the-art, and the importance of planetary boundary-layer schemes from the associated meteorological model. In addition, this section presents the context of this Ph.D. in relationship to the Initial Training for Atmospheric Remote Sensing (ITaRS) network, which included one secondment to the National Technical University of Athens during an international field campaign. Finally, the motivation, objectives, and organization of the Ph.D. thesis are discussed.

1.1 Air quality over Europe

Air quality (AQ) is of major concern worldwide, and in particular over Europe for various environmental and human health effects. According to the European Environmental Agency (EEA) (Guerreiro et al., 2012) air pollutant concentrations are still too high and harm our health and the ecosystems we depend on. The EEA went on to mention that a significant proportion of Europe's population lives in areas, especially large cities, where air quality standards are routinely exceeded. In addition, Janez Potočnik, European Union (EU) Commissioner for the Environment (EU, 2010) states, “Air pollution is bad for our health. It reduces human life expectancy by more than eight months on average and by more than two years in the most polluted cities and regions”.

The United States Environmental Protection Agency (EPA, 2015) defines air pollution as the presence of contaminants or pollutant substances in the air that interfere with human health or welfare, or produce other harmful environmental effects. These contaminants or pollutant substances can be a result of natural or anthropogenic sources. Natural sources of air pollutants include emitted particulate matter and gases from

wild fires, dust storms, and volcanoes. Air pollution comes from major anthropogenic sources such as the burning of fossil fuels at power plants and the emissions of primary pollutants from motor vehicles.

AQ is a term used when measuring the concentration of pollutants in the air. AQ concentrations are typically measured by several different means, including direct observations from ground stations or indirect measurements from remote sensing instruments such as lidar (laser radar) and satellites. Baldasano et al. (2003) compiled AQ data from large cities worldwide and found that the most important pollutants to measure are nitrogen dioxide (NO_2), particulate matter (PM_{10} and $\text{PM}_{2.5}$), and ground level ozone (O_3). Since AQ is predominantly a problem for human health and the environment, the lowest levels of the atmosphere are the most important to investigate.

Air pollution in Europe is a local, regional, and intercontinental problem caused by the emission of specific pollutants, such as particulate matter and ozone, with the following main effects:

- Damage to human health caused by exposure to pollutants
- Ecosystem degradation such as acidification, toxicity, and eutrophication
- Damage and yield losses to agricultural crops due to ground-level O_3
- Contribution of atmospheric pollutants to climate
- Reduction of atmospheric visibility

Great efforts have been put forth by the EU community to control and help mitigate AQ issues. The AQ Directive 2008/50/EC (EU, 2008) sets legal limits for EU Member states for ground-level concentrations of air pollutants such as PM, O_3 , NO_2 , SO_2 , etc. Key elements of the EU legislation set limit values and target values for specific pollutants. However in the REVIHAAP technical report (WHO, 2013) it is found that there is no evidence of a safe level of exposure or a threshold below which no adverse health effects occur. They continue to state that more than 80% of the population in the WHO European Region (including the EU) lives in cities with levels of PM exceeding WHO Air Quality Guidelines. It is clear that more efforts are required to control and mitigate this major concern.

Various types of instruments are used to record and monitor AQ data ranging from worldwide down to the local scale. These include direct in situ measurements (e.g., ground AQ stations) and indirect measurements from remote sensing platforms (e.g., lidar, ceilometer, or satellites). In the context of ground stations, the European Environment Information and Observation Network (EIONET) is a partnership network of the European Environment Agency (EEA) and its member and cooperating countries, involving approximately

1000 experts and more than 350 national institutions. The three main elements of EIONET are the collection of data, measurements of air and precipitation quality, and modeling of air pollution. For background stations, the European Monitoring and Evaluation Programme (EMEP) is an international cooperation to solve trans-boundary air pollution problems (EMEP, 2013). Figure 1.1 shows the available AQ ground stations from the observing networks over Europe. The stations have been color-coded based on a forecast from the CALIOPE air quality forecast system (AQFS) using Directive 2008/50/EC and Royal Decree 102/2011 classifications.

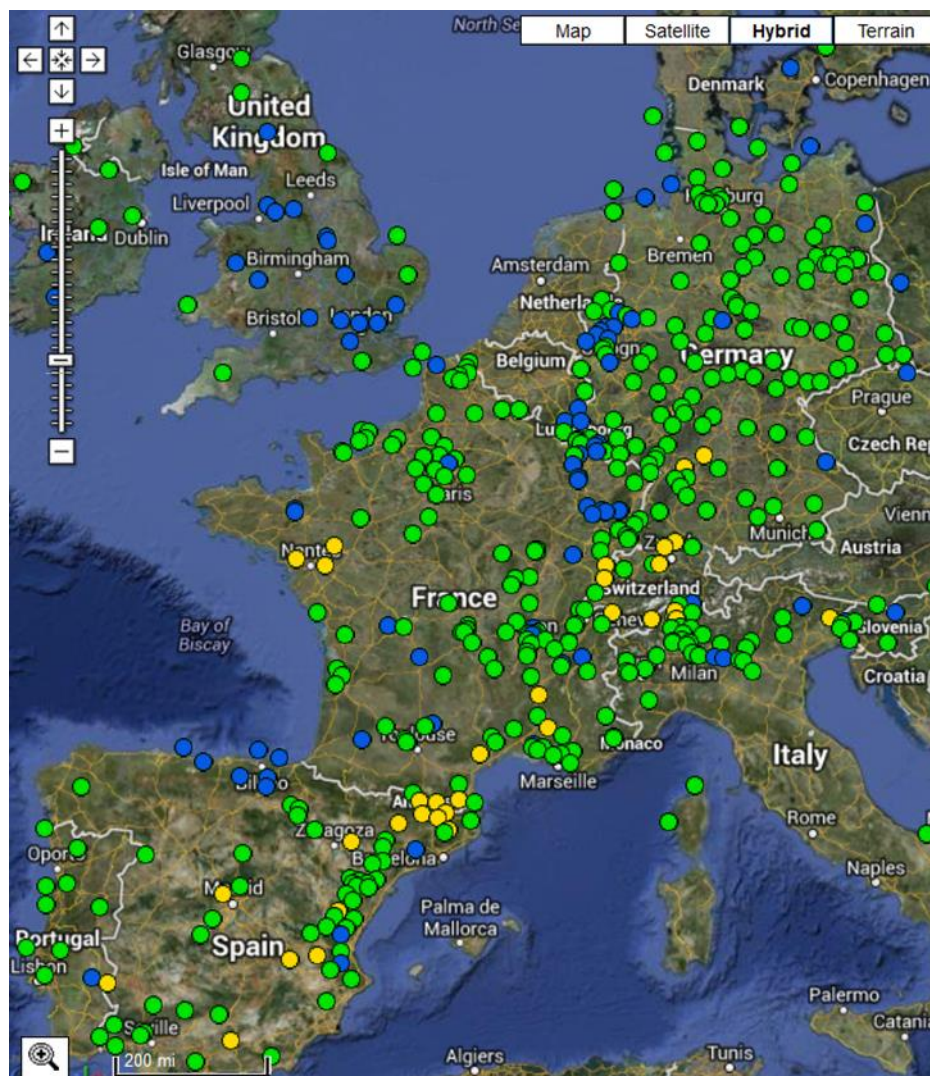


Figure 1.1 Map of stations over Europe which measure air quality (AQ) variables. Color code of the station represents the classification of the forecast most negative AQ variable for the day based on Directive 2008/50/EC and Royal Decree 102/2011 where blue = good, green = admissible, yellow = improvable, red = bad, and dark red = very bad. Source: <http://www.bsc.es/caliope/en/niveles/Europa>

Satellite-based instruments can also be used to detect AQ parameters indirectly using algorithms. A couple of current satellite-based instruments with missions to observe AQ are the Ozone Monitoring Instrument (OMI) and the Atmospheric Infrared Sounder (AIRS). OMI is on-board the Aura satellite and is a nadir-viewing, wide-field-imaging spectrometer, providing daily global coverage of tropospheric ozone (OMI, 2013). The instrument derives tropospheric ozone by distinguishing between aerosol types (i.e., smoke, dust, and sulfates) and measuring cloud pressure and coverage.

Another state-of-the-art instrument, AIRS (AIRS, 2013), is on-board of the Aqua satellite. AIRS can measure trace greenhouse gases such as ozone, carbon monoxide, carbon dioxide, and methane using similar techniques. The main advantage to using satellite-based instruments is their broad spatial coverage compared with individual ground stations. In return, observations from ground stations are critical for calibration and validation of the satellite-based sensors.

1.1.1 Air quality forecast systems: why are they needed?

AQ forecast systems (AQFS) can be useful tools for simulating the coverage and transport of atmospheric pollutants over both global and regional unified domains. The link between emissions and ambient concentrations can only become evident and fully understood by means of air quality modelling since ground-based stations are single point. Zhang et al. (2012) reviewed the history, techniques, and state of the science of AQFS. They found that the biggest improvement in the field of AQFS is the addition of online coupling of meteorological models and chemistry models.

Currently there are multiple global and regional AQFS in Europe. Examples of global AQFS include the LMDzt-INCA (Hauglustaine et al., 2004; Folberth et al., 2006) run by France and the ECHAM5 (Roeckner et al., 2006; Zhang et al., 2010) maintained in Germany. Both are online coupled models with LMDzt-INCA exploiting the European Centre for Medium-Range Weather Forecasts (ECMWF) global integrated forecast system as its meteorological model.

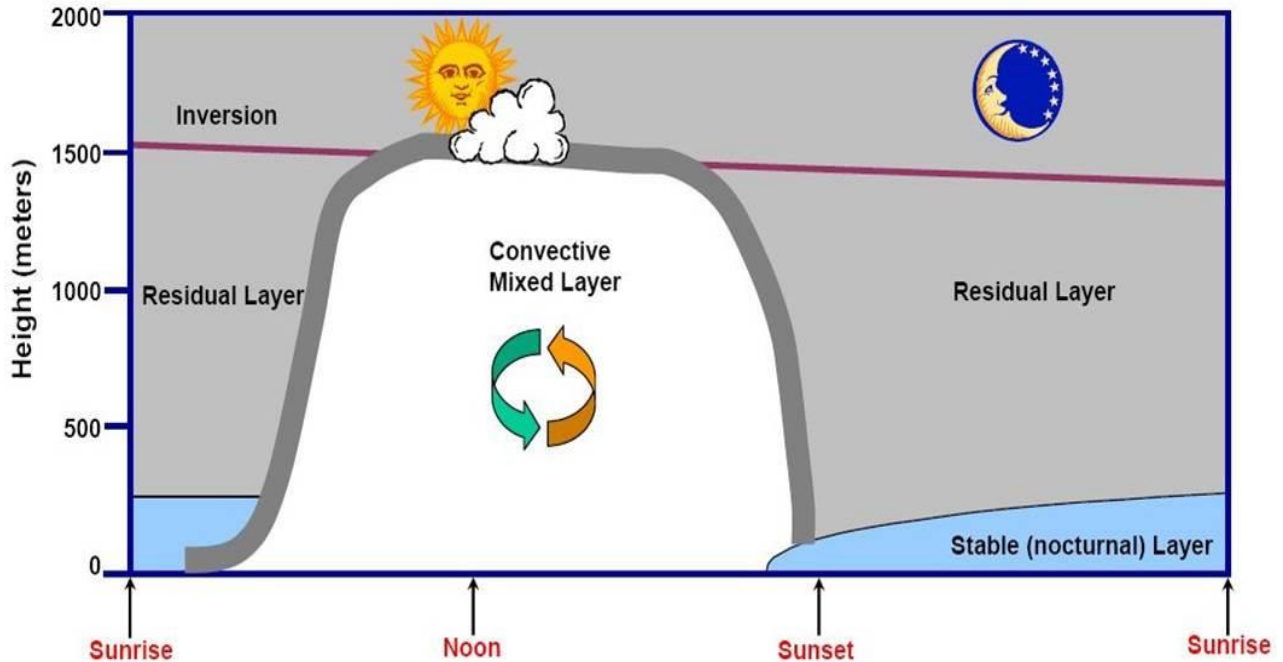
A regional initiative, Monitoring Atmospheric Composition and Climate (MACC), is coordinated by ECMWF for the purposes of combining state-of-the-art atmospheric modelling with Earth observation data to provide information services covering European air quality, global atmospheric composition, climate forcing, the ozone layer and UV and solar energy, and emissions and surface fluxes (MACC, 2016). Examples of regional AQFS are the CALIOPE AQFS (Baldasano et al., 2008) maintained and operated by the Barcelona

Supercomputing Centre (BSC-CNS) in Spain, the French AQFS using the CHIMERE chemical transport model run in part by the L'Institut National de l'Environnement Industriel et des Risques (INERIS, 2016), and the German EURAD system operated from the University of Cologne (EURAD, 2016).

1.1.2 Importance of PBL schemes in numerical weather prediction

The planetary boundary-layer (PBL) is the part of the troposphere that is directly influenced by the presence of the earth's surface, and responds to surface forcing with a timescale of about an hour or less (Stull, 1988). Convective turbulent mixing processes are dominant in the mixed layer (ML) of the PBL and have a major influence on the growth and transport of atmospheric pollutants. Meteorological variables (i.e. temperature, humidity, winds) in the PBL are critically important as inputs for reliable simulations in AQ models. One of the key parameters which determine the vertical extent of the ML is the PBL height.

A typical diurnal cycle of PBL structure is shown in Fig. 1.2. Just after sunrise the convective ML starts to grow, then usually reaches a maximum height around noon during the period of maximum solar radiation. Decay of the ML generally occurs around sunset, when a stable layer forms near the surface due to radiational cooling. During the evening and nighttime hours, remnant turbulence from the ML is called the residual layer (RL). The solid purple line around 1.5 km indicates the inversion layer between the PBL and free troposphere.



Adapted from *Introduction to Boundary Layer Meteorology* -R.B. Stull, 1988

Figure 1.2 Schematic of a typical PBL diurnal cycle. Adapted from Stull (1988)

From an observational perspective, PBL height has historically been measured with radiosondes (Holzworth, 1964; Troen and Mahrt, 1986; Beljaars and Betts, 1992) but in recent years remote sensing instruments such as lidar have been utilized (Sicard et al., 2011; Tsaknakis et al., 2011; Mao et al., 2012). The concept of using lidar to detect PBL height relies on the assumption that there is a strong gradient in the concentration of aerosols in the ML versus the free atmosphere (FA). Several methods have been applied to detect these gradients using aerosols as tracers. An advantage of using remote sensing instruments over radiosondes for detection of the PBL height is the possibility of nearly continuous monitoring versus typical observations of twice per day from radiosondes. Continuous monitoring of PBL height will allow for a better understanding of the depth of convective turbulent processes in the mixed-layer which are a primary driver of air pollutants.

From a modelling standpoint PBL height can be extremely complex to compute accurately. This is due to the fact that boundary layer turbulent processes occur at smaller geographical scales than even high-resolution mesoscale meteorological models can resolve. To that end, atmospheric models normally make use of parameterizations to represent the boundary layer structure in the lowest levels of the atmosphere. Many



different schemes exist for incorporation into the models with unique characteristics to parameterize the turbulent fluxes in the boundary layer. Several studies in the past have compared PBL schemes in mesoscale meteorological models with varying results.

Figure 1.3 shows an illustration of the different processes occurring in the PBL. Turbulent fluxes of sensible and latent heat are emitted from the land surface into the boundary layer. Due to the combination of shear and buoyancy flux mechanisms different layers then form in the PBL. Mixing happens through two different methods; local and non-local processes. Local mixing only takes into account exchanges in fluxes between adjacent layers while non-local mixing includes mixing from other layers as well. Eventually the PBL reaches a maximum and this is near the entrainment zone (EZ). More stable air from the FA enters the PBL in the EZ. Vertical diffusion is a mechanism in which turbulent fluxes are exchanged between the top of the PBL and the FA. The primary role of PBL parameterization schemes is to handle the diffusion process.

Boundary-layer and land-surface interactions have serious implications on an AQFS. It's well-known that the treatment of PBL processes in meteorological models has direct impacts on predicting the dynamics of photochemical pollutants (Pérez et al., 2006a). In AQFS a few of the most important PBL parameters for reliable simulations are the PBL height, wind speed and direction, temperature, and cloud cover.

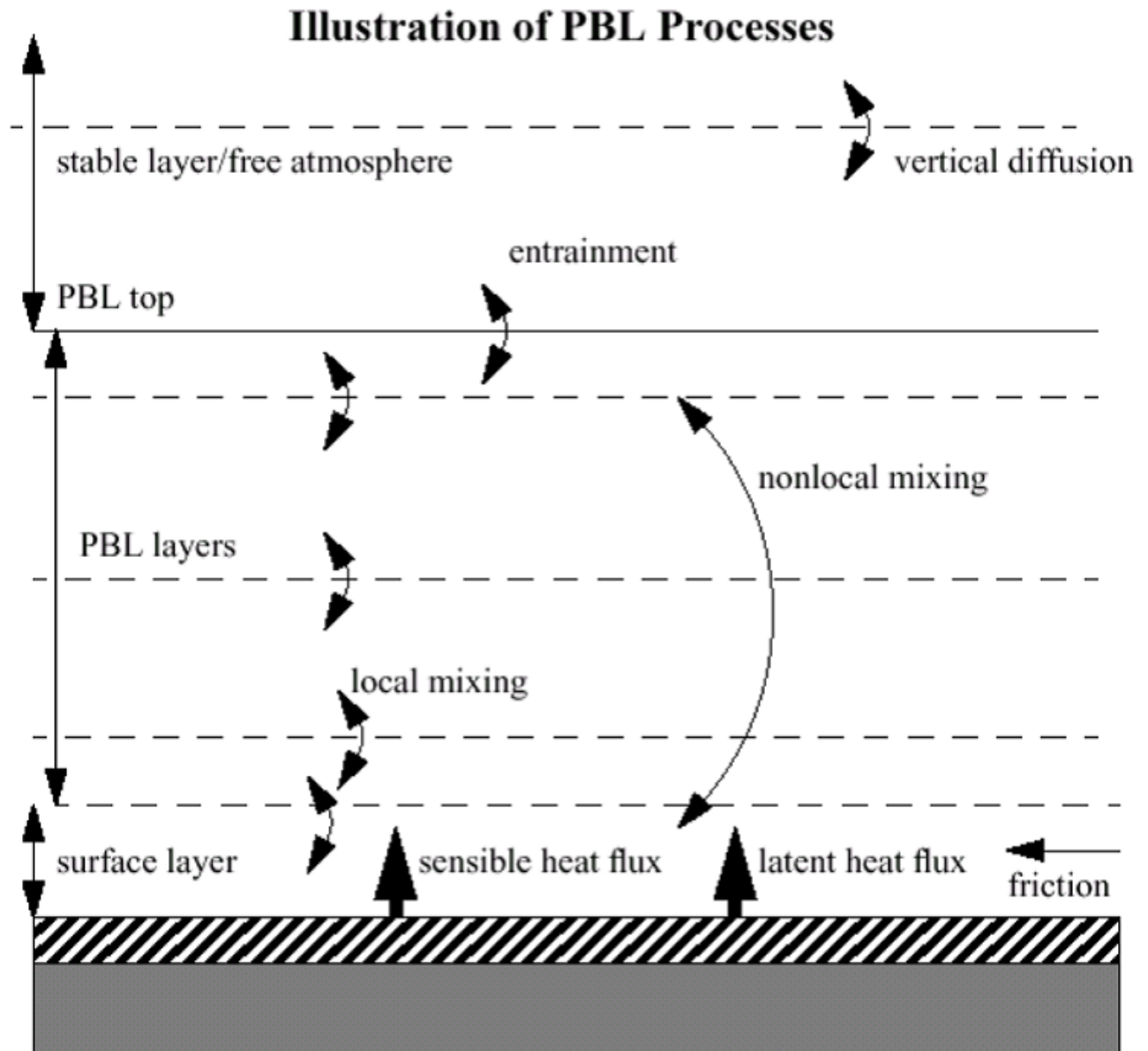


Figure 1.3 Illustration of different processes occurring in the PBL. credit Jimy Dudhia, NCAR

1.1.3 Previous works evaluating PBL schemes and AQ models

The distribution, transport, and accumulation of atmospheric pollutants are dominated by processes in the lower atmosphere. Knowing an accurate depiction of the state of the boundary layer, including PBL height, is critical to reliable simulations from AQ models. Most mesoscale meteorological models don't possess the necessary horizontal grid spacing needed to directly resolve the turbulent mixing processes occurring in the PBL. To account for this deficiency, meteorological models parameterize processes in the PBL through different methods involving turbulent kinetic energy and closure theories.

Dynamic variables in the PBL such as temperature, wind speed, and PBL height can vary greatly depending on the PBL scheme selected. Previous works have evaluated the sensitivities of AQ models to different PBL schemes in both the MM5 and WRF models and those will be reviewed in this section.

Past works have utilized PBL schemes in the MM5 model to evaluate sensitivity in AQ simulations (Mao et al., 2006; Pérez et al., 2006a; Bossioli et al., 2009; Kim et al., 2010). Mao et al. (2006) compared five of the seven PBL schemes in MM5 over the Central and Eastern United States to evaluate the sensitivity with CMAQ simulations. Two 37-day periods were simulated in summer and winter, including a seven day spin-up period. The AQ outputs from CMAQ were compared with hourly observations from 2,217 AQ sites and the meteorological variables from MM5 were compared with surface and 850-hPa measurements from 50 surface sites and 21 upper-air sites. They discovered the largest sensitivity to various schemes was found with the PBL height. The Pleim-Xiu PBL scheme was on order of 800 m higher than other schemes in summer and 350 m higher in winter. This translated into AQ differences at the urban scale, with greater than 5% differences in maximum concentration of O_3 and $PM_{2.5}$.

Similar results were found in Pérez et al. (2006a) where they compared three PBL schemes from MM5 over summertime in the Barcelona area. The meteorological outputs from MM5 were compared with lidar and radiosoundings measurements, while the AQ outputs from CMAQ were compared with hourly observations from AQ sites, but averaged over the entire domain. They discovered that 1-hr daily maximum O_3 and CO concentrations vary in magnitude and location depending on the PBL scheme chosen. In their comparisons the O_3 bias was negative for all schemes with a bias ranging from -9.1% to -14.8%. However, the Gayno-Seaman scheme was determined to provide the least error and lowest bias among those compared.

In more recent studies the concentration has focused more on the evaluation of PBL schemes in the WRF model (Misenis and Zhang, 2010; Gan et al., 2011; Cheng et al., 2012). In Misenis and Zhang (2010) two

PBL schemes (MYJ and YSU) in the WRF model were compared over the Houston, Texas area for a five-day summer episode. AQ outputs from WRF-Chem were compared with hourly measurements from AQ stations and aircraft. They found 20-40% lower PBL heights with the MYJ scheme than the YSU scheme which resulted in higher levels of CO, O₃, and PM_{2.5}. This was a similar finding to a study by Bossioli et al. (2009) where PBL height predictions had 13% differences in the afternoon hours over Athens, Greece.

Another study which investigated the effects of AQ simulations to the YSU and MYJ schemes was Cheng et al. (2012). Their efforts were focused on the Taiwan area during two very different atmospheric cases in springtime; long-range transport of pollutants from a cold frontal passage and a local land-seabreeze regime. In the case of the cold frontal passage they discovered differences up to 50 µg m⁻³ in O₃ concentration near the front with the simulation using the YSU scheme higher than the MYJ scheme. They attributed this difference to higher PBL heights diagnosed by the YSU scheme. In the case of local land-seabreeze effects they found that during the daytime the YSU scheme predicts a stronger seabreeze than the MYJ scheme which is more capable of carrying aged species back to land (on the order > 40 µg m⁻³).

After this review of previous efforts it is clearly seen that PBL schemes in mesoscale meteorological models have an impact on AQ simulations. The main variables that enhance sensitivity in the AQ simulations are the PBL height, temperature, moisture, and winds.

1.2 The Initial Training for Atmospheric Remote Sensing (ITaRS) network

Aerosol-cloud interaction is recognized as the single largest uncertainty in today's climate models. The European Commission funded a training network that combines multiple disciplines to exploit innovative atmospheric remote sensing techniques to advance our understanding of aerosol-cloud interaction. The Initial Training for atmospheric Remote Sensing (ITaRS) network is a 4-year project (2012 – 2016) providing support for 15 PhD students and young post-docs, which are employed at one of nine European research institutions. The ITaRS consortium is comprised of 10 associated partners, five of them manufacturers of meteorological instruments. ITaRS focuses on the synergistic application of high-end ground-based remote-sensing instrumentation to make significant improvements in our understanding of aerosols, clouds, and aerosol-cloud interaction processes, and their role for both climate and weather. Figure 1.4 shows the geographical distribution of the network, highlighting research, academic, and private partners.

1.2.1 General description of the ITaRS network

ITaRS is the first step to develop sustainable pan-European PhD training in the aerosols and clouds community. But how does a life in a graduate school work if the students are spread all over Europe? In addition to network-wide workshops and summer schools, the fellows visit other ITaRS partners for two to four week secondments. ITaRS fellows participate in comprehensive training on instrumentation, algorithms for the interpretation of the measurements, and atmospheric physics. In between meetings, weekly e-seminars ensure ongoing communication within the network.



Figure 1.4 Map representing the geographical distribution of ITaRS partners. Linkages are deepened through secondments; typically one to their co-supervisor at another academic partner (P1-P9) and one to an associated partner (i.e., a private company; P10-P19).

The two main events of the ITaRS training program were the two summer schools. The first summer school, “Aerosol Remote Sensing, Processes & Applications,” happened 23 September – 4 October 2013 hosted at the National Institute of Research and Development for Optoelectronics (INOE) in Bucharest, Romania. Using various ground-based remote sensing instruments (e.g., Raman lidar, sun photometer) group projects were presented on topics such as evolution of the PBL height and determination of aerosol optical properties.

In addition, a field campaign performed at the summer school provided an interesting dataset on surface aerosol composition from an aerosol mass spectrometer (AMS) and vertical structure from a multi-wavelength Raman lidar that was further investigated jointly by fellows at institutions in Potsdam, Bucharest, and Athens.

The second summer school on “Remote Sensing of Clouds and Precipitation: Observation and Processes” took place 8 – 17 September 2014 at the Research Center in Jülich, Germany. Participants benefited from hands-on training with instruments from the JOYCE (Jülich ObservatorY for Cloud Evolution) site, including microwave radiometer, scanning cloud radar, micro rain radar, wind lidar, sodar, and an infrared spectrometer. Polarimetric twin radars in Bonn and Jülich were also investigated. Six travel grants were granted to outstanding graduate students and early-career researchers from outside of the network. The summer school was such a success that the U.S. ARM program decided to follow the ITaRS format for a follow-on summer school in 2015.

ITaRS fellows have participated in several international field campaigns to gather ground-based remote sensing observations for applications to atmospheric research. In summer 2014, the Hygroscopic Aerosols to Cloud Droplets (HygrA-CD; hygracd.impworks.gr) and CHARacterization of Aerosol mixtures of Dust And Marine origin Experiment (CHARADMExp; charadmexp.gr) campaigns took place in Greece. Data from these campaigns are currently being analyzed with several publications expected. Banks et al. (2016) exploited lidar, radiosonde, and surface meteorological observations from HygrA-CD to evaluate PBL parametrization schemes in the WRF numerical weather prediction model. They found that non-local schemes tend to reproduce values closest to the observations. During fall 2014, several ITaRS fellows participated in the Analysis of the Composition of mixed-phase Clouds with Extended Polarization Techniques (ACCEPT; atmos.weblog.tudelft.nl) campaign in Cabauw, The Netherlands, with results presented in Vienna at the General Assembly of the European Geosciences Union in April 2015. The main objective of ACCEPT was the analysis of the composition of mixed-phase clouds with extended polarization techniques.

1.3 Ph.D. mobility context: Secondment to National Technical University of Athens

Robert Banks (ESR13) was hosted for a month-long secondment from the 17th of May to the 15th of June in the Laser Remote Sensing Unit (LRSU) at the National Technical University of Athens (NTUA) in Greece. The LRSU is a part of the Physics Department at NTUA. Opportunistically, this secondment coincided with the HygrA-CD international field campaign. The main contribution from the secondment was to make use of the established know-how of numerical weather prediction from the Barcelona Supercomputing Centre and link it with remote sensing instruments (lidars, ceilometer, and microwave radiometer) to study the PBL over Athens.

During the secondment an assessment of the sensitivity of atmospheric variables in the PBL to different model PBL parameterization schemes was initiated. Hourly numerical simulations of atmospheric variables including PBL height, 2-m air temperature, and wind speed and direction from the WRF-ARW (Advanced Research WRF) mesoscale meteorological model were evaluated against observations from a multiwavelength Raman lidar and radiosoundings from the nearby meteorological institute. PBL heights were determined from the Raman lidar using a Kalman filter approach and from radiosoundings using the bulk Richardson number method. Both lidar-estimated and radiosonde-estimated PBL heights showed good agreement.

1.3.1 Overview of the HygrA-CD field campaign

HygrA-CD was an internationally-led field campaign performed from 15 May – 19 June 2014 in the Greater Athens Area (GAA), Greece. The main goal of the HygrA-CD campaign was to bring together different instruments and expertise for the purpose of understanding more about the impact of aerosols and clouds on weather and climate on a local scale. It is a novel attempt to strengthen the links between the remote sensing and in-situ observation communities, while making use of established know-how on numerical weather prediction and atmospheric modelling. An overview of the campaign can be found in (Papayannis et al., 2016).



During the time period of the HygrA-CD campaign, it is common to observe diverse types of synoptic flows. Saharan dust events are likely over the GAA based on synoptic winds from the south and south-west, advecting dust aerosols into the region. In addition, air masses carrying mixtures of urban/continental and marine aerosols are probable, due to the influence of the Etesian winds to the wind circulation in the GAA (i.e., synoptic winds from the north-east).

1.3.2 Outcomes

The primary outcome from this secondment included the assessment of eight PBL parameterization schemes in WRF-ARW v3.4, each with a unique method of parameterizing the PBL structure and turbulent kinetic energy. See Chapter 4 for a more detailed description of the data, methodology, and results from this study.

1.4 Motivation of Ph.D.

This research project aims to evaluate the sensitivity of high-resolution AQ simulations from the CALIOPE AQFS (Baldasano et al., 2008) in the distribution of gaseous photochemical pollutants and particulate matter to different PBL schemes in the Weather Research and Forecast (WRF) Advanced Research WRF (ARW) model. Three primary questions are raised to motivate this research line:

- I. What method(s) is/are best for estimating PBL height from lidar observations?
- II. What effect will choice of meteorological model PBL physics scheme have on diagnosis of PBL height and other atmospheric variables?
- III. How will an AQFS be affected by choice of meteorological model PBL schemes in a complex geographical area?

In order to answer these questions, the research project is separated into 3 main areas. The first area evaluates methods for estimating PBL height from lidar profiles using multiple lidar instruments over the Iberian Peninsula and Greece, including continuous 72-h measurements from the European Aerosol Research Lidar Network (EARLINET) over Spain and Portugal. Classic methods are assessed, as well as a time-adaptive technique using an extended Kalman filter.

In the second area of research motivation, 8 different PBL schemes from the WRF-ARW model are evaluated against lidar-derived measurements over Barcelona, and multiple observing systems over Athens. Model-simulated PBL height is analyzed, as well as surface and upper-air meteorological variables.

In the final research area, the most significant PBL schemes from the WRF-ARW model are employed in CALIOPE AQFS simulations for sensitivity of AQ forecasts as compared with surface air quality measurements over Catalonia, Spain. The geographical area contains complex terrain which provokes mesoscale meteorological processes, providing a good dataset for the evaluation.

1.5 Main objectives

Three main objectives are proposed in this Ph.D. thesis:

1. Evaluate methods currently available to estimate the PBL height from lidar observations.
2. Investigate PBL parameterization schemes in the WRF model.
3. Determine impacts of WRF model PBL schemes on simulations from the CALIOPE AQFS.

1.5.1 Obj. 1: Evaluation of available methods for estimating PBL height from lidar measurements

First, is an evaluation of available methods for estimating PBL height from lidar measurements based on data from the European Aerosol Research Lidar Network (EARLINET; <http://www.earlinet.org/>), including the Barcelona multiwavelength Raman lidar (Banks et al., 2014). Classic methods found in the literature are compared with a time-adaptive technique using an extended Kalman filter. PBL heights estimated with the various lidar methods are compared with estimates of the PBL height obtained from radiosoundings.

1.5.2 Obj. 2: Examine sensitivity of model-simulated boundary-layer variables to PBL parameterization schemes in the WRF model

Secondly, eight PBL schemes from the WRF model are evaluated as compared to observations over Barcelona (Banks et al., 2015) and Athens (Banks et al., 2016). Instrumentation includes two lidars, and numerous radiosondes and surface meteorological stations. Data from Athens was collected during the HygrA-CD campaign (<http://hygracd.impworks.gr/>), which took place in summer 2014.

1.5.3 Obj. 3: Analyze impact of WRF PBL schemes to photochemical and aerosol simulations from the CALIOPE air quality forecast system

Finally, four WRF PBL schemes are sensitivity-tested with CALIOPE AQ simulations, as compared with surface observations from ground AQ stations and lidar data from the Barcelona micropulse lidar (MPL), a new station in the NASA MPLNET (Banks and Baldasano, 2016).

Outcomes from this Ph.D. project will lead to preferred method(s) for estimating the PBL height from lidar, an evaluation of model PBL schemes at two locations, and finally greater knowledge of the sensitivity of AQ simulations to model PBL schemes, which may result in more accurate operational AQ forecasts over Europe.

1.6 Organization of the Ph.D. thesis

The thesis is structured around six chapters, with most chapters consisting of extracted or full-length peer-reviewed publications. The reference of each publication is presented at the beginning of each sub-chapter.

The rest of the document is as follows. Chapter 2 presents an inter-comparison of methods for obtaining PBL height from lidar during a July 2012 monitoring campaign over the Iberian Peninsula in the framework of EARLINET. Next, a performance evaluation of PBL height from lidar and the WRF model over Barcelona is discussed in Chapter 3. The analysis is expanded in Chapter 4 to examine the sensitivity of boundary-layer variables to PBL schemes in the WRF model in Greece. The analysis is based on surface meteorological observations, lidar, and radiosondes collected during the HygrA-CD field campaign. In Chapter 5, the impact of WRF model PBL schemes on air quality simulations over Catalonia, Spain is presented. Finally, conclusions and future research lines are drawn in Chapter 6.



Chapter 2

2 Inter-comparison of lidar methods for obtaining planetary boundary-layer height from a July 2012 monitoring campaign over the Iberian Peninsula in the framework of EARLINET

This chapter introduces three classic methods for estimating planetary boundary-layer height from lidar observations. Continuously-operated lidar data are taken from a field campaign from lidar instruments in the European Aerosol Research Lidar Network (EARLINET).

2.1 Introduction

The depth of the planetary boundary-layer (PBL) is defined as the height of the inversion level separating the free troposphere (FT) from the boundary-layer (Stull, 1988). Reliable representation of PBL height is important in applications ranging from climate studies to air quality modeling. Convective turbulent mixing processes are dominant in the mixing layer of the PBL and have a major influence on the growth and transport of atmospheric pollutants.

In recent years, lidar (laser radar) has proven to be a useful operational tool for nearly continuous monitoring of the lowest levels of the atmosphere with high spatial (~ 3.75 m) and temporal (< 5 min) resolutions. Four

Raman-elastic multi-wavelength lidar stations from EARLINET (European Aerosol Research Lidar Network) conducted a 72-hr campaign of continuous observations over Spain (Barcelona, Granada, Madrid) and Portugal (Evora) in early July 2012. This study systematically exploits 1-min averaged, range-squared-corrected lidar signals (RSCS) from the 532 nm analog reception channel of the instruments.

Several methods that have been applied in previous literature to derive PBL height from vertical aerosol backscatter profiles are compared. Most widely used are derivative techniques such as the gradient method (GM), inflection point method (IPM), and covariance techniques such as the wavelet covariance transform (WCT) method using a Haar wavelet. The methods function by detecting steep gradients in the aerosol backscatter profile, a proxy for the transition zone between the PBL and FT.

In addition, spatial patterns and diurnal variation of the PBL height and an analysis of the meteorological situation over the study area are also conducted. Backward trajectories from the NOAA HYSPLIT model indicate aerosols arrived from tropical maritime origins over the eastern Atlantic Ocean.

2.2 Data and methodology

2.2.1 Characteristics of lidar instruments used

The European Aerosol Research Lidar Network (EARLINET), to establish an aerosol climatology over Europe, is the first aerosol lidar network, established in May 2000 (Bösenberg et al., 2001), with the main goal to provide a quantitative dataset describing the aerosol vertical, horizontal, and temporal distribution, including its variability on a continental scale. The dataset is used to validate and improve models that predict the future state of the atmosphere and its dependence on different scenarios describing economic development, including those actions taken to preserve the quality of the environment. The data from multiple EARLINET sites across the Iberian Peninsula are exploited in this study for 9-12 July 2012.

Currently, there are three EARLINET sites over Spain and one station in Portugal. The three locations in Spain are Barcelona (41.389°N, 2.112°E), Madrid (40.456°N, 3.726°W), and Granada (37.164°N, 3.605°W). The only lidar station in Portugal is located in Evora (38.568°N, 7.912°W). Figure 2.1 shows the locations of the four lidar instruments used in this study, including elevation above the station and vertical range resolution of data recording. In general, the first measurements were recorded at 6:00 UTC on 9 July 2012, with a 1-3 min calibration period at the end of each hour's observations.

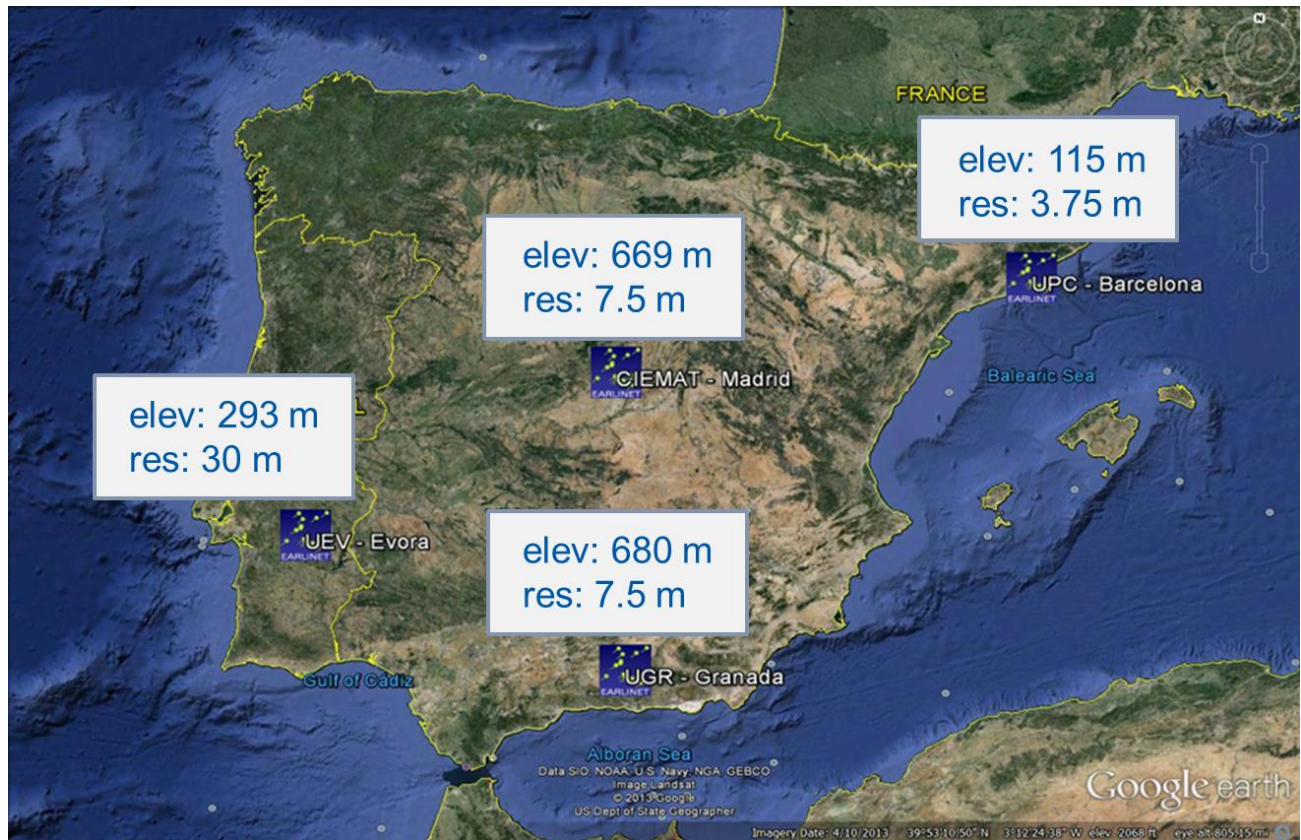


Figure 2.1 Locations of the four EARLINET lidar instruments, including elevation above sea level (m) and vertical range resolution of the raw lidar measurements.

In addition, Table 2.1 summarizes the main characteristics of each lidar instrument. The main differences between the lidar instruments are commercial versus laboratory built, maximum range, raw vertical range resolution, and line-of-sight. The full overlap height is similar for all instruments, ranging from 400-500 m.

Initially, the background lidar signal is removed using an average of the last 150 vertical points of each individual profile. It should be noted this approach has shown some signal-to-noise ratio (SNR) limitations, which will be discussed in a later section. A 15-min time-average is used for the application of all classic methods to estimate the PBL height. Other previous testing included 5-, 10-, 20-, and 30-min time-averages but 15-min was found to be optimal.

Table 2.1 Characteristics of the four EARLINET lidar stations, as of the 2012 monitoring campaign.

 EARLINET	Lidar stations in the Iberian Peninsula			
	Barcelona	Granada	Madrid	Evora
Latitude/longitude Elevation	41.389 N, 2.112 E 115 m	37.164 N, 3.605 W 680 m	40.456 N, 3.726 W 669 m	38.568 N, 7.912 W 293 m
Lidar model	laboratory	Raymetrics LR321	laboratory	PollyXT
Number of vertical points	8,190	16,000	4,096	2,048
Pulse repetition frequency	20 Hz	20 Hz	20 Hz	20 Hz
Overlap height	~ 500 m	~ 500 m	~ 400 m	~ 450 m
Maximum range	~ 30 km	60-90 km	30 km	60 km
Vertical resolution (Raw)	3.75 m	7.5 m	7.5 m	30 m
Distance from radiosounding	720 m	12 m	13.28 km	N/A
Line-of-sight	52°	0°	0°	5°

2.2.2 Methods for estimating PBL height from lidar

Three objectively-based methods are compared in this chapter. The first and most widely used derivative method is the gradient method (GM) (Sicard et al., 2006, 2011). This approach looks for the height, h , of the largest absolute local minimum of the first derivative of the $RSCS$ as a function of range, r :

$$h_{GM} = \min \left[\frac{\partial RSCS}{\partial r} \right] \quad (2.1)$$

The GM works very well in cases where the boundary-layer is well-mixed and the mixed-layer (ML) and the residual-layer (RL) are well disconnected. This two-layer effect is described by Stull (1988). This most often occurs in situations where shear is minimal and convective buoyancy is the driving mechanism, which occurs often in summertime situations due to maximum periods of solar insolation. In cases where advected aerosol layers are present the GM can have a difficult time diagnosing which layer is the true PBL height. Multiple

local minima will be present due to the advected aerosol particles in different layers of the atmosphere. Most often this situation occurs in the wintertime when long-range transport of aerosols is more of a concern, but it can happen anytime during the year. An example of a non-wintertime situation would be the intrusion of Saharan dust from North Africa towards Europe.

The next derivative method commonly used is the inflection point method (IPM) (Menut et al., 1999; Pérez et al., 2004) which searches the lidar backscatter profile for the height of the minimum of the second derivative:

$$h_{IPM} = \min \left[\frac{\partial^2 RSCS}{\partial r^2} \right] \quad (2.2)$$

Unless the GM fails to detect the strongest negative peak of the lidar signal the height determined from the IPM is not independent of the GM and will be found just below the height resolved by the GM. In the case of more complicated profiles (e.g., multiple layers) if the GM fails to detect the lowest negative peak then the IPM will be used to show the transition zone between the ML and the FT. The advection of Saharan dust into an area is a good example of the multiple layers concept. The RSCS is range-averaged using a rectangular window (60-m) for application of the GM and IPM.

The final method used to objectively determine the PBL height from lidar observations are wavelet-based methods, in particular the wavelet covariance transform (WCT) with a Haar wavelet. The general approach is to employ a Haar wavelet function to extract scale-dependent information from the original lidar backscatter profile. It is defined as a means of detecting step changes in the RSCS. The WCT method has been used by many authors (Gan et al., 2011; Mao et al., 2012) and has proven to be a very computationally robust technique.

The Haar wavelet function is defined as:

$$H\left(\frac{z-b}{a}\right) = \begin{cases} 1 & \text{for } b - a/2 \leq z \leq b \\ -1 & \text{for } b < z \leq b + a/2 \\ 0 & \text{otherwise} \end{cases} \quad (2.3)$$

where z is the profile height and a and b are the dilation and translation parameters of the wavelet, respectively. The covariance (Gamage and Hagelberg, 1993) is simply the convolution, $W_f(a, b)$ of the Haar function with the lidar backscatter profile:

$$W_f(a, b) = a^{-1} \int_{z_b}^{z_t} B(z) h \left(\frac{z-b}{a} \right) dz \quad (2.4)$$

where z_b and z_t are the bottom and top heights of the lidar profile and $B(z)$ is the lidar backscatter as a function of height. Here $B(z)$ is the RSCS. The maximum value of the covariance transform corresponds to the strong step-like decrease in the lidar backscatter signal where the gradient in aerosol concentration is the most defined. The corresponding height of the resulting maximum is identified as the PBL height. It has been discovered (Pal et al., 2012) that key uncertainties in the determination of the PBL height by this technique lie in the choice of the upper and lower limits of integration (z_b and z_t) for calculating the WCT and proper choice of the dilation parameter, a . The WCT is applied here using a 90-m dilation.

2.2.3 Calculation of PBL height from radiosonde launches

Radiosonde launches were available at 00:00 UTC and 12:00 UTC at both Barcelona (0.72 km from lidar) and Madrid (13.28 km from lidar) throughout the 72-h field campaign. Radiosondes were launched from Granada at a nearly co-located location each evening around 20:00 UTC. No radiosoundings were available near Evora, as the closest station is Lisbon over 100 km to the west.

PBL height was calculated from the radiosonde data using the bulk Richardson number (Ri_b) method (Holtslag et al., 1990). The Ri_b method is generally accepted and used in numerous previous studies. A critical Ri_b threshold is selected as 0.25 to find the transition height, which is a commonly-used value in the literature. The Ri_b attempts to identify the stable boundary layer at nighttime, but the lidar will have difficulty at these low heights due to overlap effects. However, visual inspection of virtual potential temperature (Θ_v) profiles can provide the residual layer height which can then be compared to lidar estimates.

2.2.4 Synoptic situation

Figure 2.2 shows the surface meteorological analysis on 9 July 2012 at 12:00 UTC, and an infrared satellite image captured around the same time. The pattern was dominated by a typical summertime situation with surface thermal low pressure (1011-hPa) over the IP, and broad high pressure situated near the Azores. A stationary frontal boundary was located over the northeast IP early in the period, but weakens by 10 July.

Light winds (< 10 kt) are observed at the surface. Imagery from the Moderate Resolution Imaging Spectroradiometer (MODIS) instrument (not pictured) reveals several areas of minor African dust throughout the period. These dust layers are evident in the lidar images from the different stations shown in the results. The synoptic set-up leads to nearly cloud- and rain- free conditions over Spain and Portugal through the period. Only some small areas of low clouds are found over the coastlines.

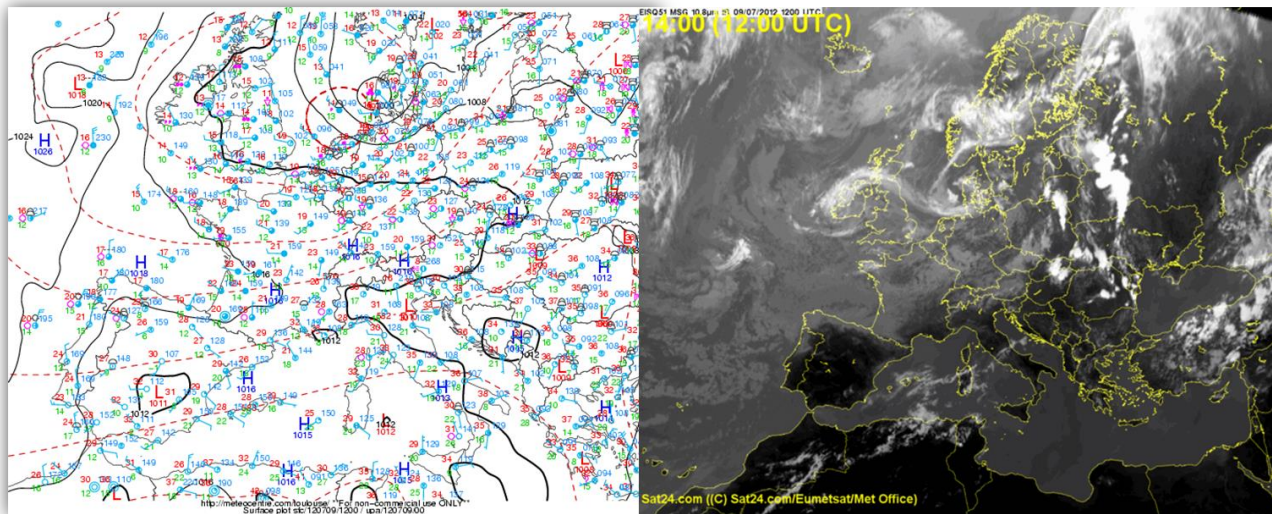


Figure 2.2 (Left) Surface meteorological analysis from 12:00 UTC on 9 July 2012, including mean sea-level pressure (hPa, black lines), 500-hPa geopotential heights (orange dashed lines), and surface station data. (Right) Infrared satellite image from 12:00 UTC on 9 July 2012. credits: MeteoCentre and Sat24.com

Two-day backward trajectories from the NOAA HYSPLIT model are shown in Fig. 2.3 for endpoints of the four lidar stations. General west to south-west flow is shown for all stations for tracers arriving at 3 km, a possible source region for mineral dust. The results are different at 500 m arriving altitude, with slow west to north-west flow at Granada, Evora, and Madrid. A pattern of regional recirculations is found at Barcelona.



Figure 2.3 Two-day backward trajectory analysis from the NOAA HYSPLIT model, with endpoints of the four lidar stations on 9 July 2012. The analysis is performed arriving at three heights; 500-m, 1500-m, and 3000-m.

2.3 Results and discussion

Results from Evora, Granada, and Madrid stations exhibit the daily evolution of PBL height well, with an average daytime maximum PBL height between 1.0 – 1.5 km. The best correlation ($R^2 = 0.88$) is found when using the WCT method at Barcelona when compared against 12:00 UTC radiosounding estimates. All lidar methods have issues when multiple aerosol layers are present, and these are discussed in detail below. The stable nocturnal boundary-layer (NBL) is difficult to retrieve with lidar due to overlap effects. Results are shown for Barcelona, Granada, and Evora lidar stations. The results from Madrid are not presented as there were some instrumental limitations which caused poor outcomes.

First, Figure 2.4 shows the full 72-h lidar time-height series for Barcelona, overlaid with 15-min estimates of the PBL height using the GM, IPM, and WCT methods. It is shown that the 9th of July is affected by low aerosol loads in the PBL, with very small gradients in the low levels. Issues with low clouds in the PBL begin on the 10th of July, complicating the comparisons between lidar methods and radiosounding. The comparison on the 11th at 0:00 UTC was ignored due to many low-level clouds. The WCT method performed the best

compared with daytime radiosoundings, with a mean bias around 200 m from the three launches. Toward the end of the time period multiple aerosol layers are apparent, making the PBL height retrievals unreliable.

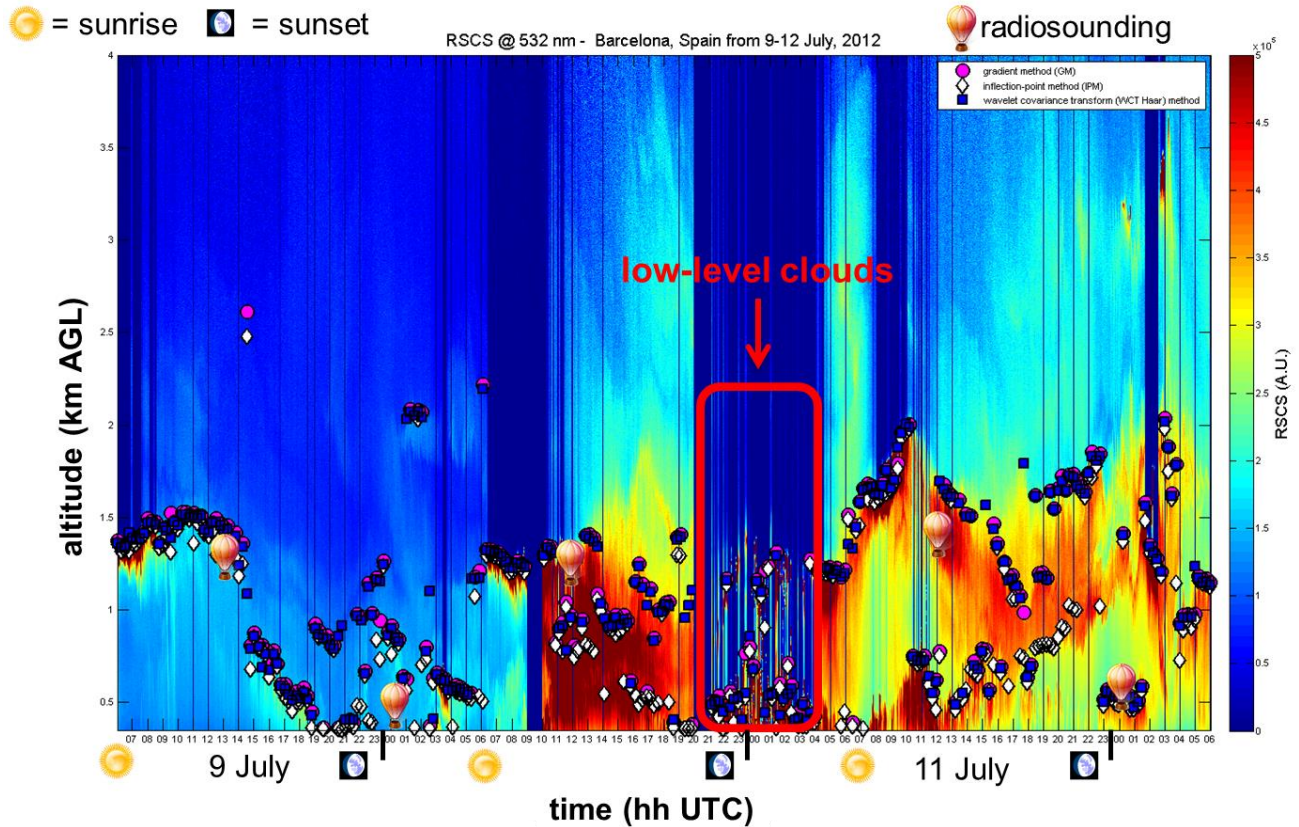


Figure 2.4 Lidar RSCS time-height series from 6:00 UTC on 9 July 2012 to 6:00 UTC on 12 July 2012 at Barcelona. Overlaid are 15-min time-averaged PBL height estimates using the GM, IPM, and WCT methods. Also shown are the estimates of PBL height from radiosonde launches (balloons) using the bulk Richardson number approach. Approximate sunrise and sunset times are indicated with symbols. An extended time period with low-level clouds is highlighted by a bold red box.

Secondly, Figure 2.5 shows the full 72-h lidar time-height series for Granada, overlaid with 15-min estimates of the PBL height using the GM, IPM, and WCT methods. It is found the classic methods have issues with the secondary aerosol layers due to dust, evident between 1.5 – 3 km. The lidar methods jump between the true PBL height closer to 1.5 km, and these secondary aerosol layers. PBL height estimates calculated from the radiosonde launches are higher than the lidar on the 9th and 10th, with a closer bias on the 11th. The IPM performs the worst of all methods at this station, capturing the incorrect aerosol gradient.

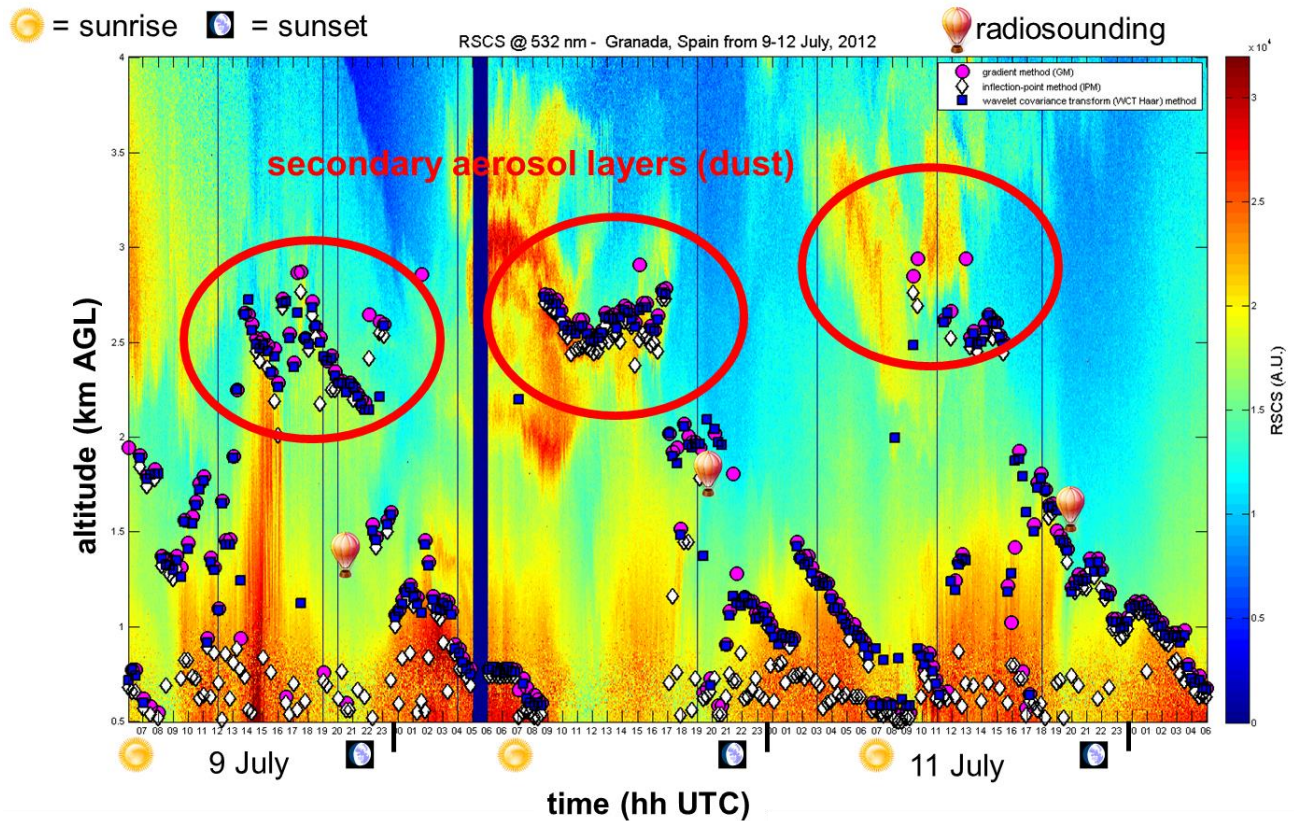


Figure 2.5 Lidar RSCS time-height series from 6:00 UTC on 9 July 2012 to 6:00 UTC on 12 July 2012 at Granada. Overlaid are 15-min time-averaged PBL height estimates using the GM, IPM, and WCT methods. Also shown are the estimates of PBL height from radiosonde launches (balloons) using the bulk Richardson number approach. Approximate sunrise and sunset times are indicated with symbols. Areas of secondary aerosol layers (dust) are highlighted with bold red ovals.

Finally, in Figure 2.6 is the full 72-h lidar time-height series for Evora, overlaid with 15-min estimates of the PBL height using the GM, IPM, and WCT methods. This station shows the daily evolution of the PBL very well, with a maximum PBL height around 1.5 km on 9 July and 10 July and 1.25 km on 11 July. The GM and WCT are very similar, with slightly lower estimates using the IPM. All the lidar methods have issues with low SNR at nighttime, most likely due to the background subtraction methodology. The background subtraction degrades SNR; when you subtract two random processes (i.e., the 150-point time-averaged profile from the lidar profile of interest) variances always add up, so SNR degrades.

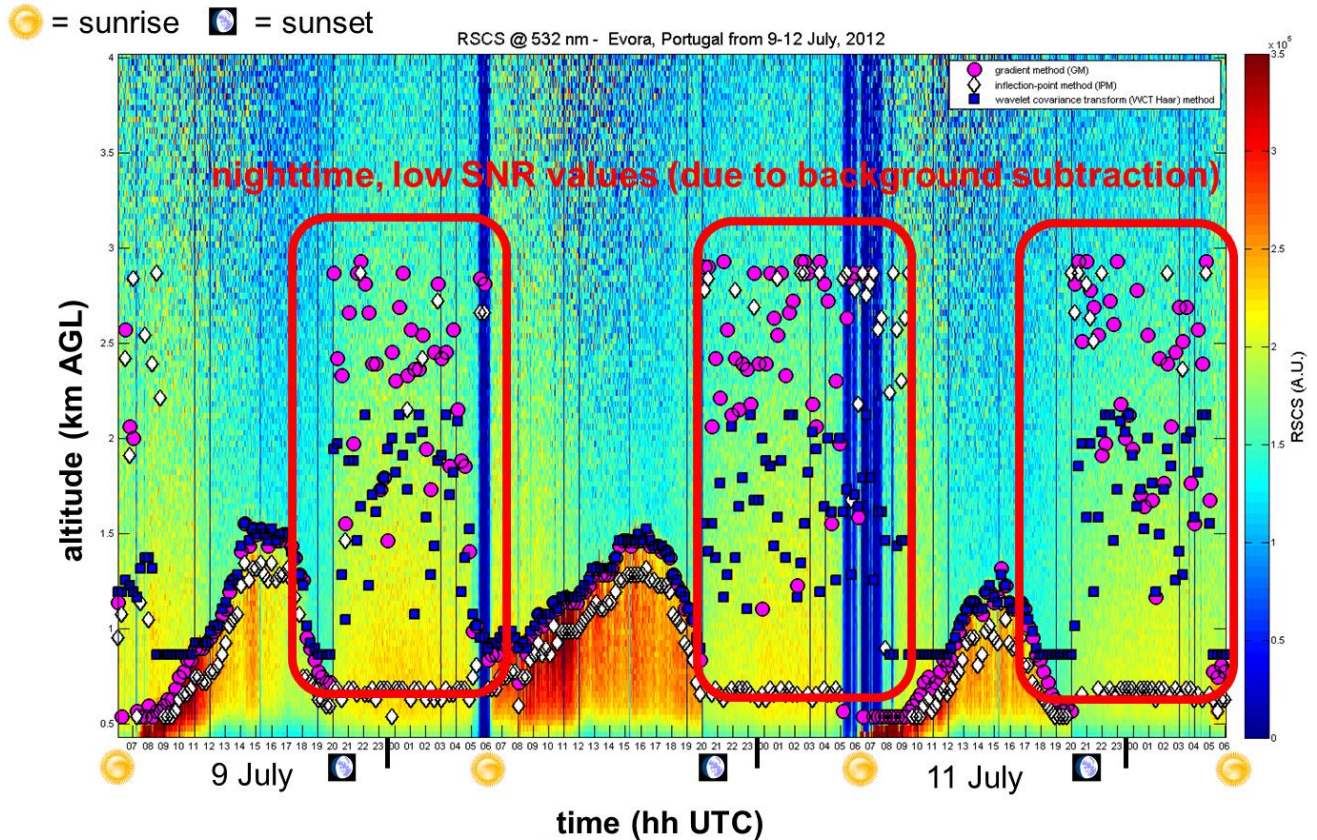


Figure 2.6 Lidar RSCS time-height series from 6:00 UTC on 9 July 2012 to 6:00 UTC on 12 July 2012 at Evora. Overlaid are 15-min time-averaged PBL height estimates using the GM, IPM, and WCT methods. Approximate sunrise and sunset times are indicated with symbols. Areas of low SNR are highlighted with bold red rectangles.

2.4 Conclusions

This chapter examined three classic methods for estimating the planetary boundary-layer (PBL) height from lidar observations. The lidar measurements were collected during a 72-h period of continuous observations from 9-12 July 2012, in the framework of EARLINET. PBL height estimates from the lidar are compared against radiosonde-calculated heights.

It is found that all the methods provide comparable results in optimal observing conditions. However, it is determined that the WCT is an optimal method, as it is more computationally efficient than the derivative techniques (GM and IPM). The best results are shown in daytime, clear air convective situations. In summer, PBL heights over the Iberian Peninsula are typically from 1 to 3 km.



Lidar proves to be a modern tool for near-continuous monitoring of PBL height. In addition, (Comerón et al., 2013) use linear system theory to prove the WCT and the GM are the same. Overall, it has been shown that lidar can be used as an effective means of obtaining accurate PBL heights on a nearly continuous basis.

Chapter 3

3 Performance evaluation of boundary-layer height from lidar and the Weather Research and Forecasting model at an urban coastal site in the north-east Iberian Peninsula

In this chapter is an evaluation of planetary boundary-layer (PBL) parametrizations in the Weather Research and Forecasting (WRF) numerical model, with three connected objectives: first, we use a cluster analysis algorithm of three-day back-trajectories to determine general synoptic flow patterns over Barcelona, Spain arriving at heights of 0.5 km, 1.5 km, and 3 km for a 16-year period; to represent the lower PBL, upper PBL, and low free troposphere, respectively. Seven clusters are determined at each arriving altitude. Regional recirculations account for 54 % of the annual total at 0.5 km, especially in summertime. In the second objective, we assess a time-adaptive approach using an extended Kalman filter to estimate PBL height from backscatter lidar returns at 1200 UTC \pm 30 min for 45 individual days during a seven-year period. PBL heights retrieved with this technique are compared with three classic methods used in the literature to estimate PBL height from lidar. The methods are validated against PBL heights calculated from daytime radiosoundings. Lidar and radiosonde estimated PBL heights are classified under objectively-determined synoptic clusters. With the final objective, WRF model-simulated PBL heights are validated against lidar estimates using eight unique PBL schemes as inputs. Evaluation of WRF model-simulated PBL heights are performed under different synoptic situations. Determination coefficients with lidar estimates indicate the non-local asymmetric convective model scheme is the most reliable, with the widely-tested local Mellor-

Yamada-Janjic scheme showing the weakest correlations with lidar retrievals. Overall, there is a systematic underestimation of PBL height simulated in the WRF model.

The contents presented in this chapter have been published in the journal, *Boundary-Layer Meteorology*, and is made available as an electronic reprint with the permission of BLM. The full paper (Banks et al., 2015) can be found at the following URL on the BLM website: <http://link.springer.com/article/10.1007/s10546-015-0056-2>. Systematic or multiple reproduction or distribution to multiple locations via electronic or other means is prohibited and is subject to penalties under law.

3.1 Introduction

The planetary boundary-layer (PBL) height is often calculated as the altitude of the inversion level separating the free troposphere from the boundary layer (Stull, 1988). Turbulent fluxes within the PBL occur at temporal and spatial scales that are much smaller than the grid sizes and temporal resolution of today's advanced mesoscale meteorological models. PBL parametrization schemes are employed in atmospheric models to handle the vertical diffusion in the whole column of the boundary layer (Skamarock and Klemp, 2008), while surface-layer and land-surface schemes provide the surface fluxes needed for PBL schemes to determine the flux profiles within the well-mixed boundary layer and the stable layer using the surfaces fluxes as inputs, thus providing atmospheric tendencies of temperature, moisture, and horizontal momentum in the entire atmospheric column.

Air quality forecast systems require timely, reliable, and accurate meteorological representations of boundary-layer properties. PBL height is an important input in an air quality forecast system (Seaman, 2000), as it delineates the top of the atmospheric mixing layer. Numerous operational definitions exist for determining PBL height from both observations and model simulations. Lidars (Light Detection and Ranging) with high spatial (< 30 m) and temporal resolutions (< 1 min) can be employed to monitor the PBL height using the backscattered light from aerosols as tracers.

Lidar presents some advantages over the more traditional use of radiosondes to retrieve PBL height, advantages that include lidar high temporal frequency and vertical spatial coverage, possible continuous operation and in a nearly automated way. Thus, a continuously-recorded PBL height allows for more in-depth analysis such as diurnal evolution and long-term climate studies. Typically, radiosondes are launched only twice each day, with limited vertical resolution and potential tracking problems in the lower boundary layer.

Several methods have been applied previously to determine the PBL height from lidar observations; here we refer to these past methods as classic methods. They are comprised of both objective and subjective methods: objective methods consist of various forms of derivative methods (Flamant et al. 1997, Sicard et al. 2006, 2011), wavelet analysis methods (Baars et al. 2008, Gan et al. 2011), threshold method (Melfi et al. 1985, Boers and Eloranta 2006), and the variance method (Menut et al. 1999, Hennemuth and Lammert 2006). Visual inspection methods (Quan et al. 2013) are infrequently used as a subjective approach, which adds levels of ambiguity that could possibly lead to poor results. Finally, an objective approach using an adaptive extended Kalman filter has recently been developed and tested (Lange et al. 2014).

These methods have been inter-compared previously (Seibert et al. 2000, Pal et al. 2010). Based upon the outcomes of these previous studies an optimum method has never been determined for estimating PBL height in all atmospheric conditions, especially complex lidar scenes with multiple aerosol layers. The choice of the operational definition of PBL height can have a large impact on the results, especially for the validation of model simulations.

A large number of previous studies have been carried out to validate PBL parametrization schemes in mesoscale meteorological models using observations (e.g., lidar, surface, upper air) and to evaluate the sensitivity of atmospheric parameters (i.e., PBL height, temperature) to the schemes. In areas surrounding the Mediterranean region the two primary meteorological models used in earlier efforts were the fifth generation Penn State-NCAR mesoscale model (MM5) model (Pérez et al. 2006a, Bossioli et al. 2009) and the Weather Research and Forecasting (WRF) model (Borge et al. 2008, Pichelli et al. 2014). Overall, it has been determined that no PBL scheme is superior to the others under all conditions, and each scheme has strengths and weaknesses. However, these previous efforts have shown that non-local PBL schemes usually provide lower biases and errors in certain cases, mainly in situations dominated by strong convection and little or no shear (Pérez et al. 2006a).

The region of interest in the present study is the urban metropolis of Barcelona, Spain, which is a complex geographical area located in the north-east Iberian Peninsula. The regional climate is affected by synoptic and mesoscale meteorological processes (Baldasano et al. 1994, Gonçalves et al. 2009), with some mesoscale processes in this region the result of the orientation of topographic features (pre-coastal and coastal mountain ranges) relative to the Mediterranean Sea (Fig. 3.1c). Previous work has found that both synoptic circulations and mesoscale processes combine to influence the height of the PBL (Sicard et al. 2006), which in the north-east Iberian Peninsula is highly variable and dependent on the general synoptic flow.



There are three main objectives of our study: the first is to provide an updated clustering of general synoptic flow patterns that affect the north-eastern Iberian Peninsula. This is accomplished utilizing a long period of kinematic back-trajectories and a cluster analysis algorithm. Secondly, results of the cluster analysis are used as complementary information to evaluate an adaptive technique using an extended Kalman filter (EKF) to estimate PBL height from lidar observations. The technique is compared with classic methods under different objectively determined atmospheric situations produced with the cluster analysis. Lidar data are selected around the time of daily daytime radiosonde launches to ensure a significantly comparative analysis. The final objective is to evaluate PBL height simulated from the WRF model using different PBL parametrization schemes. Model-simulated PBL heights are validated against those estimated with lidar using the EKF method.

Section 3.2 describes the set-up of the WRF model, the instrumentation used for PBL height estimates, and the cluster analysis algorithm, while Sect. 3.3 summarizes classic methods for estimating PBL height from lidar and presents descriptive information on the EKF technique. In Sect. 3.4 we present the results of the cluster analysis, the comparisons between lidar methods and radiosoundings, and the performance evaluation of the WRF model PBL schemes. Finally, conclusions are drawn and future work is discussed in Sect. 3.5.

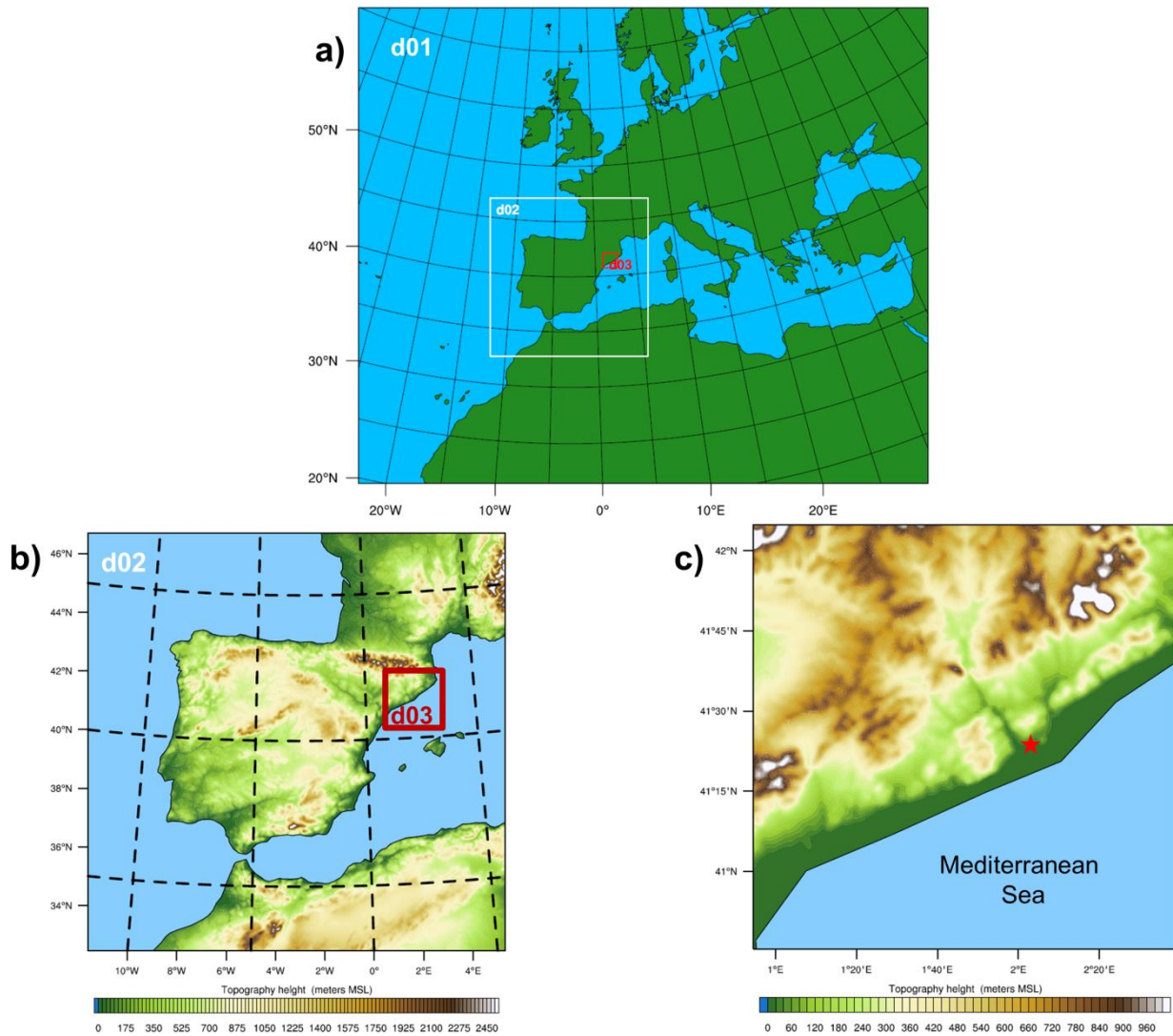


Figure 3.1 Model domain configuration (a) with the European-level parent domain (d01, 12 km × 12 km resolution), Iberian Peninsula domain (d02, 4 km × 4 km resolution), and the Barcelona geographical area domain (d03, 1 km × 1 km resolution). The Iberian Peninsula and Barcelona domains with associated topography are shown in (b). The topographic map is further zoomed in to the Barcelona domain (c), with a bold red star denoting the location of the lidar site.

3.2 Model configuration, observations, and cluster analysis

3.2.1 WRF model set-up

Here we use WRF model version 3.4.1 in diagnostic mode with the Advanced Research WRF (ARW) dynamical core. Three model domains (Fig. 3.1) were configured with varying horizontal grid spacing at the

parent European level ($12 \text{ km} \times 12 \text{ km}$), and two one-way nested domains for the Iberian Peninsula ($4 \text{ km} \times 4 \text{ km}$) and Catalonia ($1 \text{ km} \times 1 \text{ km}$) regions. It is assumed that $1 \text{ km} \times 1 \text{ km}$ spatial resolution is of fine enough detail to resolve most mesoscale features in the complex study area.

Initial and boundary conditions were obtained from the National Centers for Environmental Prediction (NCEP) Final Analysis product (NCEP, 2000), with operational global analysis data on $1^\circ \times 1^\circ$ grids available at six-hourly timesteps. The final analyses are available for the surface and 26 mandatory levels from 1000 hPa to 10 hPa.

Daily WRF model simulations were computed with a 36-hr forecast cycle, including the recommended minimum of 12 h allotted for model spin-up. Each simulation was initialized from 1200 UTC of the previous day, with a spin-up cycle added to counter instability issues with the simulation. The PBL height is evaluated at each time step after 24 h of runtime. An output temporal resolution of 1 hour was chosen, and the model was run with 38 terrain-following vertical levels, with the top at 50 hPa.

The physics options selected include WRF single-moment 3-class microphysics (Hong et al. 2004), Kain-Fritsch cumulus parametrization (Kain 2004), Dudhia shortwave radiation (Dudhia 1989), Rapid Radiative Transfer Model longwave radiation (Mlawer et al. 1997), and the Noah land-surface model (Tewari et al. 2004) - see Skamarock and Klemp (2008) for details.

One of our primary objectives is to provide a performance evaluation of PBL height simulated by different PBL parametrizations. In version 3.4.1 of the WRF-ARW model there is the option to choose from nine PBL schemes. Each PBL scheme is associated with one or more surface-layer schemes. So a summary of the eight PBL schemes and selected surface-layer schemes used herein is shown in Table 3.1.

The PBL parametrizations selected consist of five local and three non-local closure schemes. The operational definition of PBL height in the individual schemes falls into one of two general classes: the first class calculates the PBL height as the lowest level at which the bulk Richardson number (Ri_b) exceeds a certain threshold. This lowest level needs to be located above a certain pre-determined minimum height. The second class determines the PBL height at a level where the turbulent kinetic energy (TKE) profile decreases to some pre-defined threshold value. A brief description of the schemes follows.

Table 3.1 Summary of WRF model v3.4.1 experiment sets with PBL parametrization schemes and surface-layer schemes used in the study. Also shown are the operational methods of PBL height for each scheme, along with the threshold values used.

Set	PBL Scheme	Closure	Surface layer	PBL height method	Threshold
1	Yonsei University (YSU)	1.0 non-local	Monin-Obukhov	Ri_b calculated from surface	zero (unstable) 0.25 (stable)
2	Mellor-Yamada-Janjic (MYJ)	1.5 local	Eta similarity	TKE-prescribed threshold	$0.2 \text{ m}^2 \text{ s}^{-2}$
3	Quasi-Normal Scale Elimination (QNSE)	1.5 local	QNSE	TKE-prescribed threshold	$0.01 \text{ m}^2 \text{ s}^{-2}$
4	Mellor-Yamada-Nakanishi-Niino level 2.5 (MYNN2)	1.5 local	MYNN	TKE-prescribed threshold	$1.0 \times 10^{-6} \text{ m}^2 \text{ s}^{-2}$
5	Asymmetric Convective Model version 2 (ACM2)	1.0 non-local	Monin-Obukhov	Ri_b calculated above neutral buoyancy level	0.25 (all)
6	Bougeault-Lacarrère (BouLac)	1.5 local	Monin-Obukhov	TKE-prescribed threshold	$0.005 \text{ m}^2 \text{ s}^{-2}$
7	University of Washington (UW)	1.5 local	Monin-Obukhov	Ri_b threshold	0.25 (all)
8	Total Energy – Mass Flux (TEMF)	1.5 non-local	TEMF	Ri_b threshold	zero (all)

The first and most widely-used PBL scheme is the Yonsei University (YSU) scheme (Hong et al. 2006), which is a first order, non-local scheme with an explicit entrainment layer and a parabolic K-profile in an unstable mixed layer. It is a modified version of the medium-range forecast scheme (Hong and Pan 1996) from the legacy MM5 model (Dudhia 1993). The largest improvement to the YSU scheme was the addition of an explicit term for the treatment of the entrainment zone. PBL height in the YSU scheme is determined from the Ri_b method, with a threshold value of zero.

The next most widely used PBL scheme is the Mellor-Yamada-Janjic (MYJ) scheme (Janjic 2002), which is a 1.5-order prognostic TKE scheme with local vertical mixing, and a modified version of the old Eta scheme from the MM5 model (Janjic 1990). PBL height is determined from the TKE, where the PBL top is defined as the level at which the profile decreases to a prescribed small value, here taken as $0.2 \text{ m}^2 \text{ s}^{-2}$. This scheme is appropriate for all stable and slightly unstable flows; however, it is not recognized as appropriate for simulating convective processes.

The third scheme is the Quasi-Normal Scale Elimination (QNSE) scheme (Sukoriansky et al. 2005), which is a 1.5-order, local closure scheme and has a TKE prediction option for stably stratified regions. Here, the PBL height is defined as the height at which the TKE decreases to a prescribed low value, as in the MYJ scheme. In WRF model v3.4 the value is $0.01 \text{ m}^2 \text{ s}^{-2}$. The scheme is valid for stable stratification and weakly unstable conditions, but needs improvement in truly unstable cases.

The fourth scheme is the Mellor-Yamada-Nakanishi-Niino level-2.5 (MYNN2) scheme (Nakanishi and Niino 2006) (the Mellor-Yamada-Nakanishi-Niino level-3 (MYNN3) scheme will not be evaluated), which is a 1.5-order, local closure scheme tuned to a database of large-eddy simulations in order to overcome the typical biases associated with other MY-type schemes, such as insufficient growth of the convective boundary layer and underestimation of TKE. The MYNN2 scheme predicts sub-grid TKE terms. PBL height is determined as the height at which the TKE falls below a critical value, $1.0 \times 10^6 \text{ m}^2 \text{ s}^{-2}$, in this version of the WRF model.

The fifth scheme is the Asymmetrical Convective Model version 2 (ACM2) scheme (Pleim 2007), which is a first-order, non-local closure scheme and features non-local upward mixing and local downward mixing. It is a modified version of the ACM1 scheme from the MM5 model, which was a derivative of the Blackadar scheme (Blackadar 1978). The scheme has an eddy-diffusion component in addition to the explicit non-local transport of the ACM1 scheme. The PBL height is determined as the height at which the Ri_b calculated above the level of neutral buoyancy exceeds a critical value ($Ri_{bc} = 0.25$). For stable or neutral flows the scheme shuts off non-local transport and uses local closure.

The sixth scheme is the Bougeault–Lacarrere (BouLac) scheme (Bougeault and Lacarrère 1989), which is a 1.5-order, local closure scheme and has a TKE prediction option designed for use with the Building Environment Parametrization multi-layer, urban canopy model (Martilli et al. 2002). The BouLac scheme diagnoses PBL height as the level at which the prognostic TKE reaches a sufficiently small value (in version 3.4 of the WRF model it is $0.005 \text{ m}^2 \text{ s}^{-2}$).

The seventh scheme is the University of Washington (UW) scheme (Bretherton and Park 2009), which is a 1.5-order, local TKE closure scheme from the Community Earth System Model (Gent et al. 2011). The PBL height is defined as the inversion height between grid levels via a Ri_b threshold, with a critical value of 0.25 used in all cases of stability, as in the ACM2 scheme.

Finally, the eighth scheme is the Total Energy-Mass Flux (TEMF) scheme (Angevine et al. 2010), which is a 1.5-order, non-local closure scheme and has a sub-grid-scale total energy prognostic variable, in addition to mass-flux type shallow convection. The TEMF scheme uses eddy diffusivity and mass flux concepts to determine vertical mixing, with the PBL height calculated through a Ri_b method with a threshold value of zero. In this study we encountered minor stability issues with seven simulation days using the TEMF scheme. The stability issues are due to a threshold exceedance of potential temperature over the desert regions in our parent domain. Decreasing the time between calls to the radiation physics scheme improved the stability for five of the seven simulation days.

3.2.2 Elastic backscatter lidar

Data from two multiwavelength elastic Raman lidars (Rocadenbosch et al. 2002) were obtained from the database of the Remote Sensing Laboratory in the Department of Signal Theory and Communications at the Universitat Politècnica de Catalunya (UPC) in Barcelona, Spain. The lidar group at the UPC is a member station of the European Aerosol Research Lidar Network (EARLINET; Bosenberg et al. 2001). Lidar observations were selected around 12:00 UTC \pm 30 min from a database covering a 7-year period between 2007 and 2013. This criterion led to a total of 45 individual measurement days. Individual daily WRF model simulations were run for the same 45 days for the evaluation of PBL parametrization schemes.

The history of the lidar program at UPC dates back to the first Spanish elastic backscatter lidar in 1993. From 2007 to August 2010 was a 3-channel instrument comprised of elastic and Raman channels, and since

September 2010, is a 6-channel multi-spectral instrument with elastic and Raman channels, and aerosol/water-vapor capabilities. Characteristics of the two instruments are shown in Table 3.2.

Table 3.2 Summary of instrument specifications for the two UPC lidar instruments used in this study: time periods (2007 – 2010) and (2010 – 2013). Also shown are the ranges determined for the initial state vector to the EKF method and the threshold ranges selected for the threshold method.

Instrument specifications	2007 – 2010	2010 – 2013
Lidar model	3-channel elastic/Raman	6-channel elastic/Raman
Received wavelengths (nm)	elastic: 532/1064 Raman: 607	elastic: 355/532/1064 Raman: 387/407/607
Spatial resolution (m)	7.5	3.75
Slant path line of sight (elevation angle)	$\theta = 50^\circ$	$\theta = 38^\circ$
Full-overlap height (m)	250	450
<u>Initial state vector ranges</u>		
PBL height (km)	0.5 – 2.0	0.75 – 1.5
EZ scaling factor (km^{-1})	3.7 – 18.5	7.4 – 36.9
Transition amplitude, normalized (A')	$0.4 \times 10^{-3} - 0.1$	0.08 – 35.0
Molecular background, normalized (c')	0.001 – 0.05	0.1 – 8.5
Threshold value range ($V \cdot \text{km}^{-2}$)	$5.5 \times 10^{-4} - 0.15$	0.8 – 22.5
* Note: Year 2007 spatial resolution = 15 m		

Raw lidar data for this analysis are obtained from the visible channel (532-nm elastic, analog acquisition) with either 15 m (2007), 7.5 m (2008 to August 2010), or 3.75 m (after August 2010) raw vertical resolution and 1-min averaged temporal resolution. The 532-nm analog channel was selected considering its acceptable signal-to-noise ratio > 5 at the maximum study range (3 km) and the contrast between aerosol and molecular backscatter returns. Pre-processing of the lidar returns include removal of the molecular background using Rayleigh fit to achieve range-corrected signal.

Lidar range-corrected signal are used as input to the PBL-retrieval algorithms explained in Sect. 3.3. Range is limited at low levels due to the incomplete overlap between the laser transmitter and the receiving telescope (Collis and Russell 1976). For boundary-layer studies overlap issues may make PBL height estimations unreliable or unavailable. The instruments used in this work have an approximate overlap range as high as 0.45 km, below which the lidar returns may be unreliable for the analysis. This is taken into account when retrieving the PBL height with the various estimation methods.

3.2.3 Radiosoundings

It is important to have a reference PBL height to compare to the estimates from lidar observations. PBL height calculated from radiosounding measurements have become an accepted reference in the community (Seibert et al. 2000) and are exploited in this evaluation. Upper-air meteorological measurements are obtained from 12:00 UTC radiosonde launches performed by the Meteorological Service of Catalunya in Barcelona (41.38°N, 2.12°E, 0.98 km asl). The meteorological service routinely launches the radiosondes approximately 0.72 km distance from the site of the UPC lidar. This radiosonde instrument records atmospheric variables of temperature (°C), relative humidity (%), wind speed (m s^{-1}) and direction (°), and barometric pressure (hPa).

PBL height is calculated here from the radiosounding data using the bulk Richardson number (Ri_b) method (Holtslag et al. 1990), the same method used in many of the WRF model PBL schemes (Sect. 3.2.1) to diagnose the PBL height. The Ri_b approach requires wind speed and direction, barometric pressure, and temperature as input variables at each altitude. The Ri_b method is a proxy of where the atmospheric state transitions from turbulent to laminar, possibly indicating the top of the PBL. PBL height is calculated at the altitude where Ri_b exceeds a so-called critical Richardson number (Ri_{bc}).

From many previous studies the Ri_{bc} is selected as a universal constant between 0.1 and 1.0 (Richardson et al., 2013). Typically higher critical values are selected in areas where the turbulent transition from an

atmosphere dominated by buoyant forces to shear is larger. In this work many critical values were tested against visual inspection of vertical profiles of potential temperature and humidity. It is found that $Ri_{bc} = 0.55$ is the most appropriate value for this dataset. This critical value is higher than used in previous studies in Barcelona (Sicard et al. 2006) but is still considered in the literature as a good transition value between the buoyancy and shear states for a complex urban area.

3.2.4 Back-trajectory cluster analysis

The aerosol load in the boundary layer can be developed and modified depending on the predominant synoptic wind flow. Changes in the aerosol load, especially in the boundary layer to lower free troposphere, can affect the PBL height estimation from lidar.

To enhance the robustness of the analysis, the methods to obtain PBL height from lidar are evaluated under different synoptic flows determined with an objective procedure. In order to objectively quantify the atmospheric dynamics from a synoptic perspective and select representative lidar cases from varying atmospheric flows, a cluster analysis technique is performed.

A semi-automated cluster analysis technique based on the methodology of a previous study (Jorba et al. 2004) is used. The technique is selected due to its relatively small computational requirements. The main component necessary for the analysis are backward trajectories (back-trajectories). Three-day back-trajectories are calculated using the Hybrid Single Particle Lagrangian Integrated Trajectory (HYSPLIT) model (Draxler and Rolph 2013) with endpoint of the Barcelona lidar site at three vertical levels: 0.5 km, 1.5 km, and 3 km. These levels are selected as altitudes representing a level within the boundary layer, near the top of the PBL, and within the low free troposphere, respectively. The back-trajectories are calculated once per day ending at 12:00 UTC. Input data are downloaded from the NCEP Global Data Assimilation System composed of a 16-yr period from 1998 to 2013. The data are interpolated onto a $1^\circ \times 1^\circ$ grid with a 6-hr temporal resolution.

Jorba et al. (2004) employed the cluster analysis algorithm over Barcelona using five years (1997 – 2002) of four-day back-trajectories. We selected three-day back-trajectories because we are interested in shorter-range local effects. The algorithm functions by determining an optimal number of cluster groups based on synthetic seed trajectories of varying lengths and curvature. The optimal number of clusters is obtained through a

multivariate statistical method. A compromise is reached between the total number of clusters retained without losing information. For this study we selected seven clusters at each arriving altitude.

3.3 Methods to estimate PBL height from lidar

3.3.1 Classic methods

Classic methods used in this study are classified as gradient-based, variance-based, or subjectively-based. In the following we describe general characteristics of the methods and highlight previous works evaluating these techniques.

Wavelet-based methods can be used to objectively determine PBL height from lidar observations, in particular, the wavelet covariance transform (WCT) with a Haar wavelet. The general approach is to employ the Haar wavelet function to extract scale-dependent information from the original lidar range-corrected signal profile; this detects step changes in the range-corrected signal. The WCT method has been used in many previous works (Baars et al. 2008, Gan et al. 2011) and has proven to be a very computationally robust technique.

With the WCT method, the maximum value of the covariance transform corresponds to the strong step-like decrease in the lidar range-corrected signal, where the gradient in aerosol concentration is the most clearly defined. The corresponding height of the resulting maximum is identified as the PBL height. Pal et al. (2012) discovered that key uncertainties in the determination of PBL height by this technique lie in the choice of the upper and lower range limits of integration for calculating the wavelet transform and proper choice of the dilation parameter. To recall, the dilation parameter is the vertical extent of the step function. Baars et al. (2008) introduced a modified version of the WCT method in an attempt to find an appropriate dilation dependent on the atmospheric situation. For this study, a series of dilation values have been tested with the Barcelona lidar data. For simplification of applying the WCT method we use a constant dilation ($20 \times \Delta R$) for the entire lidar dataset. In this application ΔR is the range resolutions of the two instruments described in Table 3.2.

Recently, it has been shown (Comerón et al. 2013) that the WCT method using a Haar wavelet is completely equivalent to derivative-based methods when applied to spatially low-pass filtered range-corrected signals. Therefore, in this study we use the WCT method as described above. The WCT method has the advantage of performing the PBL height estimate in a single, computationally efficient step.

Another classic method used in this study is the threshold method (Melfi et al. 1985, Boers and Eloranta 2006). This simple technique functions using a user-defined critical threshold value in the lidar range-corrected signal to distinguish the PBL from the free troposphere. Threshold values vary for the two instruments used in this work with their ranges shown in Table 3.2. Typically, the method also requires the user to select an upper and lower search altitude. For our purposes we constrain to a lowest altitude of 0.45 km which corresponds to the overlap range of the UPC lidar. The highest altitude is chosen as 4 km as a realistic estimate of the possible highest PBL height in Barcelona.

Finally, the variance method (Menuet et al. 1999, Hennemuth and Lammert 2006) makes use of the vertical profile of the variance of the lidar range-corrected signal. With this method the PBL height is the level at which there is a clear maximum in the variance profile. We subject 15 profiles of 1-min temporal resolution to the variance algorithm to estimate the PBL height.

3.3.2 UPC extended Kalman filter technique

An adaptive approach utilizing an extended Kalman filter (EKF) (Brown and Hwang 1982) has been developed and tested in the UPC Remote Sensing Laboratory to trace the evolution of the PBL (Lange et al. 2014). The technique builds upon previous works from Rocadenbosch (1998, 1999). Lange et al. (2014) found that the main advantages of the EKF are the ability to time-track the PBL height without need for long time averaging and range smoothing and the ability to perform well under low signal-to-noise ratio conditions. The EKF technique benefits from the knowledge of past PBL height estimates and statistical covariance information to predict present-time estimates.

The EKF approach is based on estimating four time-adaptive coefficients of a highly simplified erf-like curve model, representing the PBL transition in terms of the lidar range-corrected signal. The erf-like model, $h(R)$, is formulated as follows

$$h(R; R_{bl}, a, A, c) = \frac{A}{2} \left\{ 1 - \operatorname{erf} \left[\frac{a}{\sqrt{2}} (R - R_{bl}) \right] \right\} + c \quad (3.1)$$

where R is the range, R_{bl} is an initial guess of the PBL height, a is the entrainment zone (EZ) scaling factor, A is the amplitude of the erf transition, and c is the average molecular background at the bottom of the free troposphere. It is important in the EKF technique to initialize the state vector parameters (R_{bl} , a , A , c) properly. Ranges of the initial state vector parameters for the two instruments are shown in Table 3.2. If the state vector is not initialized correctly one can expect not so reliable estimates of PBL height.

For illustrative purposes an annotated 1-min lidar backscatter profile is shown in Fig. 3.2. The initial state vector parameters have been selected to evaluate a PBL height around 1.4 km, previously known from a radiosounding. In this case a narrow transition amplitude (A) was chosen as there are at least two other transitional zones below 1.75 km. If we had selected a broader transition amplitude most likely the filter would have taken longer to converge on a solution.

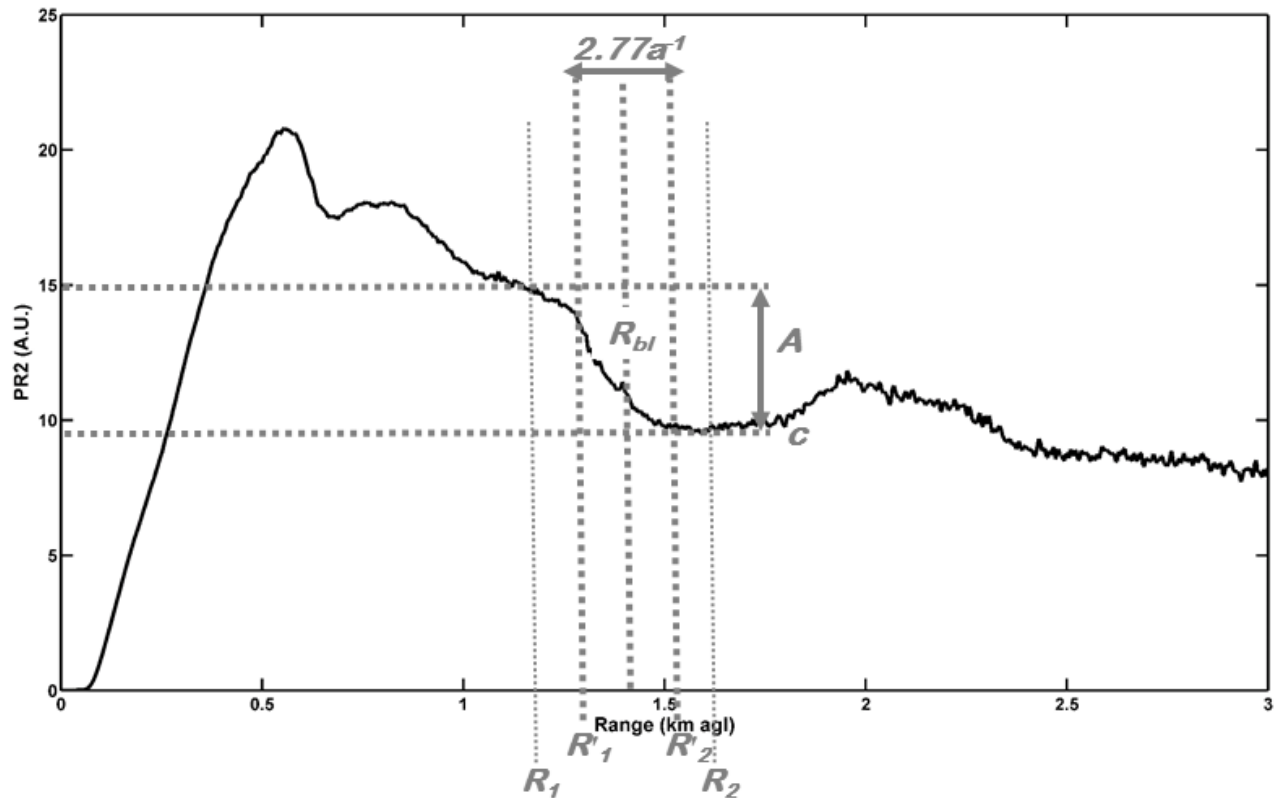


Figure 3.2 1-min lidar power \times range-squared (PR2) profile (A.U.) at 532 nm wavelength (solid black line) from 17 June 2013 at 1209 UTC. Annotated are the EKF characteristic parameters (R_{bl} , a , A , and c). R_1 and R_2 are the start and end range limits defining the length of the observation vector passed to the filter. R'_1 and R'_2 are the start and end range limits of the erf-like PBL transition zone.

EKF state vector initialization also requires statistical covariance information from the user side, accomplished using atmospheric state-noise and error covariance matrices. The statistical covariance information, along with the state vector and Kalman gain, are updated recursively at each 1-min iteration of the filter. With use of this recursive procedure, the EKF adjusts the projection trajectory of the PBL atmospheric variables, and improves estimation of the PBL parameters via a new atmospheric state vector.

It is important to note range-corrected signal input to all lidar-based estimation methods have not been further range-smoothed or time-averaged, as one objective of this work is to display the advantages of the EKF technique under these criteria. PBL heights are estimated for all lidar methods using the clean 1-min temporal resolution. An average of five 1-min PBL height estimates closest to 12:00 UTC is evaluated for each case.

This allows for a more representative comparison to radiosoundings as the PBL height can fluctuate drastically over short time periods. PBL height estimates are shown in km a.s.l. throughout this study.

A common statistical technique called the coefficient of determination (R^2) is used to measure the correspondence between the lidar-estimated and radiosonde-calculated PBL heights. The same statistic is used for the performance evaluation of the WRF simulations. R^2 (Upton and Cook, 2008) can be interpreted to explain the goodness of fit between the dependent and independent variables. Values of R^2 range from 0 – 1 with higher values indicating a closer correspondence between the variables.

3.4 Results and discussion

3.4.1 Objectively determined synoptic cluster types

From the cluster analysis, seven individual synoptic clusters are determined at each arriving altitude (0.5 km, 1.5 km, and 3 km). Overall, cluster types at the three arriving altitudes show similar patterns (Fig. 3.3). However, some key differences are found when assessing the results of the cluster analysis at the different levels and when comparing to previous results found in Jorba et al. (2004) at the 1.5 km and 3 km arriving altitudes.

Seven individual synoptic clusters arriving at 1.5 km and their associated centroids are shown in Fig. 3.3b. General synoptic flows at this altitude are a proxy as near the top of the PBL in the Barcelona area. The monthly temporal frequency of the different clusters is shown in Fig. 3.3d, expressed in terms of an annual percentage. The monthly temporal frequencies for clusters at 0.5 km and 3 km altitudes are similar to 1.5 km, and are not presented here.

Regional recirculations from the east or west are the most predominant synoptic clusters throughout the year, accounting for 44.5 % of the total (5756) back-trajectories. Regional recirculations occur most often in the summertime when the synoptic situation is stagnant, thus leading to strong mesoscale processes in the low levels of the atmosphere (Baldasano et al. 1994). For simplicity, we define the term regional recirculations as a combination of the easterly and westerly clusters for the rest of the paper.

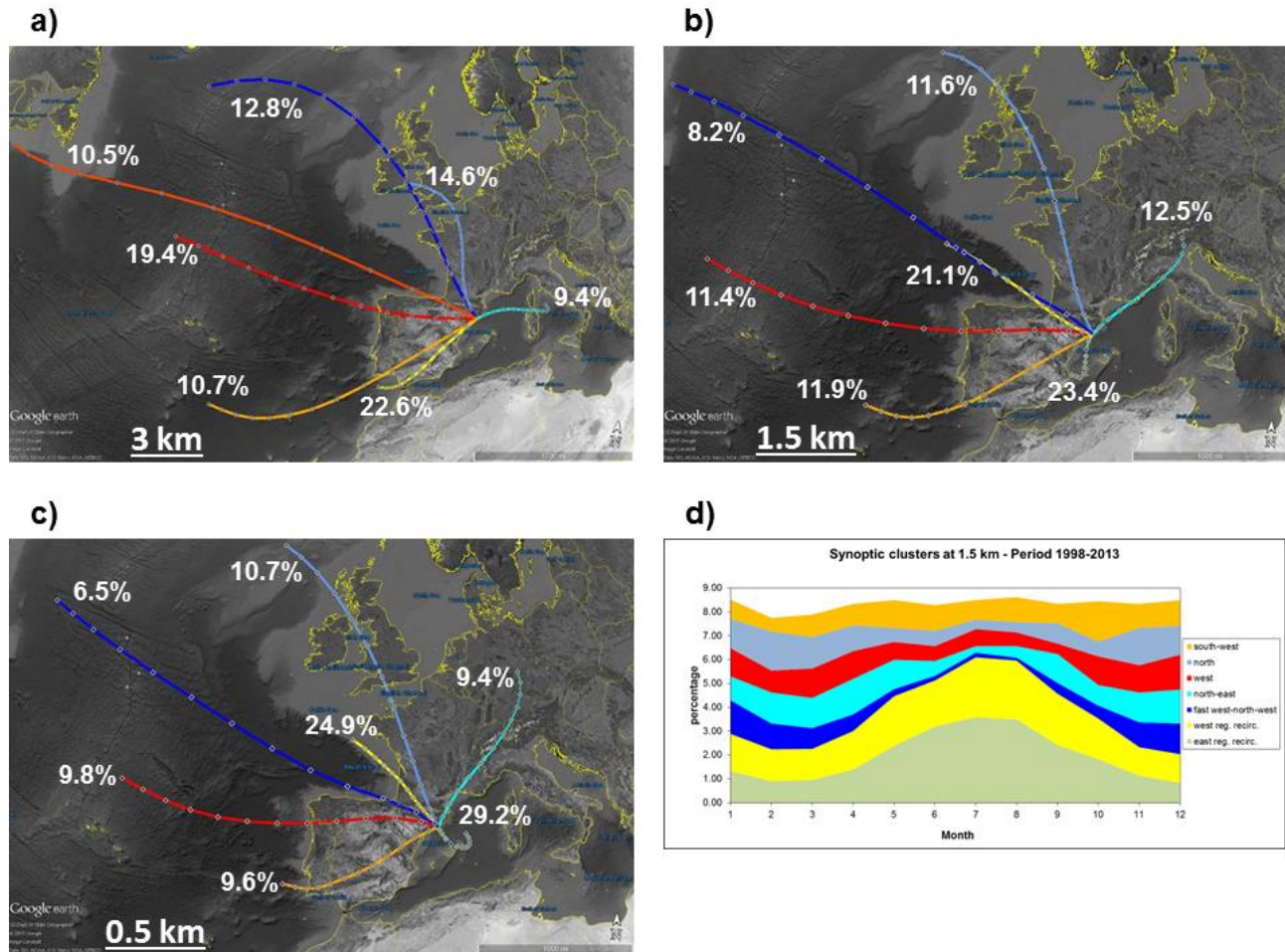


Figure 3.3 Centroids (white diamonds) and frequency (% total) of the seven clusters arriving at 3 km (a), 1.5 km (b), and 0.5 km (c) altitudes. Clusters at 3 km: north (powder blue), east (cyan), south-west (orange), west (red), fast west (orange-red), north-west (blue), and slow south-west (yellow). Clusters at 1.5 km: north (powder blue), north-east (cyan), south-west (orange), west (red), fast west-north-west (blue), recirculations from the west (yellow), and recirculations from the east (light green). Clusters at 0.5 km: north (powder blue), north-east (cyan), south-west (orange), west (red), north-west (blue), recirculations from the west (yellow), and recirculations from the east (light green). Finally (d), monthly frequency (annual %) of occurrence of each cluster arriving at 1.5 km with same colour scheme.

The frequency of lidar days in a particular cluster at 1.5 km shows that 55.6 % of the lidar data falls into the regional recirculations categories. The next most frequent cluster is synoptic flow from the north (20 %), followed by flow from the south-west (15.6 %). The other three synoptic clusters; flows from the north-east, west, and fast west-north-west, in total account for less than 10 % of the available lidar days.

Synoptic flows arriving at 0.5 km are important as it represents an altitude typically within a well-defined PBL. Centroids of the seven individual synoptic clusters arriving at 0.5 km are shown in Fig. 3.3c. Similar to

clusters at 1.5 km, regional recirculations are the most predominant synoptic pattern. The predominance of regional recirculations at both altitudes is attributable to the complex diurnal mesoscale processes which result from the location of Barcelona between the mountains and the Mediterranean Sea.

The frequency of lidar days in synoptic clusters arriving at 0.5 km altitude is similar to those at 1.5 km, except regional recirculations show an even greater dominance (73.4 %) of the available lidar days. This is mainly due to the topographic features of the area acting as a barrier to the other synoptic flows. This can be confirmed by the lack of lidar days with flows from the south-west and north-west, with only 4.4 % of the total.

Finally, the centroids of seven distinct synoptic clusters arriving at 3 km are shown in Fig. 3.3a, an altitude representative of the low free troposphere. The main difference between cluster types at this altitude and the two lower levels is the substitution of regional recirculations for slow south-west and easterly synoptic flows. This is most likely due to the lack of the topographic barriers found at the lower altitudes. This finding is a departure from Jorba et al. (2004) where they found regional recirculations at both 3 km and 1.5 km altitudes.

The frequency of lidar days in clusters arriving at 3 km show some differences from those at 1.5 km and 0.5 km. Slow south-west and north-west synoptic flows are the most predominant, accounting for 24.4 % and 22.2 % of the total, respectively. If we combine slow south-west and south-west flows into one group, they account for 42.2 % of the lidar days. Synoptic flows from the south-west are a major contributor to desert dust outbreaks in the north-east Iberian Peninsula.

It is well evident from Fig. 3.3 that the overall patterns (curvature) of the synoptic clusters are similar at all arriving altitudes selected for this study. The primary difference between results at different altitudes is the length (magnitude) of the centroids. It can be seen from Fig. 3 that the length of the centroid increases with an increase in arriving altitude, indicative of faster wind speeds. We present statistical comparisons between lidar-estimated and radiosonde-calculated PBL heights according to synoptic clusters.

3.4.2 PBL height comparisons between lidar methods and radiosounding

The comparison of PBL height estimates between the different lidar methods and radiosoundings is divided into two focus areas: first, we discuss comparisons for the total collection of lidar observations (2007 – 2013), and then comparisons are made with respect to the synoptic flows objectively determined with the cluster analysis.

Over the 2007 – 2013 data collection period the 45 individual measurement days yield an average PBL height of 1.28 ± 0.4 km (1 σ based on a normal distribution) at 12:00 UTC via the EKF method. As mentioned previously, 12:00 UTC was selected as the observation time for two main reasons. The first reason is 12:00 UTC is very close to the time of maximum solar insolation in Barcelona, which typically leads to the daytime maximum PBL height. The second reason was to compare with radiosonde launches, which we use as the reference PBL height.

The average PBL height estimated with the EKF technique is very close to the 1.27 km average height determined with the threshold method, but farther apart when compared with estimates from the WCT (1.23 km) and variance (1.16 km) methods. However, the standard deviation from each of the methods are quite similar. The average PBL height estimated with the EKF method is very similar to results found by Sicard et al. (2006, 2011) in studies over Barcelona. Sicard et al. (2011) estimated an annual average PBL height of 1.21 km using a gradient method. It is well known from previous studies that the PBL height in the north-east Iberian Peninsula doesn't vary much with time of the year. Sicard et al. (2006) estimated an average PBL height of 1.45 km in summer and 1.42 km in winter using 162 days of lidar data.

Due to a lack of observations in some synoptic clusters, the determination coefficients can only be calculated for the total collection of observations. If the whole collection of PBL height estimates is considered, including outliers, the determination coefficient between PBL heights estimated with the EKF technique and radiosoundings is relatively very high ($R^2 = 0.77$, $N = 45$). The threshold method shows the next best correspondence ($R^2 = 0.19$), but much weaker with the other two classic methods ($R^2 = 0.02$ for WCT method and $R^2 \approx 0$ for variance method), most likely due to the lack of range smoothing and temporal averaging of the range-corrected signal which these methods perform best with, especially for complex scenes.

To further improve the results, lidar-based estimates with gross outliers are removed prior to evaluating the correlation statistics. Gross outliers are defined as biased estimates (lidar PBL height – radiosounding PBL height) greater than $\pm 1 \sigma$ of the mean PBL height of the associated histogram for each method (Fig. 3.4),

which corresponds approximately to a 25 % under- or over-estimate from the lidar-retrieved PBL height. Here we apply a Gaussian distribution fit. The classic methods greatly improve under these conditions, with the threshold method ($R^2 = 0.73$, $N = 36$), variance method ($R^2 = 0.37$, $N = 34$), and WCT method ($R^2 = 0.41$, $N = 34$). However, the EKF method also improves ($R^2 = 0.96$, $N = 34$) with a strong correspondence to the lidar estimates.

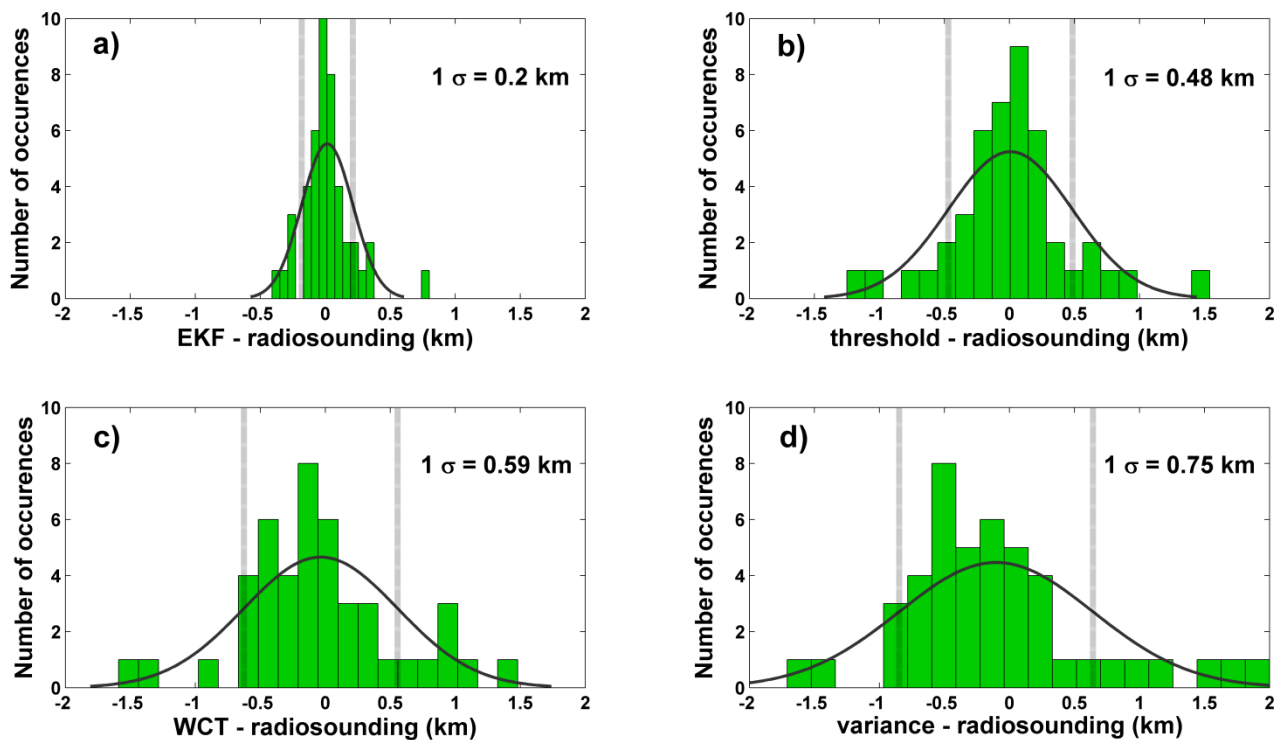


Figure 3.4 Histograms of the difference between lidar estimation method and radiosounding for a) extended Kalman filter, b) threshold, c) wavelet covariance transform, and d) variance methods. A Gaussian approximation (solid black line) and 1σ (dashed grey line) has been fit to each histogram.

Investigation of individual cases with gross under- and over-estimates reveal an association to certain synoptic flow clusters. More than 80 % of the identified outliers are associated with regional recirculations and synoptic flows from the south-west. It is well known that regional recirculations and south-west flows are complex atmospheric situations, typically with additional aerosol layers in or near the PBL. Scatter diagrams

between lidar methods and radiosoundings for each cluster type arriving at 1.5 km altitude are shown in Fig. 3.5. It is clearly seen that the EKF method performs the best under all synoptic flows, followed by the threshold method. The largest deviations from the 1:1 line occur with south-west synoptic flows and regional recirculations. Scatter plots for clusters arriving at 0.5 km and 3 km altitudes show similar patterns to 1.5 km, so they are not shown.

The lidar data are grouped into the seven synoptic clusters arriving at 1.5 km altitude. The highest PBL height estimated by the EKF method (1.35 km) occur in south-west flows and regional recirculations. Most likely this is attributable to the stronger mesoscale processes with these synoptic flows. The lowest PBL height from the EKF method (0.73 km) are associated with westerly flows. Some comparisons can be made with a study by Pandolfi et al. (2013), using a spatial derivative method on ceilometer data. In Pandolfi et al. (2013) the highest PBL heights were observed in cold Atlantic (1.88 ± 0.29 km a.g.l.) air mass, followed by stagnant regional (1.77 ± 0.31 km a.g.l.), and north African air mass (1.57 ± 0.43 km a.g.l.).

At 1.5 km arriving altitude the largest differences between any lidar-based method and radiosoundings occur in north-east and fast west-north-west flows. Both synoptic situations influence an across-the-board underestimation of the PBL height by the lidar methods, by as much as 0.43 km with the variance method.

Cluster groups at the arriving altitudes of 0.5 km and 3 km show similar results to those at 1.5 km, except for a few notable features. Synoptic clusters at 0.5 km altitude are the most complex due to unique mesoscale processes induced by the topography and close proximity to the sea. The EKF method outperforms classic methods with a small average underestimation of 0.06 km. At 3 km arriving altitude we lose the influence of regional recirculations, replaced by slow south-west and easterly flows (Fig. 3.3c). The EKF method estimates an average PBL height of 1.17 km and 0.86 km, in slow south-west and easterly flows, respectively. The low PBL height in easterly flow is possibly due to low-level clouds, which form with moisture being transported from the sea. The largest differences in PBL height between lidar and radiosoundings occur in easterly flows, with an underestimation around 0.30 km among all methods. This result highlights the possible effects of cloud distortion of the lidar range-corrected signal and its implication on PBL height retrievals.

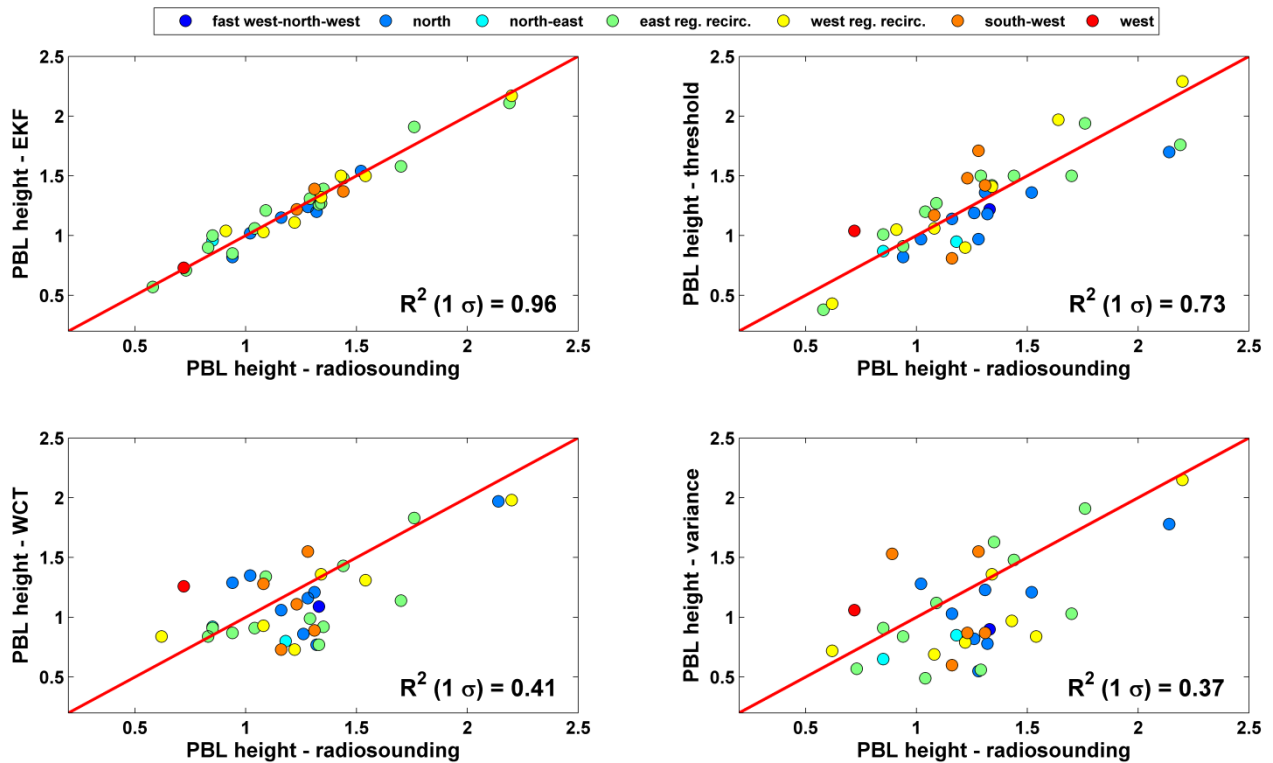


Figure 3.5 Scatter plots between PBL heights from lidar-based methods and radiosounding for extended Kalman filter (top left), threshold (top right), wavelet covariance transform (bottom left), and variance (bottom right) methods. 1 σ outliers have been removed. Lidar observations have been colour-coded according to their cluster type arriving at 1.5 km altitude. The 1:1 line (solid red) has been added.

3.4.3 Performance evaluation of WRF model PBL schemes

The lidar-EKF technique is used to validate PBL heights simulated in the WRF model. Figure 3.6 shows colour-coded scatter plots of PBL height estimated with the lidar-EKF method against those simulated with each PBL parametrization scheme, grouped according to synoptic clusters at 1.5 km altitude. The non-local scheme, ACM2, shows the highest determination coefficient ($R^2 = 0.33$) of all PBL schemes tested. Similar results were found in a study by Bossioli et al. (2009) over Athens, Greece, where non-local schemes are found superior to the other schemes tested, favouring strong vertical mixing and transport towards the surface. They found that enhanced mixing in the non-local schemes is caused by larger diffusion coefficients. The two other non-local schemes tested (YSU and TEMF) show the third highest ($R^2 = 0.22$) and sixth

highest ($R^2 = 0.18$) determination coefficients, respectively. The local MYJ scheme performs poorest ($R^2 = 0.15$) in this analysis, even though it is well-tested and preferred in previous studies.

Regional recirculations show the poorest model diagnoses of PBL height, while fast west-north-west and northerly flows show the closest WRF model-simulated PBL height to the lidar-EKF estimates. Overall, there is a systematic under-representation of PBL height simulated in the model, with five (YSU, MYNN2, BouLac, UW, and TEMF) of the eight tested schemes showing lower PBL heights than estimates from the lidar. The results at 0.5 km and 3 km arriving altitudes are very similar to 1.5 km, and are not shown here.

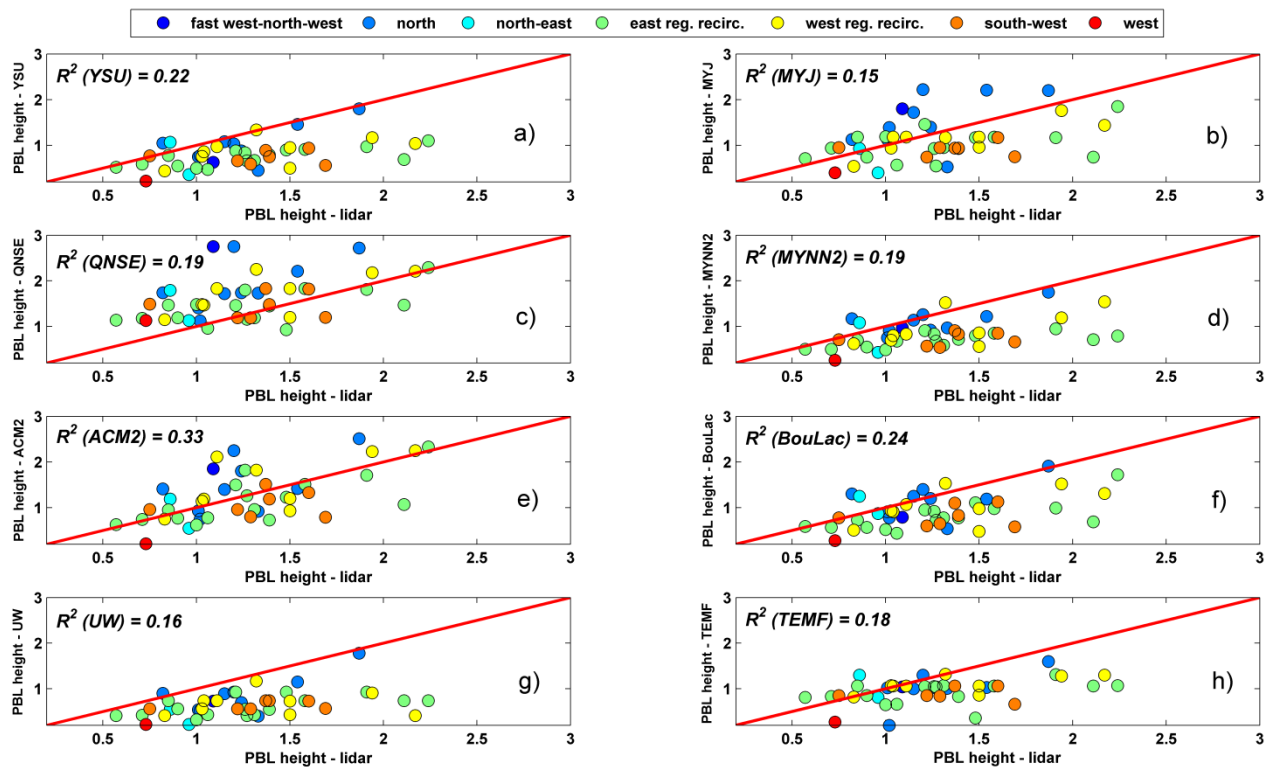


Figure 3.6 Scatter plots between PBL height diagnosed by the WRF model using eight different PBL schemes and PBL height estimated with the lidar-EKF technique. Data points have been colour-coded according to their cluster type arriving at 1.5 km altitude. The 1:1 line (solid red) has been added. Coefficient of determination (R^2) values are computed based on the total data collection ($N = 45$).

The mean value of lidar-EKF PBL height and the mean relative bias between WRF model PBL schemes and lidar at each synoptic grouping at 1.5 km altitude is shown in Table 3.3.

Table 3.3 Mean value (km) of lidar-EKF and mean relative bias ($(\text{WRF model} - \text{lidar EKF})/(\text{lidar EKF})$) of PBL heights diagnosed with WRF model simulations using eight PBL schemes. *Italic-faced type is used when the PBL height from the WRF model is within $\pm 20\%$ of the lidar estimates. Results shown for total (All) lidar days and when grouped by 7 synoptic clusters arriving at 1.5 km. Bold-faced type represent the closest PBL schemes for each synoptic cluster and the total.*

	east regional recirculations	west regional recirculations	north-east	south-west	north	west	fast west- north-west	All
lidar-EKF	1.30	1.38	0.91	1.33	1.24	0.73	1.09	1.28
YSU	-0.39	-0.33	-0.19	-0.41	-0.16	-0.70	-0.42	-0.37
MYJ	-0.15	-0.15	-0.25	-0.26	0.26	-0.45	0.65	-0.05
QNSE	0.19	0.31	0.63	0.16	0.56	0.55	1.52	0.56
MYNN2	-0.42	-0.29	-0.15	-0.43	-0.08	-0.64	-0.11	-0.30
ACM2	-0.08	0.12	-0.02	-0.15	0.21	-0.71	0.70	0.01
BouLac	-0.34	-0.24	0.18	-0.36	-0.04	-0.62	-0.28	-0.24
UW	-0.50	-0.47	-0.57	-0.50	-0.30	-0.70	-0.33	-0.48
TEMF	-0.21	-0.16	0.18	-0.38	-0.30	-0.63	-0.05	-0.22

PBL schemes within $\pm 20\%$ of the lidar-EKF PBL height are highlighted in each synoptic cluster. The ACM2 scheme shows the closest results, with only an 1% model-simulated overestimate in the total set. Also, the ACM2 scheme performs the best in regional recirculations and synoptic flows from the north-east. The MYJ scheme shows the second closest results, with an overall 5% underestimate by the WRF model. All but one PBL scheme (QNSE) show underestimations. On average, the QNSE scheme overestimates PBL height by 56% compared with the lidar estimates.

The results have a stark contrast with those found by Pérez et al. (2006a), with comparisons of three different PBL schemes from the legacy MM5 model. The study was also conducted over the Western Mediterranean, including the Barcelona geographical area, during a typical summertime case with an absence of large-scale forcing. They discovered that non-local schemes show similar results and have a tendency to overestimate the PBL height when validated with estimates from lidar and radiosoundings. They showed biases ranging from 40% to 72% and errors from 59% to 77%, attributed to the scheme-specific methods used to calculate PBL height. The complex topography of the north-east Iberian Peninsula may contribute significantly to the differences observed in the PBL schemes.

3.4.4 Representative cases of most frequent synoptic clusters

In this section we present representative days for the four most frequent atmospheric situations, validated with complementary information from satellite images, radiosoundings, mineral dust model simulations, and WRF-simulated synoptic maps. The most frequent synoptic flows over Barcelona are from the north, west, south-west, and east.

The simplest type of atmospheric pattern for PBL height estimation is when there is a clear delineation between the convective boundary layer and the free troposphere, most often in north and north-west synoptic flows. A representative day for this atmospheric situation is shown in Fig. 3.7 for 22 March 2009, with synoptic flow from the north at 1.5 km and 3 km altitudes, and from the north-east at 0.5 km altitude. A surface high pressure ridge is situated over the Iberian Peninsula (Fig. 3.7c). A dry free troposphere is confirmed with a radiosounding (not shown).

PBL height estimated with a 12:00 UTC radiosounding is 1.28 km. The EKF method provides the closest lidar-based estimate to the radiosounding (1.24 km), and is similar to the average for all lidar days in

northerly synoptic flows. The WCT method performs the second closest (1.16 km), followed by the threshold (0.97 km) and variance (0.96 km) methods.

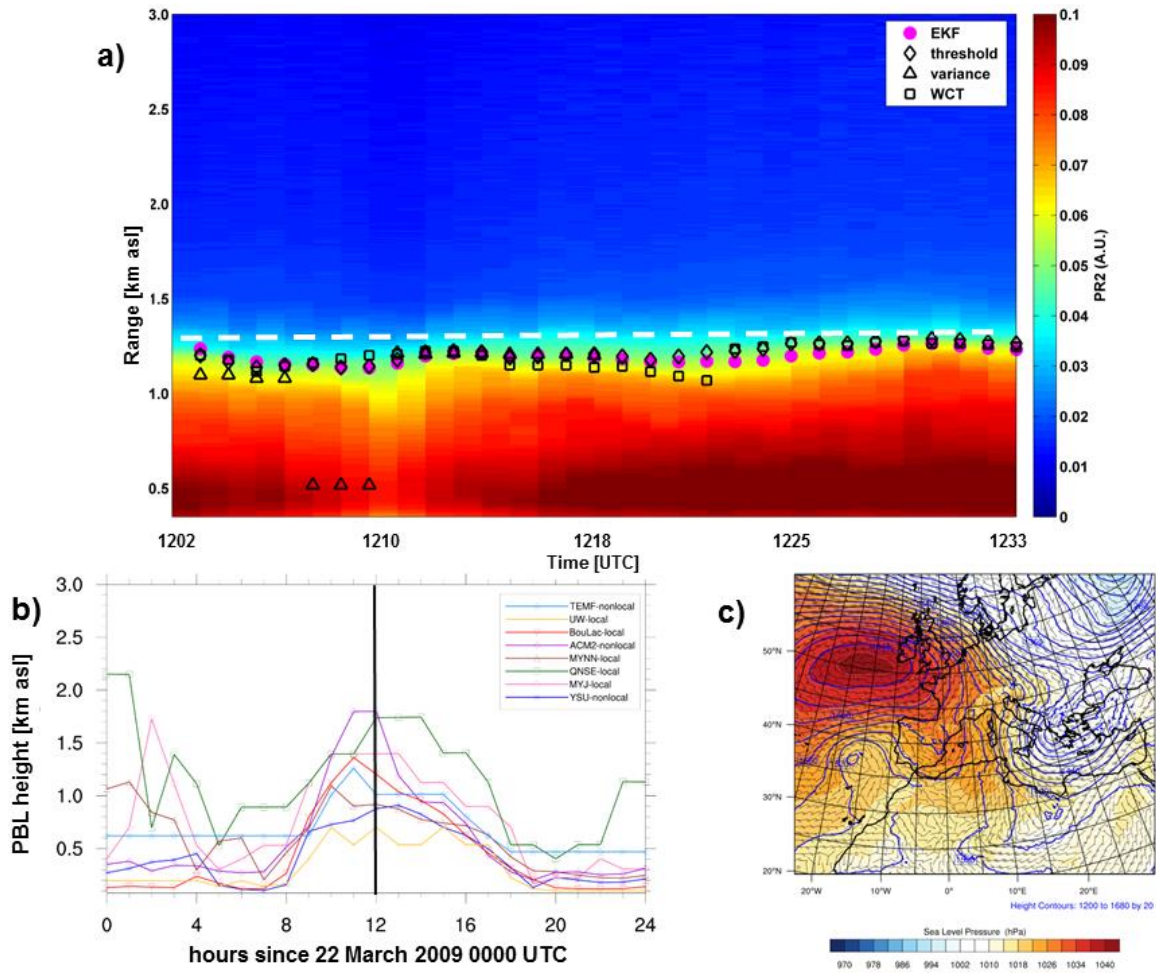


Figure 3.7 (a) Lidar power \times range-squared (PR2) time-height series (A.U.) from 1202 – 1233 UTC, with 1-min PBL height (km asl) estimates from the EKF (magenta circles), threshold (black diamonds), variance (black triangles), and WCT (black squares) methods. Radiosonde-estimated PBL height at 1200 UTC is shown with a white dashed line. (b) WRF model-simulated PBL height (km asl) with 8 PBL schemes. Coincident lidar delineated with black vertical line. (c) WRF synoptic map of sea level pressure (hPa, shaded contours), and 850 hPa geopotential heights (blue lines) and winds (vectors) valid at 1200 UTC on 22 March using the YSU PBL scheme.

Figure 3.7b shows the diurnal cycle of hourly WRF model-simulated PBL heights with each PBL scheme. The ACM2 scheme simulates the highest daytime-maximum PBL height (1.80 km at 1100 UTC and 1200 UTC), while the UW scheme simulates the lowest daytime-maximum (0.70 km at 1100 UTC). The MYJ

scheme is closest to the observed values. However, the MYJ and QNSE schemes exhibit higher model-simulated PBL heights in the morning, when other PBL schemes are grouped below 0.6 km. In the evening, the QNSE and TEMF schemes show a slower decay of the PBL height than the other six schemes.

The second main case is regional recirculations, which are especially frequent in summertime when the synoptic pattern is stagnant and mesoscale convective processes dominate. A representative day for this pattern is shown in Fig. 3.8 for 3 July 2012, with regional recirculations from the east and west, at 0.5 and 1.5 km, respectively. Figure 3.8c shows a weak surface high pressure centred over the western Mediterranean basin, which confirms a stagnant atmospheric pattern over the north-east Iberian Peninsula.

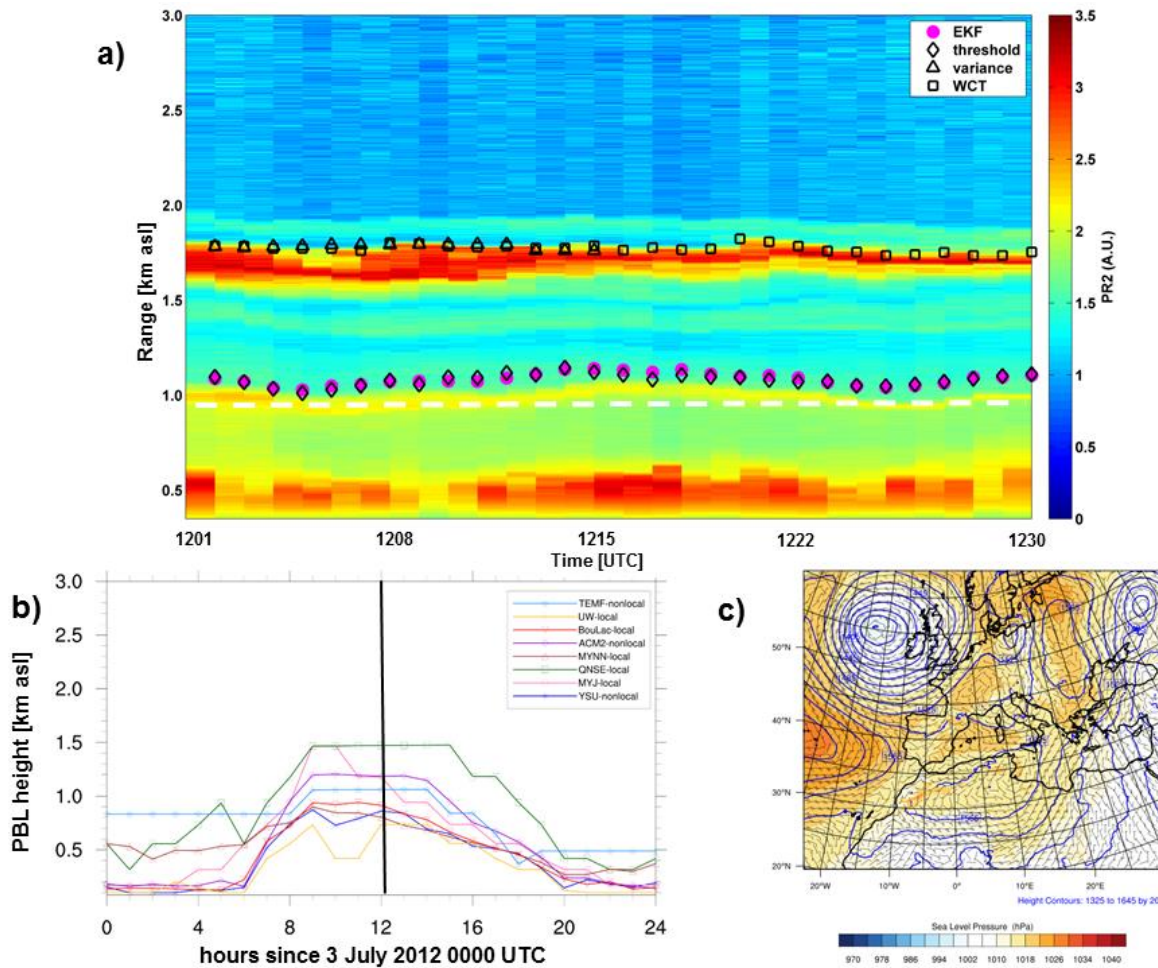


Figure 3.8 Same description as in Fig. 3.7, except for representative case on 3 July 2012.

PBL height estimated from a 12:00 UTC radiosounding is 0.91 km. The EKF and threshold methods show similar estimates, around 1.05 km, while the WCT and variance methods (both 1.78 km) follow the additional aerosol layer between 1.5 and 2 km. The additional aerosol layer is quite common at this time of the day in summertime, due to the return wind flow induced by interaction between the pre-coastal mountain range and the sea.

Hourly WRF model-simulated PBL heights are shown in Fig. 3.8b. The highest daytime-maximum PBL heights are simulated by the MYJ and QNSE schemes, around 1.48 km. The lowest daytime-maximum PBL height is associated with the UW scheme (0.74 km at 12:00 UTC), as in the previous case. The MYNN2 and BouLac schemes produce 12:00 UTC PBL heights closest to the observations. There is a large spread among PBL schemes with the growing PBL in the morning, with the TEMF, QNSE, and MYNN2 schemes showing higher PBL heights than other schemes. The model spread is smaller with respect to the decaying PBL in the evening.

The third case is a Saharan dust episode from west and south-west synoptic flows. Advections of Saharan dust from the west and south-west are a common occurrence over the north-east Iberian Peninsula and can occur anytime during the year (Salvador et al. 2014). A representative day (Fig. 3.9a) is shown for 3 August 2007, with synoptic flow from the west at 3 km, and westerly regional recirculations prevalent at 0.5 km and 1.5 km altitudes. A surface synoptic map (Fig. 3.9c) reveals a stagnant mesoscale pattern with weak west to south-west winds over Catalonia. The dust episode is confirmed using a simulation from the NMMB/BSC-Dust model (Pérez et al. 2011). Dust concentrations greater than $75 \mu\text{g m}^{-3}$ with a layer below 4 km a.g.l. are seen with a vertical profile (not shown).

PBL height estimated with a radiosounding is 1.43 km. The EKF method provides an estimate (1.5 km) closest to the radiosonde, while the classic methods (threshold = 2.41 km, WCT = 2.3 km, variance = 0.97 km) have issues determining the correct PBL height. In this complex case the EKF method has a significant advantage over classic methods due to its knowledge of the errors of past estimates of PBL height.

Figure 3.9b shows the hourly PBL height diagnosed by the WRF model. The QNSE scheme simulates the highest daytime-maximum PBL height (1.83 km at 12:00 UTC), and is closest to the observations. The lowest daytime-maximum PBL height is produced with the UW scheme (0.94 km at 13:00 UTC). The agreement amongst the schemes is much closer than in the previous two cases when analysing the full diurnal cycle.

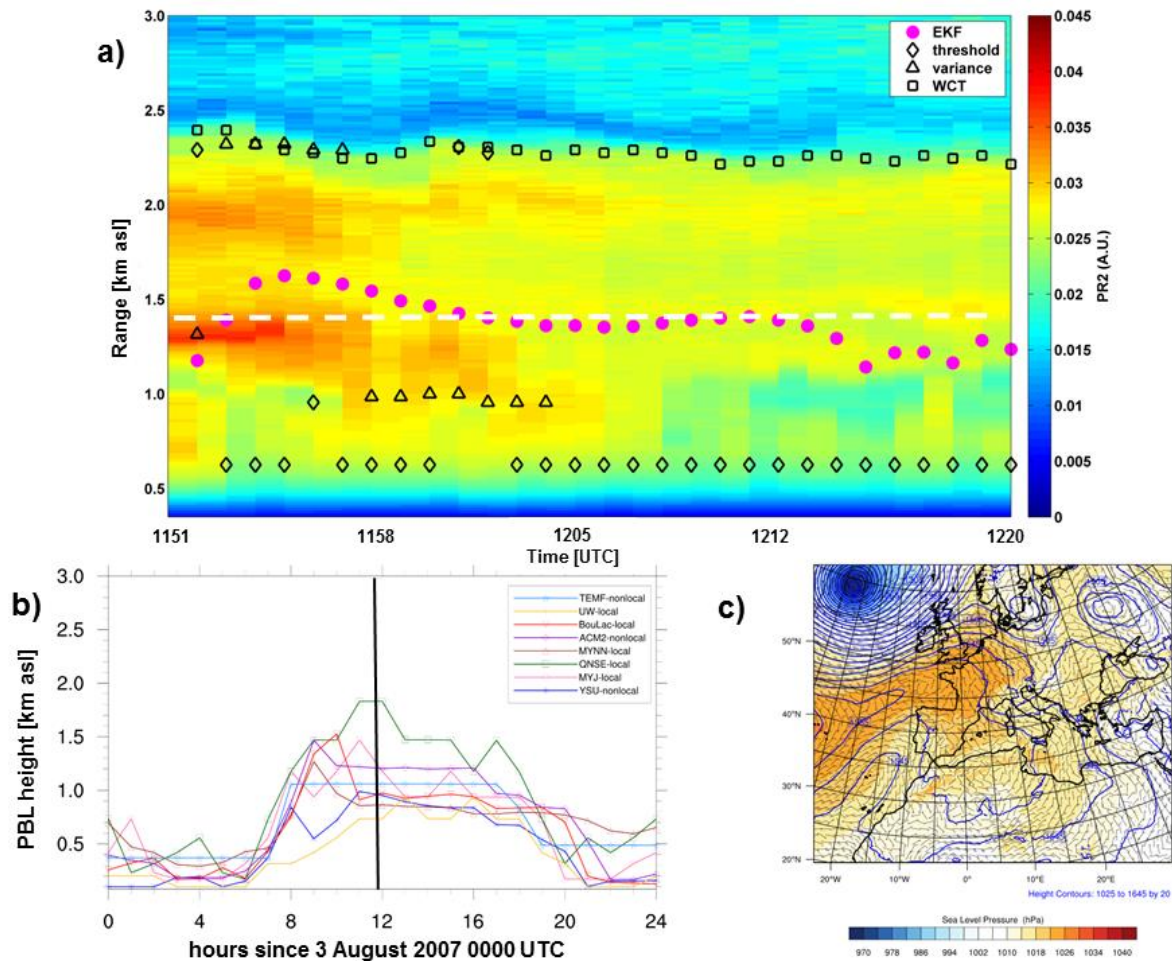


Figure 3.9 Same description as in Fig. 3.7, except for representative case on 3 August 2007.

The final atmospheric scenario which occurs frequently in the north-east Iberian Peninsula are low-level clouds induced by flows from the east. A representative day with clouds near the boundary layer is selected as 22 April 2010 (Fig. 3.10), with easterly regional recirculations at 0.5 km, easterly flow at 1.5 km, and slow south-west flow at 3 km. Clouds are denoted by the strong return (dark red colors above 4.5×10^{-3} A.U.) in the lidar range-corrected signal.

The strongly reflective cloud layer observed from 2.0 to 3.5 km can be validated with a radiosounding profile and an infrared satellite image from Meteosat-9 (not shown). The synoptic map (Fig. 3.10c) shows a low pressure area, with Barcelona situated in the easterly flow ahead of a weather front.

The PBL height on this day is the lowest of all cases, with a radiosounding-estimated PBL height of 0.58 km. This implies a heavy marine influence lowering the PBL. The EKF method is the most accurate (0.57 km), while the threshold method (0.38 km) is too low, and the WCT (1.66 km) and variance (2.58 km) methods diagnose the PBL height somewhere below or in the cloud layer.

Hourly WRF model-simulated PBL height is shown in Fig. 3.10b. The QNSE scheme simulates the highest daytime-maximum PBL height (1.14 km at 12:00 UTC), while the UW and MYNN2 schemes simulate the lowest daytime-maximum PBL heights (0.41 km and 0.50 km at 12:00 UTC, respectively). The BouLac and YSU schemes simulate 12:00 UTC PBL heights closest to the observations. Unexplained issues are noted with the evening decay of the PBL by the QNSE and MYJ schemes, which simulate sharp increases after 20:00 UTC.

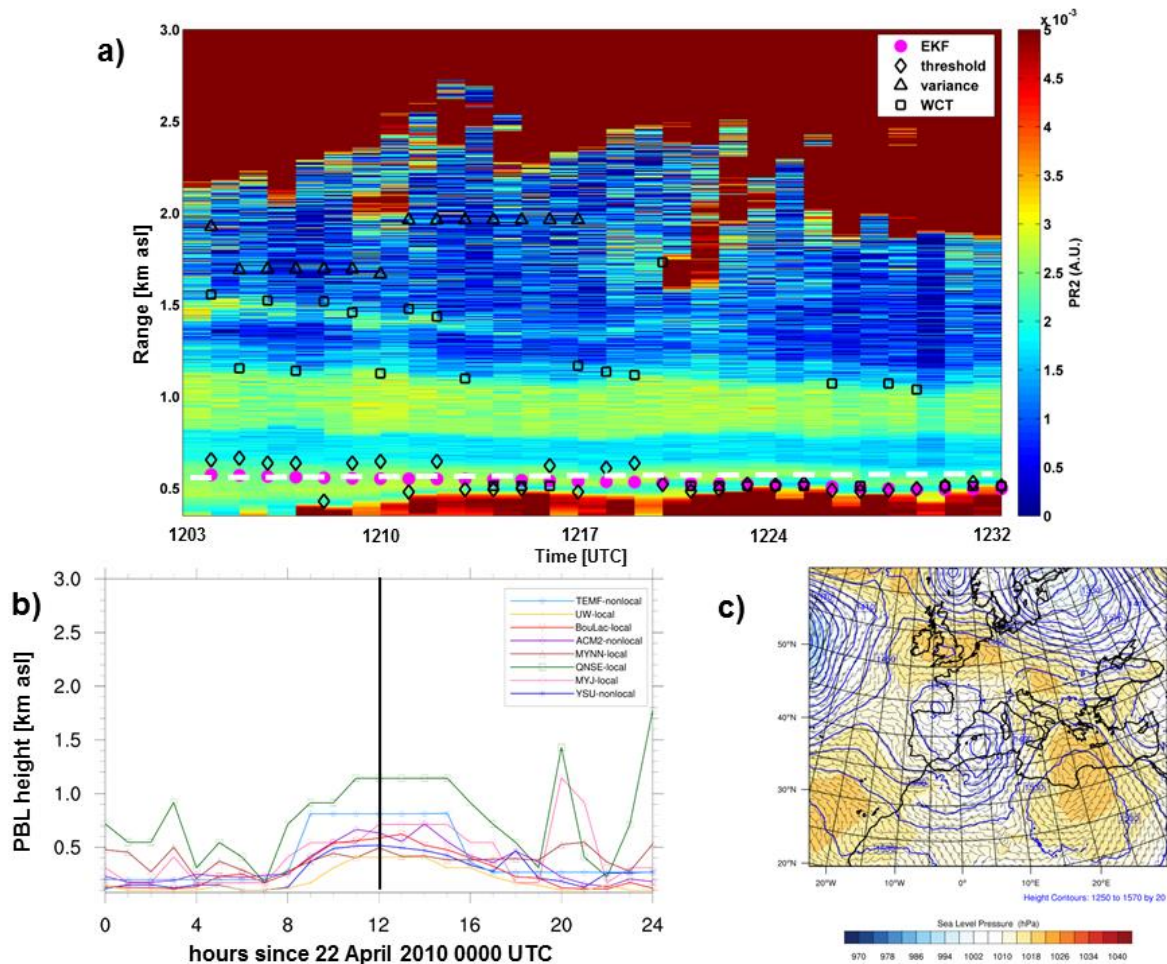


Figure 3.10 Same description as in Fig. 3.7, except for representative case on 22 April 2010.

3.4.5 Surface energy fluxes

The differences in WRF model-simulated PBL heights shown in the previous four representative cases were relatively substantial, sometimes $> 200\%$ between the lowest and highest model-simulated PBL heights. Fluxes between the land-surface and the atmosphere are an important component in PBL development. We show a brief analysis (Fig. 3.11) of the upward sensible heat flux (W m^{-2}) for the four representative cases.

Overall, WRF model-simulated sensible heat flux is within $\pm 25 \text{ W m}^{-2}$ for most of the diurnal cycle, except during the period of maximum solar insolation. The QNSE and TEMF schemes overestimate the sensible heat flux between $100 - 150 \text{ W m}^{-2}$ when compared with other PBL schemes. The difference is smallest in the case of low-level clouds in the PBL (Fig. 3.11d).

It is possible that the higher PBL heights simulated in the QNSE scheme are due to large surface heat fluxes simulated by the WRF model. However, large deviations of sensible heat flux with the TEMF scheme do not translate to the PBL heights, as they were in the middle of the spread for all cases.

In addition, differences in the PBL height among the schemes may be attributed to the entrainment formulations in the schemes, which aren't explored here. Shin and Hong (2011) found that the non-local ACM2 scheme performed well in the unstable PBL, based on the schemes explicit treatment of the entrainment flux as proportional to the surface flux. However, this is not a unique feature to this scheme.

3.6 Conclusions

In this chapter we have achieved three primary objectives: first, we used a cluster analysis algorithm to determine seven distinct synoptic flow types over the north-east Iberian Peninsula. The synoptic cluster groups are found to be similar at 0.5 km and 1.5 km arriving altitudes, with minor changes at 3 km altitude. The analysis confirms that the most predominant synoptic cluster over the north-east Iberian Peninsula is the regional recirculations from the east or west, and that the identified synoptic flows have multiple aerosol layers.

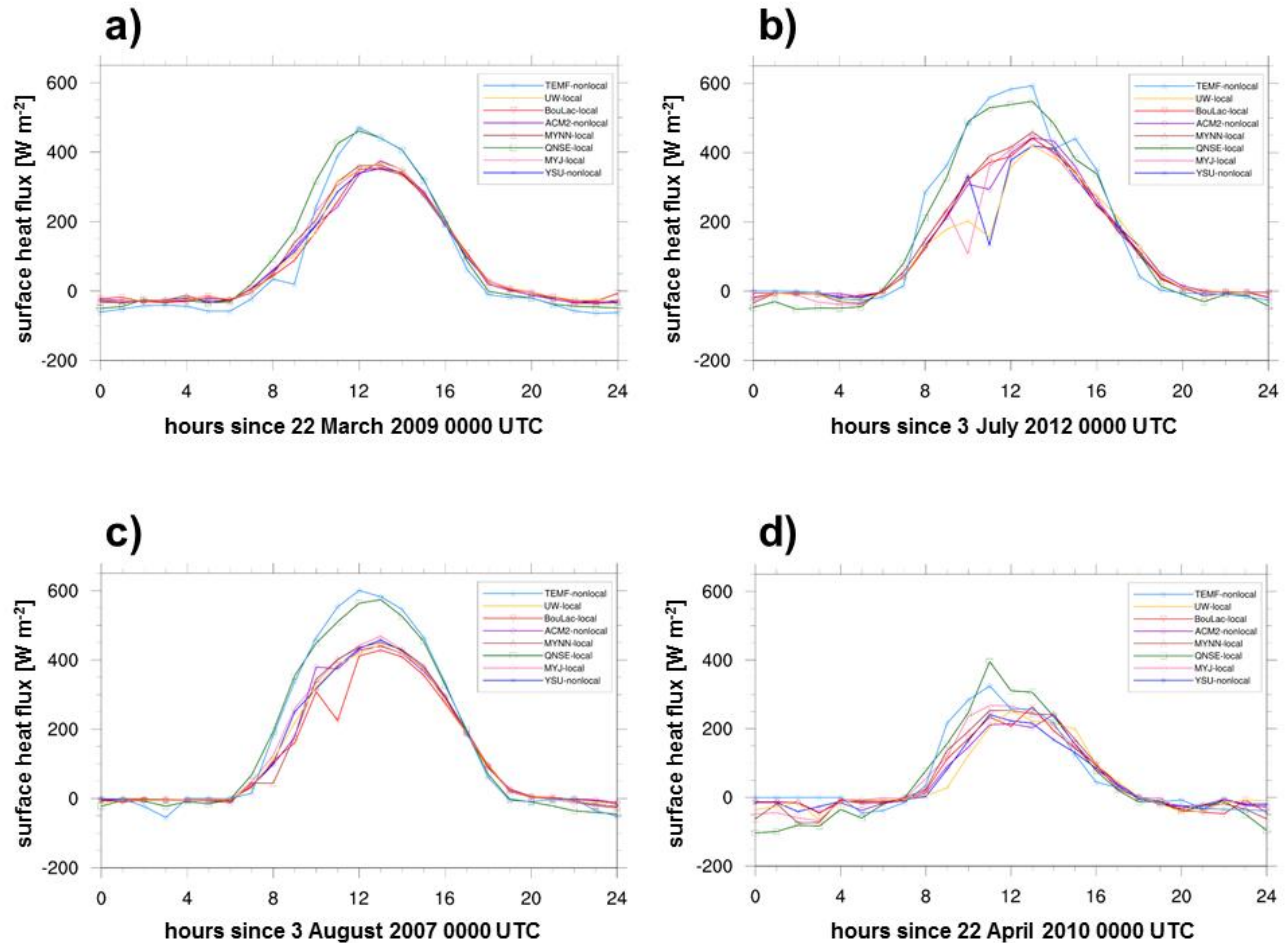


Figure 3.11 WRF model-simulated surface sensible heat flux (W m^{-2}) for a) 22 March 2009, b) 3 July 2012, c) 3 August 2007, and d) 22 April 2010. Model grid-point location closest to the Barcelona lidar site. Positive values indicate heat transfer from the land surface to the atmosphere.

Secondly, methods to obtain the planetary boundary-layer (PBL) height from lidar were compared and validated at 12:00 UTC over a 7-year period. A novel approach using an extended Kalman filter (EKF) is compared with classic methods found in the literature. The comparison of PBL height estimates provided by traditional and advanced lidar-based approaches was performed for seven objectively determined synoptic flows at different arriving altitudes representing within the PBL, at the top of the PBL, and in the free troposphere.

An advanced lidar-based approach utilizes an extended Kalman filter (EKF) to time-adaptively estimate PBL height within a range from 0.79 – 1.6 km, similar to previous studies. Moreover, the adaptive EKF approach

tends to capture the PBL height evolution quite accurately. PBL height retrieved by the EKF technique has a strong determination coefficient ($R^2 = 0.96$) when compared with PBL height estimates from daily daytime radiosonde launches. Classic lidar-based methods showed much weaker correlations, even when gross outliers outside one standard deviation were removed prior to the calculations. In contrast to the EKF approach, this is because classic methods do not rely on past estimates and associated statistical and a priori information to yield present-time estimates but on the instantaneous measurement record, instead. Besides, classic methods comparatively require a much longer time averaging and range smoothing to perform reliably and are usually limited to single-layer scenes.

Representative cases for a clean free troposphere, regional recirculations, Saharan dust episodes, and low-level cloud layers highlight the adaptability of the EKF technique when compared with classic methods. Except for cases of a clean free troposphere, the classic methods typically have issues when multiple aerosol layers are present. If the user selects a proper threshold value the threshold method performs second best to the EKF.

An approach using the EKF proves promising for continuous and automatic observation of PBL height from lidar measurements. The EKF technique can be applied directly to the lidar range-corrected signal. It has been found that optimal parameters must be chosen for the state vector initialization for the EKF method to track PBL height accurately, depending on the instrument type.

With the final objective, PBL heights simulated in the Weather Research and Forecasting (WRF) model were validated against the lidar-EKF estimates. WRF model-simulated PBL heights were evaluated using eight unique PBL schemes. Test simulations with the WRF model reveal a clear favour to non-local PBL schemes, with the ACM2 scheme showing the closest correlation to lidar-EKF estimates. Surprisingly, the widely-tested local MYJ scheme showed the weakest correlation coefficients. Ambiguous results are found when evaluating the model-simulated PBL heights under the most representative synoptic situations. In all cases, the local UW scheme produced the lowest daytime maximum PBL height. In the least complex case of a clean free troposphere the MYJ scheme showed the closest model-simulated PBL height to the observations. With more complex cases such as regional recirculations and effects due to Saharan dust intrusions the results are varied, with no clear favourite scheme.

WRF model-simulated sensible heat flux between the land-surface and the atmosphere confirmed a possible reason for the high PBL heights simulated with the QNSE scheme. However, other PBL schemes showed very similar model simulations of sensible heat flux. The large differences in PBL heights among the



schemes could be attributable to one of two primary components: first, and possibly the largest, are the operational definitions of PBL height in the individual schemes. Secondly, differences in the entrainment behaviour among the PBL schemes could be a factor.

Future work should include an evaluation of WRF model PBL schemes using the lidar-EKF method at other locations, with comparison between a complex, coastal site similar to Barcelona and a continental site (e.g., Cabauw, The Netherlands). It is possible that the skill of PBL schemes is dependent on entrainment fluxes, but also on the effect of mesoscale horizontal flow. Also, it is worthwhile to make comparisons of the PBL schemes using a unified formulation of the PBL height definition.

In addition, with the advantage of reliable tracking of diurnal PBL height the lidar-EKF method can be employed as an assimilation tool for PBL height simulations in the WRF model and other numerical weather prediction models.



Chapter 4

4 Sensitivity of boundary-layer variables to PBL schemes in the WRF model based on surface meteorological observations, lidar, and radiosondes during the HygrA-CD campaign

Air quality forecast systems need reliable and accurate representations of the planetary boundary layer (PBL) to perform well. An important question is how accurately numerical weather prediction models can reproduce conditions in diverse synoptic flow types. In this chapter, observations from the summer 2014 HygrA-CD (Hygroscopic Aerosols to Cloud Droplets) experimental campaign are used to validate simulations from the Weather Research and Forecasting (WRF) model over the complex, urban terrain of the Greater Athens Area. Three typical atmospheric flow types were identified during the 39-day campaign based upon two-day backward trajectories: Continental, Etesians, and Saharan. It is shown the numerical model simulations differ dramatically depending on the PBL scheme, atmospheric dynamics, and meteorological parameter (e.g., 2-m air temperature). Eight PBL schemes from WRF version 3.4 are tested with daily simulations on an inner domain at 1-km grid spacing. Near-surface observations of 2-m air temperature and relative humidity, and 10-m wind speed are collected from multiple meteorological stations. Estimates of the PBL height come from measurements using a multiwavelength Raman lidar, with an adaptive extended Kalman filter technique. Vertical profiles of atmospheric variables are obtained from radiosonde launches, along with PBL heights calculated using bulk Richardson number. Daytime maximum PBL heights ranged from 2.57 km during Etesian flows, to as low as 0.37 km during Saharan flows. The largest differences

between model and observations are found with simulated PBL height during Saharan synoptic flows. During the daytime, campaign-averaged near-surface variables show WRF tended to have a cool, moist bias with higher simulated wind speeds than the observations, especially near the coast. It is determined that non-local PBL schemes give the most agreeable solutions when compared with observations.

The contents presented in this chapter has been accepted by the journal, *Atmospheric Research*, and is made available here as copy with the permission of *Atmos. Res.* Systematic or multiple reproduction or distribution to multiple locations via electronic or other means is prohibited and is subject to penalties under law.

4.1 Introduction

HygrA-CD (Hygroscopic Aerosols to Cloud Droplets) was an internationally-led field campaign performed from 15 May – 19 June 2014 in the Greater Athens Area (GAA), Greece. The main goal of the HygrA-CD campaign was to bring together different instruments and expertise for the purpose of understanding more about the impact of aerosols and clouds on weather and climate on a local scale. It is a novel attempt to strengthen the links between the remote sensing and in-situ observation communities, while making use of established know-how on numerical weather prediction and atmospheric modeling. An overview of the campaign can be found in Papayannis et al. (2016).

During the time period of the HygrA-CD campaign, it is common to observe diverse types of synoptic flows. Saharan dust events are likely over the GAA based on synoptic winds from the south and south-west, advecting dust aerosols into the region. In addition, air masses carrying mixtures of urban/continental and marine aerosols are probable, due to the influence of the Etesian winds to the wind circulation in the GAA (i.e., synoptic winds from the north-east).

Model-simulated meteorological processes in the planetary boundary-layer (PBL) are critical to an air quality forecast system, as a numerical weather prediction model is used as the atmospheric driver. Important parameters include temperature, moisture, and winds throughout the PBL, and the PBL height. Most applications to air pollution rely on high-resolution mesoscale meteorological models to provide accurate simulations of PBL parameters.

The major objective of this work is to provide a performance evaluation of boundary-layer variables such as near-surface temperature, relative humidity, and wind speed, and PBL height simulated by different WRF

PBL parametrization schemes for the application to air pollution modelling. This study aims to contribute to a reduction of one of the major sources of error in top-down estimates of photochemical pollutant modelling, boundary-layer representation of meteorological processes. In the current study we aim to evaluate the operational definitions of PBL height for each scheme.

It is necessary with model horizontal grid spacing larger than 1 x 1 km to properly parametrize the vertical diffusion of surface fluxes, as they are connected with sub-grid scale processes (Chen and Dudhia, 2000). PBL parametrization schemes fall into one of two main classes; local and non-local schemes. Some local closure schemes use turbulent kinetic energy (TKE) prediction, while most non-local schemes have diagnostic components for the K-profile (Troen and Mahrt, 1986) and PBL top. Above the PBL top, both local and non-local schemes also include vertical diffusion due to turbulence.

Previous studies have evaluated the performance of model PBL parametrization schemes in locations known for complex atmospheric situations (Pérez et al., 2006a; Bossioli et al., 2009; Banks et al., 2015). In Pérez et al. (2006a) the influence of three PBL schemes from the legacy Fifth Generation Penn State-NCAR Mesoscale Model (MM5; Dudhia, 1993) on meteorological and air quality simulations over Barcelona was analyzed. The authors found that the MM5 model tended to show a cold bias, with higher model-simulated wind speeds compared with observations, depending on the PBL scheme used.

In addition, Banks et al. (2015) evaluated WRF model-simulated PBL height over Barcelona using eight PBL schemes. Model-simulated PBL height was validated with PBL height estimates from a backscatter lidar during a 7-yr period. The authors determined that a non-local scheme such as the Asymmetrical Convective Model version 2 (ACM2) provide the most accurate simulations of PBL height, even under diverse synoptic flows such as regional recirculations. Banks et al. (2015) was data-limited to the evaluation of only PBL height, while the current study compares surface and upper-air variables important for PBL applications.

Over the GAA, Bossioli et al. (2009) investigated the impact of four PBL schemes from the MM5 model on meteorological and air quality simulations. The authors found that the selection of PBL scheme shapes the horizontal and vertical extension of variables in the PBL. It was determined that non-local and semi non-local schemes were far superior to other schemes, due to the favour of strong vertical mixing and transport towards the surface. Additionally, other studies have examined the performance of WRF PBL parametrization schemes in northern areas of Europe (Kim et al., 2013; Draxl et al., 2014), and over the continental United States (Hu et al., 2010; Coniglio et al., 2013).

Treatment of PBL height from both measurements and models is quite complex with many methods applied previously. LeMone et al. (2012) subjectively confirmed WRF model-simulated PBL height against modelled virtual potential temperature (Θ_v) profiles using different threshold values of $\delta\Theta_v/\delta z$. The most accurate model-simulated PBL height was compared against field observations. The authors found the best threshold defines PBL height as the lowest model level at which $\delta\Theta_v/\delta z = 2 \text{ K km}^{-1}$, which works for all four PBL schemes they compared. In this work we estimate PBL height from radiosoundings and lidar using well-tested methods to ensure quality comparisons to model simulations.

This chapter will be presented as follows. Section 4.2 will describe the configuration of the WRF experiment sets and the various observation tools used to evaluate the model performance. Results of the performance evaluation will be presented in Section 4.3. Comparison to previous studies on this topic will be discussed in Section 4.4. Finally, a summary and conclusions will be shown in Section 4.5.

4.2 Model configuration, synoptic conditions, and observations

4.2.1 WRF model configuration

In this study we use WRF version 3.4.1 with the Advanced Research WRF (ARW) dynamical solver (Skamarock et al., 2005). Three model domains (Fig. 4.1) were configured with varying horizontal grid spacing at the parent European level ($12 \times 12 \text{ km}$; 481×401 grid points), and two one-way nested domains for the Greece ($4 \times 4 \text{ km}$; 202×202 grid points) and GAA ($1 \times 1 \text{ km}$; 101×101 grid points) regions. It is assumed that $1 \times 1 \text{ km}$ grid spacing is of fine enough detail to resolve most mesoscale features in the complex study area (Jiménez et al., 2013).

Final Analysis (FNL) data from the National Centers for Environmental Prediction (NCEP) are used as the WRF initial and lateral boundary conditions, which are operational global analysis data available on $1^\circ \times 1^\circ$ grids at six-hourly time steps. FNL analyses are available from the surface and at 26 mandatory pressure levels from 1000 hPa to 10 hPa.

Daily WRF-ARW simulations were computed with a 36-h forecast cycle, including 12 h allotted for model spin-up time. Each day's simulation was initialized from 12:00 UTC the previous day. The spin-up cycle is added to counter instability issues within the simulation and the first 12 h of each forecast cycle are not included in the evaluation process. An output temporal resolution of 1-h was chosen for comparison with

observations. The model was run with 38 terrain-following (ETA) vertical levels, of which 13 are located in the lowest 3 km of the atmosphere, with a model top set at 50 hPa.

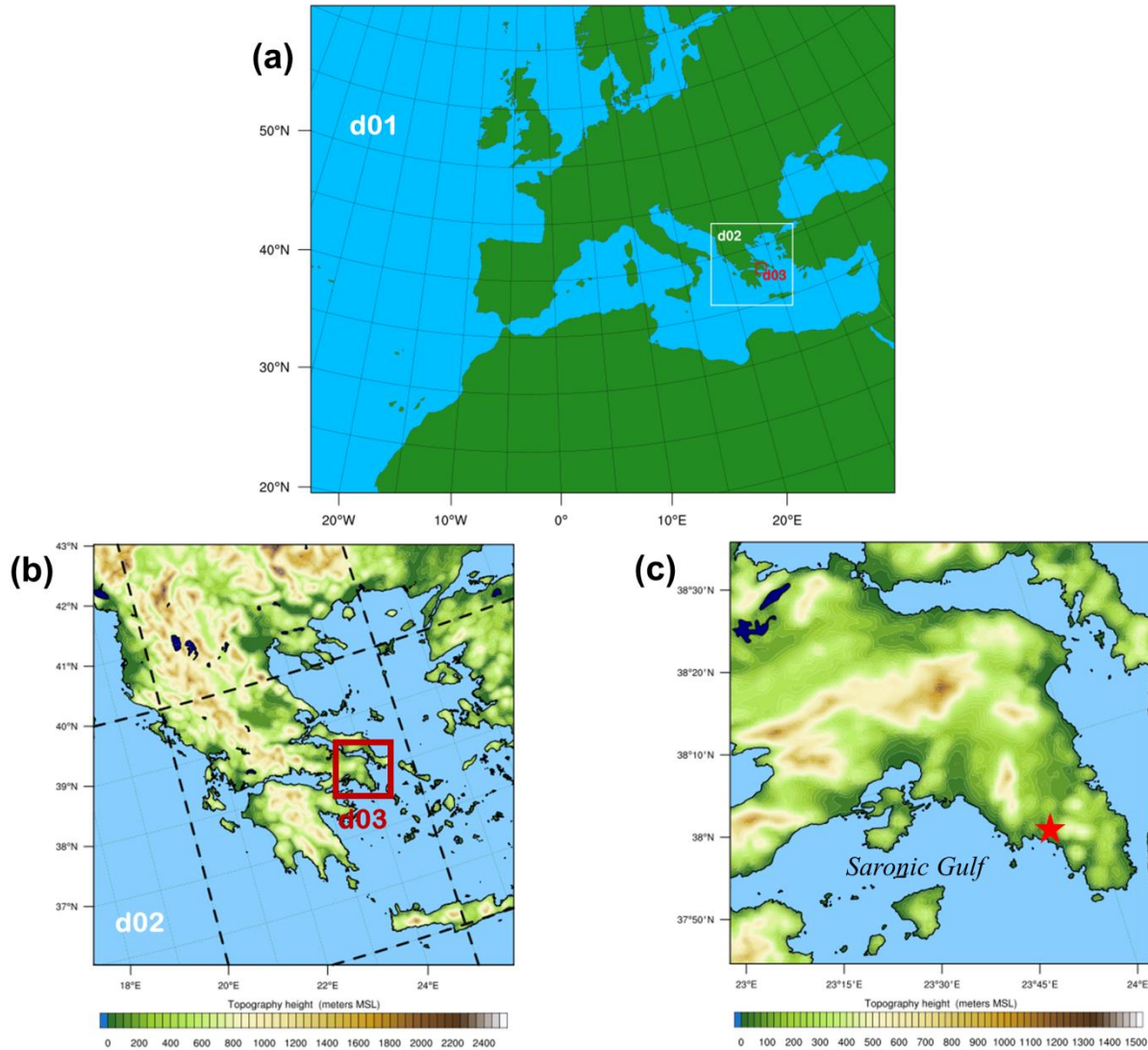


Figure 4.1 Model domain configuration for: (a) the European-level parent domain (d01, 12 × 12 km), (b) Greece domain (d02, 4 × 4 km), and (c) Greater Athens Area (GAA) domain (d03, 1 × 1 km). The Greece and GAA domains (red box) and associated topography are shown in 1b. The topographic map is further zoomed-in to the GAA domain (1c), with a bold red star denoting the location of the NTUA lidar site.

The physics options selected include WRF single-moment 3-class microphysics (Hong et al., 2004), Kain-Fritsch cumulus parametrization (Kain, 2004), Dudhia shortwave radiation (Dudhia, 1989), rapid radiative transfer model longwave radiation (Mlawer et al., 1997), and the Noah land-surface model (Tewari et al., 2004). No urban parameterization is used. More information about these physics options can be found in Skamarock and Klemp (2008).

The primary objective of this study is to evaluate the performance of boundary-layer variables simulated by WRF using varying PBL parametrization schemes. In version 3.4.1 of WRF-ARW there is the option to choose from nine PBL schemes. Each PBL scheme is associated with one or more surface-layer schemes which provide the surface fluxes of momentum, moisture, and heat to the PBL scheme. Eight PBL schemes are evaluated here since the MYNN3 (Mellor-Yamada-Nakanishi-Niino Level 3) scheme shares similar characteristics to the MYNN2 (Mellor-Yamada-Nakanishi-Niino Level 2.5) scheme. An overview of the PBL schemes selected in this study is shown in Table 4.1. Also shown are the associated surface-layer schemes, another important source of error in WRF model simulations.

Five of the eight PBL schemes selected are tied to the MM5 and ETA surface-layer schemes, which are based upon Monin-Obukhov similarity theory. The other three PBL schemes use their own unique surface-layer schemes.

The PBL parametrization schemes selected consist of five local and three non-local closure schemes. The operational definition of PBL height in the individual schemes falls into one of two general classes. The first class calculates the PBL height using the Richardson bulk number (Ri_b) method from some predetermined starting level. The second class determine the PBL height at a level where the turbulent kinetic energy (TKE) profile decreases to some predefined threshold value. A brief description of the schemes follows.

The first and most widely-used PBL scheme is the Yonsei University (YSU) scheme (Hong et al., 2006). The YSU scheme is a first order, non-local scheme with an explicit entrainment layer and a parabolic K-profile in an unstable mixed layer. It's a modified version of the Medium Range Forecast (MRF) scheme (Hong and Pan, 1996) from the MM5 (Dudhia, 1993). The largest improvement to the YSU scheme over the MRF scheme was the addition of an explicit term for the treatment of the entrainment zone. Hong (2010) implemented a modification to the scheme for the stable boundary layer. PBL height in the YSU scheme is determined from the Ri_b method, but calculated starting from the surface. A threshold value of zero is used for stable cases, while 0.25 is used for unstable flow.

Table 4.1 Summary of WRF v3.4.1 experiment sets with PBL parametrization schemes (PBL SCHEME) and surface-layer schemes (SFC LAYER) used in study.

SET	PBL SCHEME	SHORT NAME	CLOSURE TYPE	SFC LAYER	PBL height DEFINITION
1	Yonsei University	YSU	1.0 non-local	MM5 similarity	Ri_b calculated from sfc
2	Mellor-Yamada-Janjic	MYJ	1.5 local	Eta similarity	TKE-prescribed threshold
3	Quasi-Normal Scale Elimination	QNSE	1.5 local	QNSE	TKE-prescribed threshold
4	Mellor-Yamada-Nakanishi-Niino level 2.5	MYNN2	1.5 local	MYNN	TKE-prescribed threshold
5	Asymmetric Convective Model	ACM2	1.0 non-local	MM5 similarity	Ri_b calculated above neutral buoyancy level
6	Bougeault-Lacarrère	BouLac	1.5 local	MM5 similarity	TKE-prescribed threshold
7	University of Washington	UW	1.5 local	MM5 similarity	Ri_b threshold
8	Total Energy – Mass Flux	TEMF	1.5 non-local	TEMF	Ri_b threshold

The next most widely used PBL scheme is the Mellor-Yamada-Janjic (MYJ) scheme (Janjic, 2002). The MYJ scheme is a one-and-a-half order prognostic TKE scheme with local vertical mixing. It's a modified version of the old ETA scheme from the MM5 model (Janjic, 1990). PBL height is determined from the TKE where the PBL top is defined where the profile decreases to a prescribed low value ($0.2 \text{ m}^2 \text{ s}^{-2}$).

The third scheme is the Quasi-Normal Scale Elimination (QNSE) scheme (Sukoriansky et al., 2005). The QNSE scheme is a one-and-a-half order, local closure scheme and has a TKE prediction option that uses a new theory for stably stratified regions. PBL height is defined as where the TKE profile decreases to a prescribed low value ($0.01 \text{ m}^2 \text{ s}^{-2}$), similar to the MYJ scheme.

The next scheme is the Mellor-Yamada-Nakanishi-Niino Level 2.5 (MYNN2) scheme (Nakanishi and Niino, 2006). The Mellor-Yamada-Nakanishi-Niino Level 3 (MYNN3) scheme shares similar characteristics to MYNN2 so it will not be evaluated here. The MYNN2 scheme is tuned to a database of large eddy simulations (LES) in order to overcome the typical biases associated with other MY-type schemes, such as

insufficient growth of convective boundary layer and under-estimated TKE. The MYNN2 scheme is a one-and-a-half order, local closure scheme and predicts sub-grid TKE terms. PBL height is determined as the height at which the TKE falls below a critical value ($1.0 \times 10^{-6} \text{ m}^2 \text{ s}^{-2}$).

The fifth scheme is the Asymmetrical Convective Model version 2 (ACM2) scheme (Pleim, 2007). The ACM2 scheme is a first order, non-local closure scheme and features non-local upward mixing and local downward mixing. It's a modified version of the ACM1 scheme from the MM5 model, which was a derivative of the Blackadar scheme (Blackadar, 1978). The scheme has an eddy-diffusion component in addition to the explicit non-local transport of ACM1. PBL height is determined as the height where the Ri_b calculated above the level of neutral buoyancy exceeds a critical value ($Ri_{bc} = 0.25$). For stable or neutral flows the scheme shuts off non-local transport and uses local closure.

The following three schemes are lesser used and not-as-well-tested. The first is the Bougeault-Lacarrère (BouLac) scheme (Bougeault and Lacarrère, 1989). The BouLac scheme is a one-and-a-half order, local closure scheme and has a TKE prediction option designed for use with the BEP (Building Environment Parametrization) multi-layer, urban canopy model (Martilli et al., 2002). BouLac diagnoses PBL height as the height where the prognostic TKE reaches a sufficiently small value (in the current version of WRF is $0.005 \text{ m}^2 \text{ s}^{-2}$).

The University of Washington (UW) scheme (Bretherton and Park, 2009) is a one-and-a-half order, local TKE closure scheme from the Community Earth System Model (CESM), climate model (Gent et al., 2011). PBL height in the UW scheme is defined as the inversion height between grid levels via a Ri_b threshold (0.25).

The Total Energy-Mass Flux (TEMF) scheme (Angevine et al., 2010) is a one-and-a-half order, non-local closure scheme and has a sub-grid-scale total energy prognostic variable, in addition to mass-flux type shallow convection. TEMF uses eddy diffusivity and mass flux concepts to determine vertical mixing. PBL height is calculated through a Ri_b method with zero as a threshold value. In this study there were minor stability issues with five simulation days using the TEMF scheme. All these days were characterised by low-level winds from the south-west. The stability issues are caused by a threshold exceedance of potential temperature over the desert regions in our parent domain. Decreasing the time between calls to the radiation physics scheme improved the stability for two of the five simulation days.

4.2.2 Identification of primary synoptic situations

The FLEXPART-WRF (FLEXible PARTicle) dispersion model (Brioude et al., 2012; 2013) was used to provide daily backward trajectories (backtrajectories) during the campaign. FLEXPART-WRF is driven by the 12×12 km atmospheric fields from the external WRF grid. The model is set up with ten vertical levels (100, 250, 400, 600, 900, 1500, 2000, 3000, 5000, 10000 m) and the output grid is at a horizontal grid spacing of 12×12 km. A total of 50000 particles are released for each simulation and the 48-h backtrajectories are computed for the air masses arriving at 0.5, 1.0, 2.0, 3.0 and 4.0 km over Athens.

Based on visual inspection of the backtrajectories and WRF simulations, the atmospheric conditions during the campaign can be classified into one of three synoptic flow types: Continental, Etesians, and Saharan synoptic flows. Figure 4.2 shows two-day backtrajectories (a - c) from the FLEXPART-WRF dispersion model for representative cases of each flow type, along with the associated synoptic weather maps (d - f) simulated by the WRF model.

The predominant synoptic flow (41.7 % of campaign) is Continental, which is influenced by winds from the west to north-west. A representative day for this synoptic flow is 25 May 2014 (Fig. 4.2a,d). The flow is characterized by a stagnant weather pattern with a weak atmospheric pressure gradient over Greece. On this particular day a sea breeze develops in the afternoon, but this is not a mandatory feature for all cases of this flow type. Frequently, mesoscale processes dominate in this synoptic flow. This type of atmospheric situation can provoke the development of urban pollution episodes.

The second most prevalent synoptic flow during the campaign (36.1 % of days) is the Etesians. This situation is influenced by winds coming from the north to north-east. A selected representative day of this pattern is 13 June 2014 (Fig. 4.2b,e). The Etesians are caused by a gradient between strong high pressure north-west of Greece and a low pressure area over Asia and these days are characterized by increased PBL height over Athens. The weakening of the Etesians synoptic flow allows for the development of local circulation systems (sea and land breezes), sometimes accounting for a decreased PBL height (Melas et al., 1995).

The third major synoptic flow observed during the campaign (22.2 % of days) is Saharan type. In this condition winds are dominant from the south-west with a stagnant atmospheric pressure pattern over Greece. Typically this wind flow is most associated with dust intrusions from the Saharan source region in Africa. This was confirmed in a previous work by Papayannis et al. (2009) with the use of lidar measurements, satellite images, and a mineral dust transport model. A representative day during the campaign for this flow

type is shown as 16 June 2014 (Fig. 4.2c,f). In this particular case there is afternoon sea breeze initiation which may be attributable to a lower PBL height.

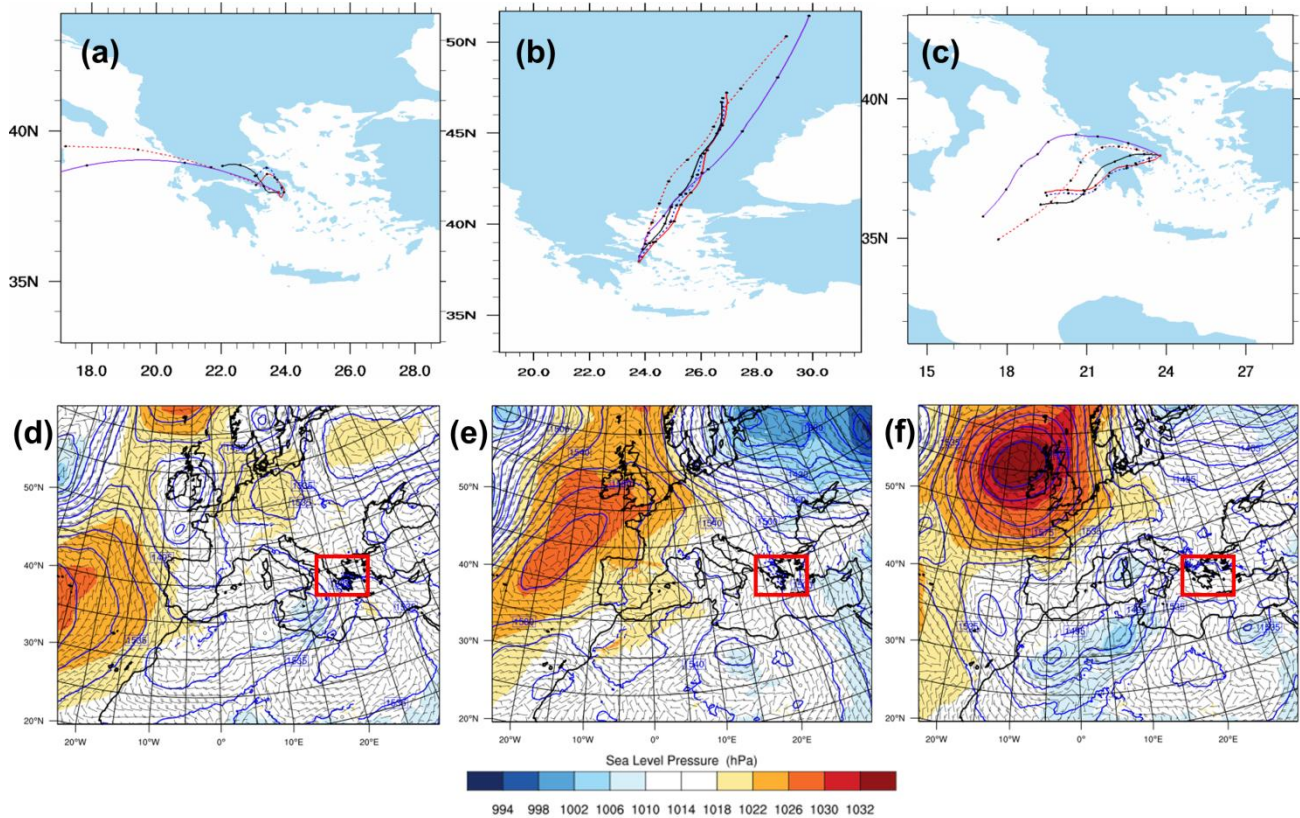


Figure 4.2 Two-day FLEXPART-WRF backtrajectories (top) ending at Athens (37.96N, 23.78E) and synoptic maps simulated with the WRF model (bottom) representing (from left to right), Continental (25 May 2014), Etesians (13 June 2014), and Saharan (16 June 2014) flow types. Backward trajectories end at 1200 UTC with black dots showing 6-h position and colors denote trajectory height at receptor for 0.5 km (red), 1 km (blue dashed), 2 km (black), 3 km (red dashed), and 4 km (purple). Synoptic maps (valid 1200 UTC) show sea level pressure in hPa (coloured contours), geopotential height at 850-hPa in metres (blue lines), and 850-hPa winds (barbs).

All datasets (lidar, WRF simulations, radiosoundings, surface meteorological instruments) are grouped into these synoptic flow types for the analysis. The results are presented as a combination of averages, differences, and representative case studies.

4.2.3 PBL height from backscatter lidar

A backscatter lidar was operated during daytime hours of the campaign at the National Technical University of Athens (NTUA; 37.98°N, 23.78°E, 212 masl). The instrument at NTUA is a six-wavelength Raman lidar system used to perform measurements of suspended aerosol particles in the PBL (Kokkalis et al., 2012). The NTUA lidar station is a member of the European Aerosol Research Lidar Network (EARLINET; Bosenberg et al., 2001).

Lidar data were collected for 36 out of 39 days of the month-long campaign (92.3 % observation frequency). No lidar data was available on 19 May 2014 (observed thick stratus clouds) and 3-4 June 2014 (observed clouds and stratiform precipitation). The majority of the lidar data was measured from 8:00-15:00 UTC, with the earliest start at 6:00 UTC and the latest finish around 18:00 UTC. Resultant lidar data was visually quality-controlled for clouds in the PBL.

In this study we use vertical profiles of the range-corrected backscattered power at 1064-nm using a temporal resolution of 100-s as a basis for the PBL height estimation. Tsaknakis et al. (2011) showed this wavelength provides sufficient transition between the suspended aerosol load in the PBL and the cleaner free troposphere (FT) above, as the molecular contribution in the near infrared becomes much smaller than that of the particles. The range resolution of the NTUA lidar is 7.5 m, with a full overlap window around 700 m.

PBL height is estimated from the lidar observations using an adaptive approach utilizing an extended Kalman filter (EKF) (Brown and Hwang, 1982). The technique has been developed and tested with simulated lidar retrievals (Rocadenbosch 1998, 1999; Lange et al., 2014, 2015), and under various atmospheric conditions over Barcelona, Spain (Banks et al., 2014). Banks et al. (2015) showed the EKF technique is suitable for well-mixed convective boundary-layers, after an extensive validation effort against classic methods of estimating PBL height from lidar and radiosondes.

The developed and tested EKF approach is based on estimating four time-adaptive coefficients of a highly simplified erf-like curve model, representing the PBL transition in terms of the RCS backscatter lidar signal. The erf-like model, $h(R)$, is formulated as follows:

$$h(R; R_{bl}, a, A, c) = \frac{A}{2} \left\{ 1 - \operatorname{erf} \left[\frac{a}{\sqrt{2}} (R - R_{bl}) \right] \right\} + c \quad (4.1)$$

where R_{bl} is an initial guess of the PBL height, a is the entrainment zone (EZ) scaling factor, A is the amplitude of the erf transition, and c is the average molecular background at the bottom of the FT. EKF state-vector initialization also requires statistical covariance information from the user's side; this is accomplished by providing state-vector-noise and a-priori error covariance matrices (in turn, related to the initial state-vector). If the state-vector $[R_{bl} \ a \ A \ c]$ is not initialized correctly one can expect not so reliable estimates of PBL height.

Lange et al. (2015) explained why the present implementation of the EKF uses both inner (R'_1, R'_2) and outer (R_1, R_2) range boundaries of the erf-like model. These ranges are allowed to change adaptively with the estimated PBL height, a computational advantage in cases where the PBL height changes sharply between adjacent time steps. The only requirement is that the inner and outer range intervals defined contain erf-transition and erf-plateau characteristics.

Also, the EKF method benefits from the Kalman gain, which corrects the projection trajectory of the PBL atmospheric variables and improves its estimation of the PBL parameters via a new state vector. The statistical covariance information, along with the state vector, observation-noise covariance, and Kalman gain, is updated recursively at each iteration of the filter.

Figure 4.3 shows the first 100-s lidar profile from 25 May 2014 started at 0701 UTC, which is used to initialize the EKF state vector. In this case the signal-to-noise ratio is > 5 up to 3 km altitude. For better numerical conditioning and physical significance the observation vector presented to the filter is a molecular-normalized version. The initial state vector parameters are subjectively selected from visual inspection of the first profile. For this case we annotated on the figure as $R_{bl} = 0.60$ km, $a = 9.23$ km⁻¹, $A' = 4.0 \times 10^4$, and $c' = 2.0 \times 10^4$. Additionally $R_1 = 0.26$ km and $R_2 = 0.75$ km, while $R'_1 = 0.375$ km and $R'_2 = 0.675$ km. We have to note that it's only necessary to provide the initial EKF state vector parameters in general terms. The convergence time to a reliable solution will depend on the complexity of the lidar scene, the initial state vector estimates, and the state-noise and error covariance matrices.

Individual daily (24-hr) WRF model simulations were run for the same 36 days lidar-EKF estimates were calculated. This dataset is used for the evaluation of simulated PBL height from the PBL parametrization schemes. For the comparison with WRF model-simulated values a 15-min average (nine 100-s estimates) of lidar-EKF PBL height is applied, centred on the hourly model output times. PBLHs estimated by lidar and simulated with WRF are shown in km asl throughout this study.

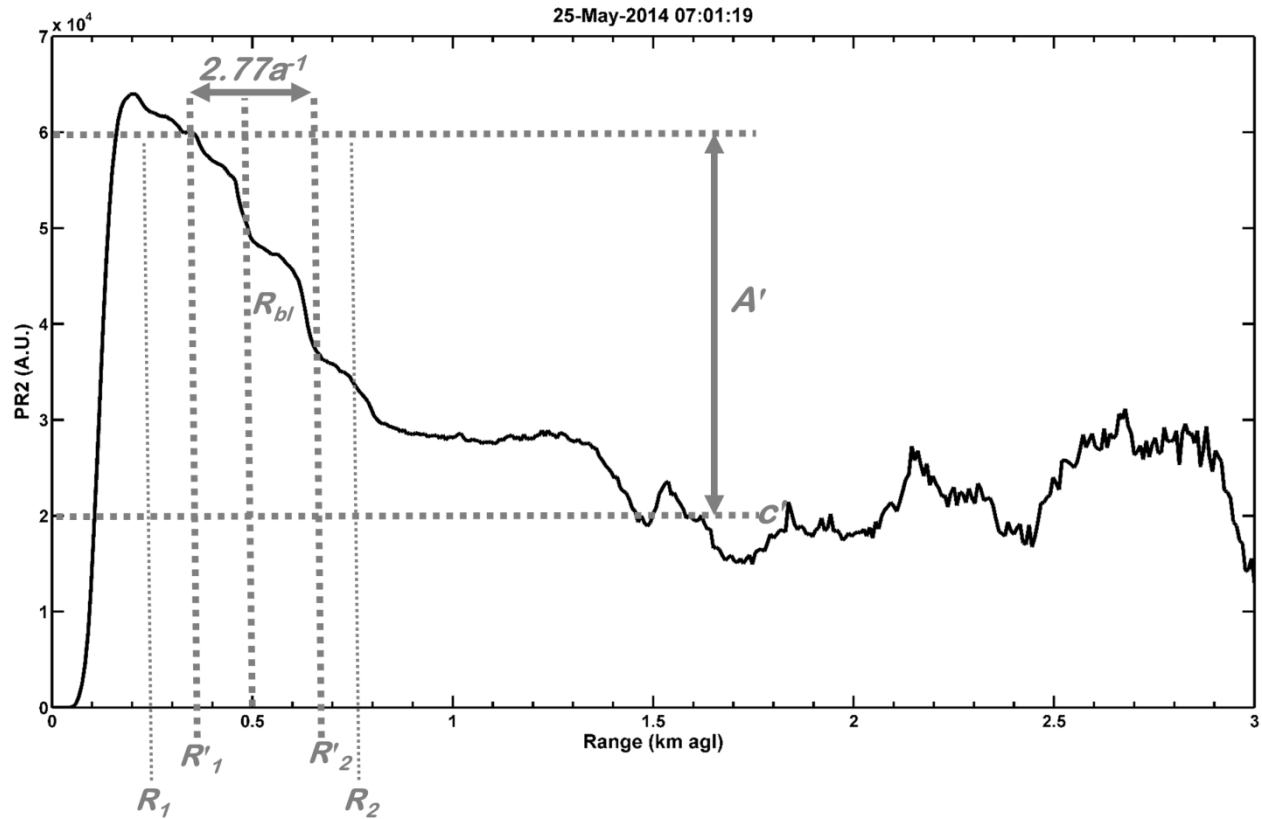


Figure 4.3 100-s profile of molecular-normalised range-corrected power from the NTUA lidar at 0701 UTC on 25 May 2014. Initial state vector $[R_{bl} \ a \ A' \ c']$ with lower- and upper-range limits $[R_1 \ R_2]$ for the extended Kalman filter (EKF) PBL height technique are annotated in gray dashed lines.

4.2.4 Surface meteorological observations and radiosoundings

Near-surface meteorological variables are important for the evaluation of PBL schemes as they represent lower boundary-layer processes. We collected 2-m air temperature (T2) and relative humidity (RH2), and 10-m wind speed (WS10) from 14 surface meteorological stations. It should be noted wind speed measurements are extrapolated to 10-m from the individual station height using the wind power law. Twelve of the stations are associated with the National Observatory of Athens (NOA) network, in addition to one station situated at the NTUA Physics Department (lidar site), and one station located at the National Centre for Scientific Research, Demokritos (NCSR). Figure 4.4 shows the geographical location and elevation of the measurement stations. The locations were selected for a diversified mix of geographical influences, ranging from 10 m asl

at Anavyssos to 565 m asl at Ippokrateios. The mean difference between WRF model-grid height and real terrain height was 3.5 m asl, indicating reliable topographic influences from the WRF model.

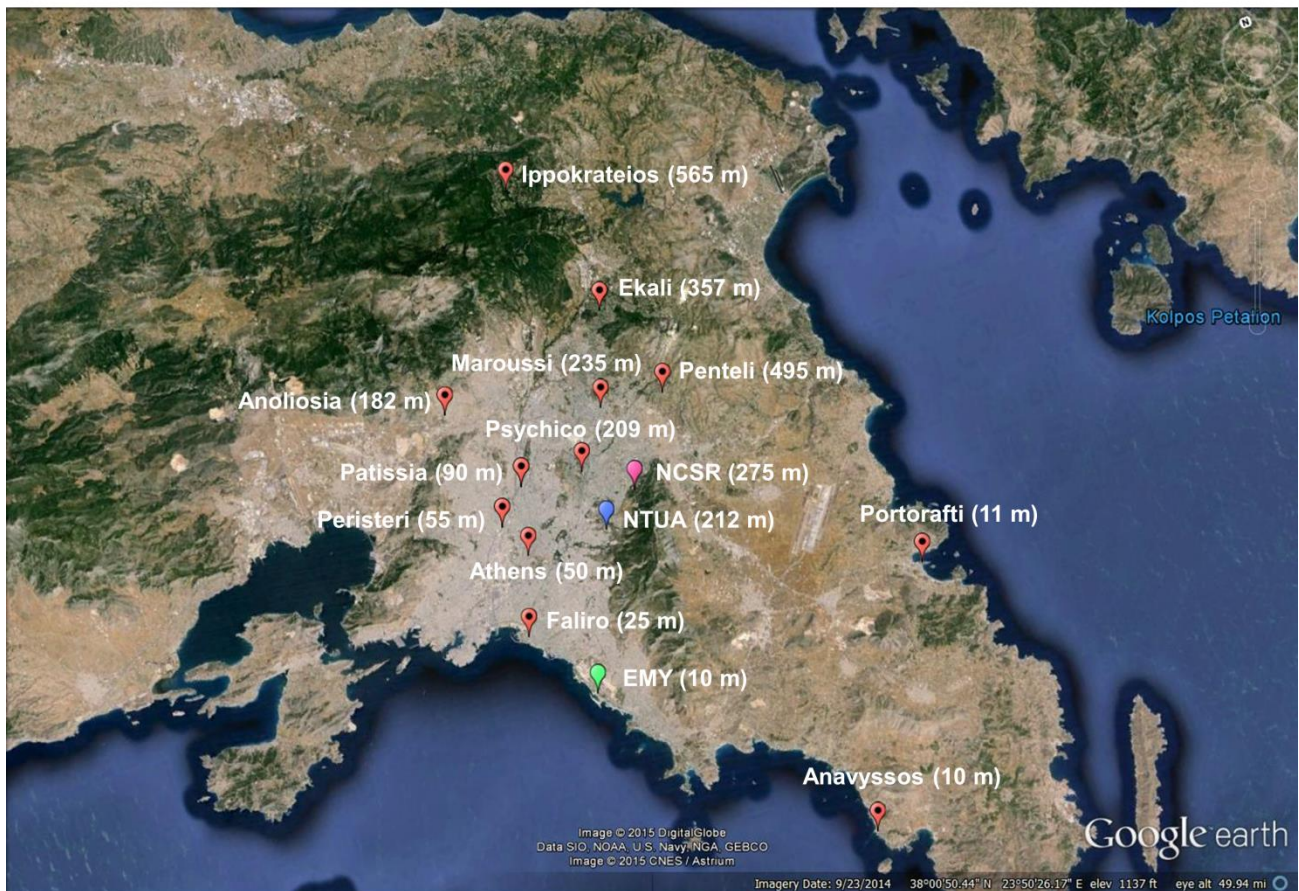


Figure 4.4 Location and elevation (meters above sea level) of the 14 surface meteorological stations (12 from the National Observatory of Athens, one from NTUA, and one from NCSR), and site of radiosonde launches (EMY). Spatial variations range from 500 m – 12 km apart and in elevation from 10 – 565 m asl.

In order to evaluate vertical profiles, 13 radiosondes were launched from the Hellenic National Meteorological Service (EMY) during the campaign. EMY is located near the sea (37.88°N , 23.73°E , 10 m asl) approximately 12 km away from the lidar site. The launches were scheduled around 11:00 UTC. The

Vaisala RS92 radiosonde instrument records atmospheric variables of temperature ($^{\circ}\text{C}$), dew point temperature ($^{\circ}\text{C}$), relative humidity (%), wind speed (m s^{-1}) and direction ($^{\circ}$), and barometric pressure (hPa).

In this study PBL height is calculated from the radiosounding data using the bulk Richardson number (Ri_b) method (Holtslag et al., 1990). It is the same method used in many of the WRF PBL schemes (Sect. 4.2.1) to diagnose the PBL height. The Ri_b approach requires wind speed and direction, barometric pressure, and temperature as input variables at each altitude (m). The Ri_b method is a proxy of where the wind transitions from turbulent to laminar, possibly indicating the top of the PBL. PBL height is calculated at the altitude where Ri_b exceeds a so-called critical Richardson number (Ri_{bc}).

From many previous studies the Ri_{bc} is selected as a universal constant anywhere between 0.1 and 1.0 (Richardson et al., 2013). Typically higher critical values are selected in areas where the flow transition from turbulent to laminar is larger. In this work many critical values were tested by visually inspecting vertical profiles of potential temperature. We found that a critical value of 0.25 provides reasonable PBL height estimates.

4.3 Results and discussion

4.3.1 Near-surface meteorological variables (T2, RH2, WS10)

First, WRF model-simulated near-surface meteorological variables are validated against measurements from the GAA surface network. Results are presented for representative coastal and inland locations, then as a statistical set of the 14 total stations. Statistical measures include mean bias (MB), root mean-squared error (RMSE), coefficient of determination (R^2), and standard deviation (STDEV). Results are organized according to the campaign average, and averages for the three synoptic flows observed during the campaign. The innermost domain from the WRF model runs is subjected to the evaluation.

Statistical significance of the results presented in Tables 4.2 and 4.3 are performed through two-sample t tests (Wilks, 2006), with a two-tailed distribution. The tests help determine whether the mean (μ) differs significantly between two independent datasets, which in this study are the WRF model simulations and observations. The outcomes of the t tests show p -values well below 0.001 for all tests, which is clearly significant at a 95% confidence interval.

Figure 4.5 shows the campaign-averaged MB (WRF model – observed) for the surface meteorological variables at two locations: Anavyssos (37.73°N, 23.91°E, 10 m asl) and Peristeri (38.00°N, 23.70°E, 55 m asl), representing coastal and inland locations, respectively. WRF model-simulated T2 (Fig. 4.5a) and RH2 (Fig. 4.5c) at Anavyssos during daytime (defined as: 8:00 – 18:00 UTC) shows a systematic cold ($\approx 1 - 3$ °C), moist (up to 23 %) bias among PBL schemes, while at Peristeri (Fig. 4.5b,d) the errors are much smaller (T2: $\approx \pm 1$ °C and RH2: $\approx -9 - 5$ %). The largest spread between the PBL schemes is observed with RH2 at Anavyssos during daytime, with the QNSE and MYNN2 schemes fitting most closely to the observations between 10:00 and 17:00 UTC. The WRF model shows a consistent over-representation of WS10 (Fig. 4.5e,f) at both locations, as high as 6 m s^{-1} at Anavyssos. The error in WS10 is fairly constant throughout the diurnal cycle.

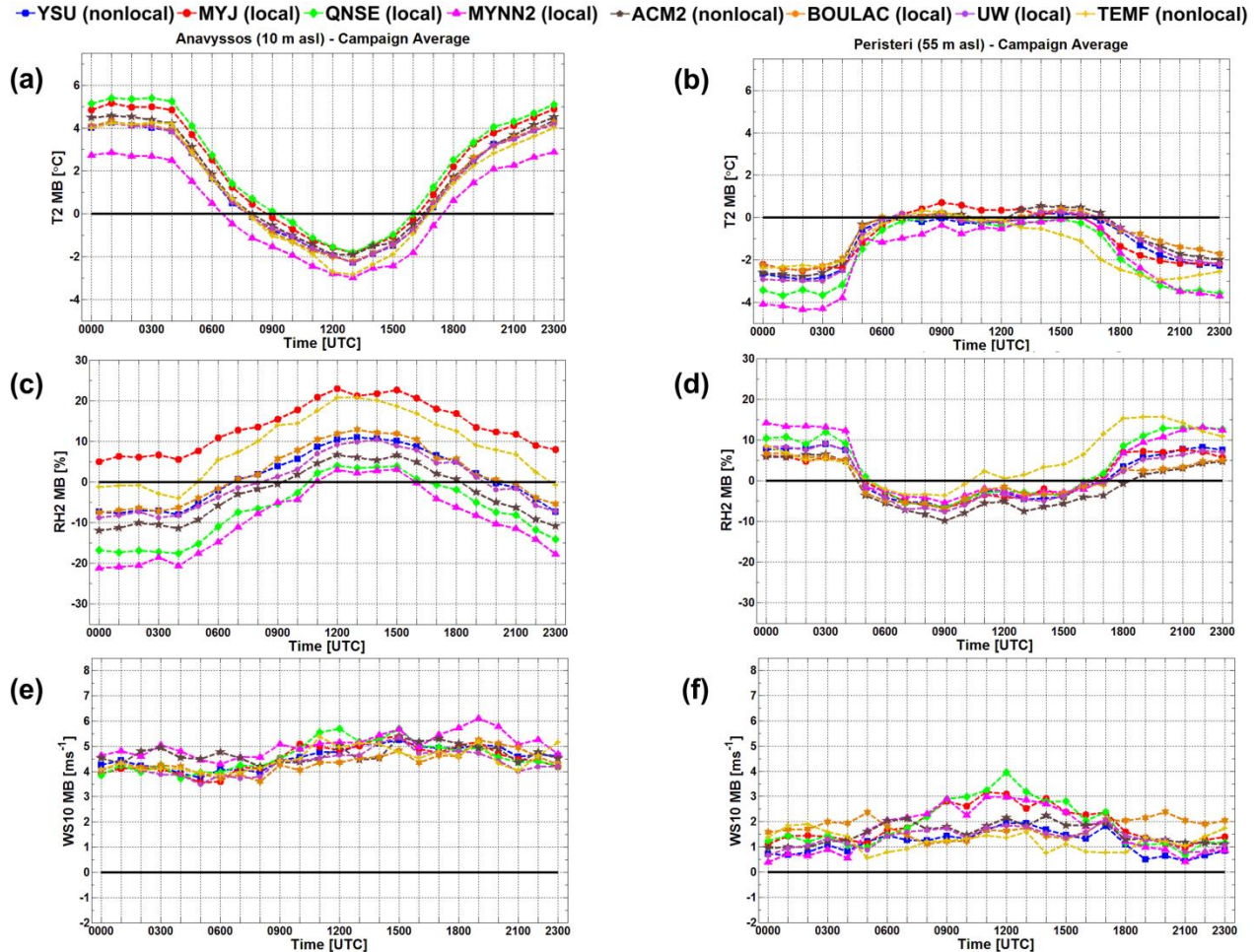


Figure 4.5 Campaign-averaged mean bias (MB, WRF – observation) for (a-b) 2-m air temperature (T2, °C), (c-d) 2-m relative humidity (RH2, %), and (e-f) 10-m wind speed (WS10, m s^{-1}) at two stations (Anavyssos and Peristeri) from the NOAA network, representative of coastal and inland influences, respectively.

In order to investigate the performance of WRF model PBL schemes in greater detail, Table 4.2 shows the performance indicators of the surface meteorological variables between each WRF PBL scheme and the observations. The results in Table 4.2 have been computed to represent all 14 stations for the campaign average ($N = 12096$) over the full diurnal period. Overall, the performance of WRF PBL schemes is quite ambiguous depending on the meteorological parameter being analysed. The BouLac scheme shows the best performance with respect to T2 ($R^2 = 0.8$ and RMSE $2.09\text{ }^\circ\text{C}$), while the MYJ scheme has the lowest MB ($-0.23\text{ }^\circ\text{C}$). The BouLac scheme also performs well in simulating RH2 (MB = -0.41%), but the ACM2 scheme shows a closer correspondence ($R^2 = 0.4$) and RMSE (12.1%) to the observed values. All PBL schemes consistently over-estimate WS10, with the non-local YSU scheme having the lowest error (MB = 2.33 m s^{-1}).

The differences between model simulations and observations have influences from the underlying daily changes in atmospheric dynamics. The three primary synoptic situations identified with the FLEXPART-WRF backtrajectories (Fig. 4.2) can be used to further analyse the impacts of the meteorological situation. These results are shown in Figs. 4.6 – 4.8, again using Anavyssos and Peristeri as proxy locations for coastal and inland impacts, respectively.

First, are the results when averaging over the days influenced by Continental synoptic flow (Fig. 4.6). The overall impression of MB for both locations looks similar to the campaign average; however, subtle differences are noted for T2 (Fig. 4.6a,b) and RH2 (Fig. 4.6c,d). At Peristeri, the TEMF scheme shows a cooler, moister bias after 12:00 UTC (T2: up to $-3\text{ }^\circ\text{C}$ and RH2: up to 25%) progressing into the evening. All PBL schemes show a slight improvement with WS10 ($\approx 1\text{ m s}^{-1}$) when compared to the campaign average (Fig. 4.6e,f), especially in the morning hours.

Table 4.3 shows the performance indicators of the surface meteorological variables between each WRF PBL scheme and the observations for each synoptic flow type. Statistics are calculated to represent all 14 stations averaged for each type. STDEV calculated for each synoptic flow was similar to the campaign average, and is not shown in the table.

Table 4.2 Statistics of 2-m air temperature (T2) and relative humidity (RH2), and 10-m wind speed (WS10) between WRF PBL schemes and observations (N=12096). Performance indicators; mean bias (MB) and standard deviation (STDEV), coefficient of determination (R^2), and root mean-squared error (RMSE) for the campaign average.

Variable	Scheme	MB (STDEV)	R^2	RMSE
<i>T2 (°C)</i>		<i>(°C)</i>		<i>(°C)</i>
	YSU	-0.56 (1.18)	0.79	2.24
	MYJ	-0.23 (1.30)	0.78	2.25
	QNSE	-0.68 (1.57)	0.77	2.55
	MYNN2	-1.14 (1.04)	0.79	2.48
	ACM2	-0.32 (1.19)	0.79	2.17
	BOULAC	-0.32 (1.12)	0.8	2.09
	UW	-0.5 (1.15)	0.79	2.18
	TEMF	-0.87 (1.26)	0.73	2.67
<i>RH2 (%)</i>		<i>(%)</i>		<i>(%)</i>
	YSU	0.57 (3.77)	0.36	12.47
	MYJ	1.99 (6.74)	0.38	13.08
	QNSE	0.57 (4.82)	0.38	12.64
	MYNN2	-0.61 (6.62)	0.39	13.65
	ACM2	-2.31 (3.90)	0.4	12.1
	BOULAC	-0.41 (3.76)	0.35	12.24
	UW	0.05 (3.72)	0.36	12.3
	TEMF	4.65 (4.50)	0.28	14.83
<i>WS10 (m s⁻¹)</i>		<i>(m s⁻¹)</i>		<i>(m s⁻¹)</i>
	YSU	2.33 (1.21)	0.39	3.1
	MYJ	3.1 (1.01)	0.42	3.86
	QNSE	3.17 (1.02)	0.41	3.98
	MYNN2	2.69 (1.23)	0.44	3.4
	ACM2	2.58 (1.17)	0.41	3.35
	BOULAC	2.5 (1.07)	0.35	3.32
	UW	2.34 (1.13)	0.39	3.15
	TEMF	2.42 (1.19)	0.29	3.23

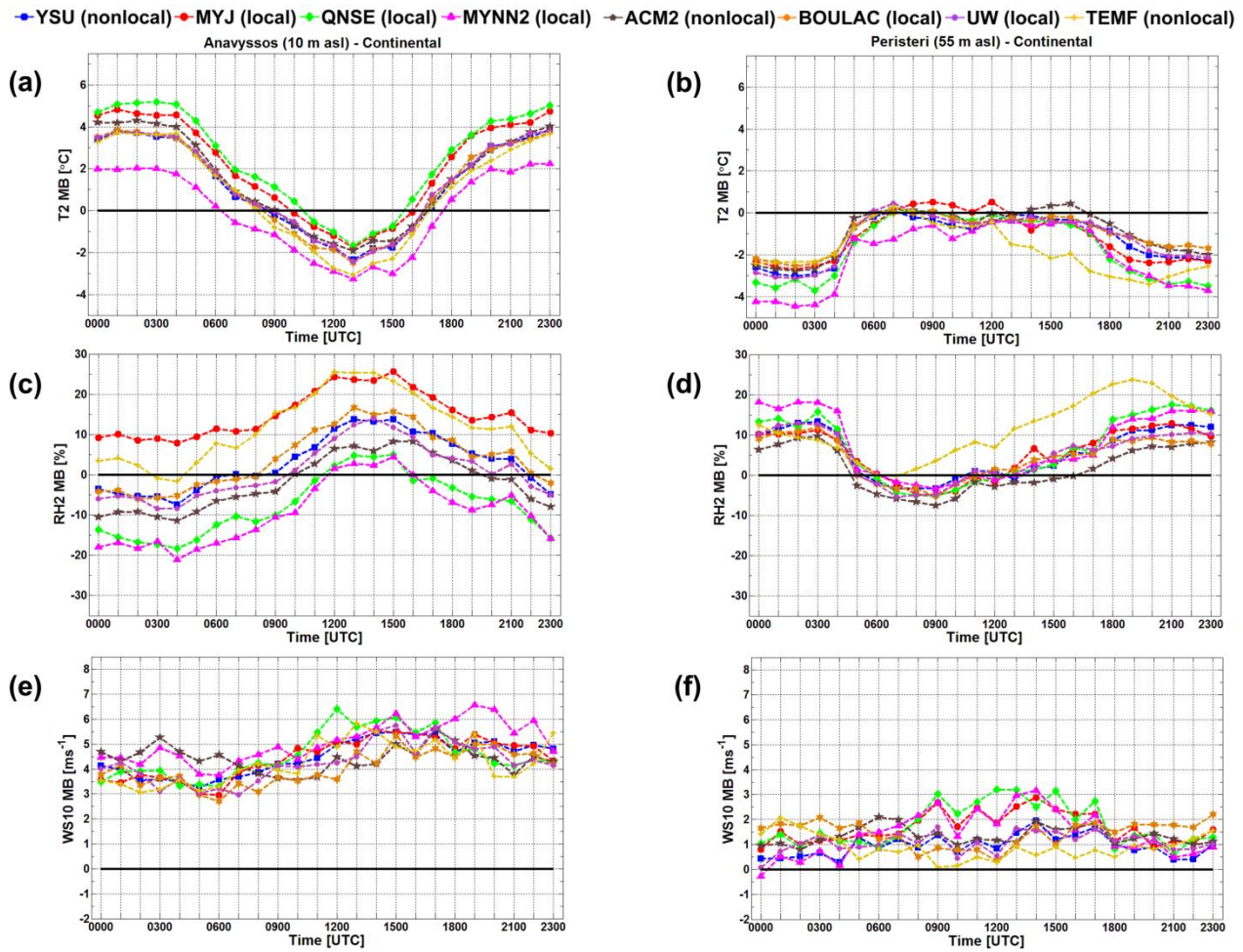


Figure 4.6 Same as in Fig. 4.5, but time-averaged for Continental synoptic flow days.

For Continental synoptic flow ($N = 5040$), the ACM2 and BouLac schemes show the closest representation ($MB = -0.41 \text{ } ^\circ\text{C}$ and $RMSE = 2.08 \text{ } ^\circ\text{C}$, respectively) to observed T_2 values. Also, the ACM2 scheme performs well with respect to RH_2 ($MB = -0.07 \text{ } \%$). The lowest errors in simulated WS_{10} are shown for the YSU (2.17 m s^{-1}) and UW (2.12 m s^{-1}) schemes.

Table 4.3 Similar to Table 4.2, except calculated according to Continental synoptic flow (N = 5040), Etesians synoptic flow (N = 4368), and Saharan synoptic flow (N=2688) types.

Variable	Scheme	Continental			Etesians			Saharan		
		MB	R ²	RMSE	MB	R ²	RMSE	MB	R ²	RMSE
<i>T2 (°C)</i>		(°C)		(°C)	(°C)		(°C)	(°C)		(°C)
	YSU	-0.71	0.82	2.15	-0.76	0.73	2.25	0.06	0.74	2.33
	MYJ	-0.38	0.82	2.22	-0.46	0.73	2.18	0.41	0.74	2.39
	QNSE	-0.69	0.81	2.47	-1.01	0.72	2.54	-0.14	0.71	2.69
	MYNN2	-1.32	0.82	2.44	-1.23	0.75	2.47	-0.66	0.73	2.52
	ACM2	-0.41	0.82	2.08	-0.54	0.74	2.16	0.2	0.75	2.31
	BOULAC	-0.54	0.82	2.08	-0.41	0.76	1.99	0.24	0.77	2.25
	UW	-0.62	0.82	2.1	-0.75	0.74	2.22	0.1	0.77	2.2
	TEMF	-1.16	0.74	2.76	-0.97	0.72	2.46	0.15	0.65	2.61
<i>RH2 (%)</i>		(%)		(%)	(%)		(%)	(%)		(%)
	YSU	3.52	0.29	12.88	-0.26	0.4	11.74	-3.62	0.43	12.58
	MYJ	4.93	0.32	13.87	1.64	0.49	11.54	-2.97	0.39	13.47
	QNSE	2.72	0.32	13.31	0.55	0.47	11.24	-3.42	0.42	13.23
	MYNN2	1.59	0.34	14.02	-0.56	0.45	12.6	-4.83	0.45	14.27
	ACM2	-0.07	0.32	11.95	-2.49	0.46	11.43	-6.21	0.48	13.05
	BOULAC	2.71	0.28	12.65	-1.33	0.42	11.05	-4.75	0.39	13.02
	UW	2.67	0.3	12.38	-0.17	0.43	11.51	-4.52	0.4	13.09
	TEMF	9.33	0.23	16.95	1.85	0.4	11.81	-2.05	0.42	12.72
<i>WS10 (m s⁻¹)</i>		(m s ⁻¹)		(m s ⁻¹)	(m s ⁻¹)		(m s ⁻¹)	(m s ⁻¹)		(m s ⁻¹)
	YSU	2.17	0.38	3.05	2.48	0.45	3.09	2.39	0.37	3.13
	MYJ	2.93	0.41	3.79	3.38	0.46	3.97	2.97	0.4	3.73
	QNSE	2.99	0.38	3.91	3.43	0.46	4.07	3.1	0.4	3.88
	MYNN2	2.53	0.43	3.34	2.91	0.48	3.51	2.6	0.42	3.28
	ACM2	2.4	0.39	3.23	2.86	0.46	3.44	2.46	0.4	3.31
	BOULAC	2.19	0.35	3.09	2.96	0.37	3.54	2.36	0.33	3.28
	UW	2.12	0.37	3.06	2.57	0.45	3.17	2.37	0.36	3.21
	TEMF	2.19	0.26	3.17	2.65	0.36	3.14	2.48	0.42	3.32

The next most frequent atmospheric flow type is the Etesians. The MB of surface meteorological variables are averaged for days in this synoptic flow group for Anavyssos and Peristeri stations (Fig. 4.7). It is shown that daytime simulated T2 at Anavyssos (Fig. 4.7a) is around 0.5 °C colder than the campaign average. The spread of T2 between the PBL schemes is similar, with MYNN2 being the coldest. With respect to simulated RH2 (Fig. 4.7c,d), the differences between the PBL schemes is largest at Anavyssos. During daytime the WRF model tends to reproduce a RH2 which is too moist (5 – 25 %) at Anavyssos and too dry (5 – 10 %) at Peristeri. Simulated values of WS10 (Fig. 4.7e, f) continue to show over-estimates with all schemes, up to 6 m s⁻¹ with MYNN2.

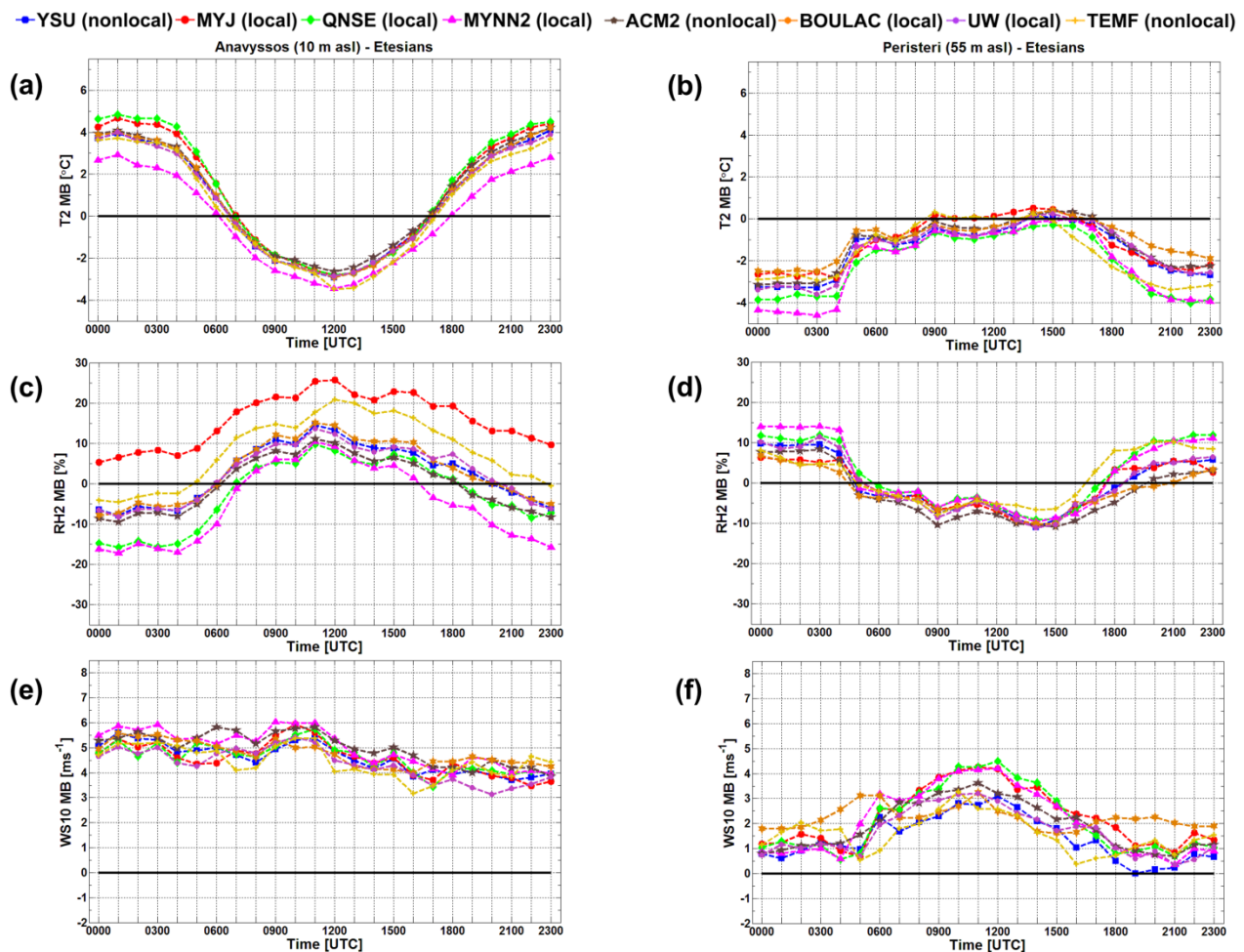


Figure 4.7 Same as in Fig. 4.5, but time-averaged for Etesians synoptic flow days.

Table 4.3 shows the performance indicators of the surface meteorological variables between each WRF PBL scheme and the observations, now computed to represent all 14 stations averaged for the synoptic flow group, Etesians (N = 4368). The BouLac scheme reproduces the closest T2 (MB = -0.41 °C) when compared with other schemes. The closest schemes with respect to the MB of RH2 are UW (-0.17 %), followed by QNSE (0.55 %). Again, WS10 is the most well-reproduced by the YSU scheme (MB = 2.48 m s⁻¹).

In the final synoptic flow type, Saharan, we show the MB of surface meteorological variables for Anavyssos and Peristeri stations (Fig. 4.8). In this synoptic situation, simulated T2 at both locations (Fig. 4.8a,b) increases by approximately 1 °C, resulting in an improvement at Anavyssos, but a degradation at Peristeri. The difference is most notable during daytime. Wind flow from the southwest also promotes a drier environment than the campaign average, which is shown in Fig. 4.8c,d. Simulated RH10 at Peristeri is very well reproduced with a ± 10 % error. Finally, simulated WS10 at Anavyssos (Fig. 4.8e) shows a large deviation from the observations (> 4 m s⁻¹) after 12:00 UTC, which is approximately 2 m s⁻¹ higher than the campaign average.

The performance indicators for surface meteorological variables between individual WRF PBL schemes and the observations, calculated to represent all 14 stations averaged for the Saharan synoptic flow group are shown in Table 4.3. The UW and BouLac schemes correspond closest ($R^2 = 0.77$ for both) to the observed T2 values, with the UW and YSU schemes having the lowest MB (0.10 and 0.06 °C, respectively). The TEMF scheme simulates RH2 closest (MB = -2.05 % and RMSE = 12.72 %) to the observed values, even though it is a poor performer with the other two synoptic flow types and the campaign average. With respect to WS10, the BouLac scheme slightly outperforms (MB = 2.36 m s⁻¹) other schemes; however, YSU is a close second (RMSE = 3.13 m s⁻¹).

In summary, the campaign-averaged near-surface variables showed that the WRF model tended to have a systematic cold, moist bias during daytime, most prominent at the coastal location. The BouLac scheme reproduced T2 and RH2 well with the campaign average, and with Etesians synoptic flow. ACM2 showed the closest T2 and RH2 during Continental flows. With Saharan synoptic flows, the UW and BouLac schemes well-represented T2, while TEMF best-reproduced RH2. WRF with the YSU scheme showed the closest WS10 to the observed values with the campaign average, and during Continental and Etesian synoptic flows. The BouLac scheme only slightly outperformed YSU during Saharan events.

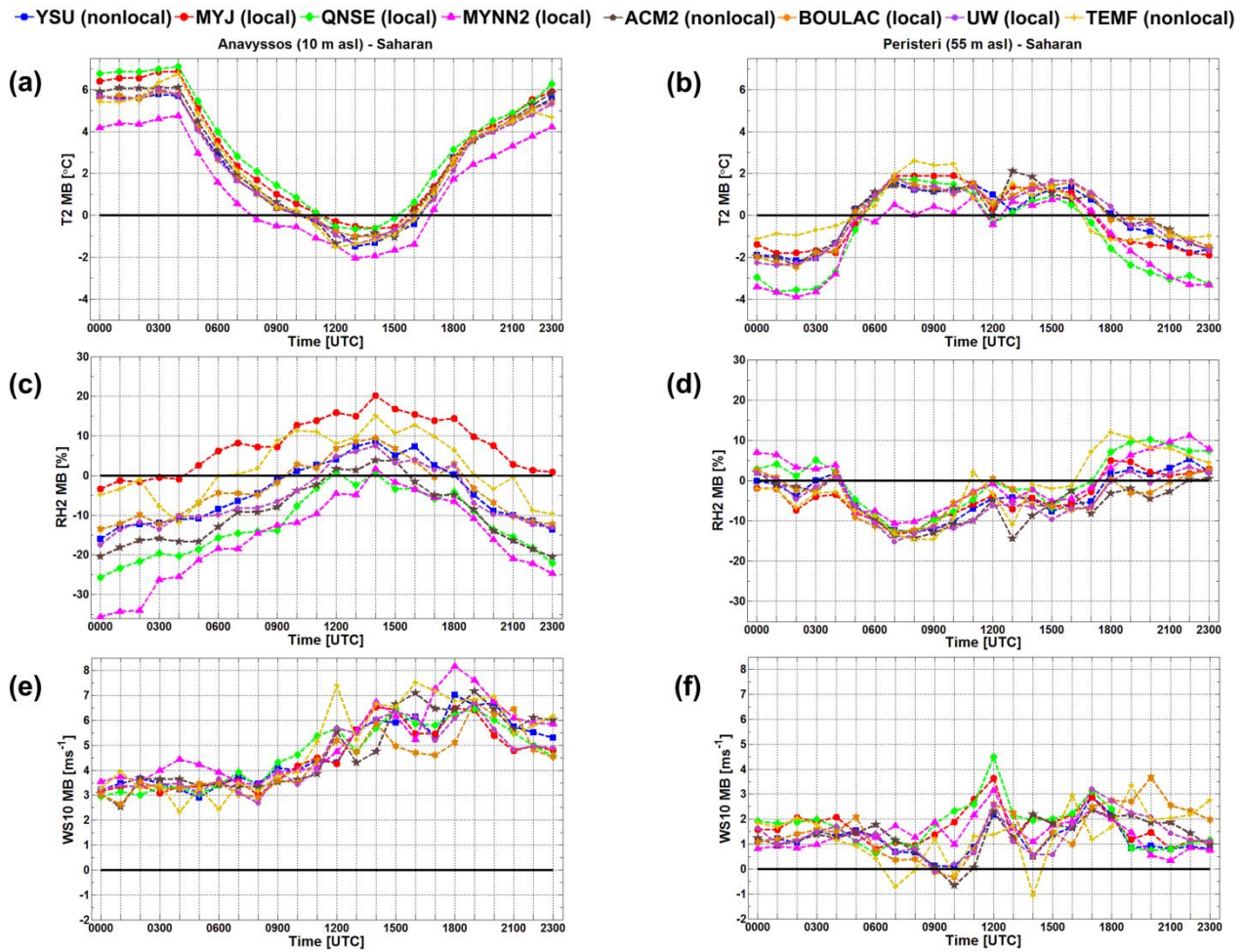


Figure 4.8 Same as in Fig. 4.5, but time-averaged for Saharan synoptic flow days.

4.3.2 PBL height intercomparison

In this section we show the results for the evaluation of the PBL height. First, will be the comparison between PBL height estimated from lidar and radiosoundings. Next, we use the lidar-EKF estimates of PBL height to perform an evaluation of WRF model-simulated PBL height using the different PBL schemes. Finally, we show representative cases of lidar and WRF model PBL height for each synoptic flow to discuss the strengths and weaknesses of the lidar-EKF technique.

PBL height is estimated from daytime lidar measurements using the EKF technique. Lidar-estimated PBL height was compared with 13 radiosounding-derived estimates using a bulk Richardson number method

(Holtslag et al. 1990). The MB (lidar – radiosonde) shows that the lidar-EKF over-estimated PBL height around 0.40 km compared to the estimation by the radiosonde over the EMY site. Possibly this can be explained by the approximate 15 km distance between NTUA and EMY. The mean difference between WRF model-simulated PBL height at EMY and NTUA was 0.56 km for the campaign. The stable nocturnal boundary layer is not evaluated in this work due to a high complete overlap region (700 m) of the lidar instrument.

Over-estimates by the lidar were largest when the daytime (11:00 UTC) PBL height was above 2 km. The performance of PBL height between lidar and radiosoundings would most likely be better with more launches from EKPA (average radiosonde PBL height = 2.29 km, $N = 2$), which has a similar atmospheric background to NTUA. In the following, PBL height retrieved from the lidar are used to evaluate model-simulated PBL height from WRF. Strengths and limitations of the lidar-EKF method are discussed at the end of the section.

Figure 4.9 shows the full diurnal cycle of WRF model-simulated PBL height from the different PBL schemes against the hourly-averaged lidar-estimated PBL height. The hourly standard deviation of lidar-estimated PBL height is represented with error bars computed by the total number of lidar estimates at each synoptic hour. Concerning the campaign average (Fig. 4.9a), the spread among the PBL schemes is quite large, with differences approaching 1.5 km between the lowest (UW \approx 1.25 km) and highest (QNSE \approx 2.75 km) simulated daytime-maximum PBL height. The spread between the schemes is reduced by around 50 % during the nighttime and early morning hours. In addition, PBLHs reproduced with the local UW and QNSE schemes are the lowest and highest, respectively, for all synoptic flow conditions.

The local BouLac scheme follows close to the lidar estimates during the campaign average (Fig. 4.9a) and Continental flows (Fig. 4.9b), while the non-local ACM2 scheme captures the PBL height well during the Etesians (Fig. 4.9c). Lidar-estimated PBL height during Etesians shows a faster growing boundary layer than other synoptic flow types, with an average PBL height already around 1.75 km at 6:00 UTC. The lowest PBLHs observed by the lidar occur during Saharan synoptic flows (Fig. 4.9d), where the daytime maximum struggles to reach around 1.5 km. PBL height calculated from radiosoundings was as low as 0.37 km. Low PBLHs during Saharan events could be caused by negative radiative feedback from the dust aerosols (Pérez et al. 2006b). Between 6:00 UTC and 13:00 UTC the non-local TEMF scheme reproduces the closest heights during Saharan flows.

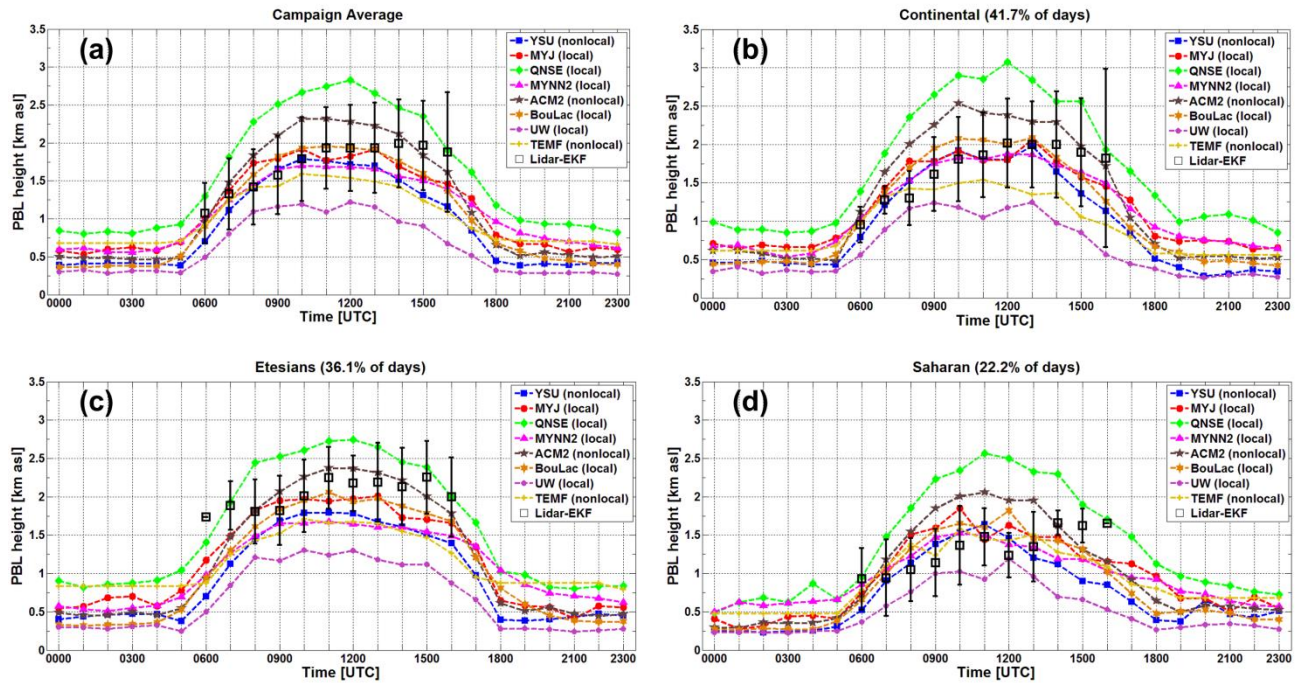


Figure 4.9 Hourly-mean PBL height comparisons between the NTUA lidar (open black squares) and WRF PBL schemes (colored lines) for (a) campaign average, and (b) Continental flow, (c) Etesians flow, and (d) Saharan flow types. PBL height estimated by lidar with extended Kalman filter (EKF) technique.

Table 4.4 shows the performance indicators (MB, STDEV, RMSE, R^2) of PBL height between individual WRF PBL schemes and the estimates from lidar using the EKF method. The performance indicators have been calculated to represent the campaign average ($N = 286$), and the three synoptic flow groupings; Continental ($N = 125$), Etesians ($N = 101$), and Saharan ($N = 60$). Again, considerable differences are evident between model-simulated PBL heights from the PBL schemes.

The determination coefficient (R^2) between model-simulated and lidar-estimated PBL height is practically insignificant for all PBL schemes, with the MYNN2 and ACM2 schemes showing the highest correspondence ($R^2 = 0.15$ for both) to the observed values with the campaign average. The MYNN2 scheme shows slightly better correlations ($R^2 = 0.22$) with the Continental and Saharan synoptic flows. The BouLac scheme follows with the third best correlation ($R^2 = 0.13$) based on campaign totals. The UW and TEMF schemes have the lowest correlations ($R^2 = 0.05$ and 0.09 , respectively) against the lidar-estimated PBL height, consistent in all synoptic flow types and the campaign average.

Table 4.4 Statistics for PBL height showing performance between eight WRF PBL schemes and lidar-EKF estimates. Performance indicators include coefficient of determination (R^2), mean bias (MB), standard deviation (STDEV) and root mean-squared error (RMSE). MB and RMSE are calculated as WRF model – lidar. Statistical sets are grouped according to campaign average (ALL), and three primary synoptic flows. Number (N) of observations are shown in parentheses.

	YSU	MYJ	QNSE	MYNN2	ACM2	BOULAC	UW	TEMF
<i>R²</i>								
ALL (N = 286)	0.09	0.1	0.09	0.15	0.15	0.13	0.05	0.09
Continental (N = 125)	0.08	0.07	0.06	0.22	0.16	0.11	0.02	0.12
Etesians (N = 101)	0.07	0.02	0.05	0.04	0.1	0.1	0.05	0.07
Sahara (N = 60)	0.05	0.13	0.08	0.22	0.13	0.13	0	0
<i>MB</i>								
ALL (N = 286)	-0.30	-0.11	0.58	-0.26	0.18	-0.12	-0.76	-0.42
Continental (N = 125)	-0.20	-0.10	0.72	-0.15	0.30	-0.02	-0.73	-0.40
Etesians (N = 101)	-0.59	-0.30	0.33	-0.59	-0.11	-0.39	-0.97	-0.60
Sahara (N = 60)	-0.02	0.19	0.73	0.07	0.39	0.13	-0.46	0.00
<i>STDEV</i>								
ALL (N = 286)	0.67	0.68	0.75	0.58	0.68	0.64	0.65	0.60
Continental (N = 125)	0.72	0.73	0.81	0.57	0.70	0.68	0.71	0.63
Etesians (N = 101)	0.51	0.56	0.56	0.49	0.55	0.51	0.51	0.47
Sahara (N = 60)	0.66	0.66	0.77	0.46	0.67	0.59	0.60	0.59
<i>RMSE</i>								
ALL (N = 286)	0.74	0.69	0.95	0.63	0.70	0.65	1.00	0.73
Continental (N = 125)	0.74	0.74	1.08	0.59	0.76	0.68	1.02	0.75
Etesians (N = 101)	0.78	0.63	0.65	0.77	0.56	0.64	1.10	0.77
Sahara (N = 60)	0.65	0.68	1.06	0.46	0.77	0.60	0.75	0.58

The MB and RMSE show better results than the goodness of fit approximations for evaluating the schemes. Simulations with the BouLac scheme only slightly under-estimate PBL height (MB = -0.12 km) and RMSE (0.65 km) with the campaign average, in addition to the Continental synoptic flow (MB = -0.02 km, RMSE = 0.68 km). The MYJ scheme shows the lowest MB with the campaign average (-0.11 km), and the second lowest during Continental (-0.10 km) and Etesians (-0.30 km) flows. The ACM2 scheme performs the best

during the Etesians with a slight under-estimate ($MB = -0.11$ km), while the TEMF scheme reproduces the best PBL height during Saharan synoptic flows ($MB \approx 0$ km, $RMSE = 0.58$ km).

A few examples of the lidar-EKF technique are shown in Fig. 4.10 to demonstrate the strengths and limitations of the method for PBL height detection. The corresponding WRF model-simulated PBL height is also shown, for additional analysis of the model results presented earlier in the section. Both the lidar and model results are shown for representative cases of the three synoptic flow types.

First, is a Continental synoptic flow on 25 May 2014 (Fig. 4.10a), a complex case characterized by winds from the north-west. There are a few sharp gradients below 2.5 km and these are probably due to stratification of the mixed aerosol layers. The additional lofted layer between 1.5 and 2 km around 12:00 UTC is coupled with the PBL top, most likely due to hygroscopic growth. From 7:01-9:00 UTC the residual layer from the previous day is still evident (light green shading) between 1 km and 1.5 km. An additional aerosol layer (green and yellow shading) around 3 km altitude at 7:01 UTC slowly descends towards the boundary-layer top during the day, merging into the boundary layer around 11:00 UTC. PBL height estimated with the EKF method is around 0.90 km at 8:00 UTC, growing to 1.83 km by 12:00 UTC. Lidar-EKF PBL height estimates are considered reasonable as they fit the erf-like curve in the individual lidar profiles. However, a narrow transition amplitude was selected to avoid complications from the coupled aerosol layer later in the day. The daily-mean standard deviation ($1-\sigma$) of the hourly lidar retrievals is 19.87 m, indicating reliable hourly estimates.

The lidar-estimated PBL height compares well with model-simulated PBL height from WRF with Continental flow (Fig. 4.10d). All PBL schemes show a MB less than 0.50 km, except for the QNSE and UW schemes. The BouLac and MYJ schemes perform the best with this case, and are similar to the average MB for this synoptic flow.

Second, is the Etesians synoptic flow type (Fig. 4.10b), represented by lidar recorded on 13 June 2014. The lidar-EKF method estimates the highest PBL height of the three synoptic flows, with a daytime-maximum near 2.5 km. However, here we show a case in which the EKF technique fails to estimate the true mixing layer. Instead the lidar estimates are closer to the residual layer. Most likely the mixing layer starts under 0.50 km in the morning, and then grows to around 1.5 km after 12:00 UTC. Over the GAA, the Etesians act as a powerful ventilator, advecting PBL aerosols away from the land and towards the sea. The result is a decreased aerosol load in the PBL. Here, the EKF technique has limitations with the state vector initialization

early in the day, mainly due to the overlap characteristics of the instrument, with a full overlap around 0.7 km.

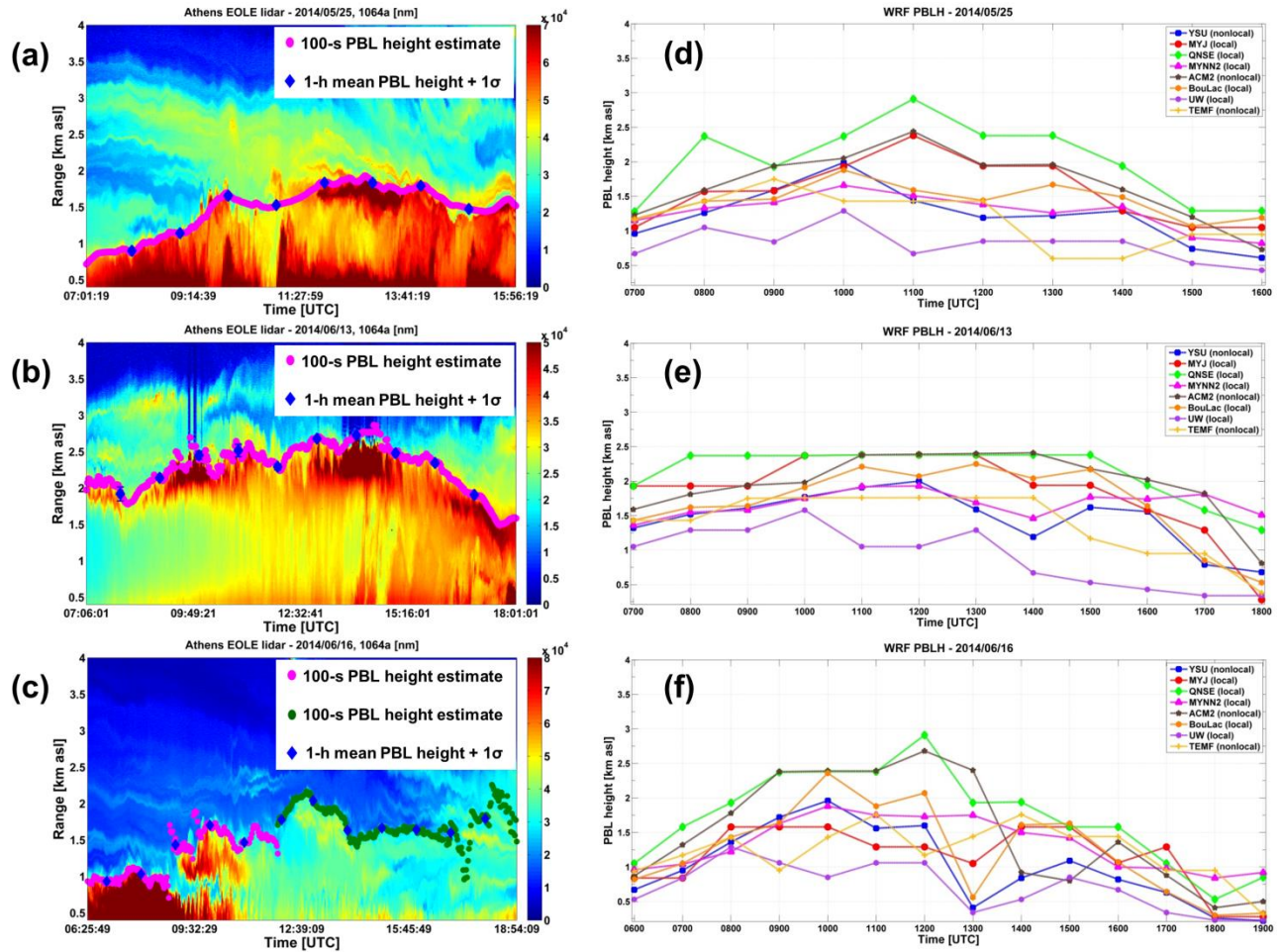


Figure 4.10 Lidar range-corrected power time-range color plots (a-c) at 1064 nm wavelength and simulated PBL height from the WRF model (d-f) for; top row) Continental, middle row) Etesians, and bottom row) Saharan synoptic flow types. Lidar time-range plots are overlaid with PBL height estimates (circles, 100-s resolution) using the extended Kalman filter technique, in addition to the 1-h mean PBL height (blue diamonds) calculated with nine 100-s estimates, along with 1σ standard deviation.

It is shown that WRF model-simulated PBL height (Fig. 4.10e) also has some complications with Etesians synoptic flow. All PBL schemes simulate the residual layer in the morning, with the UW scheme following the lowest PBL around 1 km. In contrast with the previous section, the ACM2 and MYJ schemes are not any closer to the true PBL top as the other schemes.

The third synoptic flow type (Fig. 4.10c) is Saharan (16 June 2014), and we observe the lowest PBL height of all the days during the campaign. Daytime-maximum PBL height estimated by the lidar-EKF is around 1.75 km. In this case we had to initialize the EKF a second time (green dots) around 12:30 UTC as the aerosol signature was too low to follow the initial trajectory. The concentration of aerosols may be low, even though mixing is occurring up to 2 km. We follow the mixing layer correctly until around 11:00 UTC, then the EKF method fails by jumping to the higher aerosol gradient.

Most of the PBL schemes from the WRF model appear to follow the PBL height closely with this case of Saharan synoptic flow. The WRF model results confirm the incorrect lidar estimates beginning in the afternoon hours. The TEMF scheme simulates the best PBL height values, similar to the synoptic flow average presented earlier.

In summary, the lidar-EKF technique is a useful tool for PBL height detection from lidar. However, the method has limitations in certain situations, including Etesians and Saharan synoptic flow types. WRF model-simulated PBL height during the three synoptic flows shows similar results to the averages, except in the case of Etesians flows. During this flow, both the lidar-estimated and WRF model-simulated PBL height are closer to the residual layer.

4.3.3 Impact of PBL schemes on vertical profiles

Daytime boundary-layer vertical profiles at EMY are compared with WRF model-simulated potential temperature (θ in K), water vapour mixing ratio (q_v in g kg^{-1}), and wind speed (WS in m s^{-1}) in Fig. 4.11. Vertical profiles from the WRF model are selected to the closest hour of each radiosounding launch time. Representative cases are shown for Continental (Fig. 4.11a-c), Etesians (Fig. 4.11d-f), and Saharan (Fig. 4.11g-i) synoptic flow types.

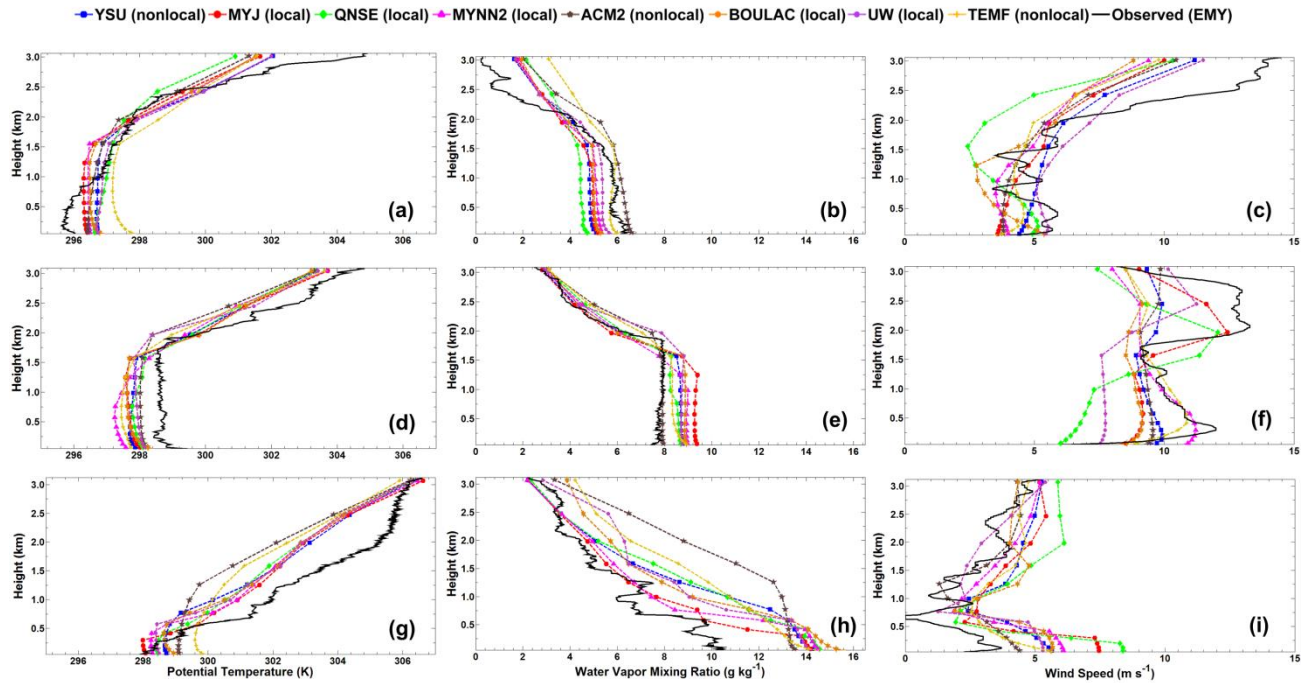


Figure 4.11 Representative vertical profiles comparison of WRF model-simulated potential temperature (K), water vapor mixing ratio (g kg^{-1}), and wind speed (m s^{-1}) versus radiosonde launches at EMY (37.88N, 23.73E, 10 m asl). One set of profiles for (a-c) Continental (2 June 2014), (d-f) Etesians (22 May 2014), and (g-i) Saharan (16 June 2014) synoptic flow types.

First, vertical profiles of Continental synoptic flow are represented by 2 June 2014 launched at 11:16 UTC (Fig. 4.11a-c). On this day the radiosonde-estimated PBL height is 1.82 km from the Richardson bulk method. Below 1 km all PBL schemes over-predict θ with the TEMF scheme showing the largest deviation (1 – 2 K) from the observed through the whole boundary layer. On the other hand, TEMF reproduces q_v closest to the observed values. ACM2 also performs well with only a small moist bias, less than 1 g kg^{-1} through the PBL. Other PBL schemes simulate a drier PBL ($\approx 1 - 2 \text{ g kg}^{-1}$). The model spread is rather large with the vertical profiles of WS, with no scheme able to capture the detailed structure shown with the radiosonde profile. However, the YSU and UW schemes follow the general pattern of the WS profile.

Next, are comparisons of vertical profiles for the Etesians synoptic flow, most representative on 22 May 2014 with a launch time at 11:20 UTC (Fig. 4.11d-f). For this day we estimate the PBL height is 2.12 km from the radiosounding. WRF model-simulated values of θ show a cold bias in the PBL ($\approx 1 \text{ K}$). Above the PBL, the MYJ and BouLac schemes perform best compared with the radiosounding. MYJ also reproduces q_v well, but only above the PBL. In the boundary layer ACM2 simulates q_v closest to the observed values. With respect to

WS, the MYNN2 and TEMF schemes are best reproduced in the PBL, while UW and MYJ simulate accurately the WS above the PBL.

Finally, vertical soundings representing Saharan synoptic flow types are shown by a 11:07 UTC launch on 16 June 2014 (Fig. 4.11g-i). Radiosonde-estimated PBL height is 1.19 km on this day. The largest spread among the PBL schemes is in the lowest 0.5 km. Again, the MYJ scheme simulates θ well, but still with a slight cold bias (1 – 2 K) compared to the sounding. Also, MYJ and MYNN2 reproduce q_v values closest to the observations above the PBL. Below 1 km all PBL schemes simulate too moist (4 – 6 g kg⁻¹). WRF over-predicts the WS in the boundary layer, then the UW and ACM2 schemes follow the structure well above the PBL.

In summary, we have shown a cold, moist bias with WRF model-simulated vertical profiles of potential temperature and water vapor mixing ratio during Etesians and Saharan flows, with the closest simulated values by the MYJ scheme. However, during Continental flow we found a slightly warm and dry bias with the WRF model, with the TEMF and ACM2 schemes showing the best results. With respect to wind speed profiles, it is more difficult to reproduce the detailed structure of the radiosoundings, with large spread among the various schemes. The closest simulated wind speed was found with the YSU scheme during Continental and Etesians flows, while the UW and ACM2 schemes work best in Saharan flows.

4.3.4 Sensible heat flux comparison

Comparisons of model PBL schemes are not meaningful unless the model-simulated surface heat fluxes are examined. Surface meteorological variables are very sensitive to the model surface-layer schemes, which provide surface fluxes of heat and moisture to the PBL schemes. Without a proper investigation of the surface heat fluxes it is difficult to ascertain whether model performance is due to the impact of the PBL scheme or the surface-layer physics.

We show the diurnal cycle of surface sensible heat flux (W m⁻²) simulated by the WRF model at the coastal station, Anavyssos, and the inland station, Peristeri (Fig. 4.12). We use the same representative simulation days as in Sec. 4.3.3 to evaluate the surface heat fluxes for Continental, Etesians, and Saharan synoptic flow types.

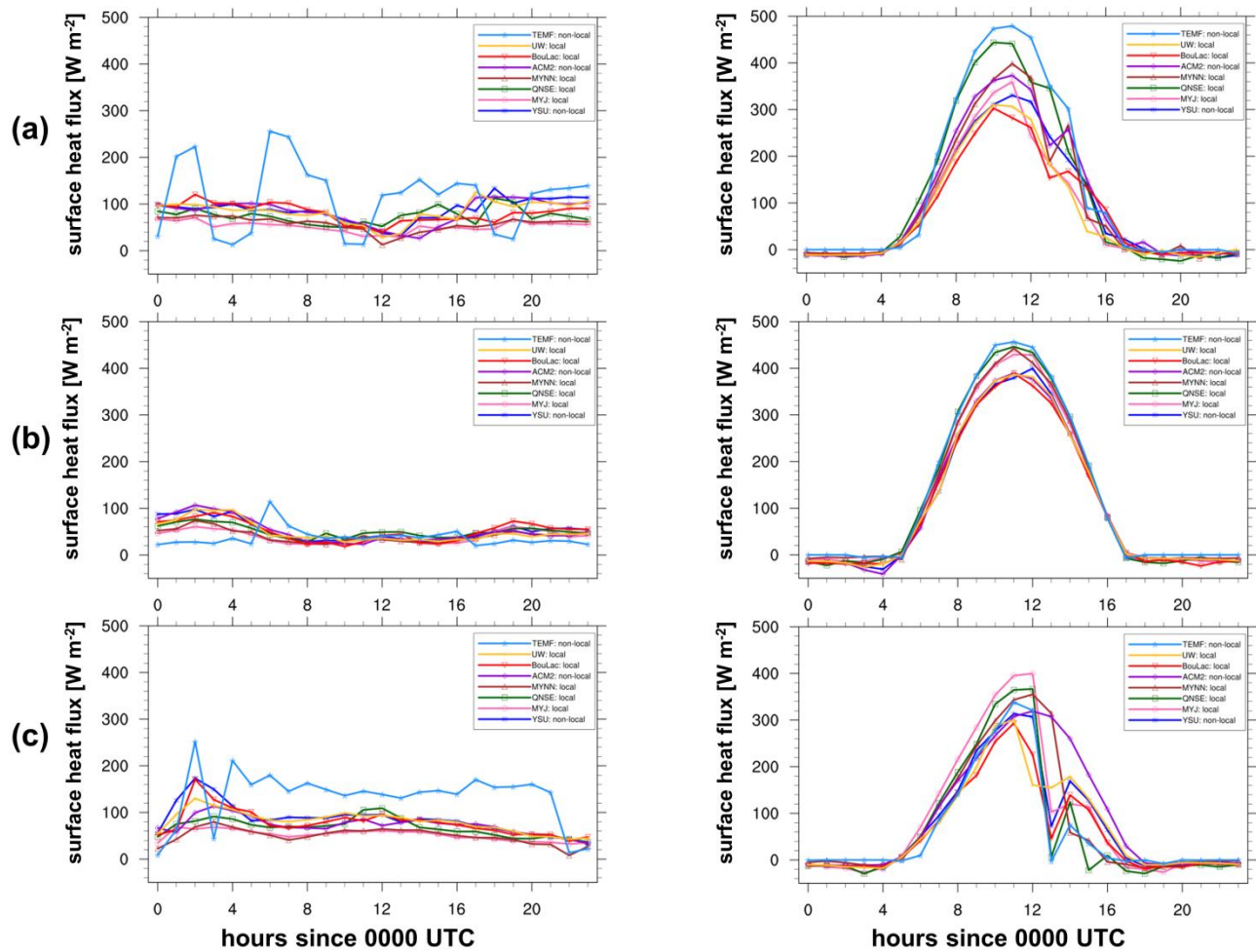


Figure 4.12 Model surface sensible heat flux ($W m^{-2}$) simulated with eight WRF PBL schemes at Anavysos (column 1) and Peristeri (column 2) stations for representative synoptic flows (rows): (a) Continental (2 June 2014), (b) Etesians (22 May 2014), and (c) Saharan (16 June 2014) synoptic flow types.

Noticeably unique patterns of the diurnal cycle are observed between the coastal and inland locations. Peristeri exhibits a classic diurnal cycle in all synoptic flow types with large daytime surface heat flux values ($>250 W m^{-2}$), while Anavysos shows a nearly constant cycle below $100 W m^{-2}$, most likely due to its moderating location near the water. Lower daytime-maximum surface heat fluxes are simulated at Peristeri during Saharan synoptic flows, which is probably a result of increased aerosols in the PBL. The increased aerosol load acts as a limiter to the amount of solar radiation which reaches the boundary layer. A drastic drop-off in surface heat fluxes at Peristeri is noted starting around 13:00 UTC in Saharan flow.

All PBL schemes simulate similar surface heat fluxes at both locations during nighttime and the early morning hours. The largest spread between the PBL schemes is seen at Peristeri during daytime in Continental synoptic flow. The PBL schemes tied to the MM5 surface-layer scheme are grouped similarly, with the lowest model-simulated values of all schemes. The three PBL schemes (QNSE, MYNN2, TEMF) that use unique surface-layer schemes simulate the highest surface heat fluxes. It is unknown what causes the large deviation in model-simulated surface heat fluxes using the TEMF scheme at Anavyssos. In summary, it is found that WRF model-simulated surface heat fluxes are more dependent on the land surface and surface-layer schemes than PBL schemes, and should be subject to further investigation against observations.

4.4 Comparison to previous studies

The WRF results presented here show some similarities to previous works evaluating model PBL schemes in complex urban areas. Past evaluations have been performed with the WRF model (Kleczek et al., 2014; Banks et al., 2015) and the legacy MM5 model (Tombrou et al., 2007; Bossioli et al., 2009).

An earlier study by Bossioli et al. (2009) analysed four PBL schemes implemented in the MM5 model over the GAA during typical summer and winter conditions. The schemes were two non-local (Blackadar and Pleim-Xiu), one semi-non-local (Medium Range Forecast; MRF), and one local scheme (Gayno-Seaman). They reported that the non-local Pleim-Xiu (PX) scheme reproduces the mean observed surface values at all stations analysed. The ACM2 scheme, which is an improved version of PX, also is favoured in our study for campaign average and Continental flow types. The enhanced turbulence of the non-local scheme is attributed to the better performance of its peers.

Tombrou et al. (2007) also used the MM5 model to evaluate simulated PBL height over the GAA. They used the same four PBL schemes as in Bossioli et al. (2009) for two different simulation days in September, 1994 and 2002, in concert with the ICAROS-NET and MEDCAPHOT-TRACE field campaigns, respectively. It was found that the non-local schemes generally provide higher values of the PBL height during the daytime, which is similar to our WRF model-simulated PBL height with the ACM2 scheme.

In addition, Banks et al. (2015) investigated the performance of eight PBL schemes from WRF version 3.4.1 over the complex urban area of Barcelona, Spain. The GAA and Barcelona can be characterised with similar atmospheric conditions (complex topography, sea breeze influences, etc). WRF model-simulated PBL height was validated against estimates from a lidar as in the current study. It was determined that the ACM2 scheme

most well-reproduced the PBL height at 12:00 UTC, with a slight under-estimate of 0.01 km. Similar to the findings of this contribution, the BouLac scheme also performed well in Barcelona with a mean error around -0.35 km.

Simulated vertical profiles of meteorological parameters show some agreements to those found in Kleczek et al. (2014) during the GABLS3 (GEWEX Atmospheric Boundary-Layer Study) campaign in Cabauw, The Netherlands. They analysed the performance of six PBL schemes in WRF version 3.4.1 against observations from a meteorological tower and radiosondes. They found that all model simulations show a similar structure for θ and q_v , with a consistent cold (≈ 2 K) and moist (up to 4 g kg^{-1}) bias in the upper PBL. This is similar to our results where the cold, moist bias is evident with Etesians and Saharan synoptic flows, and in turn, we find a slight warm, dry bias in the PBL during Continental flows.

However, we must be careful when comparing studies between the GAA and Cabauw. One must also take into consideration the contrasting atmospheric situations prevalent between a coastal Mediterranean site like the GAA, and a continental European site such as Cabauw, which can lead to significant differences in model performance. Model physics is sensitive to topographic differences, land-sea exchange, and latitudinal changes in the atmospheric radiation, just to name a few.

WRF model-simulated surface heat fluxes shown by Madala et al. (2015) over eastern India show similar findings to those presented in Sect. 4.3.4 with regards to model-simulated surface heat fluxes. They found that all PBL schemes tested could capture nighttime-minimum values well, but significant differences were found in the daytime-maximum surface heat fluxes. We found similar differences, especially with the model-simulated surface heat fluxes at Peristeri during Continental synoptic flows, grouped closely to the corresponding surface-layer schemes. Madala et al. (2015) determined the ACM2 and MYNN2 schemes performed better than other schemes when compared with observations from a fast response sonic anemometer paired to an eddy correlation technique.

4.5 Conclusions

In this chapter we evaluated the sensitivity of planetary boundary-layer (PBL) variables to various PBL parameterization schemes available in the Weather Research and Forecasting (WRF) numerical weather prediction model. The study used data we collected during the HygrA-CD (Hygroscopic Aerosols to Cloud Droplets) experimental campaign, which took place from mid-May to mid-June 2014 over the complex, urban terrain of the Greater Athens Area (GAA). Proper representation of the PBL from meteorological models is a necessary component in air quality forecast systems. We have shown the WRF model can be a valuable source for this information, however is dependent on several factors.

The PBL schemes were evaluated under diverse synoptic flow types identified with two-day backtrajectories from the FLEXPART-WRF dispersion model. Three typical atmospheric flow types were observed during the 39-day campaign: Continental, Etesians, and Saharan, which represented 41.7 %, 36.1 %, and 22.2 % of the days, respectively.

Eight PBL schemes (5 local, 3 non-local) from WRF-ARW version 3.4.1 were tested using daily simulations on a 1 km x 1 km grid over the GAA with hourly output resolution. Near-surface observations of 2-m air temperature (T2) and relative humidity (RH2), and 10-m wind speed (WS10) were collected from surface meteorological instruments at multiple locations. Estimates of the PBL height are retrieved using elastic-channel (1064-nm) backscatter measurements from a multiwavelength Raman lidar using an adaptive extended Kalman filter technique. In addition, vertical profiles of atmospheric variables are obtained from radiosonde launches. The PBL height is estimated from the radiosoundings using a bulk Richardson number approach. It is found that daytime maximum PBL heights ranged from 2.57 km during Etesian flows, to as low as 0.37 km attributed with Saharan dust episodes. Lidar-estimated PBL height compared relatively well to the radiosoundings.

WRF model simulations yield drastically different solutions depending upon the PBL scheme used, the meteorological parameter analyzed, and the general synoptic conditions. The largest differences between model and observations are associated with simulated values of the PBL height (> 400 m on average) during Saharan dust events.

The largest spread between the lowest and highest WRF model-simulated PBL height was shown to be as high as 1.5 km. It is shown that there are influences from the underlying synoptic conditions. The local BouLac scheme reproduced PBL height well with the campaign average and Continental synoptic flows, with

slight under-estimates. ACM2, a non-local scheme, is a top performer during the Etesians synoptic flow, while the TEMF scheme is best during Saharan synoptic flow.

Campaign-averaged near-surface variables showed that the WRF model tended to have a systematic cold, moist bias during daytime, most prominent at the coastal locations. The BouLac scheme reproduced T2 and RH2 well with the campaign average, and with Etesians synoptic flow. ACM2 showed the closest T2 and RH2 during Continental flows. With Saharan synoptic flows, the UW and BouLac schemes well-represented T2, while TEMF best-reproduced RH2. WRF with the YSU scheme showed the closest WS10 to the observed values with the campaign average, and during Continental and Etesian synoptic flows. The BouLac scheme only slightly outperformed YSU during Saharan events.

WRF model-simulated vertical profiles of θ mostly show an across-the-board cold, moist bias, except a slightly warm and dry bias in Continental flow. The MYJ scheme simulated the closest θ and q_v during Etesians and Saharan synoptic flows. Vertical soundings of simulated WS have a difficult time reproducing the detailed structure of the radiosoundings, with large spread among PBL schemes. The YSU scheme reproduces the closest WS with Continental and Etesians flows, while the UW and ACM2 schemes work best in Saharan flows.

Future work should further address the physical explanations of the numerous differences between the WRF PBL schemes in greater detail. Use of the urban parameterization option in WRF should be explored. In addition, the study areas should be expanded to include more experimental sites and complex locations, but also areas with a more stable atmospheric regime. Additional measurements for a future study include flux measurements from a meteorological tower, more frequent upper-air soundings, and continuous nighttime backscatter measurements from a ceilometer to analyze the nocturnal boundary layer.



Chapter 5

5 Impact of WRF model PBL schemes on air quality simulations over Catalonia, Spain

The aim of this chapter is to evaluate the impact of four planetary boundary layer (PBL) parametrization schemes (two local, two non-local) from the Weather Research and Forecasting (WRF) mesoscale model on simulations of meteorological variables and predicted pollutant concentrations from an air quality forecast system. CALIOPE, the Spanish operational air quality forecast system, is composed of the WRF-ARW V3.5.1 meteorological model, HERMES v2 emissions model, CMAQ V5.0.2 chemical transport model, and dust outputs from BSC-DREAM8bv2. The area of interest is the Catalonia region located in the northeast Iberian Peninsula, which is characterized by complex mesoscale interactions between the Western Mediterranean basin and the nearby orography. Performance of the non-local schemes, Yonsei University and Asymmetric Convective Model Version 2, and the local schemes, Mellor-Yamada-Janjic and Bougeault-Lacarrère are evaluated. The simulated diagnostic case study is selected to represent the most frequent synoptic condition in the northeast Iberian Peninsula during spring 2015, chosen using information from a cluster analysis of back-trajectories covering a 16-yr period, in addition to satellite images, lidar observations, data from air quality stations, and nearby radiosoundings. Over one-third of spring 2015 days were controlled by regional recirculations arriving at 1.5 km altitude. Model-simulated pollutant concentrations are evaluated against network urban, suburban, and rural background stations. In addition, we use METAR surface meteorological observations and vertical profiles from radiosoundings for evaluation of the WRF simulations. Daytime WRF model-simulated PBL heights are validated against estimates retrieved using a micro-pulse lidar system. It is generally determined that a non-local PBL scheme performs well with PBL height and winds, while a local

scheme is better suited for surface air and dew point temperature. Results are ambiguous with the impact of PBL schemes on model-simulated pollutant concentrations.

The contents presented in this chapter have been submitted to the journal, *Atmospheric Chemistry and Physics*, and is made available here as copy with the permission of *Atmos. Chem. Phys.* Systematic or multiple reproduction or distribution to multiple locations via electronic or other means is prohibited and is subject to penalties under law.

5.1 Introduction

Air quality (AQ) is of major concern worldwide for various environmental and human health effects. According to the European Environmental Agency (EEA) (Guerreiro et al., 2012) air pollutant concentrations are still too high and harm our health and the ecosystems we depend on. The EEA went on to mention that a significant proportion of Europe's population lives in areas, especially large cities, where air quality standards are routinely exceeded.

AQ forecast systems (AQFS) can be useful tools for simulating the coverage and transport of atmospheric pollutants over both global and regional unified domains. The link between emissions and ambient concentrations can only become evident and fully understood by means of air quality modeling since ground-based stations are single point. Zhang et al. (2012) reviewed the history, techniques, and state of the science of AQFS. They found that the biggest improvement in the field of AQFS is the addition of online coupling of meteorological models and chemistry models.

Numerous global and regional AQFS exist throughout Europe. Examples of global AQFS include the online LMDzt-INCA (Hauglustaine et al., 2004; Folberth et al., 2006) operated by France and ECHAM5 (Roeckner et al., 2006; Zhang et al., 2010) maintained in Germany. Regional AQFS include CHIMERE (Rouil et al., 2009) managed in France, and the CALIOPE AQFS (Baldasano et al., 2008), operated by the Barcelona Supercomputing Center (BSC-CNS) in Spain.

Boundary layer and land surface interactions have serious implications to AQFS simulations. It's well known that treatment of planetary boundary layer (PBL) processes in meteorological models have direct impacts on predicting the dynamics of pollutants (Pérez et al., 2006a; Cuchiara et al., 2014). In an AQFS a few of the most important PBL variables for reliable simulations are the PBL height, wind speed and direction,

temperature, and moisture. Numerical weather prediction models rely on parameterization schemes to characterize processes in the PBL.

Past works have utilized PBL parameterization schemes in the legacy fifth generation mesoscale model (MM5) to evaluate sensitivity in AQ simulations (Mao et al., 2006; Pérez et al., 2006a; Bossioli et al., 2009; Kim et al., 2010). Mao et al. (2006) compared five PBL schemes from the MM5 model over the Central and Eastern United States to evaluate the sensitivity to model simulations of primary pollutant concentrations from the Community Multiscale Air Quality (CMAQ) model. Two 37-day periods were simulated in summer and winter, including a seven day spin-up period. Outputs from the CMAQ model were compared with hourly observations from 2,217 AQ sites and the meteorological variables from MM5 were compared with surface and 850-hPa measurements from 50 surface sites and 21 upper-air sites. They discovered the largest sensitivity to various schemes was found with the PBL height. The Pleim-Xiu PBL scheme was on order of 800 m higher than other schemes in summer and 350 m higher in winter. This translated into AQ differences at the urban scale, with greater than 5% differences in maximum concentration of surface ozone (O_3) and particulate matter less than 2.5 μm ($PM_{2.5}$).

Similar results were found by Pérez et al. (2006a), where they compared three PBL schemes from the MM5 model over summertime in the Barcelona area. Meteorological outputs from the MM5 model were compared with lidar and radiosoundings measurements, while outputs from the AQFS simulations were compared with hourly observations from AQ sites, however averaged over the entire domain. They discovered that 1-hr daily maximum O_3 and carbon monoxide (CO) concentrations vary in magnitude and location depending on the PBL scheme chosen. In their comparisons the O_3 bias was negative for all schemes, with a bias ranging from -9.1% to -14.8%. The Gayno-Seaman scheme was determined to provide the least error and lowest bias among the three compared schemes.

More recent studies have focused on the evaluation of PBL schemes in the Weather Research and Forecasting (WRF) model (Misenis and Zhang, 2010; Gan et al., 2011; Cheng et al., 2012). In Misenis and Zhang (2010) two PBL schemes; Mellor-Yamada-Janjic (MYJ) and Yonsei University (YSU), in the WRF model were compared over the Houston, Texas area for a five-day summer episode. AQ outputs were compared with hourly measurements from AQ stations and aircraft. They found 20-40% lower PBL heights with the MYJ scheme than the YSU scheme, which resulted in higher levels of CO, O_3 , and $PM_{2.5}$. This was a similar finding to a study by Bossioli et al. (2009) over Athens, Greece, where PBL height predictions had 13% differences during the afternoon hours.

Another study which investigated the effects of AQ simulations to the YSU and MYJ schemes was Cheng et al. (2012). Their efforts were focused on the Taiwan area during two very different atmospheric cases in springtime; long-range transport of pollutants from a cold frontal passage and a local land-seabreeze regime. In the case of the cold frontal passage they discovered differences up to 25 ppb in O₃ concentration near the front with the simulation using the YSU scheme higher than the MYJ scheme. They attributed this difference to higher PBL heights diagnosed by the YSU scheme. In the case of local land-seabreeze effects they found that during the daytime the YSU scheme predicts a stronger seabreeze than the MYJ scheme which is more capable of carrying aged species back to land (on the order > 20 ppb).

The main objective of this chapter is to evaluate four PBL schemes from the WRF model and the impacts to AQ outputs in the Spanish CALIOPE AQFS. Three PBL schemes are compared to the current PBL scheme used in the operational AQFS. The chapter is organized as follows. In Sect. 5.2 we describe the selected case study and the models and instruments used for the evaluation. The results of the comparison between models and observations are presented in Sect. 5.3. Finally, main conclusions are summarized in Sect. 5.4.

5.2 Models, case study, and observations

5.2.1 Description of case study

In this study our primary domain of interest is the area of Catalonia, Spain, located in the northeast Iberian Peninsula (IP; Fig. 5.1). The climate of the IP is controlled in part by thermal differences between the Atlantic Ocean to the west and the Mediterranean Sea to the east. The IP is situated between two continents with vastly different climatic conditions. The European continent north of the IP is typically cold and wet, while the African continent to the south is typically warm and dry. Typical synoptic flow patterns form as a result of these climatic differences.

The validation and comparisons presented in this work are based on data from 7 May 2015, with the time period dominated by a regional recirculations synoptic flow regime. Regional recirculations are frequent over the IP, especially in the eastern Mediterranean coast. During the spring of 2015 the phenomenon occurred approximately 33% of the days. The flow type was objectively identified using information from a cluster analysis of back-trajectories covering a 16-yr period, in addition to satellite images, lidar observations, data from air quality stations, and nearby radiosoundings. Figure 5.1a shows a two-day back-trajectory analysis from the NOAA Hybrid Single Particle Lagrangian Integrated Trajectory (HYSPLIT) model (Draxler and

Rolph, 2013). A pattern of regional recirculations is clearly evident for back-trajectories arriving at 0.5 (red) and 1.5 (blue) km altitudes, with endpoint of Barcelona. The back-trajectory arriving at 3 km altitude (green) shows wind flow from the south-west, indicative of the main synoptic flow in the free troposphere.

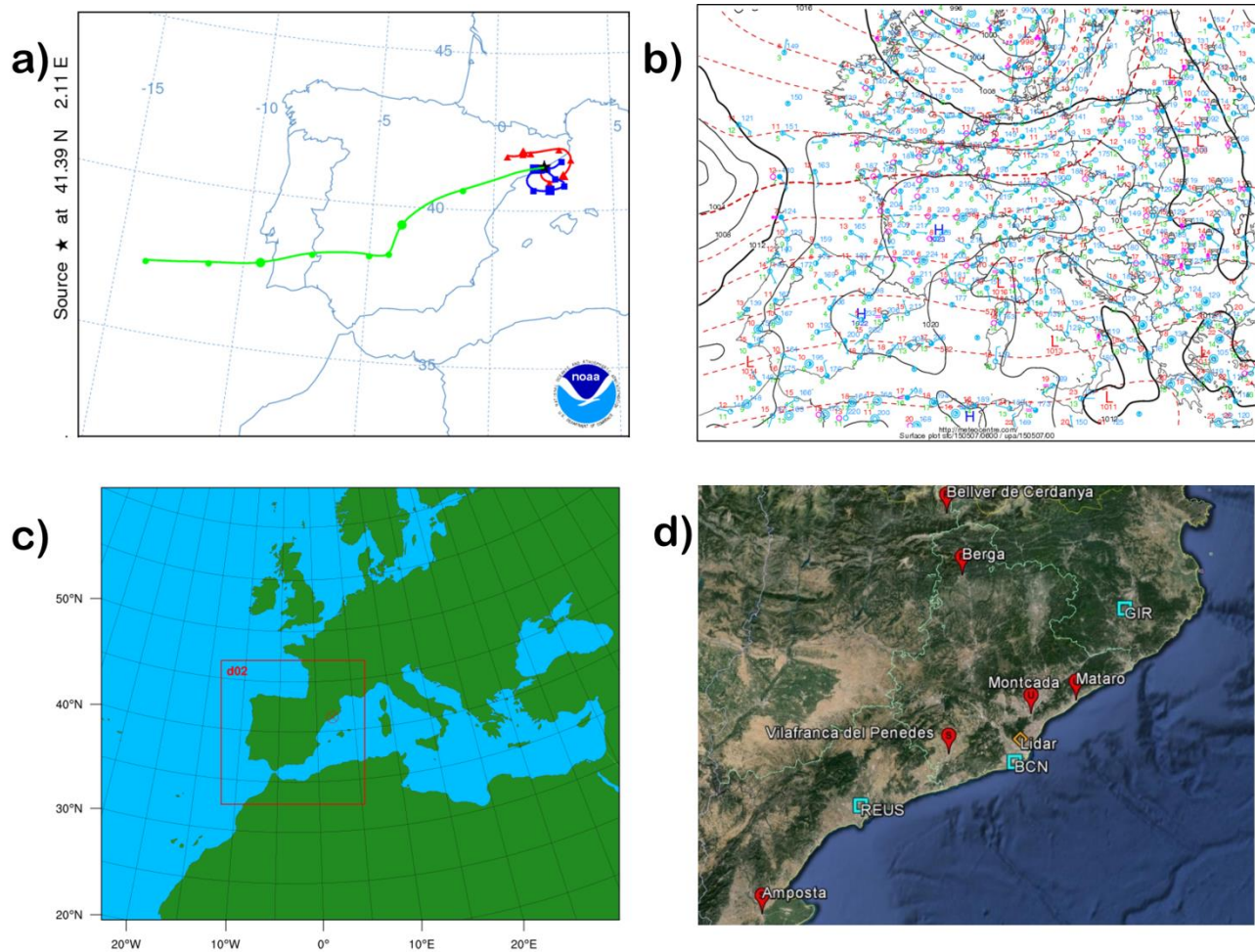


Figure 5.1 a) Two-day back-trajectory analysis ending at Barcelona on 7 May 2015 (12:00 UTC) at three arriving altitudes (0.5, 1.5, and 3 km). b) Surface analysis from 6:00 UTC on 7 May 2015, including mean sea-level pressure (hPa; solid black lines), 500-hPa geopotential heights (dashed red lines), and station observations. c) two one-way nested domains for the WRF and CALIOPE AQFS at the European level (12 × 12 km), and Iberian Peninsula (4 × 4 km). d) locations of METAR (blue boxes), lidar/radiosonde (orange diamond), and air quality measurement (red circles) stations.

Regional recirculations (Baldasano et al., 1994; Jiménez and Baldasano, 2004) of air pollutants are typical in the summertime over the IP, but also can occur any other time during the year. Regional recirculations are generally accompanied by an absence of large-scale forcing and the pattern is dominated by mesoscale circulations, which are controlled mainly by diurnal convective heating of the atmosphere. A surface analysis of mean sea-level pressure and geopotential height at 500-hPa (Fig. 5.1b) at 6:00 UTC on 7 May 2015 confirms the pattern. A high pressure ridge extends south-west over north-east Spain, with light winds observed at surface stations. With this pattern the interactions between strong compensatory subsidence over the western IP and sea-land breeze dynamics are attributed to the recirculation and accumulation of pollutants.

5.2.2 Modelling strategy

Two domains (Fig. 5.1c) were configured with varying horizontal grid spacing for the CMAQ and WRF modules of the AQFS, which include the parent European level (12×12 km; 481×401 grid points), and an one-way nested domain for the IP (4×4 km; 399×399 grid points). It is assumed that 4×4 km grid spacing is of fine enough detail to resolve most mesoscale features in the complex study area (Pay et al., 2014; Schaap et al., 2015). Pay et al. (2014) found the forecast skill between 4 km and 1 km grid spacing was not a large improvement.

The CALIOPE AQFS (Baldasano et al., 2008; www.bsc.es/caliope), is a state-of-the-art, high-resolution operational AQFS developed in the Earth Sciences Dept. at the Barcelona Supercomputing Center - Centro Nacional de Supercomputación (BSC-CNS). The original concept of CALIOPE AQFS for the Iberian Peninsula domain (4×4 km grid spacing) was funded by the Spanish Ministry of the Environment to establish an AQ forecasting system to increase the knowledge on transport and dynamics of pollutants in Spain. Since 2008, the AQ group at BSC-CNS has added and evaluated domains for Europe (12×12 km grid spacing), and for multiple regional domains ($1 \text{ km} \times 1 \text{ km}$ grid spacing). The system provides operational forecasts out to 24-hr and 48-hr depending on the domain, with a temporal resolution of 1-hr.

The system has been evaluated in several past studies for the European domain (Pay et al., 2010, 2012a; Basart et al., 2012), the Spanish domain (Baldasano et al., 2011, 2008; Pay et al., 2011, 2012, 2014; Sicardi et al., 2012), and the Barcelona and Madrid domains (Goncalves et al., 2009; Soret et al., 2011). However, the

CALIOPE AQFS hasn't been evaluated for sensitivities to the various PBL schemes available in the WRF meteorological model.

The CALIOPE AQFS is constructed of four main model components. The components consist of a meteorological model (WRF-ARW v3.5.1), an emissions inventory model (HERMES v2), a chemical transport model (CMAQ v5.0.2), and a second generation mineral dust transport model (BSC-DREAM8b v2). Aerosols are estimated from CMAQ and BSC-DREAM8b. More information about the individual components of the CALIOPE AQFS can be found online (www.bsc.es/caliope).

For the evaluation we use hourly model outputs of surface ozone (O_3), nitrogen dioxide (NO_2), and particulate matter less than $10 \mu m$ (PM_{10}) from the CALIOPE-CMAQ simulations.

In this study we use WRF version 3.5.1 with the Advanced Research WRF (ARW) dynamical solver (Skamarock et al., 2005). WRF v3.5.1 is the current version used in the operational CALIOPE AQFS. Initial and lateral boundary conditions are determined using gridded Global Forecasting System (GFS) analysis data from the National Centers for Environmental Prediction (NCEP), which are operational global analysis data available on $0.25^\circ \times 0.25^\circ$ grids at six-hourly time steps. The analyses are available from the surface and at 26 mandatory pressure levels from 1000 hPa to 10 hPa.

WRF-ARW simulations were computed with a 36-h forecast cycle, including 12 h allotted for model spin-up time. Each day's simulation was initialized from 12:00 UTC the previous day. The spin-up cycle is added to counter instability issues within the simulation and the first 12-h of each forecast cycle is not included in the evaluation process. An output temporal resolution of 1-h was chosen for comparison with observations. The model was run with 38 terrain-following (ETA) vertical levels, of which 13 are located in the lowest 3 km of the atmosphere, with a model top set at 50-hPa.

The HERMES emission model requires 48-h of previous meteorological fields from the date of interest. For our diagnostic case we have run the WRF model for 5-7 May 2015.

The physics options selected include WRF single-moment 3-class microphysics (Hong et al., 2004), Kain-Fritsch cumulus parametrization (Kain, 2004), Dudhia shortwave radiation (Dudhia, 1989), rapid radiative transfer model longwave radiation (Mlawer et al., 1997), and the Noah land-surface model (Tewari et al., 2004). An urban parameterization was tested, with similar results to those without an urban parameterization. More information about these physics options can be found in (Skamarock and Klemp, 2008).

In version 3.5.1 of WRF-ARW there is the option to choose from 11 PBL schemes. Each PBL scheme is associated with one or more surface-layer schemes which provide the surface fluxes of momentum, moisture, and heat to the PBL scheme. An overview of the four PBL schemes selected for this study is shown in Table 5.1.

The Yonsei University (YSU) PBL scheme is used in the current version of the operational CALIOPE AQFS, and will be used as the control run. The other three schemes selected showed good performance in a previous performance evaluation (Banks et al., 2015) over Barcelona. Also shown in the table are the associated surface-layer schemes, another important source of error in WRF model simulations. All four PBL schemes are associated with some variation of Monin-Obukhov similarity theory for the surface layer. Other surface layer schemes are not evaluated here.

The PBL parametrization schemes selected consist of two local and two non-local closure schemes. The operational definition of PBL height in the individual schemes falls into one of two general classes. The first class calculates the PBL height using the Richardson bulk number (Ri_b) method from some predetermined starting level. The second class determine the PBL height at a level where the turbulent kinetic energy (TKE) profile decreases to some predefined threshold value.

The first and most widely-used PBL scheme is the YSU scheme (Hong et al., 2006). The YSU scheme is a first order, non-local scheme with an explicit entrainment layer and a parabolic K-profile in an unstable mixed layer. It's a modified version of the Medium Range Forecast (MRF) scheme (Hong and Pan, 1996) from the MM5 model (Dudhia, 1993). The largest improvement to the YSU scheme over the MRF scheme was the addition of an explicit term for the treatment of the entrainment zone. (Hong, 2010) implemented a modification to the scheme for the stable boundary layer. PBL height in the YSU scheme is determined from the Ri_b method, but calculated starting from the surface. A threshold value of zero is used for stable cases, while 0.25 is used for unstable flow.

The second scheme is the Asymmetrical Convective Model version 2 (ACM2) scheme (Pleim, 2007). The ACM2 scheme is a first order, non-local closure scheme and features non-local upward mixing and local downward mixing. It's a modified version of the ACM1 scheme from the MM5 model, which was a derivative of the Blackadar scheme (Blackadar, 1978). The scheme has an eddy-diffusion component in addition to the explicit non-local transport of ACM1. PBL height is determined as the height where the Ri_b calculated above the level of neutral buoyancy exceeds a critical value ($Ri_{bc} = 0.25$). For stable or neutral flows the scheme shuts off non-local transport and uses local closure.

Table 5.1 Four WRF PBL schemes evaluated in this study, including long name, turbulent kinetic energy closure type, associated surface layer scheme, and operational method and threshold value for diagnosing PBL height

	YSU	ACM2	MYNN2	BouLac
Long name	Yonsei University	Asymmetric Convective Model v2	Mellor-Yamada-Nakanishi-Niino level 2.5	Bougeault-Lacarrère
Closure	1.0 non-local	1.0 non-local	1.5 local	1.5 local
Surface layer	Monin-Obukhov	Monin-Obukhov	MYNN	Monin-Obukhov
PBL height method	Ri_b calculated from surface	Ri_b calculated above neutral buoyancy level	TKE-prescribed threshold	TKE-prescribed threshold
Threshold	zero (unstable) 0.25 (stable)	0.25 (all)	$1.0 \times 10^{-6} \text{ m}^2 \text{ s}^{-2}$	$5.0 \times 10^{-3} \text{ m}^2 \text{ s}^{-2}$

The next scheme is the Mellor-Yamada-Nakanishi-Niino Level 2.5 (MYNN2) scheme (Nakanishi and Niino, 2006). The Mellor-Yamada-Nakanishi-Niino Level 3 (MYNN3) scheme shares similar characteristics to MYNN2 so it will not be evaluated here. The MYNN2 scheme is tuned to a database of large eddy simulations (LES) in order to overcome the typical biases associated with other MY-type schemes, such as insufficient growth of convective boundary layer and under-estimated TKE. The MYNN2 scheme is a one-and-a-half order, local closure scheme and predicts sub-grid TKE terms. PBL height is determined as the height at which the TKE falls below a critical value ($1.0 \times 10^{-6} \text{ m}^2 \text{ s}^{-2}$).

The final scheme is the Bougeault-Lacarrère (BouLac) scheme (Bougeault and Lacarrere, 1989). The BouLac scheme is a one-and-a-half order, local closure scheme and has a TKE prediction option designed for use with the BEP (Building Environment Parametrization) multi-layer, urban canopy model (Martilli et al., 2002). BouLac diagnoses PBL height as the height where the prognostic TKE reaches a sufficiently small value (in the current version of WRF is $0.005 \text{ m}^2 \text{ s}^{-2}$).

5.2.3 Evaluation data

In order to validate the model simulations from CALIOPE and WRF we use data from air quality and meteorological stations, micropulse lidar, and radiosoundings. The locations of the stations are shown in Fig. 5.1d.

Previous works (Pay et al., 2014; Schaap et al., 2015) have found that 4 km grid spacing is sufficient resolution for the comparison to observations. We selected a mix of six urban, suburban, and rural background stations (red circles, Fig. 5.1d) for the evaluation of CALIOPE AQFS simulations. Variables compared are hourly surface concentrations of O_3 , NO_2 , and PM_{10} . The evaluation is taken from a statistical perspective, comparing model output to observations, and from a two-dimensional view, evaluating the spatial differences between the YSU scheme (control run) and the three other PBL schemes.

Estimates of the hourly PBL height between 6:00 and 18:00 UTC are determined based on observations from a micropulse lidar (MPL) in Barcelona (orange diamond, Fig. 5.1d). Nighttime and early morning PBL height is not considered due to instrumental limitations (overlap range, etc.). The MPL in Barcelona is a new station of the NASA Micropulse Lidar Network (MPLNET) (Welton et al., 2001). The MPL instrument (Spinhirne et al., 1995) is operated continuously at 532-nm wavelength, using the same telescope construction to transmit an energy pulse and receive the returned backscattered signal. We exploit the lidar data at 15-m range and 1-min temporal resolutions.

The PBL height is estimated from the lidar normalized relative backscatter (NRB) using a time-adaptive extended Kalman filter technique (EKF). The EKF technique was developed and tested by the Remote Sensing Laboratory at the Technical University of Catalonia (Rocadenbosch et al., 1998; 1999). The EKF method has been evaluated by numerous studies, both with experimental and real datasets. (Lange et al., 2014; 2015) tested the technique with experimental lidar simulations and real data over Barcelona. More recently the performance of the EKF method has been evaluated with observational data from Raman lidars at Barcelona (Banks et al., 2014; 2015) and Athens (Banks et al., 2016).

Finally, surface meteorological observations are collected from three area METAR stations (light blue squares, Fig. 5.1d) at Barcelona (41.29°N 2.07°E), Girona (41.91°N 2.76°E), and Reus (41.15°N 1.18°E). We use hourly measurements of 2-m air temperature (T2) and dew point temperature (TD2), along with 10-m zonal (U10) and meridional (V10) wind components to validate simulated values from the WRF model using the four PBL schemes.



For the comparisons of WRF model vertical profiles we use upper-air data from a 12:00 UTC radiosonde launch on 7 May 2015 in Barcelona, nearby to the MPL site. Upper-air variables evaluated include temperature, dew point temperature, and zonal and meridional wind components.

5.3 Results and discussion

In this section we present the results of the comparison for CALIOPE-CMAQ and WRF simulations on 7 May 2015. First, we investigate the WRF model-simulated surface variables using the different WRF PBL schemes. Next, vertical profiles from the WRF model are compared with observations from the nearby radiosonde launch. In the last section we evaluate the photochemical and aerosol outputs from the CMAQ model simulations.

5.3.1 Evaluation of WRF meteorology

Meteorological simulations from the WRF model are an important driver for air quality simulations from the CALIOPE AQFS. We evaluate WRF model-simulated PBL height, along with surface meteorological and upper-air variables.

Typically, one of the largest sources of error in mesoscale model simulations is diagnosis of the PBL height. Figure 5.2a shows 1-min and hourly-averaged PBL heights estimated from the MPL using the EKF technique. The mean PBL height for the day is 0.77 km with a small (0.02 km) standard deviation. Additional aerosol layers are evident between the PBL top and 2.5 km, most likely due to the regional recirculation pattern. Based upon the relatively low error we can use the hourly 15-min-averaged lidar-EKF retrievals to validate PBL heights from the WRF model simulations.

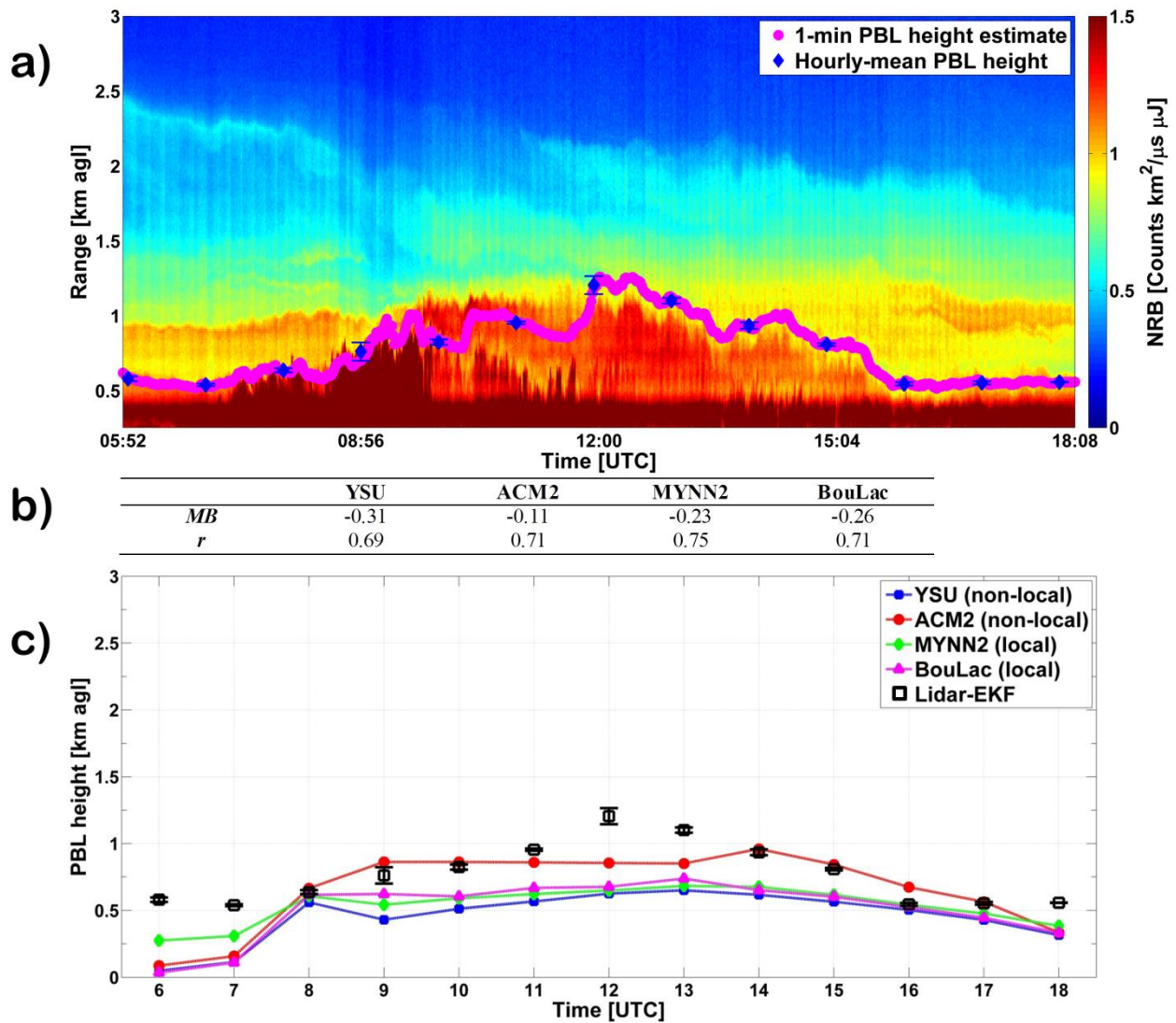


Figure 5.2 a) Time-range series of lidar normalized relative backscatter (NRB), overlaid with 1-min estimates of PBL height (magenta dots) and 15-min hourly-averaged PBL height centred on the synoptic hour (blue diamonds). b) mean bias (*MB*; WRF – lidar) and linear correlation coefficient (*r*) between PBL heights simulated from the WRF model and estimates from the lidar. c) time series on 7 May 2015 of daytime PBL height simulated by the WRF model and 15-min hourly averages (black squares) from the lidar, with 1-σ error bars.

Figure 5.2b,c compare the PBL heights simulated with the WRF model against hourly-averaged estimates from the MPL. It is shown the WRF model systematically under-estimates PBL height, as large as 0.31 km with the YSU scheme. The YSU and MYNN2 schemes diagnosis daytime-maximum PBL heights nearly 50% lower than the lidar. Overall, the ACM2 scheme leads to the lowest bias (*MB* = -0.11 km) and closest daytime-maximum PBL height (0.96 km) compared to the lidar estimate (1.2 km). It should also be noted the

WRF model simulates slow growth of the PBL, with the maximum PBL height delayed around 1 - 2 hours compared with the lidar.

The errors found in WRF model-simulated PBL height are possibly a huge contribution to the CMAQ model-simulated PM_{10} shown later in the chapter.

The 2-m air temperature (T2) and dew point temperature (TD2), and 10-m zonal (U10) and meridional (V10) wind components are also critical variables to simulate accurately to produce accurate air quality model simulations. Table 5.2 presents the mean bias (MB) and correlation coefficient (r) between WRF model-simulated surface meteorology and observations at the three METAR stations in Catalonia. T2 and TD2 are under-estimated by the WRF model with all PBL schemes at Barcelona and Reus, with the best performance from the BouLac scheme ($MB_{T2} = -1.68^{\circ}C$ at Barcelona; $MB_{T2} = -2.34^{\circ}C$ at Reus). A small over-estimate of T2 is simulated by the WRF model at Girona, as low as $0.11^{\circ}C$ with the MYNN2 scheme. The correlation between model and observations is markedly better with T2 ($r = 0.93 - 0.98$) than TD2 ($r = 0.11 - 0.79$).

The diurnal cycle of WRF model-simulated T2 and TD2 against observations from the three METAR stations is shown in Fig. 5.3. It is concluded the daily-mean over-estimate of WRF model-simulated T2 at Girona is in large part due to a significant over-estimate in the morning hours, as high as $2.68^{\circ}C$ at 7:00 UTC with the ACM2 scheme. The MYNN2 scheme provides the lowest bias throughout these morning hours. At Barcelona and Reus, the WRF model under-estimates T2 throughout the diurnal cycle, showing the largest biases in the morning and late evening hours.

The results are more ambiguous with respect to mean bias and correlation between WRF model-simulated U10 and V10 against observations (Table 5.2). The correlation between model and observations is markedly different with U10 ($r = 0.1 - 0.75$) versus V10 ($r = 0.87 - 0.98$), indicating the WRF model can resolve the meridional component of 10m winds more reliably. The WRF model under-estimates U10 and V10 at Barcelona and Reus, no matter what PBL scheme is selected. However, the ACM2 scheme provides WRF model-simulated values closest to the observations, especially with V10 ($MB = -0.64 \text{ m s}^{-1}$ at Barcelona; $MB = -0.22 \text{ m s}^{-1}$ at Reus). Both U10 and V10 are over-estimated at Girona, with the best performance from the WRF model with the YSU scheme ($MB_{U10} = 0.43 \text{ m s}^{-1}$ and $MB_{V10} = 0.39 \text{ m s}^{-1}$).

Table 5.2 Statistics of surface meteorological variables; mean bias (*MB*) and linear correlation coefficient (*r*), between WRF model-simulations and METAR observations at Barcelona, Girona, and Reus. *MB* is calculated as WRF model – observed. Variables included in the analysis are 2-m air (T2) and dew point (TD2) temperature (in °C), and 10-m zonal (U10) and meridional (V10) wind components (in m s⁻¹).

METAR – Barcelona									
	YSU		ACM2		MYNN2		BouLac		
	<i>MB</i>	<i>r</i>	<i>MB</i>	<i>r</i>	<i>MB</i>	<i>r</i>	<i>MB</i>	<i>r</i>	
T2	-1.86	0.93	-1.77	0.94	-1.85	0.94	-1.68	0.95	
TD2	-1.44	0.71	-1.65	0.79	-1.39	0.78	-1.22	0.74	
U10	-1.16	0.58	-1.07	0.57	-0.94	0.71	-0.87	0.63	
V10	-0.79	0.96	-0.64	0.96	-0.72	0.97	-0.71	0.96	

METAR – Girona									
	YSU		ACM2		MYNN2		BouLac		
	<i>MB</i>	<i>r</i>	<i>MB</i>	<i>r</i>	<i>MB</i>	<i>r</i>	<i>MB</i>	<i>r</i>	
T2	0.15	0.98	0.34	0.97	0.11	0.98	0.33	0.98	
TD2	-1.59	0.29	-1.78	0.11	-1.69	0.35	-1.54	0.61	
U10	0.43	0.10	0.65	0.13	0.63	0.23	0.77	0.35	
V10	0.39	0.87	0.62	0.88	0.38	0.87	0.64	0.88	

METAR – Reus									
	YSU		ACM2		MYNN2		BouLac		
	<i>MB</i>	<i>r</i>	<i>MB</i>	<i>r</i>	<i>MB</i>	<i>r</i>	<i>MB</i>	<i>r</i>	
T2	-2.56	0.97	-2.46	0.97	-2.63	0.98	-2.34	0.98	
TD2	-1.38	0.65	-1.57	0.59	-1.26	0.67	-1.21	0.62	
U10	-0.53	0.56	0.05	0.7	-0.17	0.75	-0.3	0.52	
V10	-0.47	0.97	-0.22	0.98	-0.27	0.98	-0.56	0.98	

Finally, Figure 5.4 shows the diurnal cycle of U10 and V10 simulated by the WRF model against observations from the three METAR stations. The daily-mean over-estimate of WRF model-simulated winds at Girona is most attributable to the large deviation from the observations in the evening after 14:00 UTC, highest with model-simulated V10 with the BouLac scheme ($MB = 4.52 \text{ m s}^{-1}$ at 18:00 UTC).

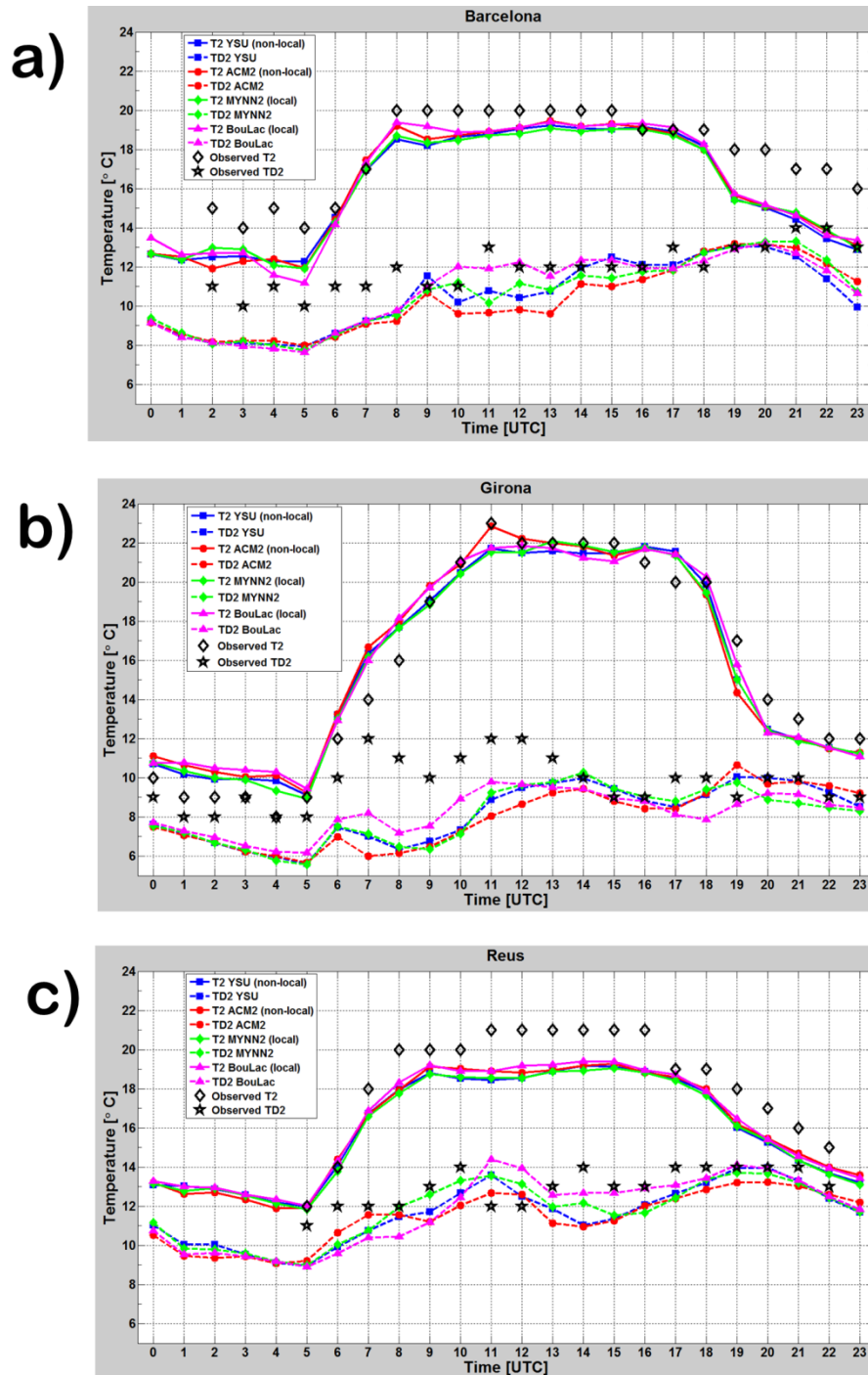


Figure 5.3 Time series on 7 May 2015 of WRF model-simulated 2-m air temperature (T2; solid lines) and dew point temperature (TD2; dashed lines) against METAR observations at a) Barcelona, b) Girona, and c) Reus.

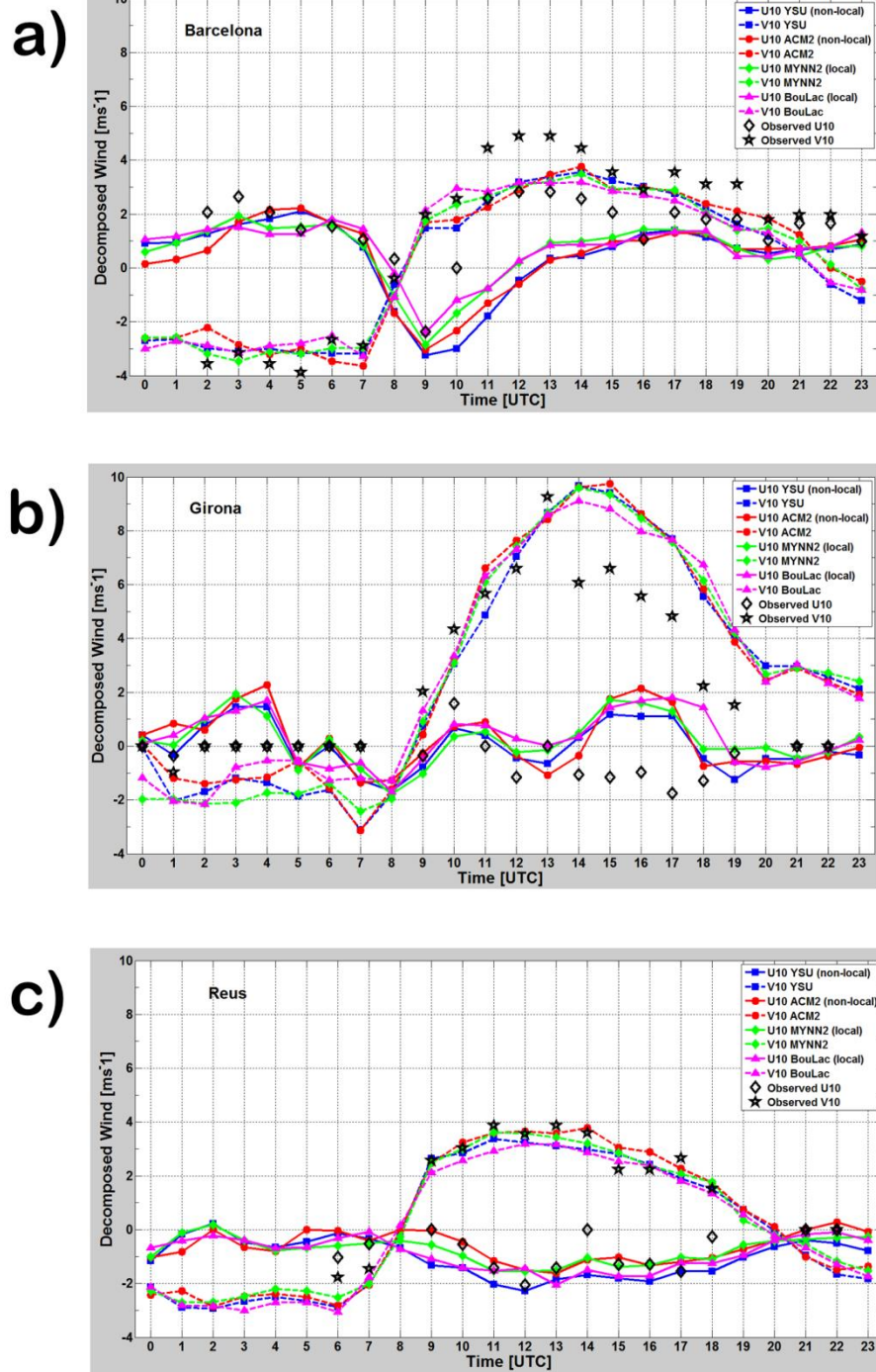


Figure 5.4 Same as in Fig. 5.3, except for zonal (U10; solid lines) and meridional (V10; dashed lines) components of 10-m winds.

We also evaluated the model performance for the lower atmospheric column (up to 3 km altitude), comparing WRF model simulations to observations from a 12:00 UTC radiosonde launch (Fig. 5.5) for a) temperature, b) dew point temperature, and c) zonal and e) meridional winds. The WRF model systematically performs well with temperature and dew point temperature, while the largest bias between the WRF model and observations is shown with the winds.

WRF model-simulated temperature is under-estimated throughout the entire PBL, with the MYNN2 scheme showing the closest simulated values to the observations. Dew point temperature is under-estimated by the WRF model from the surface up to 1.75 km altitude, and then the radiosonde observations indicate a dry layer between 2 – 2.5 km which the WRF model cannot resolve with any PBL scheme. Overall, WRF model-simulated dew point temperature with the BouLac PBL scheme has the best performance.

The zonal wind simulated by the WRF model is under-estimated with all PBL schemes, by as much as 4 m s^{-1} with local PBL schemes. Meanwhile, the meridional wind component is under-estimated by the WRF model in the boundary layer, but over-estimated above the PBL. Large differences are shown between the various PBL schemes in the PBL, with the lowest bias from the BouLac scheme.

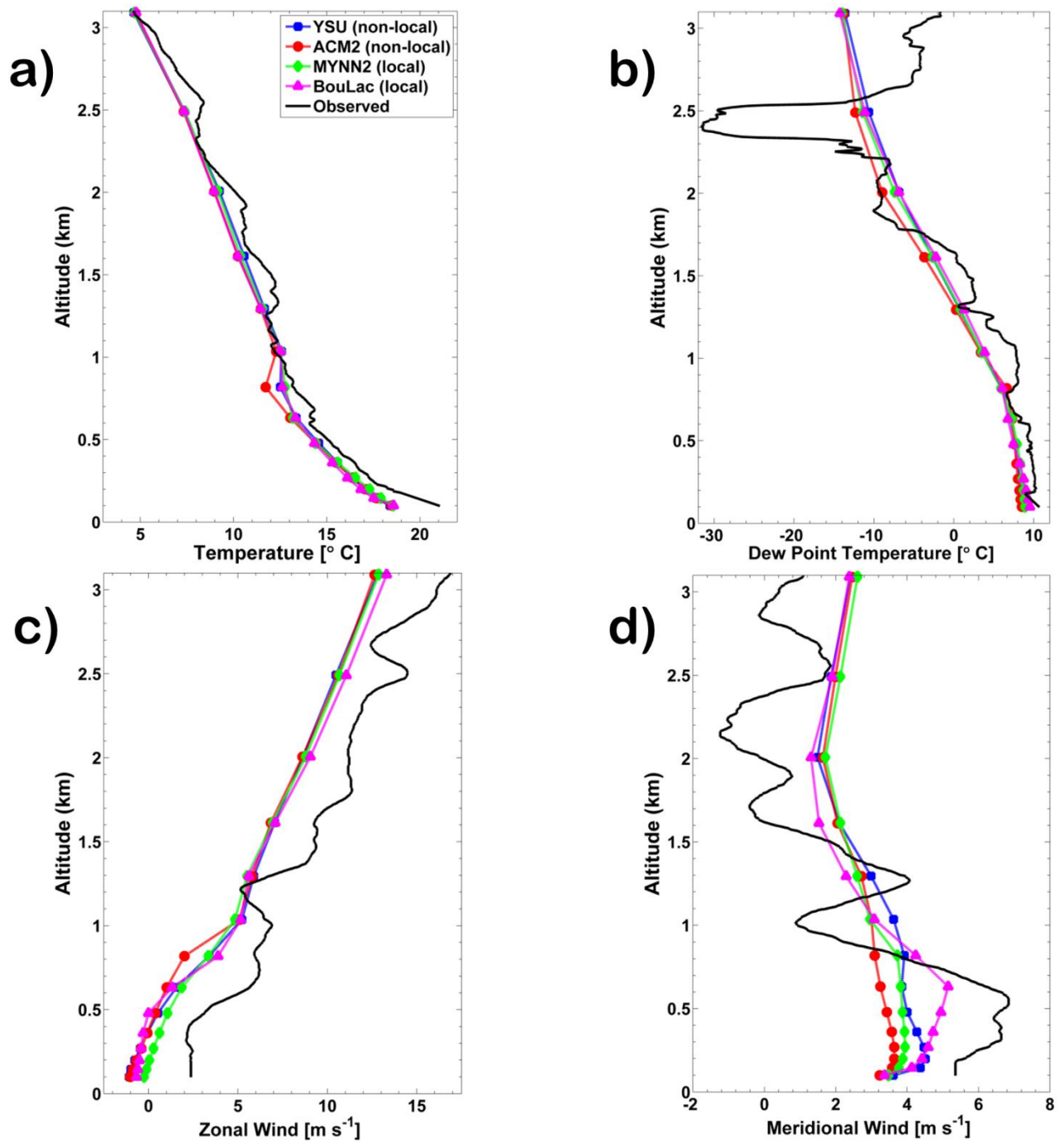


Figure 5.5 Comparison of WRF model-simulated vertical profiles (colored lines and symbols) against a radiosounding (black solid line) on 7 May 2015 at 12:00 UTC for a) temperature, b) dew point temperature, c) zonal wind speed, and d) meridional wind speed.

5.3.2 Air quality evaluation

First, we evaluate the spatial differences of surface O_3 concentration (Fig. 5.6) between the YSU scheme (control run) and the bias error (WRF scheme – control) from the three other PBL schemes at three static times during the day. The times are selected to represent the morning (6:00 UTC), afternoon (12:00 UTC), and evening (18:00 UTC) hours.

In the morning, the highest O_3 concentrations are located in the Pyrenees range near Berga and to the west. Concentrations range from $90 - 100 \mu\text{g m}^{-3}$. Effects of the topography can be shown in the bias plots, most evident with the BouLac scheme. CMAQ model-simulated O_3 with the ACM2 scheme best represents the concentrations at 6:00 UTC, with a bias error less than $5 \mu\text{g m}^{-3}$. At 12:00 UTC, maximum O_3 concentrations form just north-east of Barcelona ($> 110 \mu\text{g m}^{-3}$) and west of Mallorca ($> 95 \mu\text{g m}^{-3}$). CMAQ model-simulated O_3 with the three other PBL schemes show mainly a negative bias error ($\approx -10 - -14 \mu\text{g m}^{-3}$) near Barcelona, with a slightly smaller bias with the BouLac scheme. In addition, the CMAQ model shows a negative bias error ($\approx -10 - -14 \mu\text{g m}^{-3}$) with the plume west of Mallorca. CMAQ model simulations with the ACM2, MYNN2, and BouLac schemes all show similar bias errors. Three areas of maximum surface O_3 concentrations have formed by the evening (18:00 UTC); over the Pyrenees range, over extreme south-west Catalonia, and off the coast just east of Amposta. Surface O_3 concentrations range from 80 to $100 \mu\text{g m}^{-3}$ in these areas. Bias errors between the YSU scheme and the three other PBL schemes are similar with the Pyrenees and coastal maxima, with slightly better performance by the MYNN2 and BouLac schemes with the maximum in far south-west Catalonia.

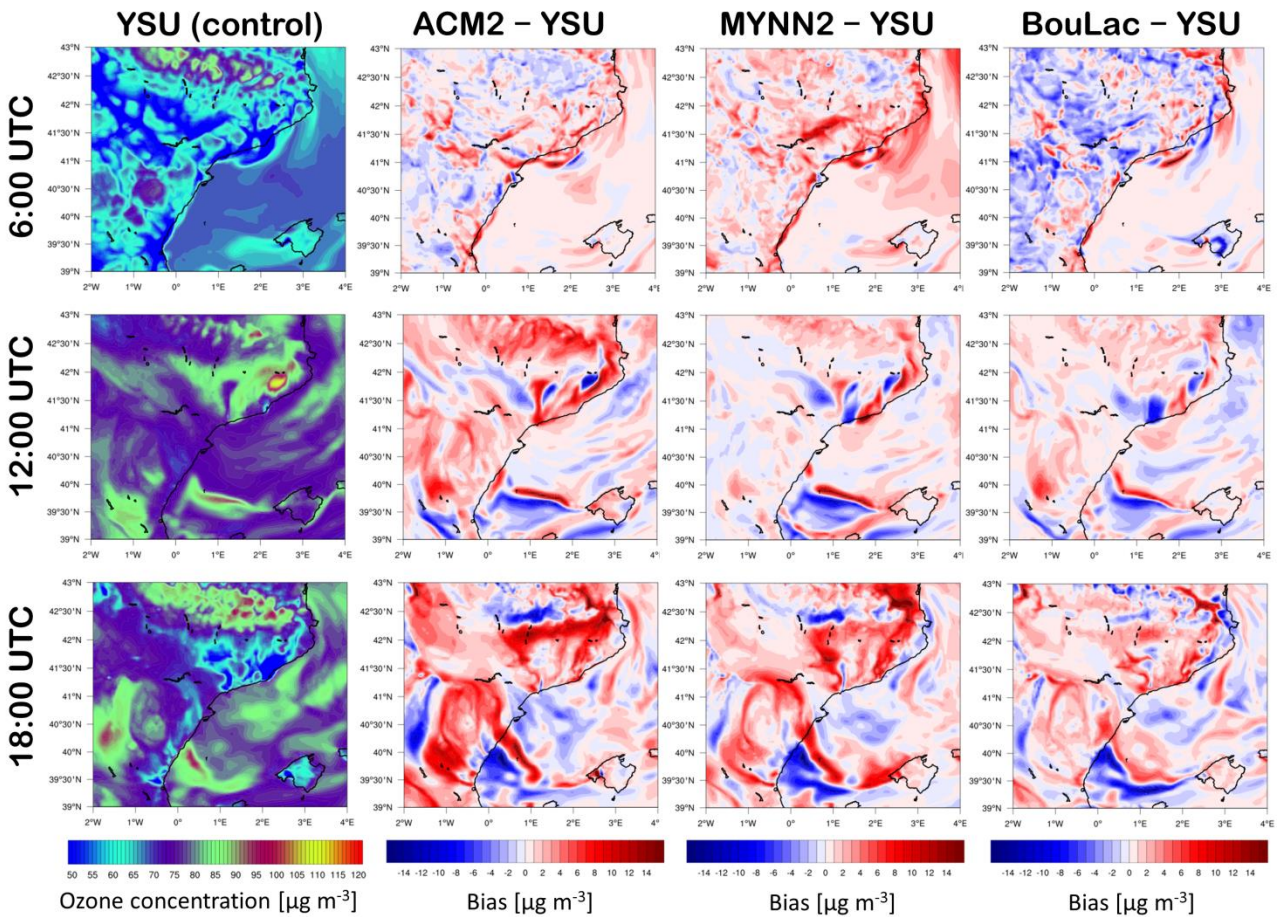


Figure 5.6 Spatial comparison of CALIOPE-simulated surface ozone concentration (O_3) from the control run (YSU; first column), and bias between tested WRF PBL schemes and the control run for the ACM2 (column 2), MYNN2 (column 3), and BouLac (column 4) schemes. Plots are shown for 6:00 UTC (first row), 12:00 UTC (second row), and 18:00 UTC (third row) on 7 May 2015.

Next, we perform a similar analysis of spatial differences of surface NO_2 concentration (Fig. 5.7) between the various PBL schemes. In the morning, the maximum NO_2 concentrations ($> 60 \mu g m^{-3}$) are focused along the coast from Reus to Girona, and inland west of Barcelona. CMAQ simulations with the ACM2 and MYNN2 schemes show mainly a negative bias, while the BouLac schemes shows a positive bias error. By 12:00 UTC, the maximum NO_2 concentration has formed over the Barcelona metropolitan area, with values greater than $60 \mu g m^{-3}$. The mean bias for CMAQ simulations with all three PBL schemes is negative, with a slightly better performance by the BouLac scheme. In the evening, two main areas of maximum NO_2 concentrations have formed; one over extreme south-west Catalonia and another along the coast east of the pre-coastal

mountain range. Under-estimates are shown with all three PBL schemes, with no clear favourite at this time of the day.

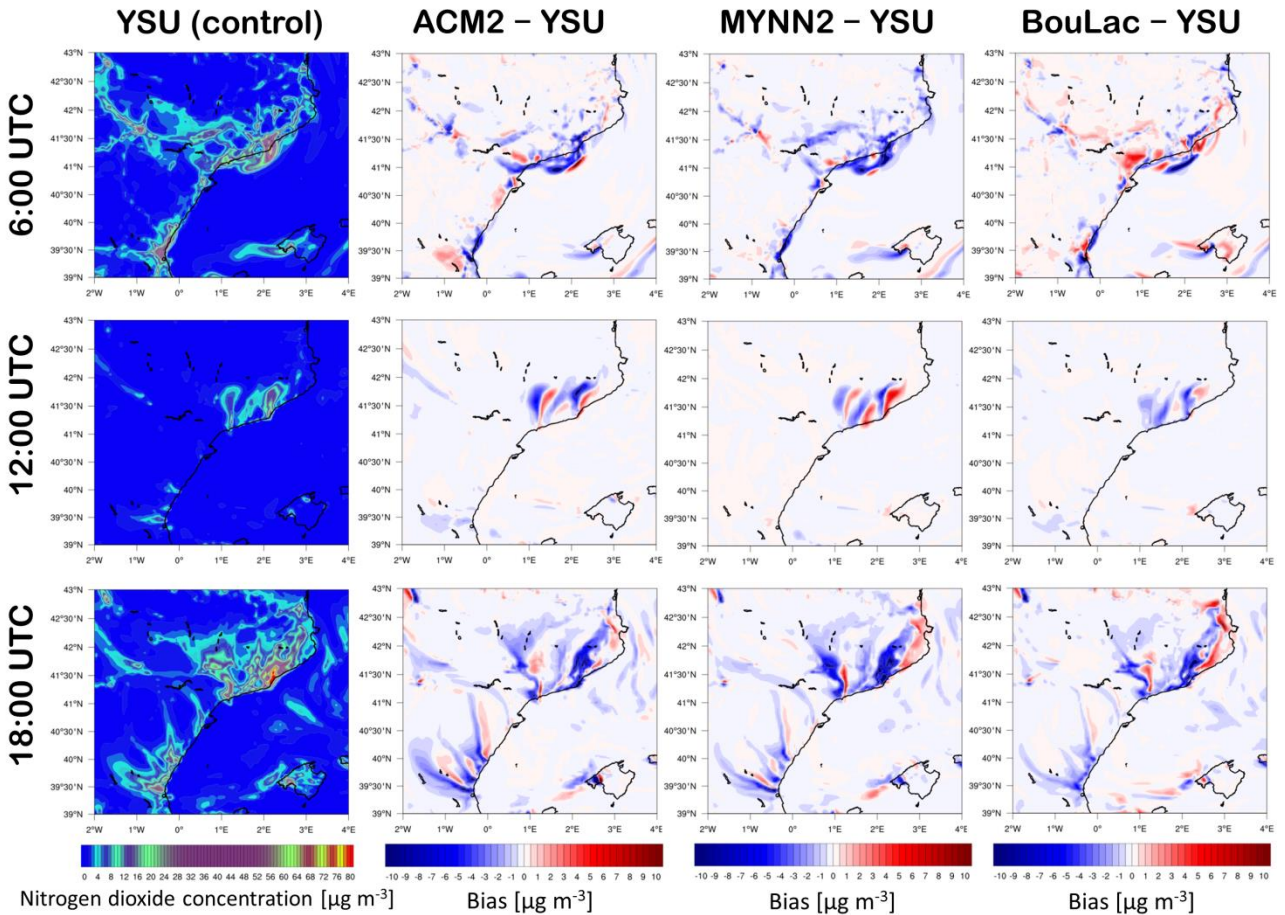


Figure 5.7 Same as in Fig. 5.6, except for surface concentration of nitrogen dioxide (NO_2).

Finally, we examine the spatial differences of surface PM_{10} (Fig. 5.8) between the YSU (control run) and the three tested PBL schemes. A large area of surface PM_{10} ($> 15 \mu\text{g m}^{-3}$) sits just offshore in the morning hours. CMAQ model-simulated PM_{10} with the MYNN2 scheme under-estimates the area by around 30%. The ACM2 and BouLac schemes mainly over-estimate the plume magnitude, with a slightly higher over-estimate from ACM2. At 12:00 UTC the maximum area of PM_{10} is concentrated over the Sea between Amposta and Palma, with highest around $20 \mu\text{g m}^{-3}$ near Palma. All three CMAQ model simulations using different PBL

schemes under-estimate the plume, however with a slightly lower bias error with the ACM2 scheme. In the evening, an area of high PM₁₀ (> 20 μg m⁻³) forms along the coast just east of Girona. However, CMAQ simulations with all three PBL schemes strongly under-estimate (30 – 40%) the plume magnitude.

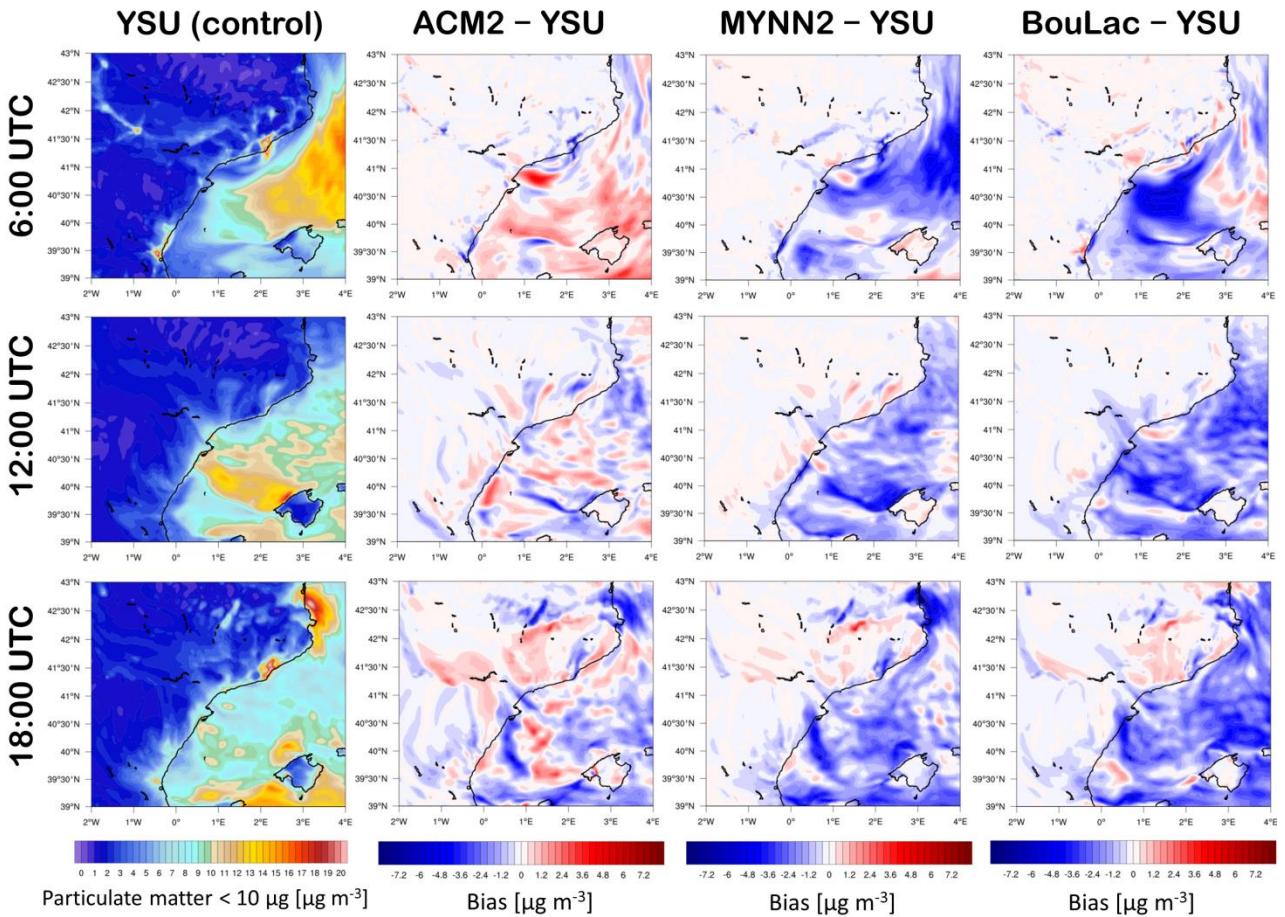


Figure 5.8 Same as in Fig. 5.6, except for surface concentration of particulate matter < 10 μm (PM₁₀).

The differences between PBL schemes can be further highlighted by comparing daily grid-point values from the CMAQ model simulations to observations at six air quality stations for urban, suburban, and rural background station types. Mean bias (*MB*) and correlation (*r*) for each scheme is shown in Table 5.3. The statistics are calculated to represent the average performance of O₃, NO₂, and PM₁₀ for each station type. Overall, the CMAQ model under-estimates all evaluated variables, no matter which PBL scheme is selected.

Table 5.3 Statistics of surface photochemical and aerosol variables; mean bias (*MB*) and linear correlation coefficient (*r*), between CALIOPE AQFS-simulations and network observations at urban, suburban, and rural background stations. Two stations are averaged for each station type (shown in Fig. 1d). *MB* is calculated as CALIOPE AQFS – observed. Variables included ($\mu\text{g m}^{-3}$) are surface ozone (O_3), nitrogen dioxide (NO_2), and particulate matter less than $10\ \mu\text{m}$ (PM_{10}).

Urban									
	YSU		ACM2		MYNN2		BouLac		
	<i>MB</i>	<i>r</i>	<i>MB</i>	<i>r</i>	<i>MB</i>	<i>r</i>	<i>MB</i>	<i>r</i>	
O_3	-2.53	0.53	-0.96	0.54	-1.6	0.51	-2.01	0.55	
NO_2	-17.44	0.22	-18.1	0.2	-17.58	0.22	-17.14	0.24	
PM_{10}	-28.63	0.15	-28.68	0.28	-28.76	0.22	-28.77	0.22	
Suburban									
	YSU		ACM2		MYNN2		BouLac		
	<i>MB</i>	<i>r</i>	<i>MB</i>	<i>r</i>	<i>MB</i>	<i>r</i>	<i>MB</i>	<i>r</i>	
O_3	-14.69	0.72	-12.75	0.56	-12.78	0.58	-13.04	0.74	
NO_2	-6.48	0.57	-7.36	0.44	-6.99	0.47	-7.27	0.56	
PM_{10}	-16.29	0.2	-16.61	0.13	-16.81	0.11	-17.05	0.2	
Rural									
	YSU		ACM2		MYNN2		BouLac		
	<i>MB</i>	<i>r</i>	<i>MB</i>	<i>r</i>	<i>MB</i>	<i>r</i>	<i>MB</i>	<i>r</i>	
O_3	-8.23	0.75	-6.27	0.82	-7.94	0.81	-8.34	0.79	
NO_2	-7.42	0.57	-7.57	0.57	-7.54	0.54	-7.48	0.53	
PM_{10}	-12.84	0.05	-12.77	0.39	-12.75	0.39	-12.72	0.37	

The CMAQ model performs the best with the comparisons of O_3 to observations. CMAQ model simulations with the ACM2 scheme have the lowest bias error with all station types, as low as $-0.96\ \mu\text{g m}^{-3}$ at urban sites. The correlation between CMAQ model and observations is the closest with rural stations (0.75 – 0.82), along with the second lowest *MB*.

Performance statistics show mixed results with surface NO_2 and PM_{10} concentrations against the observed values. At suburban and rural stations, CMAQ model simulations with the YSU and BouLac schemes perform well, with the YSU scheme slightly better ($MB = -6.48\ \mu\text{g m}^{-3}$ at suburban; $MB = -7.42\ \mu\text{g m}^{-3}$ at rural). Similar to surface O_3 , the closest correlation of model to observations is associated with rural sites (0.53 – 0.57), however lower than O_3 .

The performance of the CMAQ model in simulating PM_{10} was the worst of all variables analysed, both in terms of bias and correlation statistics. In addition, differences between CMAQ simulations with each PBL scheme are the closest of all variables. Low correlations between the CMAQ model and observations show a lack of confidence in the comparison. Similar to surface NO_2 , CMAQ model simulations with the YSU and BouLac schemes show the best performance.

5.4 Conclusions

This chapter showed the impact of four planetary boundary layer (PBL) parametrization schemes (two local, two non-local) from the Weather Research and Forecasting (WRF) mesoscale model on simulations of meteorological variables and predicted pollutant concentrations from the CALIOPE air quality forecast system (AQFS), maintained and operated at the Barcelona Supercomputing Center. The CALIOPE AQFS is composed of the WRF-ARW V3.5.1 meteorological model, HERMES v2 emissions model, CMAQ V5.0.2 chemical transport model, and dust outputs from BSC-DREAM8bv2.

The area of interest was the Catalonia region located in the northeast Iberian Peninsula during 7 May 2015, a day dominated by regional recirculations flow. Performance of the non-local schemes, Yonsei University (YSU; control run) and Assymetric Convective Model Version 2 (ACM2), and the local schemes, Mellor-Yamada-Janjic (MYJ) and Bougeault-Lacarrère (BouLac) were evaluated. AQFS-simulated pollutant concentrations were evaluated against six network urban, suburban, and rural background stations. In addition, we used METAR surface meteorological observations and vertical profiles from a radiosounding for an evaluation of the WRF simulations. Daytime WRF model-simulated PBL heights were validated against estimates retrieved using a micro-pulse lidar system.

Large differences were found with the WRF model simulations of PBL height. WRF model simulations with all four PBL schemes under-estimated the height of the PBL when compared with estimates from the lidar. However, WRF model-simulated PBL height was best represented by a non-local scheme, such as ACM2 ($MB = 0.11$ km).

Surface meteorological variables showed ambiguous results, especially for 10 m zonal (U10) and meridional (V10) wind speed components, with under-estimates by the WRF model at Barcelona and Reus, and an over-estimate at Girona. The non-local YSU and ACM2 schemes simulated the closest values to the observations.

2-m air temperature (T2) and dew point temperature (TD2) were most accurately represented by a local PBL scheme, with the best performance from the BouLac scheme.

The comparison of WRF model vertical profiles against a 12:00 UTC radiosounding showed the largest biases with zonal and meridional winds. Overall, non-local schemes provided the lowest biases in the boundary layer. Local PBL schemes, such as BouLac, showed the closest temperature and dew point temperature to the observed values. However, no PBL scheme could help to resolve an extreme dry layer in the lower atmosphere.

The best performances from the CMAQ simulations were with the surface ozone (O_3) and nitrogen dioxide (NO_2) concentrations. Local PBL schemes, BouLac and MYNN2, showed the lowest bias error against the control run when comparing spatially. Performance statistics of the CMAQ model against observations showed the BouLac scheme with a low mean bias for NO_2 , while the non-local ACM2 performed well with O_3 .

Surface particulate matter less than $10\ \mu m$ (PM_{10}) showed the worst performance of all the air quality variables evaluated, with low correlations between the CMAQ model and observations. The poor performance of CMAQ model-simulated PM_{10} is most likely attributable to bad representations of the PBL from the WRF model.

In conclusion, we found that a non-local PBL scheme (ACM2) performs well for model simulations of the PBL height and surface and upper-air winds. In contrast, a local scheme (BouLac) is preferred for surface air and dew point temperature. In addition, the ACM2 and BouLac schemes performed better than the YSU (control run) scheme for air quality simulations. Further studies are needed to determine if the current PBL scheme in the CALIOPE AQFS should be changed.



Chapter 6

6 Conclusions and future research

In the present Ph.D. thesis an overview of the scientific context and the objectives were presented in the introductory Chapter 1. An inter-comparison of methods for obtaining the planetary boundary-layer (PBL) height from lidar during a July 2012 monitoring campaign over the Iberian Peninsula in the framework of EARLINET was presented in Chapter 2. Next, a performance evaluation of PBL height from lidar and the Weather Research and Forecasting (WRF) model over Barcelona, Spain was discussed in Chapter 3. The analysis was expanded in Chapter 4 to examine the sensitivity of boundary-layer variables to PBL schemes in the WRF model in Athens, Greece. The analysis was based on surface meteorological observations, lidar, and radiosondes collected during the HygrA-CD field campaign. In Chapter 5, the impact of WRF model PBL schemes on air quality simulations over Catalonia, Spain was presented. The most important conclusions from these chapters are presented as a summary in this section. The final sub-section is devoted to future work related to the evaluation of lidar methods for estimation of PBL height, along with the future assessment of model PBL schemes for air quality applications.

6.1 Synthesis of results

The research conducted in this Ph.D. dissertation has been centred on the evaluation of the sensitivity of high-resolution air quality (AQ) simulations from the CALIOPE air quality forecast system (AQFS) in the distribution of gaseous photochemical pollutants and particulate matter to different PBL schemes in the WRF

Advanced Research WRF (ARW) model. The primary work packages in this project were focused on the Iberian Peninsula and the Greater Athens Area (GAA). Three main conclusions are drawn from this work:

- 1. Estimates of the PBL height from lidar observations with a time-adaptive extended Kalman filter (EKF) approach show promising results ($R^2 = 0.96$ for Barcelona), showing lidar can be a useful tool for the validation of model-simulated PBL heights.**
- 2. WRF model simulations using non-local PBL parameterization schemes, especially the asymmetric convective model version 2 (ACM2) scheme, show the most accurate model-simulated PBL heights. In addition, WRF model simulations with the ACM2 scheme showed more accurate surface and upper-air meteorological variables over complex, urban areas such as Barcelona and Athens.**
- 3. Selection of meteorological model PBL scheme associated with an air quality forecast system plays an important role in accurate model simulations of air pollution variables.**

More specific conclusions of the Ph.D. research are presented in the following sub-sections.

6.1.1 Methods to estimate PBL height from lidar

The concept of using lidar to detect PBL height relies on the assumption that there is a strong gradient in the concentration of aerosols in the ML versus the free atmosphere (FA). Several methods have been applied to detect these gradients using aerosols as tracers. An advantage of using remote sensing instruments over typical radiosondes for detection of the PBL height is the possibility of nearly continuous monitoring versus only observations of twice per day from radiosondes. Continuous monitoring of PBL height will allow for a better understanding of the depth of convective turbulent processes in the mixed-layer which are a primary driver of air pollutants. The conclusions are based upon work separated into three activities.

First, three classic methods were compared over the Iberian Peninsula. The lidar measurements were collected during a 72-h period of continuous observations from 9-12 July 2012, in the framework of EARLINET. PBL height estimates from the lidar are compared against radiosonde-calculated heights. It is found that all the methods provide comparable results in optimal observing conditions. However, it is determined that the WCT is an optimal method, as it is more computationally efficient than the derivative



techniques (GM and IPM). The best results are shown in daytime, clear air convective situations. In summer, PBL heights over the Iberian Peninsula are typically from 1 to 3 km, with the highest PBL heights in the south. Lidar proves to be a modern tool for near-continuous monitoring of PBL height. Comerón et al. (2013) use linear system theory to prove the WCT and the GM are the same. Overall, it has been shown that lidar can be used as an effective means of obtaining accurate PBL heights on a nearly continuous basis.

Secondly, methods to obtain the PBL height from lidar were compared and validated at 12:00 UTC over a 7-year period using the Barcelona multiwavelength Raman lidar. A novel approach using an extended Kalman filter (EKF) is compared with classic methods found in the literature. The comparison of PBL height estimates provided by traditional and advanced lidar-based approaches was performed for seven objectively determined synoptic flows at different arriving altitudes representing within the PBL, at the top of the PBL, and in the free troposphere. An advanced lidar-based approach utilizes an EKF to time-adaptively estimate PBL height within a range from 0.79 – 1.6 km over Barcelona, which is similar to previous studies. Moreover, the adaptive EKF approach tends to capture the PBL height evolution quite accurately. PBL height retrieved by the EKF technique has a strong determination coefficient ($R^2 = 0.96$) when compared with PBL height estimates from daily daytime radiosonde launches. Classic lidar-based methods showed much weaker correlations, even when gross outliers outside one standard deviation were removed prior to the calculations. In contrast to the EKF approach, this is because classic methods do not rely on past estimates and associated statistical and a priori information to yield present-time estimates but on the instantaneous measurement record, instead. Besides, classic methods comparatively require a much longer time averaging and range smoothing to perform reliably and are usually limited to single-layer scenes. Representative cases for a clean free troposphere, regional recirculations, Saharan dust episodes, and low-level cloud layers highlight the adaptability of the EKF technique when compared with classic methods. Except for cases of a clean free troposphere, the classic methods typically have issues when multiple aerosol layers are present. If the user selects a proper threshold value the threshold method performs second best to the EKF. An approach using the EKF proves promising for continuous and automatic observation of PBL height from lidar measurements. The EKF technique can be applied directly to the lidar range-corrected signal. It has been found that optimal parameters must be chosen for the state vector initialization for the EKF method to track PBL height accurately, depending on the instrument type.

Finally, estimates of the PBL height are retrieved using elastic-channel (1064-nm) backscatter measurements from a multiwavelength Raman lidar using the EKF technique during the Athens HygrA-CD international field campaign. The results were evaluated under diverse synoptic flow types identified with two-day

backtrajectories from the FLEXPART-WRF dispersion model. Three typical atmospheric flow types were observed during the 39-day campaign: Continental, Etesians, and Saharan, which represented 41.7 %, 36.1 %, and 22.2 % of the days, respectively. The PBL height was estimated from radiosoundings using a bulk Richardson number approach. It was found that daytime maximum PBL heights ranged from 2.57 km during Etesian flows, to as low as 0.37 km attributed with Saharan dust episodes. Lidar-estimated PBL heights compared relatively well to the radiosoundings.

6.1.2 Evaluation of model PBL schemes over Barcelona and Athens

The evaluation of WRF model PBL parameterization schemes was separated into two main research works.

First, PBL heights simulated in the WRF model were validated against the lidar-EKF estimates over Barcelona. WRF model-simulated PBL heights were evaluated using eight unique PBL schemes. Test simulations with the WRF model reveal a clear favour to non-local PBL schemes, with the Asymmetric Convective Model Version 2 (ACM2) scheme showing the closest correlation to lidar-EKF estimates. Surprisingly, the widely-tested local Mellor-Yamada-Janjic (MYJ) scheme showed the weakest correlation coefficients. Ambiguous results are found when evaluating the model-simulated PBL heights under the most representative synoptic situations. In all cases, the local University of Washington (UW) scheme produced the lowest daytime maximum PBL height. In the least complex case of a clean free troposphere the MYJ scheme showed the closest model-simulated PBL height to the observations. With more complex cases such as regional recirculations and effects due to Saharan dust intrusions the results are varied, with no clear favourite scheme.

WRF model-simulated sensible heat flux between the land-surface and the atmosphere confirmed a possible reason for the high PBL heights simulated with the Quasi-Normal Scale Elimination (QNSE) scheme. However, other PBL schemes showed very similar model simulations of sensible heat flux. The large differences in PBL heights among the schemes could be attributable to one of two primary components: first, and possibly the largest, are the operational definitions of PBL height in the individual schemes. Secondly, differences in the entrainment behaviour among the PBL schemes could be a factor.

In the second study, eight PBL schemes (5 local, 3 non-local) from WRF-ARW version 3.4.1 were tested using daily simulations on a 1 km x 1 km grid over the GAA with hourly output resolution. Near-surface observations of 2-m air temperature (T2) and relative humidity (RH2), and 10-m wind speed (WS10) were

collected from surface meteorological instruments at multiple locations. WRF model simulations yield drastically different solutions depending upon the PBL scheme used, the meteorological parameter analyzed, and the general synoptic conditions. The largest differences between model and observations are associated with simulated values of the PBL height (> 400 m on average) during Saharan dust events.

The largest spread between the lowest and highest WRF model-simulated PBL height was shown to be as high as 1.5 km. It is shown that there are influences from the underlying synoptic conditions. The local Bougeault-Lacarrère (BouLac) scheme reproduced PBL height well with the campaign average and Continental synoptic flows, with slight under-estimates. ACM2, a non-local scheme, is a top performer during the Etesians synoptic flow, while the Total Energy Mass-Flux (TEMF) scheme is best during Saharan synoptic flow.

Campaign-averaged near-surface variables showed that the WRF model tended to have a systematic cold, moist bias during daytime, most prominent at the coastal locations. The BouLac scheme reproduced T2 and RH2 well with the campaign average, and with Etesians synoptic flow. ACM2 showed the closest T2 and RH2 during Continental flows. With Saharan synoptic flows, the UW and BouLac schemes well-represented T2, while TEMF best-reproduced RH2. WRF with the Yonsei University (YSU) scheme showed the closest WS10 to the observed values with the campaign average, and during Continental and Etesian synoptic flows. The BouLac scheme only slightly outperformed YSU during Saharan events.

WRF model-simulated vertical profiles of θ mostly show an across-the-board cold, moist bias, except a slightly warm and dry bias in Continental flow. The MYJ scheme simulated the closest θ and q_v during Etesians and Saharan synoptic flows. Vertical soundings of simulated WS have a difficult time reproducing the detailed structure of the radiosoundings, with large spread among PBL schemes. The YSU scheme reproduces the closest WS with Continental and Etesians flows, while the UW and ACM2 schemes work best in Saharan flows.

6.1.3 Impact of WRF PBL schemes on air quality simulations

The final conclusions concern the impact of four PBL parametrization schemes (two local, two non-local) from the WRF mesoscale model on simulations of meteorological variables and predicted pollutant concentrations from the CALIOPE AQFS, maintained and operated at the Barcelona Supercomputing Center.

The CALIOPE AQFS is composed of the WRF-ARW V3.5.1 meteorological model, HERMES v2 emissions model, CMAQ V5.0.2 chemical transport model, and dust outputs from BSC-DREAM8bv2.

The area of interest was the Catalonia region located in the northeast Iberian Peninsula during 7 May 2015, a day dominated by regional recirculations flow. Performance of the non-local schemes, YSU (control run) and ACM2, and the local schemes, MYNN2 and BouLac were evaluated. AQFS-simulated pollutant concentrations were evaluated against six network urban, suburban, and rural background stations. In addition, we used METAR surface meteorological observations and vertical profiles from a radiosounding for an evaluation of the WRF simulations. Daytime WRF model-simulated PBL heights were validated against estimates retrieved using a micro-pulse lidar system.

Large differences were found with the WRF model simulations of PBL height. WRF model simulations with all four PBL schemes under-estimated the height of the PBL when compared with estimates from the lidar. However, WRF model-simulated PBL height was best represented by a non-local scheme, such as ACM2 ($MB = 0.11$ km).

Surface meteorological variables showed ambiguous results, especially for 10 m zonal (U10) and meridional (V10) wind speed components, with under-estimates by the WRF model at Barcelona and Reus, and an over-estimate at Girona. The non-local YSU and ACM2 schemes simulated the closest values to the observations. 2-m air temperature (T2) and dew point temperature (TD2) were most accurately represented by a local PBL scheme, with the best performance from the BouLac scheme.

The comparison of WRF model vertical profiles against a 12:00 UTC radiosounding showed the largest biases with zonal and meridional winds. Overall, non-local schemes provided the lowest biases in the boundary layer. Local PBL schemes, such as BouLac, showed the closest temperature and dew point temperature to the observed values. However, no PBL scheme could help to resolve an extreme dry layer in the lower atmosphere.

The best performances from the CMAQ simulations were with the surface ozone (O_3) and nitrogen dioxide (NO_2) concentrations. Local PBL schemes, BouLac and MYNN2, showed the lowest bias error against the control run when comparing spatially. Performance statistics of the CMAQ model against observations showed the BouLac scheme with a low mean bias for NO_2 (under-estimate $\sim 7 \mu g m^{-3}$) at suburban and rural stations, while the non-local ACM2 scheme performed well with O_3 ($r = 0.82$ at rural stations).

Surface particulate matter less than 10 μm (PM_{10}) showed the worst performance of all the air quality variables evaluated, with low correlations between the CMAQ model and observations. The poor performance of CMAQ model-simulated PM_{10} is most likely attributable to bad representations of the PBL from the WRF model.

In conclusion, we found that a non-local PBL scheme (ACM2) performs well for model simulations of the PBL height and surface and upper-air winds. In contrast, a local scheme (BouLac) is preferred for surface air and dew point temperature. In addition, the ACM2 and BouLac schemes performed better than the YSU (control run) scheme for air quality simulations.

6.2 Future research lines

Future work should include an evaluation of WRF model PBL schemes using the lidar-EKF method at other locations, with comparison between a complex, coastal site similar to Barcelona and a continental site (e.g., Cabauw, The Netherlands). It is possible that the skill of PBL schemes is dependent on entrainment fluxes, but also on the effect of mesoscale horizontal flow. Also, it is worthwhile to make comparisons of the PBL schemes using a unified formulation of the PBL height definition.

In addition, with the advantage of reliable tracking of diurnal PBL height the lidar-EKF method can be employed as an assimilation tool for PBL height simulations in the WRF model and other numerical weather prediction models. However, it is necessary for the lidar to operate in a nearly continuous mode.

Future work should further address the physical explanations of the numerous differences between the WRF PBL schemes in greater detail. Use of the urban parameterization option in WRF should be explored. In addition, the study areas should be expanded to include more experimental sites and complex locations, but also areas with a more stable atmospheric regime. Additional measurements for a future study include flux measurements from a meteorological tower, more frequent upper-air soundings, and continuous nighttime backscatter measurements from a ceilometer to analyze the nocturnal boundary layer.

Further studies are needed to determine if the current PBL scheme in the CALIOPE AQFS should be changed.



References

- AIRS, 2013. AIRS Mission Description [WWWDocument]. URL <http://airs.jpl.nasa.gov/mission/description/> (accessed 6.13.13).
- Angevine, W.M., Jiang, H., Mauritsen, T., 2010. Performance of an Eddy Diffusivity–Mass Flux Scheme for Shallow Cumulus Boundary Layers. *Mon. Weather Rev.* 138, 2895–2912, doi:10.1175/2010MWR3142.1
- Baars, H., Ansmann, A., Engelmann, R., Althausen, D., 2008. Continuous monitoring of the boundary-layer top with lidar. *Atmos. Chem. Phys.* 8(23), 7281–7296
- Baldasano, J.M., Cremades, L., Soriano, C., 1994. Circulation of air pollutants over the Barcelona geographical area in summer, in: *Proceedings of Sixth European Symposium Physico-Chemical Behavior of Atmospheric Pollutants*. Report EUR 15609/1 EN, Varese, pp. 474–479.
- Baldasano, J.M., Valera, E., Jiménez, P., 2003. Air quality data from large cities. *Sci. Total Environ.* 307, 141–165. doi:10.1016/S0048-9697(02)00537-5
- Baldasano, J.M., Jiménez-Guerrero, P., Jorba, O., Pérez, C., López, E., Güereca, P., Martín, F., Vivanco, M.G., Palomino, I., Querol, X., Pandolfi, M., Sanz, M.J., Diéguez, J.J., 2008. Caliope: an operational air quality forecasting system for the Iberian Peninsula, Balearic Islands and Canary Islands – first annual evaluation and ongoing developments. *Adv. Sci. Res.* 2, 89–98. doi:10.5194/asr-2-89-2008
- Baldasano, J.M., Pay, M.T., Jorba, O., Gassó, S., Jiménez-Guerrero, P., 2011. An annual assessment of air quality with the CALIOPE modeling system over Spain. *Sci. Total Environ.* 409, 2163–2178. doi:10.1016/j.scitotenv.2011.01.041
- Banks, R.F., Tiana-Alsina, J., María Baldasano, J., Rocadenbosch, F., 2014. Retrieval of boundary layer height from lidar using extended Kalman filter approach, classic methods, and backtrajectory cluster analysis, in: *Proc. SPIE 9242, Remote Sensing of Clouds and the Atmosphere XIX; and Optics in Atmospheric Propagation and Adaptive Systems XVII*, 92420F, 17 October 2014, doi:10.1117/12.2072049
- Banks, R.F., Tiana-Alsina, J., Rocadenbosch, F., Baldasano, J.M., 2015. Performance Evaluation of the Boundary-Layer Height from Lidar and the Weather Research and Forecasting Model at an Urban Coastal Site in the North-East Iberian Peninsula. *Boundary-Layer Meteorol.* 157(2), 265–292, doi:10.1007/s10546-015-0056-2

- Banks, R.F., Tiana-Alsina, J., Baldasano, J.M., Rocadenbosch, F., Papayannis, A., Solomos, S., Tzanis, C.G., 2016. Sensitivity of boundary layer variables to PBL schemes in the WRF model based on surface meteorological observations, lidar, and radiosondes during the HygrA-CD campaign. *Atmos. Res.*, In press
- Banks, R.F., Baldasano, J.M., 2016. Impact of WRF model PBL schemes on air quality simulations over Catalonia, Spain. *Atmos. Chem. Phys. Disc.*, Submitted
- Basart, S., Pay, M.T., Jorba, O., Perez, C., Jimenez-Guerrero, P., Schulz, M., Baldasano, J.M., 2012. Aerosols in the CALIOPE air quality modelling system: evaluation and analysis of PM levels, optical depths and chemical composition over Europe. *Atmos. Chem. Phys.* 12, 3363–3392. doi:10.5194/acp-12-3363-2012
- Beljaars, A.C.M., Betts, A.K., 1992. Validation of the boundary layer representation in the ECMWF model, in: *ECMWF Seminar Proceedings: Validation of Models over Europe*. Reading.
- Blackadar, A.K., 1978. Modeling pollutant transfer during daytime convection, in: *Preprints Fourth Symposium on Atmospheric Turbulence, Diffusion, and Air Quality*. American Meteorological Society, Reno, pp. 443–447.
- Boers, R., Eloranta, EW, 2006. Lidar measurements of the atmospheric entrainment zone and the potential temperature jump across the top of the mixed layer. *Boundary-Layer Meteorol.* 34(4), 357–375
- Borge, R., Alexandrov, V., José del Vas, J., Lumbreras, J., Rodríguez, E., 2008. A comprehensive sensitivity analysis of the WRF model for air quality applications over the Iberian Peninsula. *Atmos. Environ.* 42(37), 8560-8574
- Bösenberg, J., CoAuthors, 2001. EARLINET: A European Aerosol Research Lidar Network, in: *Laser Remote Sensing of the Atmosphere, Selected Papers of the 2001 International Laser Radar Conference*. pp. 155–158.
- Bossioli, E., Tombrou, M., Dandou, A., Athanasopoulou, E., Varotsos, K. V., 2009. The role of planetary boundary-layer parameterizations in the air quality of an urban area with complex topography. *Boundary-Layer Meteorol.* 131, 53–72. doi:10.1007/s10546-009-9349-7
- Bougeault, P., Lacarrere, P., 1989. Parameterization of Orography-Induced Turbulence in a Mesobeta--Scale Model. *Mon. Weather Rev.* doi:10.1175/1520-0493(1989)117<1872:POOITI>2.0.CO;2
- Bretherton, C.S., Park, S., 2009. A new moist turbulence parameterization in the community atmosphere model. *J. Clim.* 22, 3422–3448. doi:10.1175/2008JCLI2556.1
- Brioude, J., Angevine, W.M., McKeen, S.A., Hsie, E.-Y., 2012. Numerical uncertainty at mesoscale in a Lagrangian model in complex terrain. *Geosci. Model Dev. Discuss.* doi:10.5194/gmdd-5-967-2012
- Brioude, J., CoAuthors, 2013. The Lagrangian particle dispersion model FLEXPART-WRF version 3.1. *Geosci. Model Dev.* 6, 1889-1904. doi:10.5194/gmd-6-1889-2013
- Brown, R.G., Hwang, P.Y.C., 1982. Introduction to Random Signals and Applied Kalman Filtering, First. ed. Wiley, New York.

- Chen, S.-H., Dudhia, J., 2000. Annual report: WRF physics. *Air Force Weather Agency*, 38pp.
- Cheng, F.Y., Chin, S.C., Liu, T.H., 2012. The role of boundary layer schemes in meteorological and air quality simulations of the Taiwan area. *Atmos. Environ.* 54, 714–727. doi:10.1016/j.atmosenv.2012.01.029
- Collis, R., Russell, P., 1976. Lidar measurements of particles and gases by elastic backscattering and differential absorption. In: *Hinkley, E (eds) Laser Monitoring of the atmosphere*. Springer-Verlag, New York, pp 71-102
- Comerón, A., Sicard, M., Rocadenbosch, F., 2013. Wavelet correlation transform method and gradient method to determine aerosol layering from lidar returns: Some comments. *J. Atmos. Ocean. Technol.* 30, 1189–1193. doi:10.1175/JTECH-D-12-00233.1
- Coniglio, M.C., Correia, J., Marsh, P.T., Kong, F., 2013. Verification of Convection-Allowing WRF Model Forecasts of the Planetary Boundary Layer Using Sounding Observations. *Weather Forecast.* 28, 842–862. doi:10.1175/WAF-D-12-00103.1
- Cuchiara, G.C., Li, X., Carvalho, J., Rappenglück, B., 2014. Intercomparison of planetary boundary layer parameterization and its impacts on surface ozone concentration in the WRF/Chem model for a case study in houston/texas. *Atmos. Environ.* 96, 175–185. doi:10.1016/j.atmosenv.2014.07.013
- Draxl, C., Hahmann, A.N., Peña, A., Giebel, G., 2014. Evaluating winds and vertical wind shear from Weather Research and Forecasting model forecasts using seven planetary boundary layer schemes. *Wind Energy* 17, 39–55. doi:10.1002/we.1555
- Draxler, R.R., Rolph, G.D., 2013. HYSPLIT (HYbrid Single-Particle Lagrangian Integrated Trajectory) [WWW Document]. NOAA Air Resour. Lab. Coll. Park. MD. URL <http://www.arl.noaa.gov/HYSPLIT.php>
- Dudhia, J., 1989. Numerical Study of Convection Observed during the Winter Monsoon Experiment Using a Mesoscale Two-Dimensional Model. *J. Atmos. Sci.* doi:10.1175/1520-0469(1989)046<3077:NSOCOD>2.0.CO;2
- Dudhia, J., 1993. A non-hydrostatic version of the Penn State-NCAR mesoscale model: Validation tests and simulation of an Atlantic cyclone and cold front. *Mon. Weather Rev.* 121, 1493–1513.
- EMEP, 2013. EMEP History and Structure [WWW Document]. URL http://www.emep.int/emep_overview.html (accessed 6.13.13).
- EPA, 2015. What Are the Six Common Air Pollutants? [WWW Document]. URL <http://www3.epa.gov/airquality/urbanair/> (accessed 9.9.15).
- EU, 2008. Directive 2008/50/EC of the European Parliament and of the Council of 21 May 2008 on ambient air quality and cleaner air for Europe (OJ L 152, 11.6.2008, p. 1–44) [WWW Document]. URL <http://eur-lex.europa.eu/LexUriServ/LexUriServ.do?uri=OJ:L:2008:152:0001:0044:EN:PDF> (accessed 7.6.13).
- EU, 2010. Press release IP/10/687 (03.06.2010) [WWW Document].

- EURAD, 2016. Air Quality Forecast [WWW Document]. URL http://db.eurad.uni-koeln.de/index_e.html/ (accessed 1.26.16).
- Flamant, C, Pelon, J, Flamant, PH, Durand, P, 1997. Lidar determination of the entrainment zone thickness at the top of the unstable marine atmospheric boundary layer. *Boundary-Layer Meteorol.* 83(2), 247-284
- Folberth, G.A., Hauglustaine, D.A., Lathièrre, J., Brocheton, F., 2006. Interactive chemistry in the Laboratoire de Météorologie Dynamique general circulation model: model description and impact analysis of biogenic hydrocarbons on tropospheric chemistry. *Atmos. Chem. Phys.* 6, 2273–2319. doi:10.5194/acp-6-2273-2006
- Gamage, N., Hagelberg, C., 1993. Detection and Analysis of Microfronts and Associated Coherent Events using Localized Transforms. *J. Atmos. Sci.* 50, 750–756.
- Gan, C.M., Wu, Y., Madhavan, B.L., Gross, B., Moshary, F., 2011. Application of active optical sensors to probe the vertical structure of the urban boundary layer and assess anomalies in air quality model PM2.5 forecasts. *Atmos. Environ.* 45, 6613–6621. doi:10.1016/j.atmosenv.2011.09.013
- Gent, P.R., Danabasoglu, G., Donner, L.J., Holland, M.M., Hunke, E.C., Jayne, S.R., Lawrence, D.M., Neale, R.B., Rasch, P.J., Vertenstein, M., Worley, P.H., Yang, Z.L., Zhang, M., 2011. The community climate system model version 4. *J. Clim.* 24, 4973–4991. doi:10.1175/2011JCLI4083.1
- Goncalves, M., Jimenez-Guerrero, P., Baldasano, J.M., 2009. Contribution of atmospheric processes affecting the dynamics of air pollution in South-Western Europe during a typical summertime photochemical episode. *Atmos. Chem. Phys.* 849–864. doi:10.5194/acpd-8-18457-2008
- Guerreiro, C., de Leeuw, F., Foltescu, V., Schilling, J., van Aardenne, J., Lükewille, A., Adams, M., 2012. Air quality in Europe - 2012 report, *EEA Report No 4/2012*. doi:10.2800/55823
- Hauglustaine, D.A., Hourdin, F., Jourdain, L., Filiberti, M.-A., Walters, S., Lamarque, J.-F., Holland, E.A., 2004. Interactive chemistry in the Laboratoire de Météorologie Dynamique general circulation model: Description and background tropospheric chemistry evaluation. *J. Geophys. Res. Atmos.* 109, D04314. doi:10.1029/2003JD003957
- Hennemuth, B, Lammert, A, 2006. Determination of the atmospheric boundary layer height from radiosonde and lidar backscatter. *Boundary-Layer Meteorol.* 120(1), 181-200
- Holtzlag, A.A.M., De Bruijn, E.I.F., Pan, H.-L., 1990. A High Resolution Air Mass Transformation Model for Short-Range Weather Forecasting. *Mon. Weather Rev.* doi:10.1175/1520-0493(1990)118<1561:AHRAMT>2.0.CO;2
- Holzworth, G.C., 1964. Estimates of Mean Maximum Mixing Depths in the Contiguous United States. *Mon. Weather Rev.* 92, 235–242. doi:10.1175/1520-0493(1964)092<0235:EOMMMD>2.3.CO;2
- Hong, S.-Y., Pan, H.-L., 1996. Nonlocal Boundary Layer Vertical Diffusion in a Medium-Range Forecast Model. *Mon. Weather Rev.* doi:10.1175/1520-0493(1996)124<2322:NBLVDI>2.0.CO;2

- Hong, S.-Y., Dudhia, J., Chen, S.-H., 2004. A Revised Approach to Ice Microphysical Processes for the Bulk Parameterization of Clouds and Precipitation. *Mon. Weather Rev.* doi:10.1175/1520-0493(2004)132<0103:ARATIM>2.0.CO;2
- Hong, S.-Y., Noh, Y., Dudhia, J., 2006. A New Vertical Diffusion Package with an Explicit Treatment of Entrainment Processes. *Mon. Weather Rev.* doi:10.1175/MWR3199.1
- Hong, S.-Y., 2010. A new stable boundary-layer mixing scheme and its impact on the simulated East Asian summer monsoon. *Q. J. R. Meteorol. Soc.* 136, 1481–1496. doi:10.1002/qj.665
- Hu, X.M., Nielsen-Gammon, J.W., Zhang, F., 2010. Evaluation of three planetary boundary layer schemes in the WRF model. *J. Appl. Meteorol. Climatol.* 49, 1831–1844. doi:10.1175/2010JAMC2432.1
- INERIS, 2016. Air quality management at INERIS [WWW Document]. URL <http://www.ineris.fr/centredoc/fiche-qualite-air-anglais-bat-bd-dalisson-280515-16h29-1436342594.pdf> (accessed 1.26.16).
- Janjić, Z.I., 1990. The Step-Mountain Coordinate: Physical Package. *Mon. Weather Rev.* doi:10.1175/1520-0493(1990)118<1429:TSMCPP>2.0.CO;2
- Janjić, Z.I., 2002. Nonsingular implementation of the Mellor–Yamada Level 2.5 scheme in the NCEP meso model. *NCEP Office Note* 437, 61 pp.
- Jiménez, P., Baldasano, J.M., 2004. Ozone response to precursor controls in very complex terrains: Use of photochemical indicators to assess O₃-NO_x-VOC sensitivity in the northeastern Iberian Peninsula. *J. Geophys. Res. Atmos.* 109. doi:10.1029/2004JD004985
- Jiménez, P., Dudhia, J., González-Rouco, J.F., Montávez, J.P., García-Bustamante, E., Navarro, J., Vilà-Guerau De Arellano, J., Muñoz-Roldán, 2013. An evaluation of WRF's ability to reproduce the surface wind over complex terrain based on typical circulation patterns. *J. Geophys. Res. Atmos.* 118, 7651–7669. doi:10.1002/jgrd.50585
- Jorba, O, Pérez, C, Rocadenbosch, F, Baldasano, J, 2004. Cluster analysis of 4-day back trajectories arriving in the Barcelona area, Spain, from 1997 to 2002. *J. Appl. Meteorol.* 43(6), 887-901
- Kain, J.S., 2004. The Kain–Fritsch Convective Parameterization: An Update. *J. Appl. Meteorol.* doi:10.1175/1520-0450(2004)043<0170:TKCPAU>2.0.CO;2
- Kim, Y., Fu, J.S., Miller, T.L., 2010. Improving ozone modeling in complex terrain at a fine grid resolution: Part I - examination of analysis nudging and all PBL schemes associated with LSMs in meteorological model. *Atmos. Environ.* 44, 523–532. doi:10.1016/j.atmosenv.2009.10.045
- Kim, Y., Sartelet, K., Raut, J.C., Chazette, P., 2013. Evaluation of the Weather Research and Forecast/Urban Model Over Greater Paris. *Boundary-Layer Meteorol.* 149, 105–132. doi:10.1007/s10546-013-9838-6
- Kleczek, M.A., Steeneveld, G.J., Holtslag, A.A.M., 2014. Evaluation of the Weather Research and Forecasting Mesoscale Model for GABLS3: Impact of Boundary-Layer Schemes, Boundary Conditions and Spin-Up. *Boundary-Layer Meteorol.* 152, 213–243. doi:10.1007/s10546-014-9925-3

- Kokkalis, P., Papayannis, A., Mamouri, R.E., Tsaknakis, G., Amiridis, V., 2012. The EOLE lidar system of the National Technical University of Athens, *in: 26th International Laser Radar Conference (26th ILRC)*. Porto Heli, Greece, pp. 629–632.
- Lange, D., Tiana-Alsina, J., Saeed, U., Tomás, S., Rocadenbosch, F., 2014. Atmospheric boundary layer height monitoring using a kalman filter and backscatter lidar returns. *IEEE Trans. Geosci. Remote Sens.* 52, 4717–4728. doi:10.1109/TGRS.2013.2284110
- Lange, D., Rocadenbosch, F., Tiana-alsina, J., Frasier, S., 2015. Atmospheric-Boundary-Layer Height estimation using a Kalman Filter and a Frequency-Modulated Continuous-Wave Radar. *IEEE Trans. Geosci. Remote Sens.* 53, 3338–3349. doi:10.1109/TGRS.2014.2374233
- LeMone, M.A., Tewari, M., Chen, F., Dudhia, J., 2012. Objectively-determined fair-weather CBL depths in the ARW-WRF model and their comparison to CASES-97 observations. *Mon. Weather Rev.* 141, 30-54, doi:10.1175/MWR-D-12-00106.1
- MACC, 2016. MACC project description [WWW Document]. URL <https://www.gmes-atmosphere.eu/about/project/> (accessed 1.26.16).
- Madala, S., Satyanarayana, A.N.V., Srinivas, C.V., Kumar, M., 2015. Mesoscale atmospheric flow-field simulations for air quality modeling over complex terrain region of Ranchi in eastern India using WRF. *Atmos. Environ.* 107, 315–328. doi:10.1016/j.atmosenv.2015.02.059
- Mao, F., Gong, W., Song, S., Zhu, Z., 2012. Determination of the boundary layer top from lidar backscatter profiles using a Haar wavelet method over Wuhan, China. *Opt. Laser Technol.* 1–7. doi:10.1016/j.optlastec.2012.08.017
- Mao, Q., Gautney, L.L., Cook, T.M., Jacobs, M.E., Smith, S.N., Kelsoe, J.J., 2006. Numerical experiments on MM5-CMAQ sensitivity to various PBL schemes. *Atmos. Environ.* 40, 3092–3110. doi:10.1016/j.atmosenv.2005.12.055
- Martilli, A., Clappier, A., Rotach, M.W., 2002. An urban surface exchange parameterisation for mesoscale models. *Boundary-Layer Meteorol.* 104, 261–304. doi:10.1023/A:1016099921195
- Melas, D., Ziomas, I.C., Zerefos, C.S., 1995. Boundary layer dynamics in an urban coastal environment under sea breeze conditions. *Atmos. Environ.* 29, 3605–3617.
- Melfi, S.H., Spinhirne, J.D., Chou, S.H., Palm, S.P., 1985. Lidar observations of vertically organized convection in the planetary boundary layer over the ocean. *J. Appl. Meteorol. Clim.* 24(8), 806-821
- Menut, L., Flamant, C., Pelon, J., Flamant, P.H., 1999. Urban boundary-layer height determination from lidar measurements over the Paris area. *Appl. Opt.* 38, 945–954. doi:10.1364/AO.38.000945
- Misenis, C., Zhang, Y., 2010. An examination of sensitivity of WRF/Chem predictions to physical parameterizations, horizontal grid spacing, and nesting options. *Atmos. Res.* 97, 315–334. doi:10.1016/j.atmosres.2010.04.005

- Mlawer, E.J., Taubman, S.J., Brown, P.D., Iacono, M.J., Clough, S.A., 1997. Radiative transfer for inhomogeneous atmospheres: RRTM, a validated correlated-k model for the longwave. *J. Geophys. Res.* doi:10.1029/97JD00237
- Nakanishi, M., Niino, H., 2006. An improved Mellor-Yamada Level-3 model: Its numerical stability and application to a regional prediction of advection fog. *Boundary-Layer Meteorol.* 119, 397–407. doi:10.1007/s10546-005-9030-8
- NCEP, 2000. National Centers for Environmental Prediction/National Weather Service/NOAA/U.S. Department of Commerce: NCEP FNL Operational Model Global Tropospheric Analyses, continuing from July 1999, Research Data Archive at the National Center for Atmospheric Research, Computational and Information Systems Laboratory. <http://dx.doi.org/10.5065/D6M043C6>, last access: 10 May 2014
- OMI, 2013. About OMI [WWW Document]. URL <http://aura.gsfc.nasa.gov/instruments/omi.html> (accessed 6.13.13).
- Pal, S., Behrendt, A., Wulfmeyer, V., 2010. Elastic-backscatter-lidar-based characterization of the convective boundary layer and investigation of related statistics. *Ann. Geophys.* 28(3), 825-847
- Pal, S., Xueref-Remy, I., Ammoura, L., Chazette, P., Gibert, F., Royer, P., Dieudonné, E., Dupont, J.C., Haefelin, M., Lac, C., Lopez, M., Morille, Y., Ravetta, F., 2012. Spatio-temporal variability of the atmospheric boundary layer depth over the Paris agglomeration: An assessment of the impact of the urban heat island intensity. *Atmos. Environ.* 63, 261–275. doi:10.1016/j.atmosenv.2012.09.046
- Pandolfi, M., Martucci, G., Querol, X., Alastuey, A., Wilsenack, F., Frey, S., D'owd, CD, Dall'Osto, M, 2013. Continuous atmospheric boundary layer observations in the coastal urban area of Barcelona, Spain. *Atmos. Chem. Phys. Discuss.* 13, 345-377
- Papayannis, A., Mamouri, R.E., Amiridis, V., Kazadzis, S., Pérez, C., Tsaknakis, G., Kokkalis, P., Baldasano, J.M., 2009. Systematic lidar observations of Saharan dust layers over Athens, Greece in the frame of EARLINET project (2004-2006). *Ann. Geophys.* 27, 3611–3620. doi:10.5194/angeo-27-3611-2009
- Papayannis, A., Argyrouli, A., Bougiatioti, A., Remoundaki, E., Eleftheriadis, E., Nenes, A., Van de Hey, J., Kompula, M., Solomos, S., Kazadzis, S., Banks, R.F., Labzovskii, L., Kalogiros, I., Tzanis, C.G., 2016. From hygroscopic aerosols to cloud droplets: the HYGRA-CD campaign in the Athens Basin – An outline. *Sci. Total Environ.*, Submitted
- Pay, M.T., Piot, M., Jorba, O., Gassó, S., Gonçalves, M., Basart, S., Dabdub, D., Jiménez-Guerrero, P., Baldasano, J.M., 2010. A full year evaluation of the CALIOPE-EU air quality modeling system over Europe for 2004. *Atmos. Environ.* 44, 3322–3342. doi:10.1016/j.atmosenv.2010.05.040
- Pay, M.T., Jiménez-Guerrero, P., Baldasano, J.M., 2011. Implementation of resuspension from paved roads for the improvement of CALIOPE air quality system in Spain. *Atmos. Environ.* 45, 802–807. doi:10.1016/j.atmosenv.2010.10.032
- Pay, M.T., Jiménez-Guerrero, P., Baldasano, J.M., 2012a. Assessing sensitivity regimes of secondary inorganic aerosol formation in Europe with the CALIOPE-EU modeling system. *Atmos. Environ.* 51, 146–164. doi:10.1016/j.atmosenv.2012.01.027

- Pay, M.T., Jiménez-Guerrero, P., Jorba, O., Basart, S., Querol, X., Pandolfi, M., Baldasano, J.M., 2012b. Spatio-temporal variability of concentrations and speciation of particulate matter across Spain in the CALIOPE modeling system. *Atmos. Environ.* 46, 376–396. doi:10.1016/j.atmosenv.2011.09.049
- Pay, M.T., Martínez, F., Guevara, M., Baldasano, J.M., 2014. Air quality forecasts at kilometer scale grid over Spanish complex terrains. *Geosci. Model Dev.* 7, 1979–2014. doi:10.5194/gmd-7-1979-2014
- Pérez, C., Sicard, M., Jorba, O., Comerón, A., Baldasano, J.M., 2004. Summertime re-circulations of air pollutants over the north-eastern Iberian coast observed from systematic EARLINET lidar measurements in Barcelona. *Atmos. Environ.* 38, 3983–4000. doi:10.1016/j.atmosenv.2004.04.010
- Pérez, C., Jiménez, P., Jorba, O., Sicard, M., Baldasano, J.M., 2006a. Influence of the PBL scheme on high-resolution photochemical simulations in an urban coastal area over the Western Mediterranean. *Atmos. Environ.* 40, 5274–5297. doi:10.1016/j.atmosenv.2006.04.039
- Pérez, C., Nickovic, S., Pejanovic, G., Baldasano, J.M., Özsoy, E., 2006b. Interactive dust-radiation modeling: A step to improve weather forecasts. *J. Geophys. Res. Atmos.* 111. doi:10.1029/2005JD006717
- Pérez C., Haustein, K., Janjic, Z., Jorba, O., Hunees, N., Baldasano, J.M., Black, T., Basart, S., Nickovic, S., Miller, L., Perlwitz, J.P., Schulz, M., Thomson, M., 2011. Atmospheric dust modeling from meso to global scales with the online NMMB/BSC-Dust model – Part 1: Model description, annual simulations and evaluation. *Atmos. Chem. Phys.* 11, 13001-13027, doi:10.5194/acp-11-13001-2011
- Pichelli, E., Ferretti, R., Cacciani, M., Siani, A.M., Ciardini, V., Di Iorio, T., 2014. The role of urban boundary layer investigated with high-resolution models and ground-based observations in Rome area: a step towards understanding parameterization potentialities. *Atmos. Meas. Tech.* 7(1), 315-332
- Pleim, J.E., 2007. A combined local and nonlocal closure model for the atmospheric boundary layer. Part I: Model description and testing. *J. Appl. Meteorol. Climatol.* 46, 1383–1395. doi:10.1175/JAM2539.1
- Quan, J., Gao, Y., Zhang, Q., Tie, X., Cao, J., Han, S., Meng, J., Chen, P., Zhao, D., 2013. Evolution of planetary boundary layer under different weather conditions, and its impact on aerosol concentrations. *Particuology* 11(1), 34-40
- Richardson, H., Basu, S., Holtslag, A.A.M., 2013. Improving Stable Boundary-Layer Height Estimation Using a Stability-Dependent Critical Bulk Richardson Number. *Boundary-Layer Meteorol.* 148, 93–109. doi:10.1007/s10546-013-9812-3
- Rocadenbosch, F., Vázquez, G., Comerón, A., 1998. Adaptive filter solution for processing lidar returns: optical parameter estimation. *Appl. Opt.* 37, 7019–7034. doi:10.1364/AO.37.007019
- Rocadenbosch, F., Soriano, C., Comerón, A., Baldasano, J.M., 1999. Lidar inversion of atmospheric backscatter and extinction-to-backscatter ratios by use of a Kalman filter. *Appl. Opt.* 38, 3175–3189.
- Rocadenbosch, F., Sicard, M., Comerón, A., Baldasano, J.M., Rodríguez, A., Agishev, R., Muñoz, C., Lopez, M.A., Garcia-Vizcaino, D., 2002. The UPC scanning Raman lidar: An engineering overview. In: *Lidar Remote Sensing in Atmospheric and Earth Sciences – Reviewed and revised papers presented at the 21st ILRC*, pp 69–70

- Roeckner, E., Brokopf, R., Esch, M., Giorgetta, M. a., Hagemann, S., Kornblueh, L., Manzini, E., Schlese, U., Schulzweida, U., 2006. Sensitivity of simulated climate to horizontal and vertical resolution in the ECHAM5 atmosphere model. *J. Clim.* 19, 3771–3791. doi:10.1175/JCLI3824.1
- Rouil, L., Honoré, C., Vautard, R., Beekman, M., Bessagnet, B., Malherbe, L., Meleux, F., Dufour, A., Elichegaray, C., Flaud, J.M., Menut, L., Martin, D., Peuch, A., Peuch, V.H., Poisson, N., 2009. Prev'air: An operational forecasting and mapping system for air quality in Europe. *Bull. Am. Meteorol. Soc.* 90, 73–83. doi:10.1175/2008BAMS2390.1
- Salvador, P., Alonso, S., Pey, J., Artñano, B., de Bustos, J.J., Alastuey, A., Querol, X., 2014. African dust outbreaks over the western Mediterranean basin: 11 year characterization of atmospheric circulation patterns and dust source areas. *Atmos. Chem. Phys.* 14, 6759–6775, doi:10.5194/acp-14-6759-2014
- Schaap, M., Hendriks, C., Kranenburg, R., 2015. Performance of European chemistry transport models as function of horizontal resolution. *Unece.Org* 112, 90–105. doi:10.1016/j.atmosenv.2015.04.003
- Seaman, N.L., 2000. Meteorological modeling for air-quality assessments. *Atmos. Environ.* 34, 2231–2259. doi:10.1016/S1352-2310(99)00466-5
- Seibert, P., Beyrich, F., Gryning, S.E., Joffre, S., Rasmussen, A., Tercier, P., 2000. Review and intercomparison of operational methods for the determination of the mixing height. *Atmos. Environ.* 34(7), 1001–1027
- Shin, H.H., Hong, S.-Y., 2011. Intercomparison of planetary boundary-layer parametrizations in the WRF model for a single day from CASES-99. *Boundary-Layer Meteorol.* 139(2), 261–281
- Sicard, M., Pérez, C., Rocadenbosch, F., Baldasano, J.M., García-Vizcaino, D., 2006. Mixed-layer depth determination in the Barcelona coastal area from regular lidar measurements: Methods, results and limitations. *Boundary-Layer Meteorol.* 119, 135–157. doi:10.1007/s10546-005-9005-9
- Sicard, M., Rocadenbosch, F., Reba, M.N.M., Comerón, A., Tomás, S., García-Vizcaino, D., Batet, O., Barrios, R., Kumar, D., Baldasano, J.M., 2011. Seasonal variability of aerosol optical properties observed by means of a Raman lidar at an EARLINET site over Northeastern Spain. *Atmos. Chem. Phys.* 11, 175–190. doi:10.5194/acp-11-175-2011
- Sicardi, V., Ortiz, J., Rincón, A., Jorba, O., Pay, M.T., Gassó, S., Baldasano, J.M., 2012. Assessment of Kalman filter bias-adjustment technique to improve the simulation of ground-level ozone over Spain. *Sci. Total Environ.* 416, 329–42. doi:10.1016/j.scitotenv.2011.11.050
- Skamarock, W.C., Klemp, J.B., Dudhia, J., Gill, D.O., Barker, D.M., Wang, W., Powers, J.G., 2005. A description of the Advanced Research WRF Version 2. *NCAR Tech. Note NCAR/TN-468+STR*, doi:10.1.1.127.5949
- Skamarock, W.C., Klemp, J.B., 2008. A time-split nonhydrostatic atmospheric model for weather research and forecasting applications. *J. Comput. Phys.* 227(7):3465–3485
- Soret, A., Jimenez-Guerrero, P., Baldasano, J.M., 2011. Comprehensive air quality planning for the Barcelona Metropolitan area through traffic management. *Atmos. Pollut. Res.* 2, 255–266. doi:10.5094/APR.2011.032

- Spinhirne, J.D., Rall, J.A.R., Scott, V.S., 1995. Compact eye safe lidar systems. *Rev. Laser Eng.* 23, 112–118.
- Stull, R.B., 1988. An Introduction to Boundary Layer Meteorology. *Book 666*. doi:10.1007/978-94-009-3027-8
- Sukoriansky, S., Galperin, B., Perov, V., 2005. Application of a new spectral theory of stably stratified turbulence to the atmospheric boundary layer over sea ice. *Boundary-Layer Meteorol.* 117, 231–257. doi:10.1007/s10546-004-6848-4
- Tewari, M., CoAuthors, 2004. Implementation and verification of the unified NOAA land surface model in the WRF model, in: *20th Conference on Weather Analysis and forecasting/16th Conference on Numerical Weather Prediction*. pp. 11–15.
- Tombrou, M., Dandou, A., Helmis, C., Akylas, E., Angelopoulos, G., Flocas, H., Assimakopoulos, V., Soulakellis, N., 2007. Model evaluation of the atmospheric boundary layer and mixed-layer evolution. *Boundary-Layer Meteorol.* 124, 61–79. doi:10.1007/s10546-006-9146-5
- Troen, I.B., Mahrt, L., 1986. A simple model of the atmospheric boundary layer; sensitivity to surface evaporation. *Boundary-Layer Meteorol.* 37, 129–148. doi:10.1007/BF00122760
- Tsaknakis, G., Papayannis, A., Kokkalis, P., Amiridis, V., Kambezidis, H.D., Mamouri, R.E., Georgoussis, G., Avdikos, G., 2011. Inter-comparison of lidar and ceilometer retrievals for aerosol and Planetary Boundary Layer profiling over Athens, Greece. *Atmos. Meas. Tech.* 4, 1261–1273. doi:10.5194/amt-4-1261-2011
- Upton, G., Cook, I., 2008. A Dictionary of Statistics 2nd edition. *Oxford University Press*, Oxford, United Kingdom, 496 pp
- Welton, E., Campbell, J., Spinhirne, J., Scott, V., 2001. Global monitoring of clouds and aerosols using a network of micro-pulse lidar systems, in: *Proc. SPIE*. pp. 151–158. doi:10.1117/12.417040
- WHO, 2013. Review of evidence on health aspects of air pollution – REVIHAAP Project. Bonn.
- Wilks, D.S., 2006. *Statistical Methods in the Atmospheric Sciences, Meteorological Applications*.
- Zhang, K., Wan, H., Wang, B., Zhang, M., Feichter, J., Liu, X., 2010. Tropospheric aerosol size distributions simulated by three online global aerosol models using the M7 microphysics module. *Atmos. Chem. Phys.* 10, 6409–6434, doi:10.5194/acp-10-6409-2010
- Zhang, Y., Bocquet, M., Mallet, V., Seigneur, C., Baklanov, A., 2012. Real-time air quality forecasting, part I: History, techniques, and current status. *Atmos. Environ.* 60, 632–655. doi:10.1016/j.atmosenv.2012.06.031